**KTH Chemical Science
and Engineering**

Reactions of aqueous radiolysis products with oxide surfaces:

An experimental and DFT study

Cláudio Miguel Lousada Patrício

AKADEMISK AVHANDLING

som med tillstånd av Kungliga Tekniska Högskolan i Stockholm framlägges till offentlig granskning för avläggande av teknisk doktorsexamen fredagen den 12 April 2013, kl 10.00 i sal K2 Teknikringen 28, KTH, Stockholm. Avhandlingen försvaras på engelska. Opponent: Doktor Jean-Philippe Renault från Cea Saclay, Frankrike.

List of Papers

This thesis is based on the following papers:

I   "Kinetics, Mechanism, and Activation Energy of H_2O_2 Decomposition on the Surface of ZrO_2"
    Cláudio M. Lousada and Mats Jonsson, *Journal of Physical Chemistry C*, **2010**, 114, 11202–11208

II "Reactivity of H_2O_2 towards different UO_2-based materials: The relative Impact of Radiolysis Products Revisited"
    Cláudio M. Lousada, Martin Trummer, and Mats Jonsson, *Journal of Nuclear Materials*, **2013**, 434, 434–439 *(accepted in the beginning of 2012)*

III "On the redox reactivity of doped UO_2 pellets-Influence of dopants on the H_2O_2 decomposition mechanism"
    Reijo Pehrman, Martin Trummer, Cláudio M. Lousada, and Mats Jonsson, *Journal of Nuclear Materials*, **2012**, 430, 6–11

IV "Mechanism of H_2O_2 Decomposition on Transition Metal Oxide Surfaces" Cláudio M. Lousada, Adam Johannes Johansson, Tore Brinck, and Mats Jonsson, *Journal of Physical Chemistry C*, **2012**, 116, 9533–9543

V   "Reactivity of metal oxide clusters with hydrogen peroxide and water – a DFT study evaluating the performance of different exchange–correlation functionals"
    Cláudio M. Lousada, Adam Johannes Johansson, Tore Brinck and Mats Jonsson, *Physical Chemistry Chemical Physics*, **2013**, DOI: 10.1039/c3cp44559c

VI "Enhanced hydrogen formation during the catalytic decomposition of H_2O_2 on metal oxide surfaces in the presence of HO radical scavengers"
    Cláudio M. Lousada, Jay A. LaVerne, and Mats Jonsson, *Journal of Physical Chemisty C*, under review

VII "Catalytic decomposition of hydrogen peroxide on transition metal and lanthanide oxides"
    Cláudio M. Lousada, Miao Yang, Kristina Nilsson, and Mats Jonsson, *Applied Catalysis - Section A*, under review

My contributions to the papers:

Papers I, IV, VI: I did the experiments and most of the DFT calculations (IV) and wrote the first draft of the text.

Papers II: I did half of the experiments and wrote half of the first draft of the texts

Paper III: I did some of the experiments and wrote parts of the first drafts of the texts.

Paper VII: I did part of the experiments and wrote the first draft of the text.

Papers V, VIII: I did the DFT calculations and wrote the first draft of the text.

Abstract

The reactions between aqueous radiolysis products and oxide surfaces are important in nuclear technology in many ways. In solid-liquid systems, they affect (and at the same time are dependent on) both the solution chemistry and the stability of materials under the influence of ionizing radiation. The stability of surface oxides is a factor that determines the longevity of the materials where such oxides are formed. Additionally, the aqueous radiolysis products are responsible for corrosion and erosion of the materials.

In this study, the reactions between radiolysis products of water – mainly H_2O_2 and HO radicals – with metal, lanthanide and actinide oxides are investigated. For this, experimental and computational chemistry methods are employed. For the experimental study of these systems it was necessary to implement new methodologies especially for the study of the reactive species – the HO radicals. Similarly, the computational study also required the development of models and benchmarking of methods. The experiments combined with the computational chemistry studies produced valuable kinetic, energetic and mechanistic data.

It is demonstrated here that the HO radicals are a primary product of the decomposition of H_2O_2. For all the materials, the catalytic decomposition of H_2O_2 consists first of molecular adsorption onto the surfaces of the oxides. This step is followed by the cleavage of the O-O bond in H_2O_2 to form HO radicals. The HO radicals are able to react further with the hydroxylated surfaces of the oxides to form water and a surface bound $HO^\bullet$ center. The dynamics of formation of $HO^\bullet$ vary widely for the different materials studied. These differences are also observed in the activation energies and kinetics for decomposition of H_2O_2. It is found further that the removal of $HO^\bullet$ from the system where H_2O_2 undergoes decomposition, by means of a scavenger, leads to the spontaneous formation of H_2.

The combined theoretical-experimental methodology led to mechanistic understanding of the reactivity of the oxide materials towards H_2O_2 and HO radicals. This reactivity can be expressed in terms of fundamental properties of the cations present in the oxides. Correlations were found between several properties of the metal cations present in the oxides and adsorption energies of H_2O, adsorption energies of HO radicals and energy barriers for H_2O_2 decomposition. This knowledge can aid in improving materials and processes important for nuclear technological systems, catalysis, and energy storage, and also help to better understand geochemical processes.

Sammanfattning

Inom kärnteknik är reaktioner mellan radiolysprodukter i vätskefas och metallytors oxider viktiga på många sätt. I fastfas-vätskefassystem påverkar de (och påverkas samtidigt av) både lösningens kemi och materialens stabilitet när de utsätts för joniserande strålning. Stabiliteten hos ytoxider är en faktor som delvis bestämmer materialens livslängd där sådana oxider bildas. Dessutom orsakar radiolysprodukter från vatten korrosion och erosion av materialen.

I denna studie undersöks de kemiska reaktionerna mellan vattens radiolysprodukter -främst H_2O_2 och HO radikaler- och metall-, lantanid- och aktinid-oxider. Studien omfattar båda experimentella och kvantkemiska beräknings- metoder. För de experimentella studierna av de här systemen behövdes nya metoder utvecklas och användas, särskilt för att studera de reaktiva HO radikalerna. Även för att utföra kvantkemiska beräkningar krävdes det utveckling av modeller och benchmarking av befintliga metoder. Experimenten, tillsammans med kvantkemiska beräkningar, producerade värdefulla kinetiska, energetiska och mekanistiska data.

Det är här bevisat att HO radikaler är en primär produkt från den katalytiska nedbrytningen av H_2O_2. För samtliga material sker den katalytiska sönderdelningen av H_2O_2 först genom molekylär adsorption på ytorna av oxiderna. Detta steg följs av klyvning av väteperoxidens O-O bindning, vilket leder till bildning av HO radikaler. HO radikalerna kan sedan reagera vidare med de hydroxylerade oxidernas ytor. Det leder till bildning av vatten och ett ytbundet $HO^\bullet$. Dynamiken för bildandet av $HO^\bullet$ varierar betydligt för de olika material som studerats. Dessa skillnader observerades också i aktiveringsenergier och i kinetiken för sönderdelning av H_2O_2. Det visar sig vidare att när $HO^\bullet$ avlägsnas -med hjälp av en radikalinfångare- från systemet där H_2O_2 genomgår nedbrytning bildas H_2 spontant.

Den kombinerade teoretiska-experimentella metodiken ger en mekanistisk förståelse av reaktiviteten av oxidmaterial gentemot H_2O_2 och HO radikaler. Denna reaktivitet kan uttryckas i termer av fundamentala egenskaper hos katjonerna som är närvarande i oxiderna. Korrelationer konstaterades finnas mellan flera egenskaper hos metallkatjoner närvarande i oxiderna och adsorptionsenergier för H_2O, adsorptionsenergier för HO radikaler och energibarriärer för H_2O_2s nedbrytning. Denna kunskap kan hjälpa till att förbättra material och processer som är viktiga för kärntekniska system, katalys och energilagring, och även bidra till att bättre förstå vissa geokemiska processer.

List of Abbreviations

DFT - Density functional theory

$G(x)$ - Radiation chemical yield for the species x

$\dot{C}(x)$ - Amount of species x produced

$\dot{D}$ - Radiation dose rate

ρ - Solvent density

k_2 - Second-order rate constant

k_2 - First-order rate constant

k_0 - Zeroth-order rate constant

k_c - Catalytic capacity of the surface

Sa -Surface area of solid

k - Reaction rate constant

E_a - Arrhenius activation energy

$E_{a,ads}$ - Arrhenius activation energy of adsorption

A - Arrhenius pre-exponential or frequency factor

R - Gas constant

T - Absolute temperature

$\Delta H^{\ddagger}$ - Enthalpy of activation

k_B - Boltzmann constant

h - Planck constant

$\Delta S^{\ddagger}$ - Entropy of activation

$\Delta G^{\ddagger}$ - Gibbs energy of activation

ΔG° - Gibbs free energy for the reaction

BEP - Brønsted, Evans and Polanyi

ΔE_{ads} - Adsorption energy

ΔH_{ads} - Adsorption enthalpy

α_{BEP} - Brønsted, Evans and Polanyi proportionality constant

AFM – Atomic force microscopy

SEM - Scanning electron microscopy

XRD - X-ray diffraction

UHV - Ultra-high vacuum

PW91 – Perdew-Wang functional

PBE - Perdew-Burke-Ernzerhof functional

GGA - Generalized gradient approach

MGGA - Meta-GGA

τ - Kinetic-energy density

HF - Hartree-Fock

LDA - Local density approximation

B3LYP - Becke, three-parameter, Lee-Yang-Parr functional

B3LYP-D - Becke, three-parameter, Lee-Yang-Parr functional supplemented with dispersion

B3LYP* - Becke, three-parameter, Lee-Yang-Parr functional with 15% Hartree-Fock exchange

PBE0 - Perdew-Burke-Ernzerhof functional supplemented with Hartree-Fock exchange

M06 - Minnesota 2006 functional

M06-L - Minnesota 2006 local functional

SIE - Self-interaction error

ECP - Effective core potential

GRD - Global reactivity descriptors

μ - Chemical potential

E - Electronic energy

N - Number of electrons

Z - Atomic number

χ - Electronegativity

IP- Ionization potential

EA - Electron affinity

KS - Kohn-Sham

η - Chemical hardness

HOMO - Highest occupied molecular orbital

LUMO - Lowest unoccupied molecular orbital

PBC - Periodic boundary conditions

SIMFUEL - Simulated high-burnup UO_2-based fuel

Tris - Tris(hydroxymethyl)aminomethane

TAPS - N-[Tris(hydroxymethyl)methyl]-3-aminopropanesulfonic acid

AAA - Acetoacetanilide

PWPW91 - Perdew-Wang 1991 (gradient correction) functional with correlation by Perdew-Wang 1991

LACVP - Los Alamos effective core potential with split valence basis set 6-31+G(d)

* - Polarization functions

+ - Diffuse functions

E_{HF}^{XC} - Hartree-Fock exchange

QST - Quadratic synchronous transit

CSDZ - Cundari-Stevens effective core potential basis set for lanthanides

t - Time

Sa/V - Solid surface area to solution volume ratio

BDE - Bond dissociation energy

B.E.T. - Brunauer, Emmet, and Teller

P - Pressure

I.C.P. - Inductively coupled plasma spectroscopy

b_2 - Intercept at zero coordinate

EPR/ESR - Electron paramagnetic resonance/electron spin resonance spectroscopy

ΔE_r - Reaction electronic energy

CCSD(T) - Coupled-cluster with triple excitations allowed

PES - Potential energy surface

D_{exp} - Absolute deviation from the experimental value for the activation energy

E_a^{ZPE} - Activation energy with zero point energy correction

S_{CA} - Surface catalytically active site

K - Langmuir adsorption equilibrium constant

X_m - Amount of adsorbate required for a monolayer coverage on the surface of an adsorbent

k_a/k_d - Rate constants of adsorption/desorption

C_e - Equilibrium concentration of adsorbate in solution

e - Change in Mulliken charge

χ_P - Pauling electronegativity

λ_{max} – Wavelength of maximum absorbance

Table of Contents

1. The context of this work

1.1   Chemical processes in nuclear technology

The chemistry of a nuclear reactor is a special topic in many ways. The extreme temperature and pressure at which nuclear reactors operate makes *in situ* studies of their chemistry a difficult subject. In addition, very intense ionizing radiation is emitted from the reactor core. The materials that constitute a nuclear reactor have to withstand these extreme conditions and still be unsusceptible to unexpected failure. These features, which the public, operators and authorities expect from the materials present in a nuclear reactor, are to a very large extent controlled by the chemistry of the system. In general, the high temperature and pressure stability of the materials in nuclear reactors is extrapolated from laboratory data which are often obtained under conditions that are not as extreme as the ones in operating reactors.[1] Though, the tools of thermodynamics make this approach possible and the materials stability can be predicted to a good extent from phase diagrams obtained under diverse conditions of temperature, pressure, concentration of solutes, ionic strengths of solutions, etc.

The fact that the materials surfaces suffer from wear and exhaustion in nuclear reactors is evident in deposits of corrosion products that appear in coolant circulation systems, valves, pumps, etc. These deposits, also called CRUD (Chalk River Unidentified Deposit), are the result of the materials wear and tear.[2] They are a consequence of chemical processes and can affect the performance of the components where they build up deposits. Such deposits are very often radioactive, a feature which increases the occupational radiation exposure levels for technicians and other personnel.[3] It is known that these deposits are corrosion products and as such are composed mostly of oxides of the metals that constitute the surfaces of the reactor. The stability of the reactor components surface oxides is a determinant factor for the longevity of the materials and the formation of deposits. The build-up of stable oxide layers leads to a decrease in the corrosion rate of the system surfaces.[4] It is desirable that these oxides are as stable as possible in order to minimize the materials wear and erosion. The stability of the protective layers of oxides is dependent on a number of physical and chemical parameters such as pH, types of solutes present in the coolant, temperature, pressure, mechanical impact and radiation dose.[5]

Even though thermodynamic stability data for reactor materials exist for a considerable range of: temperatures, pressures, solute concentrations and pH; at the atomic scale, little is known about the chemical processes occurring at the reactor materials surfaces.[6] Initially there is the chemistry of the radiolysis products of water and solutes that leads to the formation of the oxide layers. This is mainly redox chemistry. After the formation of the

oxide, the chemistry changes and other types of reactions start to occur. The reactivity of the radiolysis products of water and the oxides surfaces involves more than pure redox chemistry. Instead, it becomes an ensemble of different chemical processes that affect the chemistry of the reactor and the stability of the protective oxides.

1.2   Interfacial processes in nuclear technology

The important processes in reactor chemistry described in section 1.1 are in water-cooled reactors, mainly solid-liquid processes. The build-up of an oxide layer occurs at the interface between the solid and the liquid phases. The chemistry of the interfacial processes is dependent on the properties of the solid material and of the liquid phase. The chemistry of a nuclear reactor is the result of a very large number of chemical reactions that occur in the liquid phase and at the interfaces between the liquid phase and the solid surfaces. The degree of complexity of this system is increased due to the presence of ionizing radiation and its interaction with the materials.[7] This drives chemical phenomena that would not occur in the absence of ionizing radiation. Even though complex, this system can be understood by studying the key reactions that have a higher impact on the overall reactor chemistry.

The radiation chemistry of liquid water is a well-known phenomenon that had its main expansion in the middle of the twentieth century.[8] The fast development in the knowledge of radiation chemistry of water was mainly due to the need of some developed nations to drive their nuclear programs. The fierce competition for the knowledge of radiation induced phenomena in water lead to the production of a large quantity of radiation chemical yields– so called G-values, rate constants for formation and reaction and stability constants for the radiolysis products of water. This knowledge lead to the development of other important fields of chemistry and many radiolytic species of water were studied thoroughly in solution. But even the most studied of those species, the solvated electron, still raises questions today, for example, in processes such as its interactions with organic molecules or other solutes besides pure water. With the development of the nuclear power technology, the deep knowledge of the radiolysis of water had proven to be of utmost importance for the understanding and control of the chemistry of reactors and to determine the stability of reactor materials under operation. Though, in spite of their importance for determining the stability of the materials and the reactor chemistry, the radiation induced processes occurring at the interfaces between the solid and the liquid phases remain scarcely understood.[9] The existing knowledge on interfacial radiation chemistry processes is somewhat restrained to macroscale phenomena, such as the thermodynamic data for formation and stability of oxide layers, dissolution of corrosion products etc. These macroscopic processes are

though the result of microscale phenomena. This means, processes occurring at the atomic and molecular scale. To better understand and predict the macroscale observations, it is necessary to know what is happening at the microscale level that leads to a certain observable macroscale phenomenon.[10] This will ultimately lead to a better control of chemical processes in nuclear technology, better understanding of the materials chemistry and aid in the development of improved materials for future usage in reactors and in nuclear waste management.

1.3   The scope of this work

  It is the purpose of this work to bring knowledge to the field of radiation induced processes at solid-liquid interfaces. This means contributing to the understanding of the reactivity of radiolytic products of water and solid surfaces of relevance in nuclear technology. This knowledge is relevant not only for reactor technology applications but also for applications related with spent nuclear fuel, catalysis, and geochemistry or semi-conductor chemistry. It is the goal of this thesis to present and discuss studies which ultimately focus on the atomic and molecular scale understanding of solid-liquid interfacial processes. It is also the goal of this work to develop experimental and theoretical methodologies that can be used for future studies of such phenomena. Ultimately it is my wish to provide the materials scientists with information on chemical reactivity of metal oxides present in nuclear technological environments and to find correlations between properties of the materials and their reactivity towards a given radiolysis product.

2. Introduction

2.1   Water radiolysis

  The interaction between ionizing radiation and matter, with this either in solid, liquid or gaseous state, leads to a multitude of physical and chemical phenomena.[11,12] Water is no exception and its interaction with ionizing radiation leads to the formation of an array of chemical species with both diverse and interesting chemistry. Upon deposition of energy in a water molecule, it undergoes excitation to a higher energy level (*i.e.* electronic and/or vibrational and/or rotational).[13] From there, one of two things can happen: the energy of the radiation is not enough to excite the water molecule to an electronic meta-stable state and the water molecule returns from the excited state to the ground state, releasing the excess energy as kinetic energy–radiant, translational, rotational or vibrational; the other outcome happens if the incident radiation is energetic enough to excite the water molecule to a meta-stable state where it will decompose into its

constituent species. The interaction of ionizing radiation with water leads to the second process, as the energy of this type of radiation is enough to transform the water molecule into its constituents which by means of further reactions form the so called radiolytic products of water. Under a given dose rate, the amount of these products reaches a constant value, a steady-state concentration. The process of formation of the primary radiolysis products is complete in times in the order of 10^{-7} s after energy deposition.[14] At this time, the products formed in a spur by the deposition of energy will have diffused away from the spur and the probability for their reactions with species formed in the same spur is negligible. Under these conditions, the water chemistry can be summarized by[14]

$$H_2O \longrightarrow e_{aq}^-, H^\cdot, HO^\cdot, H_2, H_2O_2, H_3O^+ \tag{R1}$$
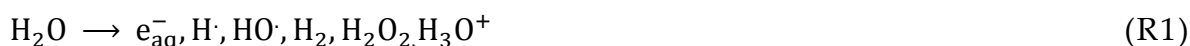
The amount of products formed per unit of energy deposited is the radiation chemical yield or *G*-value. This is defined as the number of specified chemical events in an irradiated substance, produced per 100 eV of energy absorbed from ionizing radiation.[15] The products of water radiolysis are well reported and their radiation chemical yields are known under a diversity of conditions. The *G*-value for a radiolysis product in a medium depends on the presence of solutes in that medium. The *G*-value is expressed in S.I. units as

$$G(x) = \frac{n_x}{\delta E} \tag{1}$$

where $G(x)$ is the radiation chemical yield for the species x and n_x is the number of moles of x formed per unit of energy (δE) in Joules (J) deposited in the medium. This definition of G value applies for any solvent, but the *G*-value for a certain species is solvent dependent. In systems where only pure water is present, the time dependency of the events that lead to the formation of water radiolysis products can be represented by Figure 1.
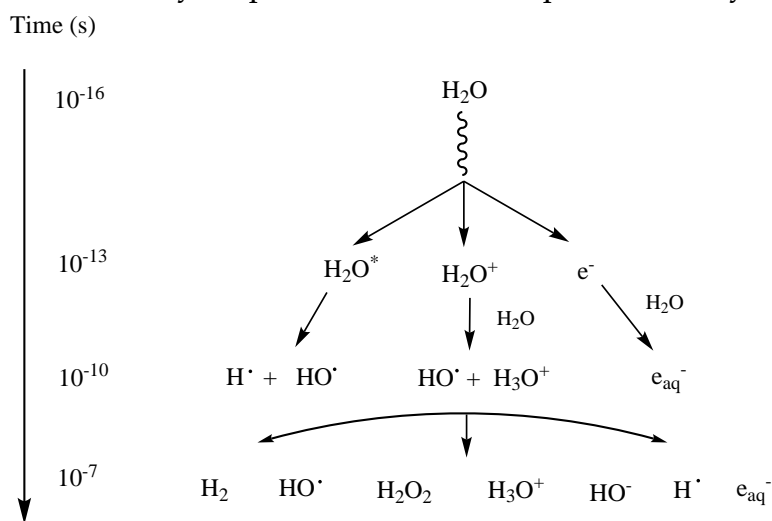

Figure 1. Time scale of events in water radiolysis leading to the primary products.

The G-values for the primary γ-radiolysis products of water for the pH range 3 to 11 are

$$G(e_{aq}^-) = G(HO^\bullet) = G(H_3O^+) = 2.7 \ (\times 10^{-7}) \ \text{mol·J}^{-1}$$
$$G(H^\bullet) = 0.6, \ G(H_2) = 0.45, \ G(H_2O_2) = 0.7 \ (\times 10^{-7}) \ \text{mol·J}^{-1}$$

the G-values for a given radiolysis product can be used to obtain its concentration as a function of the time dependent energy deposition through

$$\dot{C}(x) = G\dot{D}\rho \tag{2}$$

where $\dot{C}(x)$ is the amount of the species x produced in mol·dm^{-3}·s^{-1}, $\dot{D}$ is the radiation dose rate, and ρ is the solvent density. The concentration of a radiolysis product can be controlled by adding a reactant to the media that reacts with the precursors of that radiolysis product which will lead to a different G-value. As an example, the G-value for the HO radical in pure water is 2.7×10^{-7} mol·J^{-1}. In a solution saturated with N$_2$O, the following reactions will take place[12]

$$e_{aq}^- + N_2O \longrightarrow N_2 + O^{\bullet-} \qquad k = 9.1 \times 10^9 \ \text{L·mol}^{-1}\text{·s}^{-1} \tag{R2}$$
$$O^{-\bullet} + H_2O \longrightarrow HO^\bullet + HO^- \qquad k = 1.8 \times 10^6 \ \text{L·mol}^{-1}\text{·s}^{-1} \tag{R3}$$
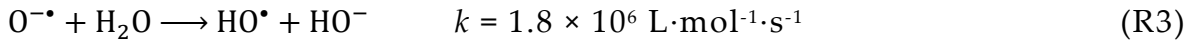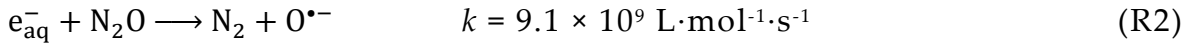
where k is the rate constant for the respective reaction. Under these conditions, the G-value for HO$^\bullet$ becomes 5.5×10^{-7} mol·J^{-1}. Under reactor conditions, similar changes in G-values of radiolysis products occur when additives are added to control the reactor chemistry. For example the addition of H$_2$ to a reactor coolant[16] is done in order to mitigate the formation of oxidative water radiolysis products such as H$_2$O$_2$ and O$_2$ and leads to the following reactions

$$H_2 + HO^\bullet \longrightarrow H_2O + H^\bullet \tag{R4}$$

$$H^\bullet + H_2O_2 \longrightarrow H_2O + HO^\bullet \tag{R5}$$
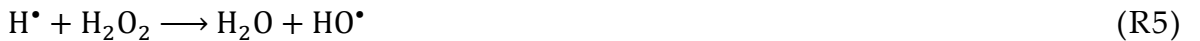
H$_2$O$_2$ and HO$^\bullet$ are precursors of O$_2$ according to

$$HO^\bullet + H_2O_2 \longrightarrow HO_2^\bullet + H_2O \tag{R6}$$

$$HO_2^\bullet + HO_2^\bullet \longrightarrow O_2 + H_2O_2 \tag{R7}$$

In the presence of an excess H$_2$, the O$_2$ concentration is reduced following

$$H^\bullet + O_2 \longrightarrow HO_2^\bullet \tag{R8}$$

The decrease in H$_2$O$_2$ concentration is explained with the fact that the overall rate of the reactions that destroy H$_2$O$_2$ are increased. Even though other species are more powerful oxidants, such as the HO radical, these are usually short lived and the time necessary for their diffusion until they reach a surface will be longer than their half-life in solution. The HO radical

contribution to the oxidative power of the radiolysis products of water is then much less than that of H_2O_2 which is a long lived species in comparison. H_2O_2 is the most important molecular oxidant from the radiolysis products of water.

2.2 Chemical kinetics and transition state theory

It is known that some processes that lead to a lower energy state of a chemical system take place readily. Though, the majority of chemical reactions, even though they lead to a decrease in the systems energy upon formation of products, have a rate which in many cases is low. One of the features regarding the study of reaction rates is that with the exception of very specific simple systems which are far from real – laboratory sized – systems, a rate cannot be calculated from first principles. Theory is not yet developed to the point where it is possible to calculate how fast most reactions will take place, with the exception of some simple reactions. Though, for complex systems, obtaining kinetic parameters from first-principles is still a field in development.[17] Chemical kinetics is then, largely, an experimental science. Under reactor conditions, the kinetics determines the steady-state concentrations of radiolysis products. Even though the reactions of the very reactive radicals formed according to (R1) are thermodynamically favorable, these radicals exist in steady-state concentrations under a constant dose rate of radiation. This is because at steady-state conditions the rates of their formation are equal to the rates of their consumption.

For some reactions, in a wide range of concentrations, the rate law is independent of the concentration of reactant. An example of this is the decomposition of a reactant on the surface of a catalyst.[18] The reaction takes place on the catalytically active sites of the surface of the catalyst. This happens because the reactant is adsorbed to the surface and, within a range of reactant concentrations and catalyst surface areas the catalyst surface becomes essentially saturated with reactant. As such, the total concentration of reactant in solution does not influence the surface processes as long as there is enough reactant to cover the active sites on the surface of the catalyst. Consequently, the decomposition of a reactant on a specific, fixed amount of catalyst occurs at a constant rate over a wide range of reactant concentrations. This is no longer valid as the reaction approaches completion. Under such conditions, the concentration of reactant does affect the rate of the reaction because its concentration determines the rate at which the active sites on the solid surface become occupied. For conditions where the reaction rate is independent of the reactant concentration, the reaction is zeroth-order with respect to that reactant.

For a heterogeneous reaction – such as the case of as a solute R reacting with an aqueous particle suspension of a solid – which obeys first-order kinetics, the second-order rate constant can be determined by studying the variation in the first-order rate constant as a function of solid surface area to solution volume ratio. The second-order rate expression is given by

$$-\frac{d[R]}{dt} = k_2 \left(\frac{Sa}{V}\right) [R] \tag{3}$$

where Sa denotes the surface area of the solid, V is the volume of the solution where the reaction takes place and k_2 is the second-order rate constant. For the case where the reaction obeys zeroth-order, its catalyst surface area dependency gives a quantity which represents the catalytic capacity of the surface and is expressed in the units of $mol \cdot m^{-2} \cdot s^{-1}$.

The transition-state theory initially formulated by Eyring in 1935, and its further developments provide tools to extract energetic data from kinetic parameters.[19] The transition state theory allowed for a major breakthrough in the understanding of chemical reactivity because it is based in the premise that thermodynamic data can be obtained from kinetic data. And in turn the kinetic parameters of chemical reactions depend on thermodynamic properties of the system such as the activation enthalpy and entropy. Though, prior to this less empirical treatment of the effect of temperature in the reaction rates, an empirical approach to extract energetic data from reaction kinetics had been developed by Svante Arrhenius. His equation relates the temperature dependency of the rate constant of a reaction with the reaction activation energy according to

$$k = Ae^{-Ea/(RT)} \tag{4}$$

where k is the reaction rate constant, R is the gas constant, T is the absolute temperature, E_a is the Arrhenius activation energy and A is the pre-exponential or frequency factor. Following the Arrhenius approach and applying concepts from thermodynamics, kinetic theory and statistical thermodynamics, Eyring developed the concepts of the transition-state theory which relates the temperature dependency of a reaction rate with thermodynamic quantities according to

$$k = \frac{k_B T}{h} e^{-\frac{\Delta G^{\ddagger}}{RT}} \quad or, \quad k = \left(\frac{k_B T}{h}\right) e^{\left(\frac{\Delta S^{\ddagger}}{R}\right)} e^{\left(-\frac{\Delta H^{\ddagger}}{RT}\right)} \tag{5}$$

here k is the reaction rate constant, T is the absolute temperature, $\Delta H^{\ddagger}$ is the enthalpy of activation, R is the gas constant, k_B is the Boltzmann constant, h is the Planck constant and $\Delta S^{\ddagger}$ is the entropy of activation and $\Delta G^{\ddagger}$ is the Gibbs energy of activation. Although the significance of the quantities A and E_a extracted from equations (4) and (5) have been debated since many years, at T = 298.15 K, $\Delta H^{\ddagger}$ is lower than E_a by 2.5 kJ·mol⁻¹ according to

$$\Delta H^{\ddagger} = E_a + RT \tag{6}$$

In a similar way, the Arrhenius quantity A relates with $\Delta S^{\ddagger}$ according to

$$A = \frac{k_B T}{h} e^{(1 + \Delta S^{\ddagger}/R)} \tag{7}$$

The application of the equations (4) and (5) to kinetic data can produce valuable mechanistic information. For example, the rigidity of the path from the reactant to the transition-states for the same reaction occurring at two different catalyst surface sites can be better understood by comparing the obtained quantities $\Delta S^{\ddagger}$ for the reactions, provided that both reaction rates obey the same rate law.

2.3 Surface reactions and catalysis

The typical processes of a surface reaction involving a solute and a solid phase are represented in Figure 2.
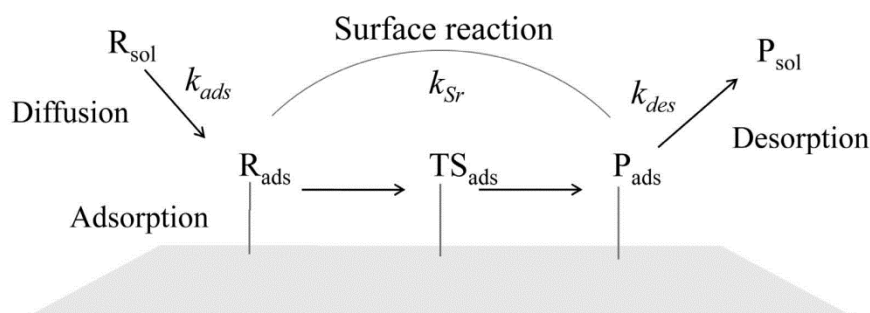
Figure 2. Stages of a surface reaction. R_{sol} and R_{ads} represent the reactant in solution and adsorbed onto the surface respectively. TS_{ads} represents the transition state for the reaction occurring at the surface. P_{ads} and P_{sol} represent the reaction products adsorbed and in solution. k_{ads}; k_{sr} and k_{des} are the rate constants for the adsorption, surface reaction and desorption respectively.

For a catalytic process, the surface will suffer none or only negligible alterations during those stages. While for a non-catalytic process, the surface will suffer alterations such as corrosion, surface dissolution, poisoning, formation of complexes, etc. If the path taken by the reactant is followed from the initial stage where the reactant is free in solution, until the products are released from the surface into solution, there are several steps such as: diffusion to the interface, adsorption onto the surface followed by the surface reaction which can itself consist of several steps, and desorption of products into solution. Each of these transformations will have an energy cost associated and as such these steps can have different rates. The kinetic study

of surface processes such as the one represented in Figure 2 poses a challenge in the sense that each of these steps have to occur on time scales different enough in order for the obtained kinetic data to correspond to the process of interest. This is not always possible and the study of surface reaction kinetics is a multidisciplinary field in what concerns the strategies used to study the individual processes represented above.[20,21]

The concept of catalysis was introduced by Jöns Jacob Berzelius in the early 1800s to describe a number of phenomena that had been practiced prior to his definition. The special feature of a catalyst is that it lowers the energy cost necessary for a chemical transformation to occur. An example is shown in Figure 3.
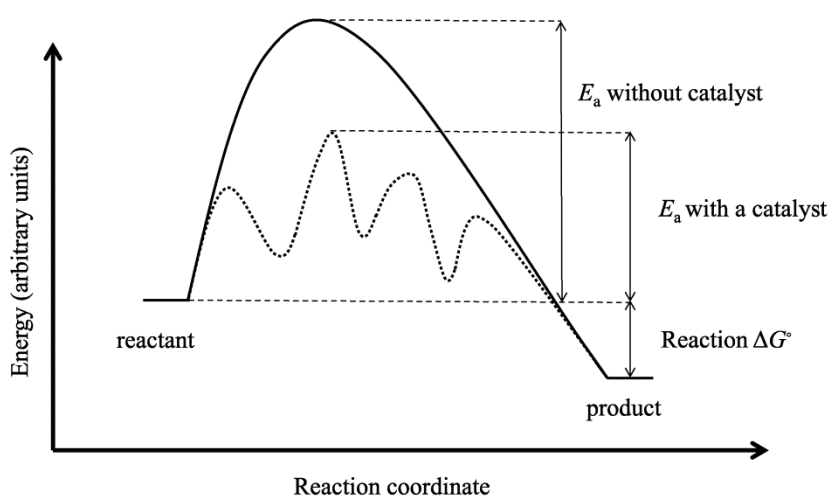
Figure 3. Potential energy surface for a non-catalyzed reaction (higher line) and for a surface catalyzed reaction (lower dashed line). E_a – activation energy for the reaction. $\Delta G°$ – Gibbs free energy for the reaction.

The potential energy surface shown for the catalyzed reaction usually consists of a series of processes that differ from the non-catalyzed reaction pathway. In the case of a surface reaction, there might exist several energy barriers associated with each of the processes represented in Figure 2. Even if this is the case, the activation energy for the catalyzed reaction will be less than for the case of the non-catalyzed process. The rate of a reaction is inversely proportional to the height of its activation energy and this means that the catalyzed reaction proceeds faster.

Molecular diffusion is a function of temperature, solvent viscosity and size of the molecule undergoing diffusion. For small molecules within the approximate size range of water molecules, when the solvent is water, the energy barrier for diffusion in the bulk is usually very low or even nonexistent. For some cases where temperature-induced enhancement of the local viscosity causes anisotropy in solvent micro-solvation mechanisms

which leads to changes in the micro-viscosity, Arrhenius activation energy barriers such as 33 kJ·mol^{-1} have been reported for a species to diffuse through such media.[22] The residence time in a solvation sphere, for a small mass molecule capable of hydrogen bonding with water, such as H_2O_2, is very short, in the order of 2.5 ps.[23] This means that the diffusion of a H_2O_2 molecule in liquid water is a process almost as fast as the diffusion of a water molecule and occurs with a negligible energy cost associated. For the majority of the surface reactions of H_2O_2 at room temperature, this process – *i.e.* diffusion in the bulk solvent or in the regions adjacent to the interface with a solid – will not be the rate determining step.

When immersed in a solvent, surfaces undergo solvation just like a solute. The major difference is that the surface causes a discontinuity of the solvent media and unlike a solute creates a potential energy barrier for the mobility of the solvent molecules. This leads to the formation of an interface between the solid surface and the solvent. An interface is a special region where the solvent molecules have a different disposition from the bulk solution. This disposition will be determined by the Coulomb interactions between the surface and solvent molecules. Recently, it has been demonstrated that for a hydrophobic surface, as the resultant interaction with water is repulsive, at the interface, the solvent density is lower than in the bulk.[24-28] For a hydrophilic surface, the Coulomb attraction between solvent water and surface increases the density of the water at the interface.[28] Both situations are dependent on the density of polar groups at the surface. It has been shown that at an interface with a diamond surface, the water density can increase up to 2.5 kg·L^{-1}. Also, in this region, the viscosity is higher and the mobility of a solute will be lower than in the bulk and a barrier for its diffusion might develop at such interfaces. In the solvent region close to the interface with a surface, the mass transfer resistance depends on the barrier for diffusion posed by slow-moving solvent adjacent to that interface.[29] As the metal oxide surfaces of interest for this study are mostly hydrophilic,[30] the discussion of interfaces from this point on will refer to hydrophilic surfaces unless otherwise stated.

In most cases the wetting of surfaces implies adsorption of water molecules.[31,32] The adsorption of water onto surfaces can be divided into two types depending on the transformation that the water molecules undergo upon adsorption. Dissociative adsorption of water means that the water molecule undergoes splitting into H^+ and HO^- upon adsorption. These products will bind to the nucleophilic and electrophilic surface sites respectively. In a metal oxide, the nucleophilic sites will usually be the exposed surface O anions while the electrophilic sites will be the surface exposed metal cations.[30] This type of adsorbed water constitutes the adsorption layer closer to the surface and it is often the most exothermic

mode of adsorption of water. When moving from the surface towards the bulk media, the water which is adsorbed to the surface and it is not split into its constituents is molecularly adsorbed. The mobility of these water layers increases as going away from the surface towards the bulk solution. An example of this can be seen in Figure 4 for water adsorbed onto the surface of TiO_2.
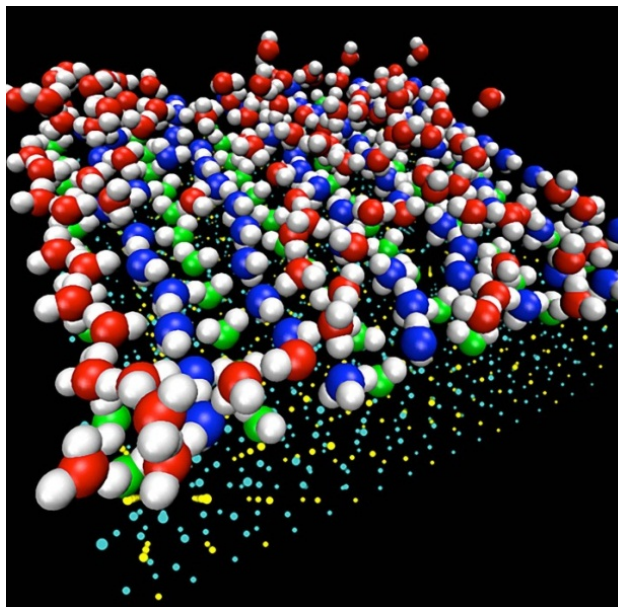
Figure 4. Water on TiO_2 surface. Surface water molecules (O atoms in red, green, and blue, H in white) on a catalytically active nanomaterial (dots under the water molecules). Image: courtesy of Oak Ridge National Laboratory, Tennessee, USA.

The rigidity of the layers of water molecules shown in Figure 4 is higher for the green water molecules followed by the blue labeled layer. The least rigid is the layer labeled in red. Layers further from the surface will have more resemblance with the bulk solvent. At the layers closer to the surface, the water structure usually resembles that of ice in what concerns its mobility, even though it shows a different arrangement in terms of bonding angles and structure.[33,34] The processes involved in the diffusion of a reactant from the bulk liquid until it adsorbs onto the surface, are thus very different from gas-solid processes. At the water-solid interface, the surface adsorbed water layers have an important role in determining the reactivity of the surface.[35] Because this will affect phenomena such as: involvement of the dissociatively adsorbed water on the reaction mechanisms, energy transfer from adsorbates onto the surface upon impact; surface sideways diffusion of adsorbates, hydrogen atom transfer mechanisms, surface reconstruction upon water adsorption, etc. The energy cost for sideways diffusion of adsorbates will usually be higher for a solvated surface than for a gas-phase exposed surface.[36]

Adsorption is a process that consists of chemical interactions between an adsorbate and a surface. These interactions can be of several types, ranging from van der Waals type, to covalent or ionic bonding.[37] Depending on the type of interaction between adsorbate and substrate, adsorption is usually categorized into two kinds: chemisorption or physisorption. According to IUPAC: "*The problem of distinguishing between chemisorption and physisorption is basically the same as that of distinguishing between chemical and physical interaction in general.*" Even though difficult to distinguish clearly, some aspects of each of these types of adsorption are characteristic and a distinction can be made to some extent. In physisorption, the forces involved are weaker than in chemisorption. These are usually intermolecular forces (van der Waals forces) of the same kind as those responsible for the imperfection of real gases and the condensation of vapors, and which do not involve a significant change in the electronic orbital patterns of the species involved. This type of bonding is rather weak. In chemisorption, bonds of the same kind as those that lead to the formation of chemical compounds such as covalent and ionic, are usually involved. This type of adsorption has chemical specificity and it is a process that usually has an activation energy associated. In the chemisorption process, the overlap of the wave functions of adsorbate and substrate is large and changes in the electronic structure of adsorbate and substrate can be observed. In this case, the molecular orbitals of the adsorbate interact with the substrate to produce a new set of electronic levels. Also according to IUPAC: "*No absolutely sharp distinction can be made and intermediate cases exist, for example, adsorption involving strong hydrogen bonds or weak charge transfer.*" Nevertheless, in literature, authors describe chemisorption as a type of adsorption that involves bonding stronger than 50 kJ·mol^{-1} and physisorption as involving bonding weaker than 10 kJ·mol^{-1}.[38] Other authors consider the physisorption energies to lay around 30 kJ·mol^{-1}.[39] This kind of nomenclature is somehow ambiguous and does not provide a clear description of the adsorption process. A more consistent and less ambiguous nomenclature is that of molecular and dissociative adsorption. As the names indicate, molecular adsorption is the type of interaction where upon adsorption onto a surface, the adsorbate does not suffer intramolecular bond breaking – *e.g.* water molecules in Figure 4. In turn, upon dissociative adsorption the adsorbate undergoes intramolecular bond breaking and new chemical species are formed – *e.g.* first layer of water adsorbed onto a TiO$_2$ (110) surface.[40] Adsorption of an adsorbate onto a surface will also have an impact on the surface structure. Surface reconstruction will very often occur upon adsorption. The extent of this reconstruction will depend on the strength of the chemical bonding between the surface and the adsorbate, as well as on the stability of the surface.[37] The pH has also an important effect in the adsorption processes occurring at surfaces in solution. At pH values

lower than the point of zero charge, metal oxide and hydroxide surfaces are positively charged, with an excess of protons bound to the surface. Thus, these surfaces tend to repel positively charged ions and attract negatively charged ions. In the specific case of the systems studied in this work, this can trigger the formation of more stable hydrogen-bonded clusters of hydrogen peroxide in solution and on the surface, having the effect of stabilizing the hydrogen peroxide.[41] At the pH of the point of zero charge, the surface becomes charge neutral and electrostatic repulsion of a positively or negatively charged ion is minimized. At pH above the point of zero charge, the surface becomes negatively charged because of the predominance of hydroxo (OH^-) or oxo (O^{2-}) groups on the surface. Under these conditions, a positively charged ion in solution is attracted to the surface, while a negatively charged ion is repelled.

In general terms, the reactivity of surfaces is determined by the type of chemical elements that constitute the surfaces and by their chemical connectivity and environment. The stability and reactivity of a surface adsorbed species is determined by the type of its bonding with the surface.[42] If the interactions with the surface are strong enough, the adsorbate bonds suffer changes such as elongations and bond breaking in the adsorbate can occur. For the interactions between the adsorbate and surface to occur, new molecular orbitals are formed and the resulting interaction energy is determined by the distribution of electrons over the bonding and anti-bonding orbitals that form the bonds with the surface.[39] The shape and energy of these newly formed molecular orbitals and their occupancy will determine the reactivity of the system surface-adsorbate. Consequently, the type of adsorption is an important factor for determining the reactivity of the adsorbed molecule.

The adsorption structures – *i.e.* if the molecule adsorbs atop, bridging or in higher coordination – relates to the effects that determine the structures and energies of transition-states of reacting surface species.[43,44] As such, being able to foresee the interactions that are determined by the adsorption complexes is a long term goal of surface chemists because this would mean to have a clearer idea of the transition-state structures and of the reactivity of the adsorbed complex. For a homologous series of reactions, Brønsted, Evans and Polanyi (BEP) demonstrated that there is a linear correlation between the transition state energies and the adsorption energies.[45,46] This is because for a homologous series, the changes in activation energies and the changes in adsorption energies are governed by the same physical principles. That correlation is simply explained by[47]

$$E_a = \alpha_{BEP}\Delta E_{ads} \tag{8}$$

where Ea is the activation energy, ΔE_{ads} is the adsorption energy of the reactant, and α_{BEP} is the proportionality constant. When $\alpha_{BEP} < \frac{1}{2}$ the transition state is said to occur early. When $\alpha_{BEP} > \frac{1}{2}$ the transition-state structure is considered to occur late.

All these processes depend on the connectivity between the adsorbate and the surface. Here the important role that surface defects have in the chemical bonding and reactivity of adsorbates has to be considered. This has been demonstrated by experimental and theoretical studies.[48] It was shown for example that the reaction of water with MgO(100) surface occurs only at defect sites. Also, correlations between defect density on the surface of metal oxides and their reactivity have been reported.[49] The reactivity of such surface defects can be orders of magnitude higher than the reactivity of non-defective surface sites. As such, it is expected that those surface defects play a decisive role in surface reactivity. The effect of defects on surface reactivity can have structure specificity. This means that specific types of surface defects are able to selectively catalyze certain types of reactions.[50] This is because the binding of adsorbates and reaction products to the different surface defects will be different and might involve different orbitals from the surface atoms.

While it is thought that such defects may dominate interfacial reactivity, little is known about the nature and density of such features on real particles. This is because such studies are challenging in the sense that the techniques that can be applied to surface structure studies are either very local *i.e.* AFM, SEM, etc; or global *i.e.* confocal profilometry, XRD, etc. The techniques based on electron scattering and their derivatives, produce results that are a weighted average of the contribution of the most common surface sites. Let us consider a surface defect which is 1000 times more reactive than a non-defective surface site. Let us suppose that only 1% of the total surface is constituted by such defects.[51] When running an electron diffraction based technique (for example) to study this surface, the defective site will not be visible, but it might still be the surface site that governs the overall surface reactivity.

Surface science studies are usually performed under controlled conditions using surfaces which are homogeneous in terms of their chemical composition and structure.[52] However, such surfaces exist only in ultra-high vacuum (UHV). The results of these studies are not generally applicable to real interfacial systems – *i.e.* systems where surfaces are in contact with liquids, fluids, gases, organic matter, etc. Real surfaces have structures and reactivity that may be affected by interactions with the environment. Even when only liquid water is present it will affect the geometric and/or

electronic structures of surfaces and those surfaces will not be the same as under UHV conditions.

2.4   Density functional theory

Note: for a more detailed explanation of some concepts involved in DFT see Section 7 of this thesis.

Within the framework of DFT, two of the most widely used density functionals in calculations involving solids are the Perdew-Wang functional (PW91)[53] and the Perdew-Burke-Ernzerhof functional (PBE).[54] The PBE is a parameter free functional which was constructed by making the functional form to satisfy some constrains. Though, these general gradient approach (GGA) type of functionals, in spite of producing good adsorption energies, deviate considerably from experiments in what concerns the description of open shell systems and description of energy barriers for reactions.[55] The improved GGA's, the meta-GGA's (MGGA) take into account the second derivative of the electron density, *i.e,* the Laplacian.[56] Due to difficulties in calculating numerical results for the Laplacian, an alternative MGGA formalism that is more numerically stable is to include in the exchange-correlation potential a dependence on the kinetic-energy density (τ). The cost of a calculation using a MGGA functional is similar to that for a GGA calculation, and the former is typically more accurate than the latter for a pure density functional.[57] Also, the MGGA's perform better than the GGA's in describing non-covalent interactions.

In order to correct the deviations of both the local density (LDA) and GGA based functionals from the Hartree-Fock (HF) results, new functionals were developed which include HF exchange. These functionals involve DFT correlation with a combination of DFT and HF exchange. This class of functionals is designated by hybrid functionals. In the design of hybrid functionals, the optimal amount of HF exchange to include in the functional is either chosen to assume a specific value – between 0 and 100% – or is obtained by fitting: in a way that the resulting functional performs the best in predicting the properties of a molecular database. The B3LYP functional was designed in such a way.[58] It was optimized to reproduce geometries and binding energies of molecular systems to the same accuracy as low-level post-Hartree-Fock methods with the advantage of a significantly lower computational cost. B3LYP can provide accurate molecular geometries even when hydrogen bonds are present.[59] The other approach, that consists in fixing the amount of HF exchange *a priori*, was behind the development of the PBE0 functional.[60,61] This functional form was obtained by supplying the PBE functional with a predefined amount of HF exchange. The PBE0 functional has shown very good performance for structural, thermodynamic,

kinetic and spectroscopic – magnetic, infrared and electronic – properties. The way in which the functional is derived and the lack of empirical parameters fitted to specific properties, make the PBE0 model a widely applicable method for both quantum chemistry and condensed matter physics. It has been reported improved performance of the PBE0 functional over the B3LYP for properties of systems containing light and heavy metals.[62,63]

One of the newest classes of functionals are the hybrid-meta-GGA. This type of functionals combine the inclusion of HF exchange with the meta GGA approach. The M06 functional belongs to this class, and has revealed improved performance over some meta and hybrid functionals.[64] This functional, besides of the Laplacian dependency of the density, includes a dependence on the electronic kinetic-energy density (τ). This is up-spin down-spin dependent. This functional was also parameterized to be self-interaction error (SIE) free. The SIE results from the fact that the interaction of an electron with itself is accounted for in the exchange-correlation functionals obtained from the LDA, GGA and MGGA approaches. The hybrid functionals partly correct the SIE due to the inclusion of HF exchange.[65] The SIE results from a physically unreasonable property that leads to poor performance of the functionals especially in describing systems with non-integer number of electrons.[66] This means that the functionals which are not free from SIE have problems also in describing transition states of chemical reactions (especially those involving homolytic bond cleavage) and charge-transfer complexes. For solids and surfaces, it has been recently show that hybrid DFT functionals that contain a certain amount of HF exchange are necessary to accurately describe the electronic states of nonmetallic solids and the defects in metal oxides.[67-71] In order to properly describe the electronic properties of the defects of TiO_2 surfaces for example, it is necessary to recur to the usage of functionals that incorporate a certain amount of HF exchange.[70] The pure DFT functionals, due to the SIE, fail to give a localized character to trapped electron states and holes in TiO_2 surface defects. When unpaired electronic states are present in the system, this type of functionals will tend do delocalize the electron density in order to minimize the SIE, thus giving results for electron density in surface defects that are poor when compared with experimental data. This situation has been evident whenever pure DFT functionals were used for describing defects in large band gap semiconductors and insulators.[72] Other discrepancies were found in the type of minima for the bonding between $HO^{\bullet}$ and H_2O when these systems were described with pure DFT functionals.[73,74] These situations can be improved by using HF exchange in the functionals. The empirical formalisms to correct for the SIE did not lead to good performing functionals

for systems where fractional charge behavior is present, polarizabilities of polymers and dissociation of molecules.[75]

Efficient basis sets based have been developed based on the usage of an effective core potential (ECP) which replaces the true electron core potential.[76] The number of electrons treated explicitly is then much smaller and the number of required electronic states and basis set size is reduced significantly. This approach made possible the computational study of metals for which the explicit treatment of their core electrons makes such calculations computationally prohibitive. Relativistic effects can also be incorporated in ECP basis sets.[77] This is particularly useful for calculations involving heavier transition metals or lanthanide and actinide elements.[78]

2.5 Conceptual density functional theory

The frontier molecular orbital based approaches to describe the reactivity of organic compounds are an effective way to relate intrinsic properties of organic compounds with their reactivity.[79-81] Simple descriptors such as electronegativity, electron affinities, ionization potentials, hardness and softness have been used for predicting trends on the reactivity of many molecules. These approaches are classified as global reactivity descriptors (GRD). They became wide-spread in recent times because electronic structure calculations are easier to perform due to the increase in computational power. The above mentioned GRD arise naturally from DFT as they can be described in terms of the electron density as follows

$$\mu = \left(\frac{\partial E}{\partial N}\right)_Z = -\chi \tag{9}$$

$$\mu = \begin{cases} -\text{IP} \ (Z - 1 < N < Z) \\ -\text{EA} \ (Z < N < Z + 1) \end{cases} \tag{10}$$

From Equation (9) it can be seen that the chemical potential (μ) is dependent on the derivative of the energy (E) with respect to the number of electrons (N). The second equality in this equation corresponds to the electronegativity (χ) and is valid for $N = Z$. Z is the nuclear charge of the atom, IP is the ionization potential of the system and EA is the electron affinity. The chemical potential μ of DFT measures the escaping tendency of the electrons from the system. The slope, $(dE/dN)_Z$, of Equation (9) is equal to the chemical potential μ of DFT.[82] Equation (10) was used by Perdew and coworkers to derive[83]

$$\varepsilon_{max} = \begin{cases} -\text{IP} \ (Z - 1 < N < Z) \\ -\text{EA} \ (Z < N < Z + 1) \end{cases} \tag{11}$$

where ε_{max} is the maximum Kohn-Sham (KS) occupied orbital energy. The interpretation of Equation (11) is that the highest occupied KS orbital energy of an N-electron system is the negative of the ionization potential within

exact KS-DFT.[84,85] Because of the discontinuity on μ in Equation (9), it can be inferred from Equation (10) that $\mu = -IP$ for all the $Z-1 < N < Z$ and $\mu = -EA$ for all $Z < N < Z+1$. When $N = Z$, μ becomes the average value $\mu = -(IP+EA)/2$ which is related to the Mulliken definition of electronegativity (χ).[86] According to Mullikens definition, $\chi = (IP+EA)/2$. In an analogous way, from Equation (11), when $Z-1 < N < Z$, ε_{max} represents the energy of one KS orbital corresponding to the highest occupied molecular orbital (HOMO), whereas when $Z < N < Z+1$, ε_{max} represents the KS energy of the orbital corresponding to the lowest unoccupied molecular orbital (LUMO) of the Z electron system or the HOMO of the $Z+1$ electron system.

From the formulation of Parr and Pearson was developed the concept of chemical hardness (η).[87] This is the second derivative of E with respect to N according to

$$\eta = \left(\frac{\partial^2 E}{\partial N^2}\right)_Z = \left(\frac{\partial \mu}{\partial N}\right)_Z \tag{12}$$

this definition can be expressed in terms of the KS orbitals as the gap between the HOMO-LUMO energies. Within Hartree-Fock theory, the interpretation of the orbitals energies is done according to

$$I_i = E_{HF}(n-1, i) - E_{HF}(N) \tag{13}$$

where I_i is the ionization potential of an electron in an orbital ϕ_i, $E_{HF}(N)$ is the energy of the N-electron system before ionization and $E_{HF}(N-1,i)$ is the energy of the system after removal of the electron from ϕ_i. From Koopmans theorem arises the assumption that the removal of an electron from ϕ_i, will generate a stable conformation with respect to further variation in ϕ_i. This approach neglects the fact that the removal of an electron produces a rearrangement on the spatial charge distribution in the remaining orbitals which leads to the stabilization of the ion. In a similar way as with the HF approach, with DFT, the application of the frontier molecular orbital approach is valid within the region of validity of the Koopmans theorem.[88] Politzer *et al.*,[88] have shown that the hybrid DFT functionals in spite of producing a systematic deviation from the experimental ionization potentials, produce the same deviation for all of the valence orbitals. The deviations obtained for different molecular systems were larger than those obtained for the same molecule, but still smaller than 58 kJ·mol^{-1}.

2.6 Surface chemistry and catalysis from density functional theory

DFT is a very important tool for the study of surface chemistry.[89] The challenge of understanding surface processes at the microscale level is very often only overcome with the aid of theoretical methods. Given the large size of the systems usually necessary to describe a surface, the wave function based methods are not possible to apply due to their computational

demands. DFT is then the computational tool of choice for surface chemists. There has been a rich history of success of DFT in the design of new catalysts – *e.g.* ammonia synthesis[90] – in the understanding of the several surface reaction steps that usually characterize solid-liquid and solid-gas reactions, and in the design of better materials from the prediction of their surface chemistry.[10]

Interactions between molecules and surfaces can be described theoretically using several methods. From these, the most commonly applied method for investigating adsorption and reactivity is the use of density functional theory (DFT) and periodic boundary conditions (PBC). Another approach is to use a finite cluster model of the surface. Both approaches have their advantages and disadvantages. While PBC provides a physically sound treatment of the periodicity of extended surfaces, surface defects can be a hard task to model with PBC due to the interactions of artificial periodicity of the defects introduced. Even though this can be overcome by using very large unit cells, it increases the computational time and cost significantly.[67] Besides of the restricted offer of codes[91,92] using the PBC approach which permit the access to wave function methods and consequently also to hybrid Hartree-Fock/DFT,[93] the usage of hybrid functionals with PBC requires computational power which is prohibitively expensive for many users. In general, the major source of error when using the PBC approach is due to limitations of the electronic structure methods used, *i.e.* pure DFT.[94]

The cluster approach has the advantage that one can make use of the vast array of quantum chemical methods that have been developed and implemented.[93] Quantum chemical methods such as hybrid density functionals, double hybrid density functionals or higher-order wave function methods are readily available tools for modeling surfaces using cluster models.[94,95] The cluster approach is best suited for describing local phenomena such as interactions on catalytically active sites. Due to its low computational cost, the cluster approach is efficient for modeling the reactivity of surface defects, which can be crucial for understanding experimentally observed kinetics.[96] On the other hand, finite size effects can be detrimental for obtaining reliable data for properties of extended surfaces.[97] Such problems can be overcome by increasing the cluster size or by using the embedded cluster model approach.[98] For the modeling of adsorption on ideal/perfect surfaces, the cluster approach becomes inefficient due to the size of the cluster required to accurately represent the system.[99] Nevertheless, in real applications of engineered or natural materials, ideal surfaces are rarely present. Instead, solid surfaces are typically polycrystalline and display a defective surface-structure.[35,42]

Effects of cluster size and edge geometry on calculated adsorption energies, were recently investigated in a work where cluster models were used in

combination with hybrid and double hybrid exchange-correlation functionals.[94] Accurate adsorption energies onto mineral surfaces were obtained with two layers thickness clusters that retained the correct stoichiometry and charge of the surfaces. The authors calculated adsorption energies as a function of cluster size and concluded that beyond size-convergence, the maximum error introduced was 16 kJ·mol^{-1} for adsorption from gas phase. Convergence was achieved with clusters only large enough to include the surface atoms and groups involved in the binding of the adsorbate.

The information obtained from the application of DFT methods to surfaces has led to a deeper understanding of surface processes. For example the determination of the BEP parameter described in Equation (8) has proved a very useful tool for leading the design of catalysts or for the understanding of surface reactivity. This concept had its boom due to the availability of DFT calculations at a larger scale.[47] A deeper understanding of surface reactivity has been possible due to the application of DFT. For example, a topic that has been debated for many decades is the role of defects in surface reactivity.[100] Recently, using adsorption experiments and DFT calculations it has been shown that the N_2 dissociation on the Ru(0001) surface is totally dominated by steps.[101] The adsorption rate at the steps is over 9 orders of magnitude higher than on the terraces. The corresponding calculated difference in activation energy is 145 kJ·mol^{-1}. The lower barrier at the step sites is attributed to a combination of electronic and geometrical effects. In another study, it was reported that the presence of surface defects in MgO films lower the activation energies for reactions with water by as much as 60%.[102] The same reaction that has considerable activation energy on an ideal surface, can occur without energy barrier at surface defects. Consequently, for non-ideal surfaces, the overall reaction rate is often determined by interactions with defective sites.[96] The physical-chemical properties of surface defects and the chemical reactivity of such sites are mainly the results of local structural and electronic properties, and less dependent on the properties of the extended surface.[42] The properties of surface defects are above all dependent on the types of atom exposed at the defects, their oxidation states, their coordination/ligand field and their Lewis acidity. There are several examples in the literature showing that defective surface sites, displaying coordinatively unsaturated metal atoms, can enhance the reactivity of a material.[102-104] In general, the interactions between adsorbates and surfaces are a localized event. It has been suggested that a local approximation for the study of surface reactivity could be applied without loss of precision. This because the resultant structures from adsorbed molecules onto metal atoms that constitute surfaces often resemble the structures of the corresponding organometallic complexes.[105] In the case of a

defective surface, the degree of localization of these interactions is even higher.[106] As such, the approaches such as the *d*-band type model, breaks when applied to defects, as the density of states of the bulk is broken at the surface and even more extensively at defect sites. The more undercoordinated an atom is at a defect, the more "free-atom-like-character" the density of states of that atom will have.[107] At the bulk, the density of states is influenced by the bonding on the extended crystal structure and the extent of delocalization of the bulk atoms electrons is significant. In the defects, the lack of extended structure adds more localized character to the orbitals of atoms at those sites. This makes the orbitals of the defect atom more available for interactions with adsorbates than the orbitals of less undercoordinated surface atoms. At these sites the adsorption is generally more exothermic.[107]

The effect of the defects on reaction mechanisms can be categorized as electronic or geometric.[50] A linear BEP relation between adsorption energies and reaction activation energy barriers is only obtained when the contribution to the overall relation comes either from the electronic or geometric component. Otherwise, the BEP plot deviates from an ideal straight line. This is actually the case for real surfaces (*i.e.* not grown in UHV controlled conditions) where the BEP relations are very seldom linear due to the coexistence of electronic and geometric contributions to the surface reaction pathways.[50]

2.7 Methodology for the combined experimental-theoretical study of surface reactions.

In the present thesis a combined experimental-theoretical methodology for the study of the catalytic decomposition of H_2O_2 on the surface of transition metal and lanthanide oxides under "real" conditions is used. The reaction systems are composed of particle suspensions of the oxides in aqueous solutions. These systems have complex dynamics due to the presence of surface defects, surface hydroxylation and solvation. Also, the pH of the media has an effect on the surface charge which can disturb the adsorption of charged adsorbates. The experimental study of such systems is challenging. Nevertheless, the determination and analysis of experimental kinetic and mechanistic data from these real systems combined with a theoretical investigation of the processes involved in the reaction mechanisms can aid the understanding of the microscale phenomena that leads to a certain macroscale observation.

3. Experimental and computational details

3.1 Experimental details

3.1.1 *Instrumentation*

Specific surface areas of the powders were determined using the B.E.T. method of isothermal adsorption and desorption of a gaseous mixture consisting of 30% N_2, 70% He in a Micrometrics Flowsorb II 2300 instrument. γ-Irradiation was performed using a MDS Nordion 1000 Elite Cs-137 γ-source with a dose rate of 0.15 $Gy \cdot s^{-1}$, this value was determined using Fricke dosimetry.[108] X-ray powder diffractograms (XRD) were obtained at 293 K, using CuK_α radiation, on a PANanalytical X´pert instrument. Powders were mounted into the sample holders rings. The data was collected over the range $3° \leq 2\theta \leq 80°$, with a step size of $0.033°$ (2θ). Data evaluation was done using The High Score Plus software package and the PDF-2 database was used for matching the experimentally obtained diffractograms. The samples were weighted to $\pm 10^{-5}$ g, in a Mettler Toledo AT261 Delta Range microbalance. The reactions were performed under inert atmosphere with a constant flux of N_2 gas (AGA Gas AB) and at constant known temperatures using a Huber CC1 or a Lauda E100 thermostat, calibrated against a Therma 1 Thermometer coupled to a submersible K-type (NiCrNi) temperature probe, with a precision of $\pm$ 0.1 K. UV/Vis spectra were collected using a WPA Lightwave S2000 or a WPA Biowave II UV/Vis Spectrophotometer. Trace elemental analysis were performed using the technique of inductively coupled plasma spectroscopy, on a Thermo Scientific iCAP 6000 series ICP spectrometer. The analysis for Zr was performed at the wavelength of 343.823 nm and that of U at 367 and 385.9 nm.

3.1.2 *Materials*

All the solutions used in this study were prepared using water from a Millipore Milli-Q system. ZrO_2 (CAS[1314-23-4], Aldrich 99%); TiO_2 (CAS[13463-67-7], Alfa Aesar, 99.9%); Y_2O_3 (CAS[1314-36-9], Alfa Aesar, 99.9%); Fe_2O_3, (CAS[1309-37-1], Aldrich 99%); CeO_2, (CAS[1306-38-3], Alfa Aesar 99.99%); HfO_2, (CAS[12055-23-1], Alfa Aesar 99.95%); Gd_2O_3, (CAS[12064-62-9], Aldrich 99.9%); and CuO, (CAS[1317-38-0], Aldrich 99.99%) were used without further purification. To the XRD data was applied a Rietveld refinement using ICSD-26488 as a starting model and yielded the following cell parameters for ZrO_2: *a*) 5.1458(2) Å, *b)* 5.2083(3) Å, *c)* 5.3124(3) Å. These values are in good agreement with the cell parameters attributed to the monoclinic phase.[109] For TiO_2 the Rietveld refinement yielded a composition 88.5% anatase and 11.5% rutile. The obtained cell parameters for TiO_2 are: *a = b)* 3.7856(2) Å, *c)* 9.5058(5) Å for the anatase phase and *a = b)* 4.5914(8) Å, *c)* 2.9539(10) Å for the rutile phase.[110] The obtained cell

parameters for Y_2O_3 are: *a*) 10.60398(9) Å, attributed to the cubic (bixbyite-type) structure.[111] These crystal structures match the information provided by the materials manufacturers. Based on this, the measurement of the crystal structures for the other oxides was not done and the crystal structures considered are those provided by the oxides manufacturers.

Uranium dioxide pellets and powder provided by Westinghouse Atom AB and SIMFUEL pellets provided by Atomic Energy of Canada Limited were used in the experiments after being washed with a solution 10 mM $NaHCO_3$ (Merck, p.a.) for 14 hours. The total impurities present on the UO_2 powder correspond to 48 $\mu g/_gU$. The weight of the pellets was determined to be 5.3 g for the Westinghouse pellet and 7.9 g for the SIMFUEL pellet. The composition of the SIMFUEL pellet expressed as weight ratios to uranium is as follows: $Sr(2.74 \times 10^{-3})$, $Y(6.46 \times 10^{-4})$, $Zr(5.72 \times 10^{-3})$, $Mo(5.24 \times 10^{-3})$, $Ru(3.80 \times 10^{-3})$, $Rh(6.25 \times 10^{-3})$, $Pd(2.93 \times 10^{-3})$, $Ba(3.68 \times 10^{-3})$, $La(8.77 \times 10^{-3})$, $Ce(8.77 \times 10^{-3})$, $Nd(1.00 \times 10^{-2})$.

The specific surface area of the powders are the average of three measurements, each consisting of a sorption and a desorption isotherm whose values were also averaged. The B.E.T. specific surface areas of the oxides are: ZrO_2 (5.0 ± 0.2 $m^2 \cdot g^{-1}$); TiO_2 (38.9 ± 0.2 $m^2 \cdot g^{-1}$); Y_2O_3 (4.48 ± 0.03 $m^2 \cdot g^{-1}$); Fe_2O_3 (9.0 ± 1.0 $m^2 \cdot g^{-1}$); CeO_2 (14.3 ± 1.0 $m^2 \cdot g^{-1}$); HfO_2 (10.0 ± 0.1 $m^2 \cdot g^{-1}$); Gd_2O_3 (1.7 ± 0.1 $m^2 \cdot g^{-1}$); CuO (15.3 ± 0.1 $m^2 \cdot g^{-1}$); UO_2 powder (5.4 ± 0.2 $m^2 \cdot g^{-1}$). The surface area of the uranium pellets was calculated by using a geometrical approach and produced the values of 352 mm^2 for the UO_2 pellet and 471 mm^2 for the SIMFUEL pellet.

The particle sizes were supplied by the manufactures. For Gd_2O_3 the value was obtained using the technique of confocal profilometry: The particle sizes are as follows: ZrO_2 (< 5 μm); TiO_2 (32 nm); Y_2O_3 (< 10 μm); Fe_2O_3 (< 5 μm); CeO_2 (14. μm); HfO_2 (44. μm); Gd_2O_3 (15 nm); CuO (< 50 nm); UO_2 (16 μm).

3.1.3 *Kinetic experiments*

The H_2O_2 solutions were prepared from a 30% standard solution (Merck). The particle suspensions where the reactions with H_2O_2 took place consisted of ZrO_2 [0.5–4.5 g]; TiO_2 [0.146–0.341 g]; Y_2O_3 [1.269–2.961 g]; Fe_2O_3 [0.2–1.5] g; CeO_2 [0.06–0.52] g; HfO_2 [0.75–0.1] g; Gd_2O_3 [0.25–1.0] g; CuO [0.0025–0.1] g in 50 mL of H_2O_2 0.5 mM. For the test experiments concentrations of H_2O_2 that varied in the range [0.2–6.0] mM were used. The H_2O_2 solutions were prepared from a 30% standard solution (Merck). After extraction of the sample from the reaction vessel, the sample was filtered through a Gema Medical 0.45μm–25mm Cellulose Acetate syringe filter. Subsequently, a sample volume of 0.2 mL was used for the measurement of the H_2O_2 concentration. The concentration of H_2O_2 was determined using the Ghormley triiodide method. In this method, I^- is oxidized to I_3^- by H_2O_2.[112,113]

The absorbance of the product I_3^- is measured spectrophotometrically at the wavelength of 350 nm. Initially, a calibration curve where the absorbance of I_3^- was plotted as a function of the concentration of H_2O_2 was obtained in the range 0.02 to 0.8 mM resulting in a linear correlation between absorbance and concentration.

3.1.4 *Mechanistic study*

The mechanistic study involved scavenging HO radicals formed during decomposition of H_2O_2. This was done by means of the reaction between tris(hydroxymethyl)aminomethane, (Tris) (CAS[77-86-1]), BDH Chemicals, 99%) or N-[Tris(hydroxymethyl)methyl]-3-aminopropanesulfonic acid sodium salt; (TAPS$^-$Na$^+$) (CAS[91000-53-2], Sigma > 99%) and the HO radicals to produce formaldehyde. The formaldehyde produced was then quantified spectrophotometrically at 368 nm, by using a modified version of the Hantzsch reaction. In this method the formaldehyde reacted with acetoacetanilide AAA (CAS[102-01-2], Alfa Aesar > 98%) in the presence of ammonium acetate (CAS[631-61-8], Lancaster 98%) to form a dihydropyridine derivative which has the maximum absorption wavelength at 368 nm. A calibration curve plotting the absorbance of the dihydropyridine derivative as a function of formaldehyde concentration was obtained at 368 nm, giving a linear correlation between absorbance and concentration, in the concentration range 0.15 μM to 1 mM in formaldehyde. The plotting of the calibration curve for formaldehyde required the preparation of several solutions of CH_2O with different rigorously known concentrations in the concentration range mentioned above. It was then necessary to proceed to the accurate determination of the concentration of formaldehyde in the solution used initially (CAS[50-00-0]), Aldrich 37% wt in H_2O) using the iodometric method.[114] The solutions and respective standardizations necessary to follow the iodometric method procedure were prepared as stated in the cited paper[114] and as described elsewhere.[115] The error associated with the determination of the concentration of formaldehyde in the initial solution was 1.15%.

The reaction media for HO$^\bullet$ detection during decomposition of H_2O_2 consisted of: ZrO_2 (1.5 g) or TiO_2 (0.197 g) or Y_2O_3 (1.678 g) Fe_2O_3 (1.5 g) or CeO_2 (1.6 g) or HfO_2 (2.25 g) or Gd_2O_3 (3.0 g) or CuO (0.06 g) with H_2O_2 (5 mM) and Tris (20mM) in 50 ml at a pH of 7.5.

3.1.5 *Affinity of ZrO$_2$, TiO$_2$ and Y$_2$O$_3$ for the HO radical*

The study of the scavenging capacities of the oxides towards HO$^\bullet$ consisted of γ-irradiating samples of the oxides in the presence of Tris. The reaction media used was ZrO_2 (1.5 g) or TiO_2 (0.197 g) or Y_2O_3 (1.678 g) in 50 ml Tris (20 mM) solution at pH 7.5. The pH was adjusted with HCl. The detection of

the amount of HO radicals scavenged by Tris followed the same procedure as described above for the mechanistic study.

3.1.6 *Determination of H_2 and O_2 during H_2O_2 decomposition*

All the solutions were purged with ultra-high purity argon (99.9999%). Hydrogen and oxygen were determined in deaerated samples using an inline technique employing a gas chromatograph. Ultrahigh purity argon was used as the carrier gas with a flow rate of about 50 mL/min. The argon passed through a constant flow regulator, an injection septum, a four-way valve and into a 5 m molecular sieve column of an SRI 8610C gas chromatograph with a thermal conductivity detector. The samples cells were connected to the gas analysis system, purged of air, isolated, crushed and then the gases injected into the carrier gas stream. H_2 and O_2 were determined in each of the samples. Calibration of the detector was performed by injecting pure H_2 and O_2 with a gastight microliter syringe. The error in gas measurement was estimated to be about 5%.

3.1.7 *Measurement of adsorption equilibrium constants for adsorption of Tris and TAPS onto ZrO_2*

The determination of the amount of Tris and TAPS in solution was done following a basic competition kinetic scheme. According to reference,[116] the bleaching of methylene blue solutions (1-16 μM) under γ-radiolysis increases linearly up to doses on the order of 500 Gy. Here, a linear correlation for the bleaching of a methylene blue solution (18 μM) was observed as a function of γ dose up to 90 Gy, which was the dose used for measurement of the competition kinetic experiments. The methylene blue concentration was measured with UV-Vis spectrophotometry at 664 nm. γ-irradiation of a methylene blue solution undergoes less bleaching in the presence of another HO$^\bullet$ radical scavenger than does a pure methylene blue solution. This protection is due to competition for the HO$^\bullet$ radical between the methylene blue and the added HO$^\bullet$ radical scavenger.[117] The competition kinetics between Tris or TAPS and the methylene blue for the HO$^\bullet$ radical was used to determine the amount of Tris or TAPS removed from solution by adsorption. The reduction in bleaching of a methylene blue (18 μM) solution and the increase in concentration of Tris or TAPS is linear in the concentration range of 50-250 μM of Tris or TAPS. The measurement of the adsorption parameters for Tris and TAPS was done at 298 K using solutions of varying concentration of adsorbate. After adsorption equilibrium was reached, a sample aliquot was taken and filtered and the competition kinetic analysis with methylene blue was performed. The reaction media for the adsorption study consisted of 5 ml of Tris or TAPS solution with concentrations in the range 100-500 μM and ZrO_2 (2.5 g, Surface Area = 8.4 m^2) at pH 7.5 adjusted with HCl. The lower value of concentration of Tris

and TAPS for which was possible to determine adsorption parameters using competition with methylene blue was 50 μM.

3.1.8 *Effects of HO$^\bullet$ scavengers on the products of H$_2$O$_2$ decomposition*

The effects of the HO$^\bullet$ scavengers on the products of H$_2$O$_2$ decomposition were investigated using reaction media consisting of 2 ml of H$_2$O$_2$ (10 mM) solution and ZrO$_2$ (0.4 g, *Sa* = 1.34 m^2) or TiO$_2$ (0.149g, *Sa* = 1.42 m^2) or CuO (0.631g, *Sa* = 1.34) at pH 7.5. The pH was adjusted with HCl. Varying concentrations of Tris and TAPS in the range [0–200] mM were used.

3.2 Computational details

DFT calculations were performed using the molecular cluster model[118] approach and the software package Jaguar 7.7.(Ref.[119]). Cluster geometries were optimized at the B3LYP/LACVP*+ level of theory.[46-49] The basis set LACVP*+ is a combination of the split valence basis set 6-31+G(d) and the Los Alamos effective core potential for transition metals. Single-point evaluations of energies were performed using exchange-correlation functionals built on the generalized gradient approximation (GGA), namely the pure density functionals PBE([54,60,61]) and PWPW91([120]); the pure meta functional M06-L([121]), the hybrid functionals PBE0([60,61]), B3LYP, and B3LYP* ([122]); and the hybrid meta functional M06([123]). The M06 functional has shown improved accuracy for describing transition metal chemistry and medium range attractive dispersion interactions.[124] In addition, the effects of adding an empirical attractive dispersion term ($-f(R)C_6 \cdot R^{-6}$) to the B3LYP functional according to the method of Grimme, were investigated.[125] The functionals used are further described in Table 1 in terms of the amount of Hartree-Fock exchange (E_{HF}^{XC}) incorporated and whether or not the electronic kinetic energy density (τ) depends on the spin.

Table 1. Density functionals used in this work described in terms of: the percentage of Hartree-Fock exchange (E_{XC}^{HF}); up-spin and down-spin electronic kinetic energy density (τ).

	B3LYP	B3LYP*	M06	M06-L	PBE0	PBE	PWPW91
E_{XC}^{HF}(%)	20	15	27	0	25	0	0
τ	No	No	Yes	Yes	No	No	No

Single point calculations were performed with the split valence triple-ζ basis set LACV3P**++, which is supplemented with polarization and diffuse functions on all atoms. The following convergence criteria were used for all geometry calculations (atomic units): rms gradient < 3 × 10^{-4}; maximum gradient < 4.5 × 10^{-4}; rms step < 1.2 × 10^{-3}; maximum step < 1.8 × 10^{-3}; maximum change in total energy between two consecutive steps < 5 × 10^{-5}.

The cluster models implemented conform to the three principles proposed to model metal oxides using clusters.[126,127] These principles are: the neutrality principle, the stoichiometry principle and the coordination principle.

The adsorption energies reported herein were calculated as

$$\Delta E_{ads} = E_{adsorbate/cluster} - (E_{adsorbate} + E_{cluster}) \tag{14}$$

where $E_{adsorbate/cluster}$, $E_{adsorbate}$, $E_{cluster}$, represent the electronic energies in gas-phase for the adsorbate binding to the cluster, free adsorbate and bare cluster respectively. This means that the more negative the adsorption energy, the stronger is the adsorption.

Transition states were located using the quadratic synchronous transit (QST) method implemented in Jaguar 7.7. Corrections to obtain zero-point vibrational effects and the thermodynamic potential enthalpy (H) were calculated from a Hessian matrix of harmonic force constants using the partition functions of an ideal -/non-interacting gas at T = 298.15 K and P = 1 atm. The vibrational frequencies obtained from the Hessian matrix were also used to verify the first-order saddle point nature of the transition states.

3.2.1 *Conceptual DFT*

The functional PBE0 has shown improved performance over other hybrid functionals in describing lanthanide and heavy metal chemistry.[63] For the clusters of HfO_2, CeO_2 and Gd_2O_3 the geometries were optimized using the PBE0 functional and the CSDZ+* basis set for the metal atoms and 6-31G+* for H and O. CSDZ is the implementation in Jaguar of the Cundari and Stevens ECP basis set for lanthanides.[78] For the clusters of transition metals the LACVP+* basis set was used for geometry optimizations. Single-point evaluations of the energies were performed using PBE0 with LACV3P++** basis set for the clusters of transition metals. For HfO_2, CeO_2 and Gd_2O_3 were used the CSDZ++** basis set for the metal atoms and the 6-311G++** for the O and H atoms. For the non-lanthanides, the Mulliken electronegativities of the cations present in the metal oxides were determined from the IP and EA both calculated at the PBE0/LACV3P++** using fully analytical accuracy and the maximum grid density.

4. Results and discussion

4.1 Kinetics and activation energies for H_2O_2 decomposition on transition metal oxide surfaces

The reactions of H_2O_2 with particle suspensions of ZrO_2, Y_2O_3, TiO_2, Fe_2O_3, HfO_2, CeO_2, Gd_2O_3, CuO and UO_2 were investigated. H_2O_2 can react with metal oxides via different pathways[128,129]

One-electron oxidation:
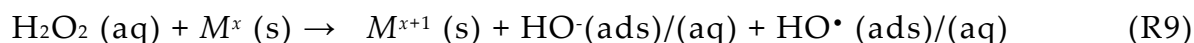
$$H_2O_2 \text{ (aq)} + M^x \text{ (s)} \rightarrow M^{x+1} \text{ (s)} + HO^- \text{(ads)/(aq)} + HO^\bullet \text{ (ads)/(aq)} \qquad \text{(R9)}$$

Two-electron oxidation:

$$H_2O_2 \text{ (aq)} + M^x \text{ (s)} \rightarrow M^{x+2} \text{ (s)} + 2HO^- \text{ (ads)/(aq)} \qquad \text{(R10)}$$

Catalytic decomposition:

$$H_2O_2 \text{ (aq)} + M^y \text{ (s)} \rightarrow 2HO^\bullet \text{ (ads)/(aq)} + M^y \text{ (s)} \qquad \text{(R11)}$$

$$HO^\bullet \text{ (ads)/(aq)} + H_2O_2 \text{ (ads)/(aq)} \rightarrow HO_2^\bullet \text{ (ads)/(aq)} + H_2O \text{ (ads)/(aq)} \qquad \text{(R12)}$$

$$2HO_2^\bullet \text{ (ads)/(aq)} \rightarrow H_2O_2 \text{ (aq)} + O_2 \text{ (g)} \qquad \text{(R13)}$$
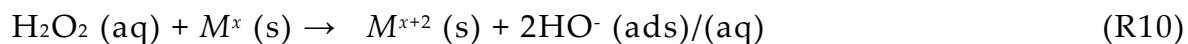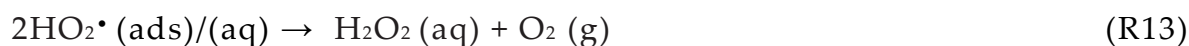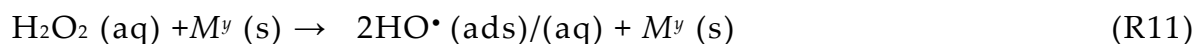
for which the overall known stoichiometry for processes (R11) to (R13) is

$$H_2O_2 \text{ (aq)} \rightarrow H_2O \text{ (l)} + 1/2 O_2 \text{ (g)} \qquad \text{(R14)}$$

where M represents a metal cation in a metal oxide, in the oxidation state x or y. In all the above mentioned metal oxides with the exception of UO_2, the metal cation is in its maximum oxidation state and cannot be further oxidized. At the surface of such materials, the reaction of H_2O_2 occurs via catalytic decomposition. It has been suggested that the reduction of Ti^{4+} in TiO_2 by H_2O_2 can take place.[130] Though, due to the lack of detailed experimental evidence and discussion of this reaction, it is considered as a side process that in case it occurs at all, is expected to have a very small yield when compared with the main path for the reactivity of H_2O_2 – the catalytic decomposition. Nevertheless, in this work, the possibility that this reaction occurs when H_2O_2 reacts with ZrO_2 was investigated. With UO_2, H_2O_2 can react both via a redox mechanism and by catalytic decomposition.[131] In general, the catalytic decomposition of H_2O_2 on a solid surface is a spontaneous process at temperatures that range from room temperature up to 286 ºC and its reported activation energy ranges from 21 kJ·mol^{-1} to 96 kJ·mol^{-1}, depending on the type of surface and on factors such as the oxidation state of the metal.[132] Reaction (R13) corresponds to the chain termination and occurs via the disproportionation of two hydroperoxyl radicals as represented. When reaction (R13) occurs with pure water as a solvent, its activation energy is 25 kJ·mol^{-1}, in the temperature range [274-316] K.[133]

4.1.1 *ZrO₂*

The evaluation of the kinetics and energetics of the catalytic decomposition of H_2O_2 has to be done within a temperature and pH range where the spontaneous non-catalyzed decomposition of H_2O_2 is negligible when compared to the rate of its decomposition on the surface of the oxide itself. In neutral water, from the species involved in the reactions (R11) to (R13), only dissociation of $HO_2^\bullet$ needs to be considered, since the $pK_a{}'$s for H_2O_2, $HO^\bullet$, and $HO_2^\bullet$ are 11.8, 11.9 and 4.88 respectively.[134] The $HO_2^\bullet$ (hydroperoxyl radical) is a weak acid and is also the protonated form of the superoxide radical anion which can be formed at and bind to the surface of ZrO_2 according to the following reaction[135]

$$HO_2^\bullet \text{ (ads)/(aq)} \xrightarrow{\;ZrO_2\;} H^+ \text{ (aq)} + O_2^{-\bullet} \text{ (ads)} \qquad\qquad (R15)$$
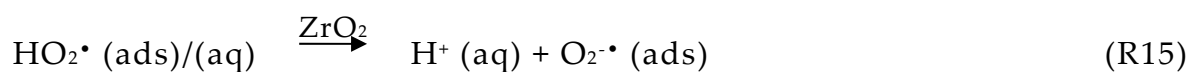
the superoxide anion radical can be stabilized by adsorption onto the surface of the ZrO_2 and has been used previously as a spin probe for the study of surfaces. This radical binds to the surface by coordination with exposed Zr^{4+} surface cations.[135]

The decomposition of H_2O_2 on the surface of ZrO_2 was investigated at T = 298.15 K by studying the variation in the concentration of H_2O_2 as a function of reaction time. The obtained data is represented in Figure 5 which shows the normalized concentration of H_2O_2 ($[H_2O_2]_t/[H_2O_2]_0$,) as a function of reaction time. $[H_2O_2]_t$ is the concentration of H_2O_2 at the time t and $[H_2O_2]_0$, is the concentration of H_2O_2 at t = 0.
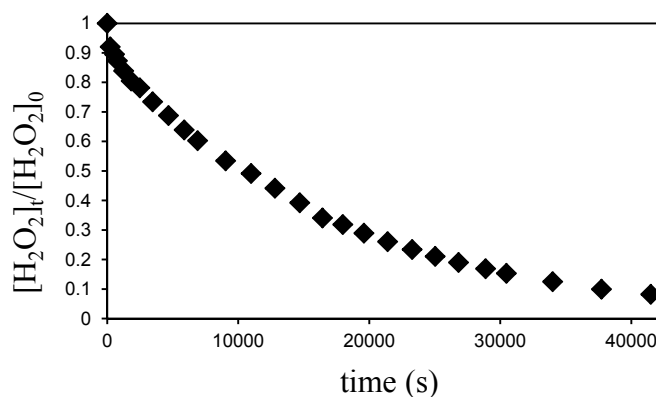
Figure 5. Normalized concentration of H_2O_2 ($[H_2O_2]_0$ = 0.5 mM) as a function of reaction time in the reaction with ZrO_2 (1.5 g; *Sa* = 7.5 m²) at T = 298.15 K in 50 ml H_2O. © American Chemical Society.

A plot of $\ln([H_2O_2]/[H_2O_2]_0)$ using the data of Figure 6, shows good agreement with a first-order kinetic law. Nevertheless, the order of the reaction with respect to H_2O_2 was confirmed by application of the method of

initial rates. The initial reaction rates were determined for different concentrations of H_2O_2 and for the same amount of ZrO_2. A plot of ln(initial reaction rate) as a function of ln($[H_2O_2]$) was obtained at T = 313.15 K. The reaction media consisted of ZrO_2 (1.5 g; Sa = 7.5 m^2) and different concentrations of H_2O_2 that ranged from 0.5 to 6 mM. Application of a linear regression of the data yielded a slope of 0.98 ± 0.04. Considering the experimental error associated with this value it is possible to conclude that the reaction is first-order with respect to H_2O_2. The kinetic data for decomposition of H_2O_2 on ZrO_2 was then treated as a first-order process. The first-order rate constant obtained from the linear correlation shown in Figure 6, for the temperature T = 298.15 K is k_1 = (6.15 ± 0.04) x 10^{-5} s^{-1}.
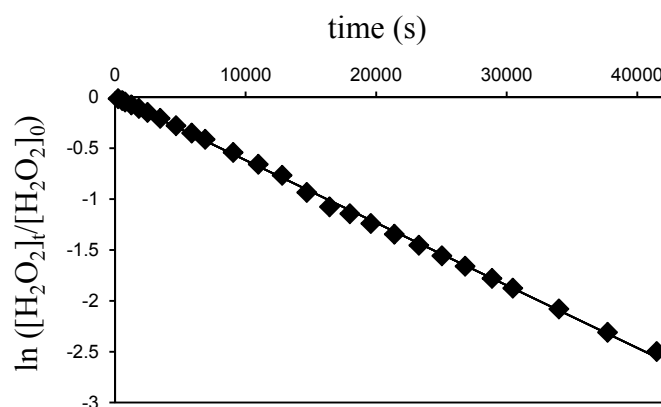
Figure 6. ln($[H_2O_2]_t/[H_2O_2]_0$) as a function of reaction time (s) for the decomposition of H_2O_2 on ZrO_2 using the data shown in Figure 5. © American Chemical Society.

The second order rate constant (k_2) was determined according to Equation (3). The Sa/V dependence of the first-order rate constant is shown in Figure 7.
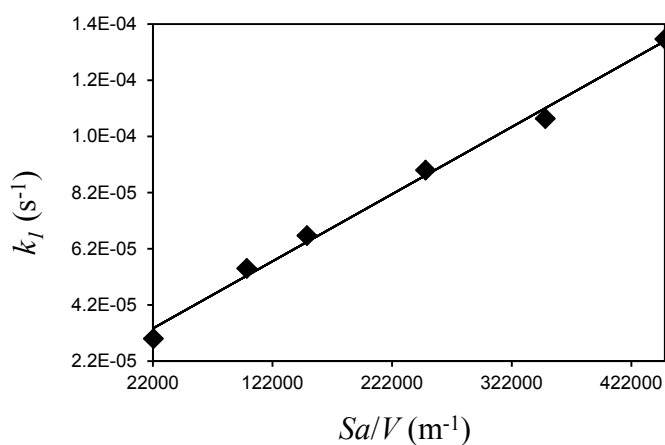
Figure 7. k_1 for decomposition of H_2O_2 (0.5 mM) as a function of ZrO_2 Sa/V obtained at T = 298.15 K. © American Chemical Society.

The value of k_2 obtained from the slope of the plot of Figure 7 for the reaction at T = 298.15 K is k_2 = (2.39 ± 0.09) x 10^{-10} m·s^{-1}. As expected, this value is very far from the value corresponding to a diffusion controlled reaction for which the rate constant is in the order of 10^{-5} m·s^{-1} for particles of this size.[9]

For the determination of the Arrhenius activation energy, the rate constants were obtained as a function of the reaction temperature for the temperature interval T = [294.15-353.15] K with a temperature step of 5 K.
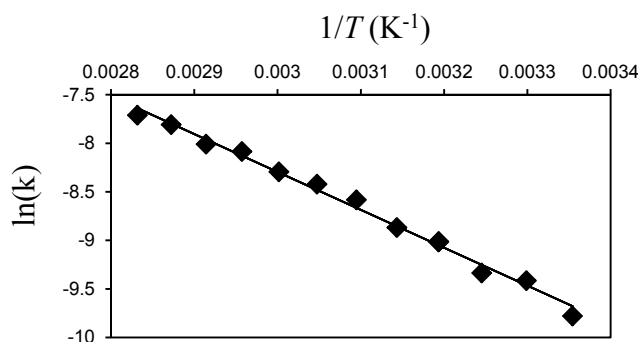

Figure 8. Arrhenius plot of ln(k) as a function of 1/T (K) for T = [294.15-353.15] K with a temperature step of 5 K. © American Chemical Society.

The values of ln(k_1) as a function of the inverse of the temperature are represented in Figure 8. For the determination of E_a, for each temperature value, three rate constant vales were obtained in three different experiments and the resulting values were averaged. The temperature dependence of the reaction rate constant displays Arrhenius behavior. The rate constant varied from (5.670 ± 0.003) x 10^{-5} s^{-1} to (4.50 ± 0.01) x 10^{-4} s^{-1}, for T = 298.15 and T = 353.15 K respectively. The half-life varied from 198.0 min for the reaction at 298.15 K, to 26.3 min for the reaction at 353.15 K. The obtained E_a value for decomposition of H_2O_2 on the ZrO_2 particle suspension in the temperature range T = [298.15-353.15] K is 33 ± 1 kJ·mol^{-1}. This value is in good agreement with previously published data for similar systems.[132] The corresponding enthalpy of activation obtained from the Eyring plot is $\Delta H^{\ddagger}$ = 30 ± 1 kJ·mol^{-1}. When comparing these values with the bond dissociation energy (BDE) of the O-O bond in H_2O_2,[136] which is ≈ 208 kJ·mol^{-1}, or the BDE for cleavage of the H-OOH bond in H_2O_2 which is ≈ 372 kJ·mol^{-1},[137] it is evident that the oxide-liquid interface is acting as a catalyst and lowers substantially the energy barrier necessary to eventually cleave one of these bonds. Judging from these BDE values, most likely, the main reaction path will be through the cleavage of the HO-OH bond.

To verify if the reaction of H_2O_2 with ZrO_2 is purely catalytic decomposition, involving no extensive modifications of the surface of the

catalyst, a B.E.T. measurement of the surface area of the powder was performed. This was done on three types of ZrO_2 samples: prior to immersion in the aqueous reactant solution, after immersion in water during a time interval equal to the reaction time, and after reaction with hydrogen peroxide. Prior to the B.E.T. specific surface area determination, the solid was dried in vacuum at $T = 353.15$ K and $P = 0.1$ Pa, the data obtained are summarized in Table 2.

Table 2. Specific surface areas of the fresh powder determined by the B.E.T. method, after immersion in water at $T = 353$ K and after reaction with H_2O_2 at $T = 353$ K.

ZrO_2 Sample	specific surface area $(m^2 \cdot g^{-1})$
fresh powder	5.0 ± 0.2
after immersion in water at $T = 353$ K	5.0 ± 0.2
after reaction with H_2O_2 in aqueous media at $T = 353$ K	5.0 ± 0.3

As can be seen (Table 2), no detectable changes occurred on the specific surface area of the solid due to immersion in water or due to the reaction with H_2O_2. To evaluate possible changes in the crystal structure of ZrO_2, a comparison of the XRD diffractograms obtained before and after reaction was done. Prior to the collection of the XRD data, the reaction between ZrO_2 and H_2O_2 was performed until complete consumption of H_2O_2. The obtained cell parameters *a*) 5.1497(7) Å, *b*) 5.2123(7) Å, *c*) 5.3164(8) Å, are in excellent agreement with the values obtained before the reaction took place (see experimental details section). This means that no extensive change occurred in the crystal structure of the powder during the course of the reaction.

The superoxide anion radical formed according to Reaction (R15) is an active reductive species and can for example reduce transition metal cations present in oxides such as Fe^{3+} in Fe_2O_3.[138] Translated to the case of Zr(IV) this reaction would be

$$O_2^{-\bullet} \text{ (ads)} + Zr^{4+} \text{ (s)} \rightarrow O_2 \text{ (g)} + Zr^{3+} \text{ (s)/(aq)} \tag{R16}$$
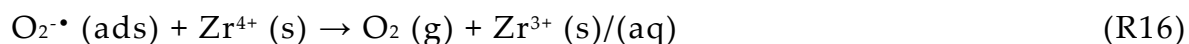
the possible reduction of Zr(IV) following a process similar to Reaction (R16) was investigated. If occurring, this reaction would cause a deviation from the equilibrium stoichiometry of the surface of the oxide, in aqueous solution this would lead to the subsequent release of Zr into the solution. This was investigated first by measuring traces of Zr in solution using inductively coupled plasma spectroscopy (I.C.P.). The I.C.P. technique allows for the detection of the total amount of an element with no distinction for oxidation state. A blank measurement was previously performed on a sample taken from a ZrO_2 (1.5 g) particle suspension in 50 ml of water where ZrO_2 was

exposed for a period of time equal to the reaction time with H_2O_2. Subsequently the solid particles were filtered and the measurement of the blank was done. The measurement to track the possible release of zirconium due to reaction with H_2O_2 was made after the reaction reached completion. The I.C.P. measurement was performed after filtration of the solid particles from the reactant solution. The value for the increase in concentration of Zr in solution after reaction is $(9.1 \pm 0.2) \times 10^{-8}$ M. When comparing the amount of zirconium in solution and the amount of hydrogen peroxide present that had reacted (*i.e.* 5 orders of magnitude higher), it can be seen that the increase in the amount of zirconium in solution is negligible. Under these conditions, Reaction (R16) if it occurs is a side reaction that has a small contribution to the overall H_2O_2 reactivity in this system. If Reaction (R16) would occur extensively – causing a change in the oxidation state of Zr(IV) to other state besides Zr(0) – it could have repercussions on the crystal structure of the solid. Eventually creating defects in the lattice due to the replacement of Zr(IV) by Zr atoms in different oxidation states and consequent re-arrangement of the surface to compensate for the non-equilibrium stoichiometry of the new created lattice.[139] If this process occurs extensively, it would lead to different cell parameters before and after reaction. This is not observed and significant reduction of Zr (IV) by superoxide anion radical is not detectable in this system.

A behavior very close to zeroth-order kinetics can be obtained when the amount of H_2O_2 is in large excess when compared to the number of adsorption sites available on the oxide surface. In this way it is possible to fit the data to zeroth-order kinetics minimizing the error of such approximation. For a reaction which is zeroth-order with respect to H_2O_2, the reaction rate constant will be independent of the concentration of H_2O_2. The lower limit of ZrO_2 mass, where the reaction changes from first-order to zeroth-order is $\approx$ 0.5 g; Sa = 2.5 m^2. For masses of ZrO_2 smaller than 0.5 g in 50 ml H_2O_2 (0.5 mM) solution, the reaction starts to obey a zeroth-order kinetic law. The zeroth-order rate constant obtained at T = 298.15 K with ZrO_2 (0.224 g) in 50 ml H_2O_2 (0.5 mM) solution, is k_0 = $(2.0 \pm 0.1) \times 10^{-5}$ M·s^{-1}. Obviously, with the reduction in ZrO_2 mass, the transition from first-order to zeroth-order is not sudden. There is a range of ZrO_2 masses where the reaction follows a non-integer rate law whose coefficient lays somewhere between 0 and 1.

As described in section 2.3, the pH of the aqueous media is an important parameter in surface processes in solution and can affect the rate of uptake of an adsorbate by a surface.[140] In the case of a system where hydrogen-bonded structures between adsorbate and solute and/or surface are possible, the pH effect might become even more important. H_2O_2 is capable of forming stable cyclic hydrogen-bonded structures in solution.[41] Also, for the system H_2O_2-ZrO_2, changes in the pH of the reactant solution can alter the concentration

of superoxide radical trapped on the surface by affecting the attractive/repulsive forces between the superoxide radical and the surface. In order to evaluate the effect of pH changes on the rate of decomposition of H_2O_2, the k_0 values were determined for different pH values. The pH was adjusted with Tris/HCl buffer. The data obtained are represented in Figure 9.
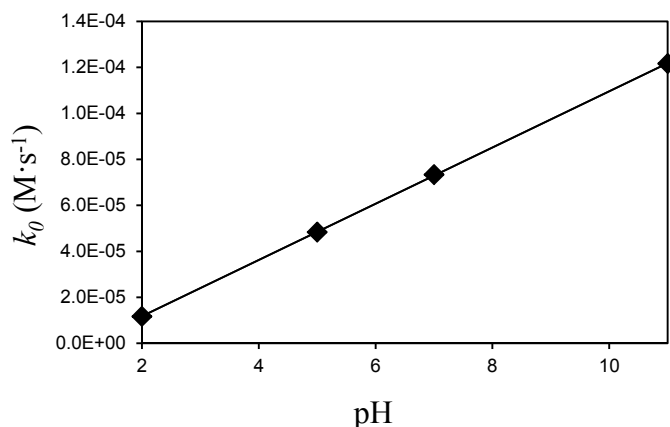

Figure 9. k_0 as a function of solution pH obtained at 298.15 K for decomposition of H_2O_2 (0.5 mM) on ZrO_2 (0.5 g) particle suspensions in 50 ml solution. © American Chemical Society.

The pH of the point of zero charge of ZrO_2 is ≈ 6.5.[141] As can be seen (Figure 9), the zeroth-order rate constant is linearly dependent on the pH of the solution. When considering the zeroth-order rate constant – where the surface concentration of H_2O_2 is close to constant with the course of the reaction – it is possible to have a picture of what is the effect of the amount of surface superoxide radical in the reaction rate. Since within the range of studied pH values the deprotonation of H_2O_2 and $HO^{\bullet}$ radical are not to be considered due to their higher pK_a values, the effect pH on the eventual intermediate reaction species translates in the amount of superoxide radical present at the surface. Reaction (R11) is dependent on the number of available sites on the surface where H_2O_2 can bind to. As such, the amount of $O_2^{-\bullet}$ bound to the surface should have an impact on the overall reaction rate by causing alterations in the interactions between H_2O_2 and the active sites in the surface due to the occupancy of the latter by the superoxide anion radical. This means that the rate at which H_2O_2 reaches the catalytically active surface sites will be decreased causing the reaction rate constant to decrease. Following this reasoning, as expected, when considering the amount of superoxide radical present on the surface, the k_0 is higher the less superoxide is present on the surface. On the other hand, it is also necessary to consider the possible effect of the presence of the buffer system used to adjust the pH.

4.1.2 *Other transition metals and lanthanide oxides*

4.1.2.1 *TiO_2 and Y_2O_3*

Data for H_2O_2 decomposition on a series of oxide materials has revealed that the rate constants can differ substantially depending on the type of oxide.[129] In order to better understand the processes involved in the decomposition of H_2O_2 it is important to understand how its kinetics and energy barriers differs for different materials. This information can possibly be correlated with properties of the materials which will be reflected by the kinetic parameters and which can help understand the mechanisms involved.

The reactions of H_2O_2 with TiO_2 and Y_2O_3 were investigated using the same *Sa/V* of oxides as for ZrO_2. This allows for direct comparison of kinetic parameters and reveals possible differences on the catalytic efficiency of the oxides. The data obtained for the reaction of H_2O_2 with TiO_2 and Y_2O_3 are represented in Figure 10.
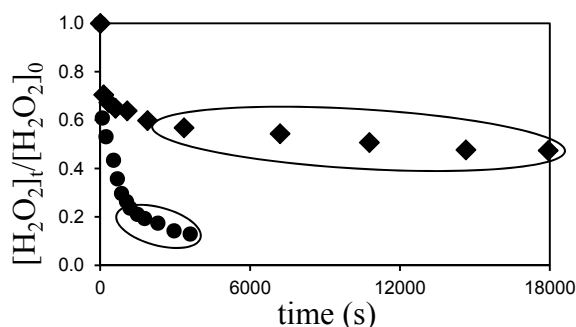

Figure 10. Normalized concentration of H_2O_2 as a function of reaction time in the reaction with TiO_2 (♦) and Y_2O_3 (●) at T = 298.15 K with $[H_2O_2]_0$ = 0.5 mM. © American Chemical Society.

Besides the data shown here previously for ZrO_2, it has been reported that for similar systems the catalytic decomposition of H_2O_2 follows first-order kinetics.[142-144] However, as shown for ZrO_2, the apparent reaction order is strongly dependent on the (S_A/V). When the available surface area of catalyst is in excess, first-order kinetics are observed. Zeroth-order kinetics are observed when the available surface area is too small. It can be seen (Figure 10) that the reaction of H_2O_2 with TiO_2 and Y_2O_3 deviates from first-order kinetics and two different trends can be observed. In both cases, after a fast initial consumption of H_2O_2, the reaction is slowed down significantly. To extract the rate constants, the two visible trends for each reaction in Figure 10 were considered to be the result of two different processes governing the kinetics. The nature of the two different kinetic trends of this reaction were investigated by performing the reaction in the presence of Tris buffer and tracking the formation of intermediate HO• radical with reaction time (this will be discussed in the section 4.2.2 of this thesis). The highlighted areas in

Figure 10 denote the regions where the kinetics start to be controlled by the decomposition of H_2O_2 after the initial adsorption process. By extracting the rate constants from these plots, taking into account the fact that the two processes, adsorption and decomposition of H_2O_2 occur on different time scales, it is possible to obtain the kinetics of decomposition and adsorption of H_2O_2 with minimal errors associated. The k_0 values obtained at T = 298.15 K, are k_0 = (5.9 ± 0.6) × 10^{-6} M·s^{-1} for the decomposition of H_2O_2 on TiO_2 and k_0 = (4.5 ± 0.4) × 10^{-5} M·s^{-1} for the decomposition of H_2O_2 on Y_2O_3. The rate constants for adsorption under the same experimental conditions were extracted from the initial parts of the plots. The obtained k_1 values for this process are k_1 = 3 × 10^{-3} s^{-1} for adsorption of H_2O_2 on TiO_2 and k_1 = 6 × 10^{-3} s^{-1} for adsorption of H_2O_2 on Y_2O_3. The good separability of processes allowing the extraction of coherent kinetic data for either the adsorption or decomposition means that it is possible to obtain a k_2 value for the adsorption process and in a similar way, to extract a quantity from the region of the plot that shows zeroth-order kinetics and which correlates with the catalytic capacity of the surfaces. The data used for determination of the k_2 values for adsorption are represented in Figure 11.
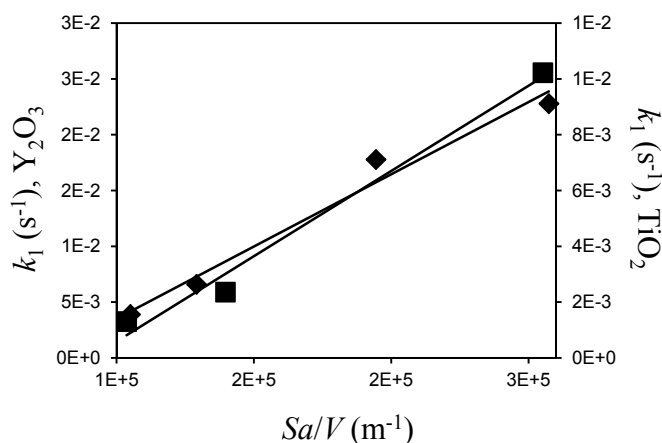
Figure 11. First order rate constants for adsorption of H_2O_2 (0.5 mM) in 50 ml, as a function of solid-surface-area-to-solution-volume-ratio (S_A/V), for adsorption onto Y_2O_3 and TiO_2 at T = 298.15 K. © American Chemical Society.

The k_2 values for adsorption of H_2O_2 extracted from these plots are k_2 = (5.2 ± 0.6) × 10^{-8} m·s^{-1} for adsorption onto TiO_2 and k_2 = (1.5 ± 0.2) × 10^{-7} m·s^{-1} for adsorption onto Y_2O_3. As for the k_2 value obtained for reaction with ZrO_2, these values are far from the diffusion limit.[9] However, the k_2 values for adsorption onto TiO_2 and Y_2O_3 are 2 and 3 orders of magnitude higher than the k_2 value obtained for decomposition of H_2O_2 onto ZrO_2 respectively.

A plot of the variation of the k_0 values for decomposition of H_2O_2 as a function of Sa/V gives the rate constant k_c which represents the catalytic

capacity of the surface. The obtained data for the variation of k_0 with mass of oxide is shown in Figure 12.
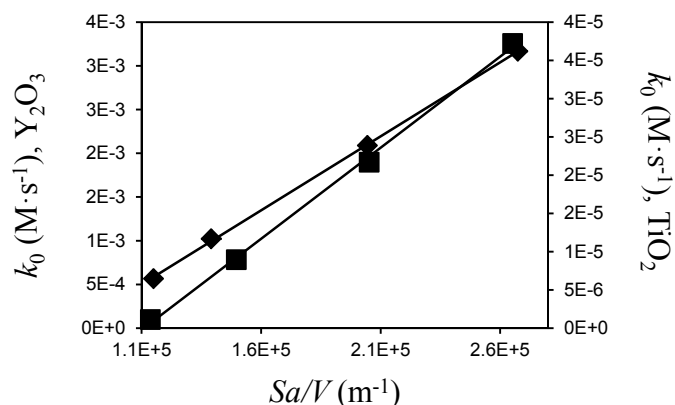
Figure 12. Zeroth-order rate constants as a function of solid-surface-area-to-solution-volume-ratio (Sa/V) for the reactions of decomposition of H_2O_2 with Y_2O_3 (■) and TiO_2 (♦) at $T = 298.15$ K. © American Chemical Society.

The rate constants k_c extracted from the plots of Figure 12, obtained at $T = 298.15$ K are $k_c = (1.93 \pm 0.02) \times 10^{-13}$ mol·m^{-2}·s^{-1} for reaction with TiO_2 and $k_c = (2.08 \pm 0.06) \times 10^{-11}$ mol·m^{-2}·s^{-1} for reaction with Y_2O_3. These values describe the catalytic efficiency of the surfaces, per unit of surface area. It can be seen that the catalytic efficiency of the surface of Y_2O_3 in catalyzing the decomposition of the H_2O_2, is higher than that of TiO_2 by 2 orders of magnitude.

Determining the amount of H_2O_2 removed from solution – in the initial process of adsorption onto the surfaces – as a function of oxide surface area, allows determination of the number of adsorption sites capable to accommodate H_2O_2, per unit surface area. The resulting data obtained for this study is represented in Figure 13.
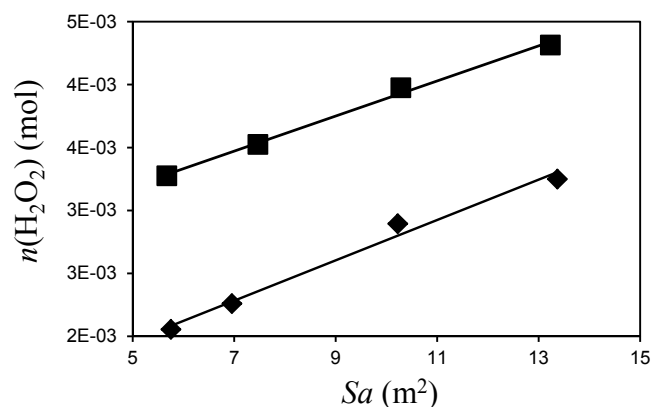
**Figure 13**. Variation in the amount (n) of H_2O_2 molecules removed from solution by adsorption onto TiO_2 (♦) and Y_2O_3 (■) as a function of the surface area of solid (Sa) present in the reaction system at T =298.15 K. Initial $[H_2O_2]$ = 0.5 mM; V = 50 mL. © American Chemical Society.

The number of surface (or interfacial) sites capable of adsorbing H_2O_2 is $(2.0 \pm 0.1) \times 10^{-4}$ mol·m^{-2} for TiO_2 and $(1.00 \pm 0.02) \times 10^{-4}$ mol·m^{-2} for Y_2O_3. It is important to note that these numbers are for the adsorption of H_2O_2 onto the hydroxylated surfaces in equilibrium, in a H_2O solution. These numbers might vary with the course of the reaction due to the adsorption of H_2O_2 reaction products onto the surfaces. These products can eventually adsorb onto the same surface sites preferred for H_2O_2 adsorption. The accumulation of reaction products at those sites could ultimately hinder the adsorption of H_2O_2. This issue will be discussed more in depth later in this work.

To determine the Arrhenius activation energies and the activation enthalpies for the reactions of decomposition of H_2O_2 on TiO_2 and Y_2O_3 the k_0 values were studied as a function of temperature in the temperature intervals T = [298.15–348.15] K for TiO_2 and T = [293.15–308.15] K for Y_2O_3. The respective Arrhenius plots are represented in Figure 14.
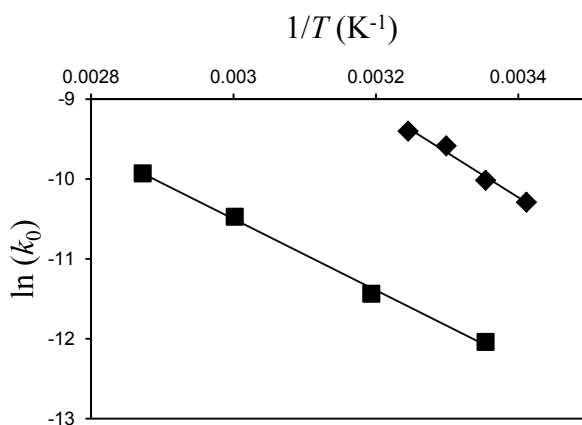
Figure 14. Arrhenius plots using the k_0 values for the reaction of decomposition of H_2O_2 on TiO_2 (■) and Y_2O_3 (♦).© American Chemical Society.

The resulting E_a values for decomposition of H_2O_2 on TiO_2 and Y_2O_3 are 37 ± 1 $kJ \cdot mol^{-1}$ and 47 ± 5 $kJ \cdot mol^{-1}$ respectively. The pre-exponential factors are 18 ± 2 $M \cdot s^{-1}$ for TiO_2 and 6228 ± 6 $M \cdot s^{-1}$ for Y_2O_3. The $\Delta H^{\ddagger}$ values for H_2O_2 decomposition are 34 ± 1 $kJ \cdot mol^{-1}$ for TiO_2 and 44 ± 5 $kJ \cdot mol^{-1}$ for Y_2O_3.

Similarly, the activation energies of adsorption ($E_{a,ads}$) were calculated from plots of the logarithm of the k_1 values for adsorption as a function of the inverse of the temperature. The activation enthalpies of adsorption ($\Delta H_{ads}^{\ddagger}$) were determined using the same k_1 values. The k_1 values for adsorption were extracted from the initial parts of the plots of $\ln([H_2O_2]_t/[H_2O_2]_0)$ as a function of reaction time (Figure 10). The resulting data are: $E_{a,ads}$ = 23 ± 1 $kJ \cdot mol^{-1}$ for adsorption of H_2O_2 on TiO_2 and $E_{a,ads}$ = 32 ± 3 $kJ \cdot mol^{-1}$ for adsorption of H_2O_2 on Y_2O_3. The frequency factors are A = 21 ± 2 s^{-1} for the adsorption on TiO_2 and A = 2625 ± 3 s^{-1} for the adsorption on Y_2O_3. The obtained $\Delta H_{ads}^{\ddagger}$ are: 21 ± 2 $kJ \cdot mol^{-1}$ for adsorption of H_2O_2 onto TiO_2 and $\Delta H_{ads}^{\ddagger}$ = 29 ± 3 $kJ \cdot mol^{-1}$ for adsorption of H_2O_2 onto Y_2O_3. The obtained values for A differ by 2 orders of magnitude – the higher value is for adsorption onto Y_2O_3. The frequency factors for a first-order process represent the number of events (controlling the kinetics) per unit time. When applied to adsorption, they are related with the accessibility of an adsorbate in reaching the adsorption sites which are able to accommodate the adsorbate. The difference in the values of A for adsorption onto TiO_2 and Y_2O_3 mean that Y_2O_3 is a more efficient adsorbent for H_2O_2. The values obtained for the adsorption site density at the surfaces of the oxides reveal that even though the surface of TiO_2 has twice as much adsorption sites – capable of accommodating H_2O_2 – per unit surface area than Y_2O_3, the Y_2O_3 surface sites are more easily accessible for H_2O_2.

4.1.2.2 *Fe_2O_3, CuO, HfO_2, CeO_2 and Gd_2O_3*

The reactions of H_2O_2 with powder suspensions of: CeO_2, Fe_2O_3, HfO_2, Gd_2O_3 and CuO; in aqueous media were also investigated. The goal is to have a complete set of data for H_2O_2 reactivity with different materials. This is important data for modeling kinetics or thermodynamics of processes that involve these chemicals, but, it is also used later in this work in conjunction with DFT calculations to describe these reaction systems in terms of intrinsic properties of the materials.

From the kinetic experiments it was verified that Fe_2O_3, CuO and Gd_2O_3 display higher overall reactivity towards H_2O_2. This caused the half-lifes of the reactions to become too short to allow collection of a fair quantity of reliable kinetic data. For this reason it was necessary to use a smaller total surface area of these oxides than for all the other oxides studied in this work. The variation in concentration of H_2O_2 with reaction time, for the reactions of H_2O_2 with CeO_2, HfO_2, CuO, Gd_2O_3 and Fe_2O_3 at T = 298.15 K are shown in Figure 15.
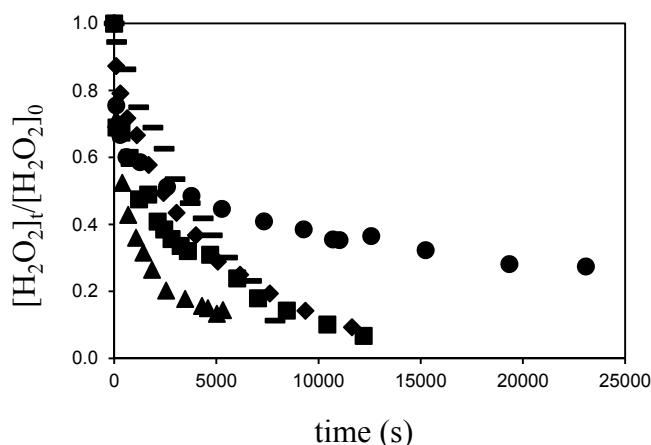
Figure 15. Normalized concentration of H_2O_2 (initially 0.5mM in 50 ml) as a function of reaction time for the reaction with CeO_2 (■), CuO (♦), HfO_2 (▲), Gd_2O_3 (●) and Fe_2O_3 (▬) at T = 298.15 k. *Sa*: Fe_2O_3 (4.5 m^2), CeO_2 (7.5 m^2); CuO (0.3 m^2); HfO_2 (7.5 m^2); Gd_2O_3 (1.7 m^2).

It can be seen (Figure 15) that in the reaction with H_2O_2, the only oxide that deviates in terms of kinetic behavior is Gd_2O_3. Interestingly, when using the same surface area as for the other oxides, Gd_2O_3 displayed a high overall reactivity towards H_2O_2. When using a surface area of 1.7 m^2, the reactivity of Gd_2O_3 towards H_2O_2 is considerably lower than for the other oxides. The initial adsorption of H_2O_2 on Gd_2O_3 is a fast process when compared with the decomposition of adsorbed H_2O_2. By reducing the surface area, the capacity to adsorb H_2O_2 is reduced and the catalytic decomposition becomes the predominant process responsible for the disappearance of H_2O_2 from

solution. This was also observed for the reaction with ZrO_2, when masses of oxide lower than 0.5 g (Sa = 2.5 m^2) were used. In order to have comparable energetic data, the process determining the kinetics, from which the data is extracted, has to be the same for all oxides. It can be seen that for all oxides there is an initial faster disappearance of H_2O_2 from solution which is followed by a process that obeys first-order kinetics. Under the conditions of the experiments (*i.e.* for these values of Sa of oxide and $[H_2O_2]_0$), the time frame for the adsorption process is different for the various oxides but considering the total reaction time, its contribution to the overall reaction is relatively small. The treatment of kinetic data for the calculation of the E_a and $\Delta H^{\ddagger}$ values used the kinetic data obtained from the first-order process that follows the initial adsorption. The k_1 values obtained from the data of Figure 15 are given in Table 3. In Figure 15 it is evident that while for CuO and HfO_2, the plot shapes resemble first-order behavior during most of the reaction time, for CeO_2 and Gd_2O_3 the reaction fits a first-order kinetic treatment only within a limited H_2O_2 concentration range. This differs from the cases of ZrO_2, TiO_2 and Y_2O_3. For ZrO_2 the first-order kinetic behavior was observed during the whole reaction time, while for TiO_2 and Y_2O_3 the reaction kinetics are zeroth-order after the fast initial adsorption step that obeys first-order. For these two oxides it was then possible to extract the adsorption kinetic and energetic data due to the good separability of the adsorption from the subsequent process. This is not the case for the other oxides.

The mass dependency of the k_1 values for the reactions with Fe_2O_3, CuO, CeO_2, HfO_2 and Gd_2O_3 are shown in Figure 16.
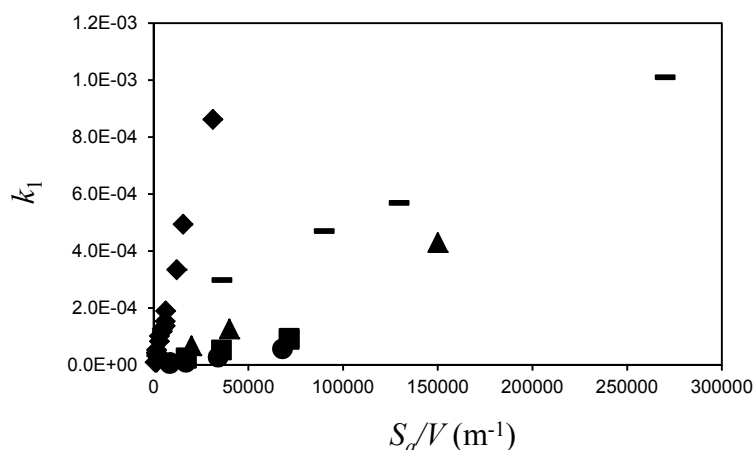
**Figure 16**. Variation in first-order rate constant with the surface-area-to-solution-volume-ratio (Sa/V) of oxide for decomposition of H_2O_2 (0.5 mM; 50 ml) at T = 298.15 K. Fe_2O_3 (▬), CuO (♦), CeO_2 (■), HfO_2 (▲) and Gd_2O_3 (●).

It can be seen that for the reaction with HfO_2 the value of k_1 shows a high mass dependency, while in the opposite extreme lays CeO_2. The

corresponding obtained k_2 values and the value of the intercept at zero coordinate (b_2) are given in Table 3.

Table 3. Obtained k_1, k_2 and b_2 for decomposition of H_2O_2 (0.5mM; 50 mL) catalyzed by different oxides at T = 298.15 K. k_1 were obtained with the following Sa of oxides: ZrO_2 (7.5 m²), TiO_2 (7.5 m²), Y_2O_3 (7.5 m²), Fe_2O_3 (4.5 m²), CeO_2 (7.5 m²); CuO (0.3 m2); HfO_2 (7.5 m²); Gd_2O_3 (1.7 m²). *Note: The rate constant values for TiO_2 and Y_2O_3 are k_0 ($M·s^{-1}$) and the k_c and b_c values are obtained from k_0 values.*

Material	k_1 (s^{-1})	k_2 ($m·s^{-1}$)	b_2 (s^{-1})
ZrO_2	$(6.15 \pm 0.04) \times 10^{-5}$	$(2.39 \pm 0.09) \times 10^{-10}$	3×10^{-5}
Fe_2O_3	$(2.1 \pm 0.4) \times 10^{-4}$	$(3.0 \pm 0.06) \times 10^{-9}$	2×10^{-4}
CeO_2	$(1.7 \pm 0.5) \times 10^{-4}$	$(2.80 \pm 0.07) \times 10^{-8}$	5×10^{-6}
CuO	$(1.90 \pm 0.05) \times 10^{-4}$	$(1.23 \pm 0.06) \times 10^{-9}$	6×10^{-6}
HfO_2	$(4.3 \pm 0.9) \times 10^{-4}$	$(2.78 \pm 0.02) \times 10^{-9}$	1×10^{-5}
Gd_2O_3	$(3.6 \pm 0.3) \times 10^{-5}$	$(9.4 \pm 1) \times 10^{-10}$	6×10^{-6}
Material	k_0 ($M·s^{-1}$)	k_c ($mol·m^{-2}·s^{-1}$)	b_c ($M·s^{-1}$)
TiO_2	$(5.9 \pm 0.6) \times 10^{-6}$	$(1.93 \pm 0.02) \times 10^{-13}$	$(1.55 \pm 0.05) \times 10^{-9}$
Y_2O_3	$(4.5 \pm 0.4) \times 10^{-5}$	$(2.08 \pm 0.06) \times 10^{-12}$	$(2.3 \pm 0.1) \times 10^{-5}$

The fastest heterogeneous process (Table 3) is for the reaction with CeO_2 while the slowest is for the case of ZrO_2. The decomposition of H_2O_2 catalyzed by Gd_2O_3 is the slowest from all the materials showing first-order kinetics for decomposition and the fastest is that on the surface of Fe_2O_3. The higher value of b_2 for the case of F_2O_3 indicates that the apparent reactivity of H_2O_2 has a higher contribution from a homogeneous process than in the case of the other materials. Most likely the homogenous process is the Fenton reaction which takes place in the bulk solution due to the presence of dissolved Fe^{2+} released from the surface of Fe_2O_3.[145] Fe^{2+} can be formed by reduction of Fe^{3+} initiated by a product of H_2O_2 decomposition, the HO_2 radical[128] and which involves directly $O_2^{-\bullet}$. to form O_2,[133] following a scheme similar to what is represented in Reaction (R16).

The E_a values were obtained from plots of the logarithm of the first-order rate constants as a function of the inverse absolute temperature. The temperature dependence of the reaction rate constants for the different oxides was studied in the temperature interval T = [298.15–334.15] K for Fe_2O_3, CuO, HfO_2 and T = [298.15–353.15] K for CeO_2 and Gd_2O_3. The upper temperature limit is the value below which it was possible to collect enough data points for the H_2O_2 concentration as a function of time, with minimal errors associated. This because the reaction becomes too fast to allow proper data collection above a certain temperature. The upper limit of error

considered acceptable was 5%. The Arrhenius plots are represented in Figure 17 and the resulting data are shown in Table 4.
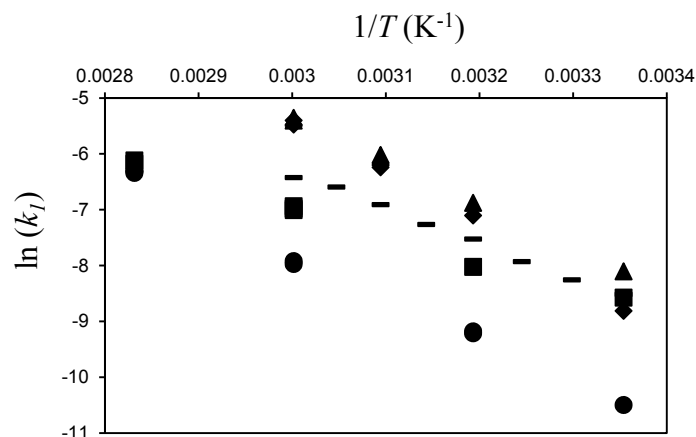

Figure 17. Arrhenius plots for the first-order rate constant as a function of reaction temperature for the decomposition of H_2O_2 (0.5mM; 50 mL) catalyzed by different oxides. CeO_2 (■), CuO (♦), HfO_2 (▲), Gd_2O_3 (●) and Fe_2O_3 (▬). *Sa*: Fe_2O_3 (4.5 m²), CeO_2 (7.5 m²); CuO (0.3 m²); HfO_2 (7.5 m²); Gd_2O_3 (1.7 m²).

Table 4. Arrhenius activation energies (E_a), surface area normalized pre-exponential factors (A), and enthalpies of activation ($\Delta H^{\ddagger}$) for the catalytic decomposition of H_2O_2 on different oxides. *Reaction parameters obtained from first-order kinetics except where stated otherwise‡.*

Material	E_a (kJ·mol⁻¹)	$\Delta H^{\ddagger}$ (kJ·mol⁻¹)	A (s⁻¹)	Particle size
ZrO_2	33 ± 1	30 ± 1	30	< 5 μm
TiO_2‡	37 ± 1	34 ± 1	18 M·s⁻¹	32 nm
Y_2O_3‡	44 ± 5	44 ± 5	6.2×10^3 M·s⁻¹	< 10 μm
Fe_2O_3	51 ± 1	44 ± 1	1.8×10^5	< 5 μm
CeO_2	40 ± 1	37 ± 1	1.4×10^3	14 μm
CuO	76 ± 1	73 ± 1	8.6×10^{10}	< 50 nm
HfO_2	60 ± 1	57 ± 1	1.1×10^7	44 μm
Gd_2O_3	63 ± 1	60 ± 1	1.5×10^7	15 nm

The obtained E_a and $\Delta H^{\ddagger}$ values vary significantly for the different oxides studied (Table 4). This indicates that the activation energies are most likely dictated by microstructural properties of the particles such as the type of atoms present at the catalytically active surface sites and the extent of hydroxylation at these sites. In aqueous solution, most of the metal oxide surfaces are hydroxylated, due to dissociative adsorption of H_2O.[146] The structure and extent of this hydroxylation layer will in turn determine the rigidity of the interfacial water layers which lay slightly further from the surface but still interact with the surface HO-groups. The more rigid the

interfacial layers of adsorbed water, the higher the barrier for diffusion of H_2O_2 through the layer before it reaches the catalytically active surface sites. Hence, the affinity of the surfaces towards water is expected to contribute to the observed activation energy barriers for H_2O_2 decomposition. Also the intermediate products formed during decomposition of H_2O_2 are oxygen species that in spite of being radicals, to some extent, have "water-like" properties such as the ability to form hydrogen bonds.[74]

4.2 Mechanistic studies – the HO radical as primary product of H_2O_2 decomposition

The kinetic and energetic data presented in section 4.1.2 shows that for the catalytic decomposition of H_2O_2 on different metal oxide surfaces the energy barriers and the pre-exponential factors differ widely. This is an indicator that distinct interfacial/surface processes might be involved or have different importance in the reactions with the different materials.

Reactions (R11) to (R13) have been suggested based on liquid phase data for H_2O_2 reactivity.[129] Direct evidence for the formation of HO radicals as primary product and their further role in the decomposition of H_2O_2 at a solid-liquid interface are processes which are not completely understood. It has been suggested that even at an interface with a surface, these radicals can react further with H_2O_2 to form $HO_2^{\bullet}$ and $O_2^{-\bullet}$.[147-149] In previous studies of this type of reaction, EPR/ESR measurements revealed the presence of $HO_2^{\bullet}$, $O_2^{-\bullet}$ and peroxyl radical species on the surface of different oxides. These radicals are normally short-lived and reactive but due to their stabilization by forming bonds with the surfaces, they had become long-lived.[135,150] It was also demonstrated that the possible existence of such chemical species is a factor that depends on the solution pH.

In order to better understand the formation of intermediate $HO^{\bullet}$ during the decomposition of H_2O_2, a mechanistic study was performed. According to the proposed mechanism, the $HO^{\bullet}$ is formed in the decomposition of H_2O_2 in the presence of a metal oxide according to Reaction (R11).[129] Studies on the dynamics of formation of $HO^{\bullet}$ produced during decomposition of H_2O_2 can help understand the process of formation of $HO^{\bullet}$ during the reaction. These studies involved determining the rate of formation of $HO^{\bullet}$ and compare its dynamics with the rate of consumption of H_2O_2. The chemical yield for the formation of formaldehyde upon reaction of the $HO^{\bullet}$ with Tris was determined by quantifying the amount of formaldehyde produced from a known amount of $HO^{\bullet}$ in the system. For that, a calibration curve was obtained by performing an experiment where a known amount of $HO^{\bullet}$ was produced by γ-radiolysis and scavenged by Tris producing formaldehyde according to the scheme shown in Figure 18.
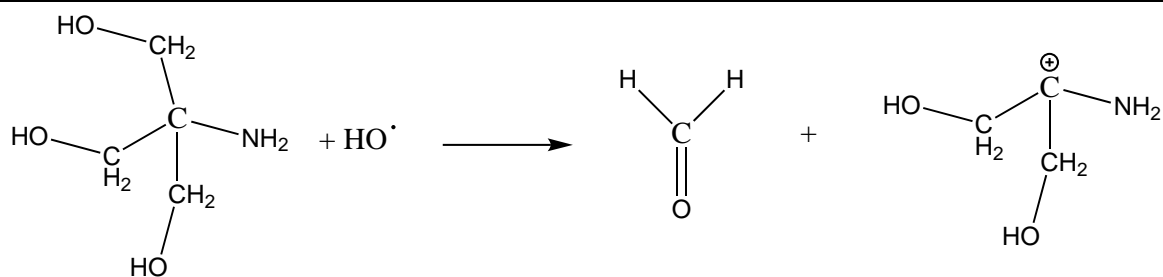
Figure 18. Reaction of tris(hydroxymethyl)aminomethane (Tris) with HO$^•$ producing formaldehyde and a radical species which can further react to form a more stable species.

The method for the spectrophotometric detection of CH_2O, based on the Hantzsch reaction,[151] has been used in previous works. In this case however it was necessary to use a modified version of this method.[152] The use of acetoacetanilide (AAA) instead of acetylacetone or 2,4-pentadione avoids interferences with H_2O_2 which made this technique possible to apply with good sensitivity to the systems studied here. A scheme of the reactions involved is shown in Figure 19.
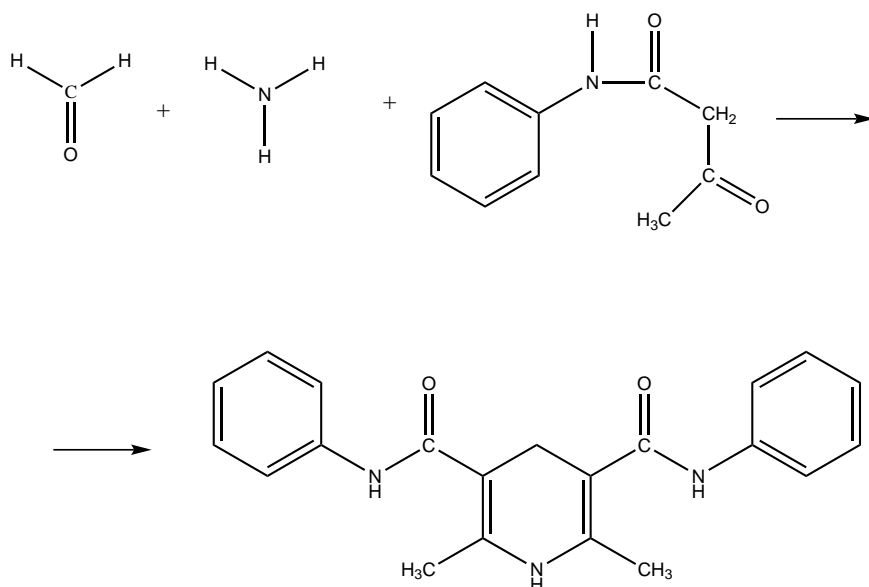
Figure 19. Formation of a pyridyl derivative from the reaction of CH_2O with acetoacetanilide (AAA) in the presence of ammonium acetate.

For the calibration of the method the principle based in Reactions (R2) and (R3) occurring upon radiolysis of water was used. The amount of hydroxyl radicals produced during water radiolysis was quantified according to Equation (2). The set of data obtained for the amount of CH_2O produced as a function of the amount of hydroxyl radicals present in solution upon irradiation of a solution 20 mM in tris/HCl buffer, pH = 7.5 in 50 ml H_2O at T = 293.25 K, are represented in Figure 20.
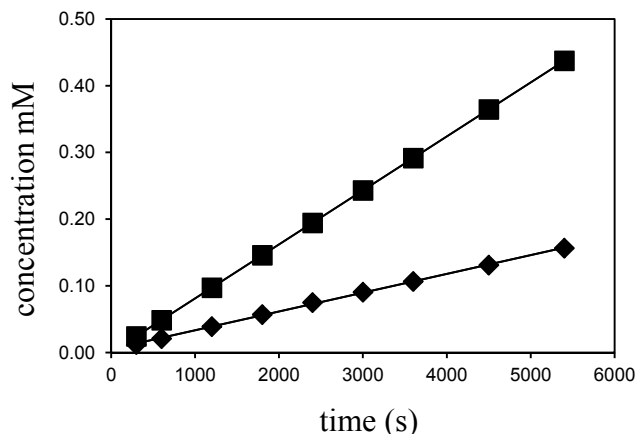
Figure 20. Comparison between the rate of formation of hydroxyl radicals (■) in water radiolysis and the corresponding concentration of formaldehyde (♦) obtained using the modified Hantzsch method. © American Chemical Society.

The yield of the method, when comparing the concentration of CH_2O produced, with the accumulated concentration of hydroxyl radicals present in solution is 35%. This means that 35% of the $HO^•$ present in the system react with Tris buffer to produce CH_2O. A result well below 100% would be expected since according to scheme 2, the reaction of $HO^•$ with Tris can take place in other positions of the molecule besides the α-hydrogen atom of the alcohol group that results in the formation of CH_2O. Hence, the reaction can follow different pathways producing different compounds not detectable by the modified Hantzsch method. The detection limit obtained for CH_2O is 0.5 µM which in the homogeneous system corresponds to a concentration in $HO^•$ equal to 1.43 µM. This is the limit of detection of the method obtained by using solutions of different formaldehyde concentration, which were put in contact with ZrO_2 particle suspensions. A literature value obtained for a system where no solid was present is 0.1 µM in CH_2O.[152] It can be concluded that this method can be applied to the metal oxide-hydrogen peroxide system without major changes in the detection limits caused by interferences due to the presence of H_2O_2 and the oxide.

4.2.1 *ZrO₂*

A study involving determining the amount of CH_2O and consequently the amount of $HO^•$ produced during the course of the reaction between H_2O_2 and ZrO_2 was performed. The reaction media consisted of ZrO_2 (4.5 g; *Sa* = 22.5 m²) at *T* = 293.25 K in 50 ml H_2O with Tris buffer (20 mM) and H_2O_2 (5 mM). The pH was adjusted to 7.5 with HCl. Samples were collected at different time intervals and filtered. Subsequently 1.5 ml of reactant solution was diluted in 2.5 ml solution of ammonium acetate (4 M) and 1 ml solution of

acetoacetanilide (0.2 M) in ethanol. The modified Hantzsch reaction was left to react during 15 minutes at a temperature of 313.15 K. The obtained set of data is represented in Figure 21.
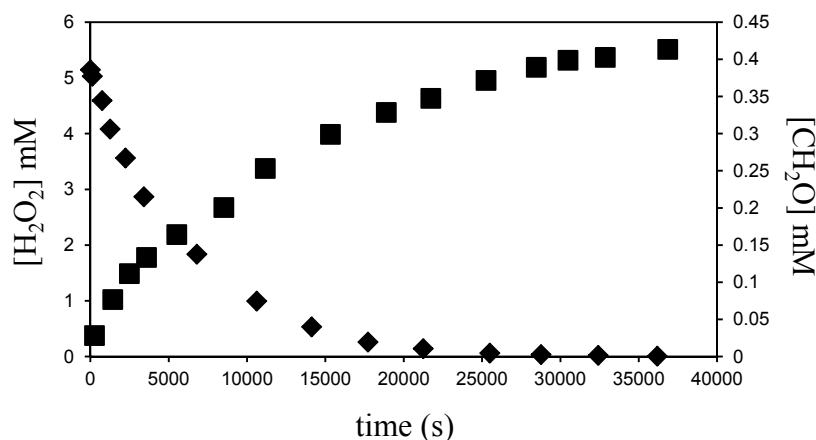

Figure 21. Evolution in the concentrations of H_2O_2 (♦) and CH_2O (■) as a function of reaction time, in the reaction of H_2O_2 with ZrO_2. © American Chemical Society.

According to the proposed overall stoichiometry for the reaction of H_2O_2 in the surface of ZrO_2, Reaction (R15), for each mole of H_2O_2 consumed, two moles of $HO^•$ are produced. The measured concentration of $HO^•$ represented in Figure 21 is ≈ 1/10 of the concentration predicted by the reaction stoichiometry. This is due to the competition between Tris buffer and H_2O_2 to react with the hydroxyl radical. The energetics of the bonds involved in both reactions are approximately of the same magnitude, the cleavage of the O-H bond in Tris buffer requires around[153] 431 kJ·mol^{-1} of energy, the cleavage of the C-H bond requires 393 kJ.mol^{-1} while the cleavage of the O-H bond in H_2O_2 requires[136] 429 kJ·mol^{-1}. Although the method used for measuring the amount of $HO^•$ does not allow discriminating if the $HO^•$ are on the surface of the oxide or in solution when scavenged by the Tris, previous studies show that for similar systems, the $HO^•$ can be trapped and stabilized on the surface of the metal oxide powder.[149] This could alter the reactivity of these radicals towards Tris and H_2O_2. The rate constant for H_2O_2 decomposition on ZrO_2, obtained in the presence of the $HO^•$ scavenging system – Tris/HCl buffer (pH = 7.5) – was compared with the rate constant obtained under normal conditions – no buffering system present (pH = 7.0). The k_1 value obtained for T = 313.15 K under normal conditions is k_1 = (1.22 ± 0.13) x 10^{-4} s^{-1} and the first-order rate constant obtained in the presence of Tris/HCl buffer at pH = 7.5 produced the value k_1 = (1.13 ± 0.70) x 10^{-4} s^{-1}. When taking the associated errors into account, the obtained values are in good agreement and it is not possible to state that the buffering system Tris/HCl at pH = 7.5 is affecting the reaction rate when compared to the reaction where no buffer is present.

It can be seen (Figure 21) that the shapes for the curves for disappearance of H_2O_2 from solution and the corresponding curve for the amount of $HO^\bullet$ scavenged by Tris are symmetrical. This is a strong indication that the scavenged $HO^\bullet$ are a primary product of the decomposition of H_2O_2 according to Reaction (R11). Also, from the good symmetry of both plots it is possible to state that the processes that lead to the formation of CH_2O and its subsequent release into solution have a rate which is in the same order of magnitude as the rate of decomposition of H_2O_2.

The modified Hantzsch method is an easy and sensitive method for the determination of the concentration of $HO^\bullet$ radicals produced as an intermediate product of the decomposition of H_2O_2. Given the complexity of the system – due to the possibility of innumerous surface phenomena that could cause interferences with the reaction of production of CH_2O and further with the modified Hantzsch reaction – one could expect that the *sensitivity* of this method would be reduced when applied to the system metal oxide-hydrogen peroxide. This is because of the possible formation of complexes between eventual metal cations released into solution – *i.e.* from the particles surfaces – and the reagents or products of the modified Hantzsch reaction – *i.e.* Acetoacetalide, ammonium acetate and the product pyridyl compound. This was not verified and the detection limit for CH_2O is in the same order of magnitude of the limit of detection of the method previously published and where no solid was present.

4.2.2 *TiO₂*

In was shown (section 4.1.2.1) that for the reaction of H_2O_2 with Y_2O_3 and TiO_2, in both cases, after a fast initial disappearance of H_2O_2 from solution, the reaction is slowed down significantly. To extract the rate constants for adsorption and for decomposition of H_2O_2, the two kinetic trends were considered to be the result of these two different processes. Verifying if $HO^\bullet$ is formed during the stage of initial fast disappearance of H_2O_2 from solution is essential in order to make valid statements regarding the surface process involved. The process can either be molecular adsorption of H_2O_2 onto the surface or decomposition of H_2O_2 or a mixed adsorption/decomposition phenomenon.

The reaction of H_2O_2 (5 mM) with TiO_2 (0.537 g) was performed in a volume of 50 ml of Tris (20 mM) solution at pH 7.5. The pH was adjusted with HCl. Both the disappearance of H_2O_2 from solution and the appearance of CH_2O were monitored as a function of reaction time. The resulting data is shown in Figure 22.
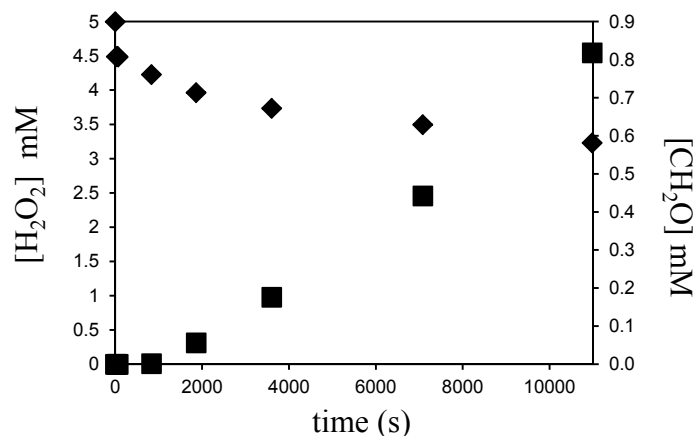
Figure 22. Evolution in the concentrations of H_2O_2 (♦) and CH_2O (■) during the reaction of H_2O_2 with a particle suspension of TiO_2 at T = 298.15 K. © American Chemical Society.

It can be seen (Figure 22) that the initial disappearance of H_2O_2 from solution is not accompanied by the formation of a detectable amount of HO radicals. From the calibration experiments (Figure 20) a consumption of the equivalent amount of H_2O_2 (0.5 mM) that disappeared from solution in the initial process of Figure 22 would produce ≈ 0.18 mM CH_2O. Though, it can be seen that no CH_2O was detected. Hence, it is possible to conclude that the initial fast disappearance of H_2O_2 can be attributed to its molecular adsorption onto the surface of TiO_2. As the reaction of decomposition of H_2O_2 proceeds with a constant rate, the rate of formation of CH_2O remains fairly constant.

4.2.3 *Y_2O_3, Fe_2O_3, CuO, HfO_2, CeO_2 and Gd_2O_3*

The mechanistic study on the formation of $HO^{\bullet}$ intermediate, was extended to the oxides: Y_2O_3, Fe_2O_3, CuO, HfO_2, CeO_2 and Gd_2O_3. The data obtained for CH_2O formation during decomposition of H_2O_2 in the presence of Tris is shown in Figure 23.
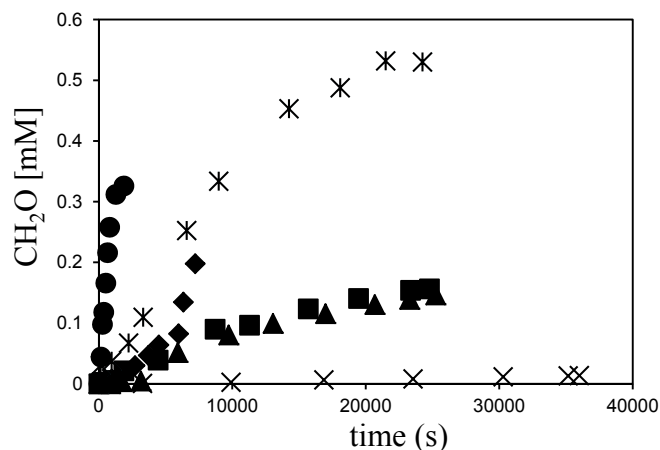
Figure 23. Formaldehyde formed by reaction of HO radicals with Tris during decomposition of H_2O_2 (5 mM; 50 mL) catalyzed by different oxides. CeO_2 (■), CuO (*), HfO_2 (▲), Y_2O_3 (•) Gd_2O_3 (×) and Fe_2O_3 (♦).

It can be seen (Figure 23) that the dynamics of formation of CH_2O vary considerably for the different oxides. Whilst for Gd_2O_3 the amount of CH_2O formed is very low throughout the whole experiment, reaching a maximum of 0.014 mM, for CuO the amount of CH_2O formed reaches a plateau at slightly above 0.5 mM. For Y_2O_3 the rate of formation is very fast when compared with the other systems. The shape of the curves is also considerably different for the different oxides. The shape of the curves in Figure 23 is dependent on the rate of the reaction of H_2O_2. A way to directly compare the yield of CH_2O for the various oxides in a H_2O_2 decomposition rate independent way is to plot the CH_2O amount as a function of the percentage of H_2O_2 that has been consumed. This plot is show in Figure 24.
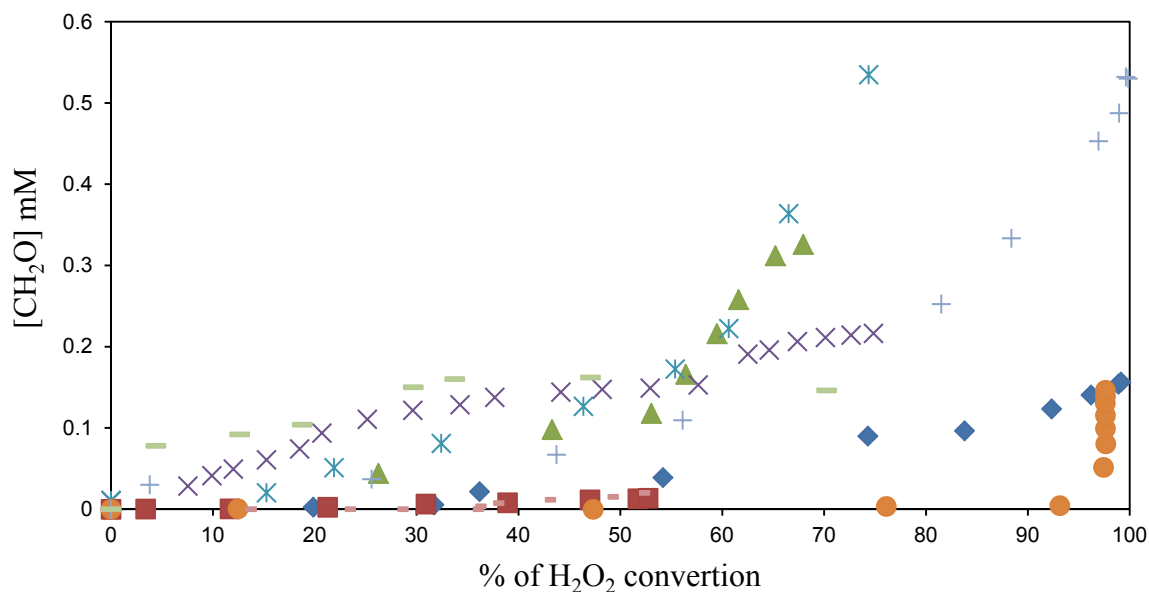
Figure 24. Amount of CH₂O present in the reaction system as a function of the percentage of H₂O₂ consumed from solution during reaction with different oxide materials. CeO₂ (♦); Gd₂O₃ (■); Y₂O₃ (▲); ZrO₂ (×); Fe₂O₃ (*); HfO₂ (●); CuO (+); TiO₂ (-); UO₂ (–).

The amount of CH₂O produced depends on the amount and also on the relative reactivity of HO˙ formed in the decomposition of H₂O₂. One question that can be raised is if the CH₂O formed at the oxide interface, has different dynamics of release into solution for the different oxides. This could ultimately lead to differences in CH₂O bulk concentration even for the same interfacial/surface concentration. A systematic study on CH₂O adsorption onto oxide surfaces – many of them analogues of the oxides investigated here – revealed that CH₂O shows a similar adsorption mechanism for different transition and non-transition metal oxides.[154] It is then plausible that the CH₂O desorption mechanisms and energy barriers are similar for the different oxides studied here. Besides this fact, in the way that it is expressed, the data of Figure 24 is time-independent in what concerns the formation of CH₂O. It is then possible to compare the data directly. It can be seen (Figure 24) that the release of CH₂O as a function of H₂O₂ conversion differs widely for the different oxides. Between some materials, at a given conversion of H₂O₂, the concentration of CH₂O differs by one order of magnitude. The differences observed in Figure 24 can be explained on the basis of the overall mechanism for CH₂O formation. Initially, H₂O₂ in solution is molecularly adsorbed onto the oxide surface. The data presented in section 4.1.2.1 shows that the catalytic decomposition step for ZrO₂ is slower than the adsorption for TiO₂ and Y₂O₃. Given this, only minute amounts of HO˙ are formed during the initial phase (*i.e.* where the adsorption is the dominating process). As the surface coverage by H₂O₂

approaches the maximum, the rate of HO$^{\bullet}$ formation will also approach its maximum. In aqueous solution the rate constants for the reactions of HO$^{\bullet}$ with both H_2O_2 and Tris differ by two orders of magnitude: 2.7×10^7 $M^{-1} \cdot s^{-1}$ and 1.1×10^9 $M^{-1} \cdot s^{-1}$ for H_2O_2 and Tris, respectively.[155,156] In this way, the presence of H_2O_2 will influence the rate of CH_2O formation. In the present case, the reactions occur at the oxide surface and the competition between H_2O_2 and Tris will depend on the rate constants for the two competing surface reactions as well as the relative surface coverage. Tris, due to its size and geometry will not be able to interact with the surfaces at such a localized level as H_2O_2. Consequently, its adsorption energy is expected to be less exothermic than that of H_2O_2. It has been demonstrated that H_2O_2 has a significantly higher affinity for oxide surfaces than Tris.[157] For several of the oxides, the formaldehyde production is very low up to a certain conversion of H_2O_2. The inflection point at which the formaldehyde production rate starts to increase can be attributed to the H_2O_2 concentration where Tris becomes the dominating reactant at the surface, in terms of its concentration weighted with the rate constant for its reaction with HO$^{\bullet}$. Interestingly, the study presented and discussed in section 4.5 of this thesis, on the effects of Tris on the production of molecular oxygen upon catalytic decomposition of H_2O_2 on ZrO_2 shows that the oxygen yield decreases with increasing Tris concentration. This is a direct consequence of the competition between H_2O_2 and Tris for hydroxyl radicals. A similar phenomenon was observed in a study of TiO_2 photocatalysis using Tris as a probe and various concentrations of H_2O_2.[157] The latter was added to capture electrons formed in the initial photolysis of TiO_2 and thereby enhance the photocatalytic activity. It is interesting to note that for oxides where H_2O_2 adsorption appears to be faster than the decomposition reaction (e.g. TiO_2 and Gd_2O_3) a clear inflection point is never reached under the present conditions and very small amounts of formaldehyde are formed. ZrO_2 is a different case where the formaldehyde production starts almost instantly. This could indicate that the adsorption of H_2O_2 is relatively slow and that catalytic decomposition is a very fast process in comparison. For other more extreme cases such as HfO_2 there is an inflection point when the H_2O_2 is almost completely consumed form the solution. Tough, for all the materials, it is not possible to attribute the position of the inflection points as the result of a single effect.

For UO_2, the yield of CH_2O reaches a plateau corresponding to 20% of H_2O_2 consumed and in spite of the continuous disappearance of H_2O_2 from solution, the CH_2O amount does not increase. For this material, besides the decomposition, H_2O_2 is also able to oxidize U(IV) to U(VI).[158] The oxidation product of this reaction is water soluble. As shown previously, the HO radicals produced in the redox reactions are not possible to scavenge with Tris.[91] The plateau in CH_2O production can be interpreted as the point in the

course of the reaction where due to the regeneration of the surface by oxidation of U(IV) to U(VI) – leading to the dissolution of the new formed surface – the contribution of the catalytic decomposition path for the overall H_2O_2 reactivity will be less.

4.2.4 *Kinetic and mechanistic studies of H_2O_2 reactivity towards UO_2 based materials*

4.2.4.1 *UO_2-powder experiments*

A mechanistic study on the formation of HO during the reaction of H_2O_2 with UO_2 materials was performed. The reaction media consisted of H_2O_2, (5 mM), Tris (20 mM), $NaHCO_3$ (1mM) and UO_2 powder (0.1 g) in 50 mL H_2O. The obtained data is shown in Figure 25.
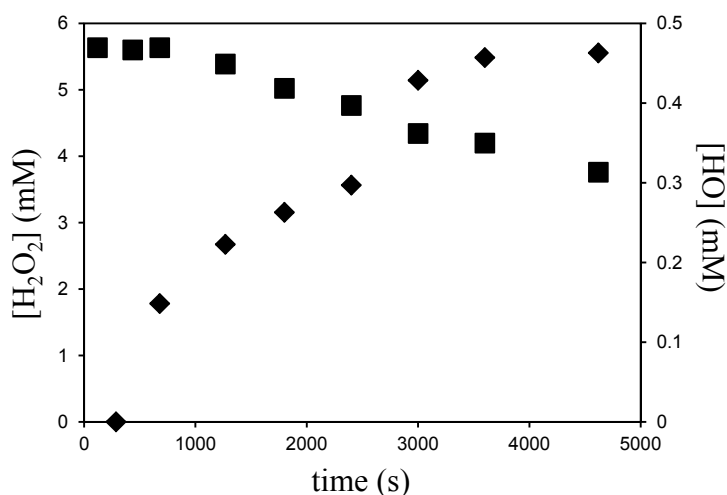
Figure 25. Concentrations of H_2O_2 (■) and scavenged $HO^\bullet$ (♦) as function of reaction time in the reaction of H_2O_2 (5 mM) with a UO_2 (0.1 g) powder suspension at T = 298.15 K in the presence of Tris (20 mM) and $NaHCO_3$ (1mM) in 50 ml H_2O.

Overall, for most of the previously discussed oxides – where H_2O_2 can only react via catalytic decomposition – the dynamics of $HO^\bullet$ formation agree with the dynamics of H_2O_2 consumption. An interesting question is if for a system where a redox mechanism can also take place, the afore mentioned dynamics are also similar. For the case of the reaction of H_2O_2 with UO_2 powder, the overall reactivity of H_2O_2 will have a high contribution from a Fenton type of reaction. According to reported dissolution yields, about 80% of the consumed H_2O_2 will react in a redox process where it oxidizes U(IV) to U(VI). $HO^\bullet$ will also be formed as an intermediate species of this reaction according to Reaction (R9). The remaining 20% of the consumed H_2O_2 will react via catalytic decomposition also leading to the formation of $HO^\bullet$. The $HO^\bullet$ formed in the oxidation of U(IV) to U(V) is not expected to be scavenged

by the Tris because the reaction of HO$^{\bullet}$ with U(V) is a very fast process[159] – the rate constant for reaction of HO$^{\bullet}$ with Tris in aqueous solution is known, but its value for when the reaction takes place at an interface or surface is not known. The scavenged HO$^{\bullet}$ are expected to be produced by the fraction of H_2O_2 that decomposes catalytically on the surface of UO_2 powder. It can be seen (Figure 25) that a significant amount of HO$^{\bullet}$ are scavenged by Tris. The amount of scavenged HO$^{\bullet}$ corresponds to about 6% of the amount of the H_2O_2 consumed in the course of the reaction – ZrO_2 this value is of 10 %. A rough calculation – using the yield of the method for scavenging HO$^{\bullet}$ from solution – can give an approximate idea of the amount of H_2O_2 that reacts by decomposition. The resulting fraction of H_2O_2 that reacts by decomposition is around 17% while the other 83% will react by electron transfer. These values are in excellent agreement with the values estimated for the percentage of H_2O_2 that reacts by decomposition and by electron transfer. These values were obtained based on the ratio between the amount of dissolved uranium and the amount of consumed H_2O_2.[160] The theory that the radicals formed in the oxidation process cannot be scavenged by the Tris is also supported by these results. Nevertheless this calculation is rather rough as it uses the HO$^{\bullet}$ scavenging yields from solution which might not be applicable to a surface. In the case of UO_2 the HO$^{\bullet}$ scavenging yield from solution is very close to the one at the surface/interface. This indicates that the interactions of the HO$^{\bullet}$ with the surface are weak or the further reactions of HO$^{\bullet}$ are very fast, which causes the HO$^{\bullet}$ formed at the interface to have a lability towards reaction with Tris which is close to that in solution.

4.2.4.1 *UO_2 and SIMFUEL pellet experiments*

It is known that the ratio between dissolved uranium and consumed H_2O_2 – dissolution yield – differs significantly depending if the reaction takes place on pure UO_2-pellets or SIMFUEL pellets.[161] SIMFUEL is a material which consists of a UO_2 matrix that has been doped with rare earth elements in order to approximate the material to the real spent nuclear fuel in terms of matrix.[162] Thus, the fact that a surface reaction shows different kinetic and mechanistic parameters for both materials is expected from elementary surface chemistry concepts, as the inclusion of dopants in a solid leads to the formation of surfaces which are different from the non-doped material, both in terms of their chemical environment but also in terms of their structure.[163-165]

H_2O_2 can also react with these materials via a redox process or via catalytic decomposition. It is known[161] that SIMFUEL displays a much lower dissolution yield than UO_2. This indicates that for SIMFUEL, a larger fraction of the H_2O_2 is consumed by catalytic decomposition when compared to UO_2. The overall reactivity of H_2O_2 was found to be 50 % lower on SIMFUEL when compared to pure UO_2. To investigate the mechanistic reasons behind the

observed differences between UO$_2$ and SIMFUEL the amount of scavenged HO$^\bullet$ and dissolved U as a function of reaction time were determined. The presence of the HO$^\bullet$ scavenger – Tris – leads to the formation of a soluble complex with U. This complex has its λ_{max} at 340 nm. This fact does not allow for the direct measurement of the H$_2$O$_2$ in solution using the Ghormley method (λ_{max} at 350 nm). Though, in these systems, the amount of H$_2$O$_2$ consumed in the reaction with the pellets can be determined indirectly. This quantity is related to the amount of uranium in solution – corresponding to the fraction of H$_2$O$_2$ consumed in redox reactions – plus half of the HO$^\bullet$ produced – corresponding to the fraction of H$_2$O$_2$ consumed by catalytic decomposition. It should be noted again that these are rough approximations because it is considered that the yield of the method for HO$^\bullet$ determination does not vary between both materials. This might not correspond to reality. It should be also noted that the *Sa* is significantly lower in the experiments using pellets than in the experiments using powders. Hence, the rate of oxidant consumption will be much lower in the pellet experiment.

The resulting data for the mechanistic experiments on H$_2$O$_2$ reactions with UO$_2$ and SIMFUEL pellets are shown on Figure 26 and Figure 27.
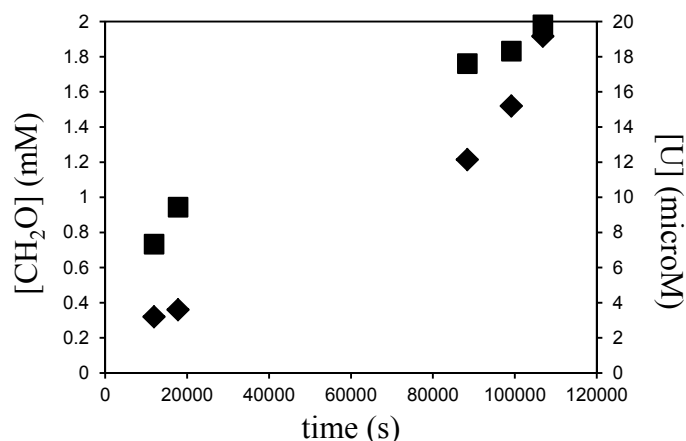
Figure 26. Evolution in the concentrations of U(VI) in solution (■) and CH$_2$O (♦) during the reaction of H$_2$O$_2$ with a UO$_2$ pellet as a function of reaction time at T = 298.15 K. The reaction media consisted of a UO$_2$ pellet in 5 mM H$_2$O$_2$, 20 mM Tris-HCl buffer, 1 mM NaHCO$_3$ in 50 ml H$_2$O.
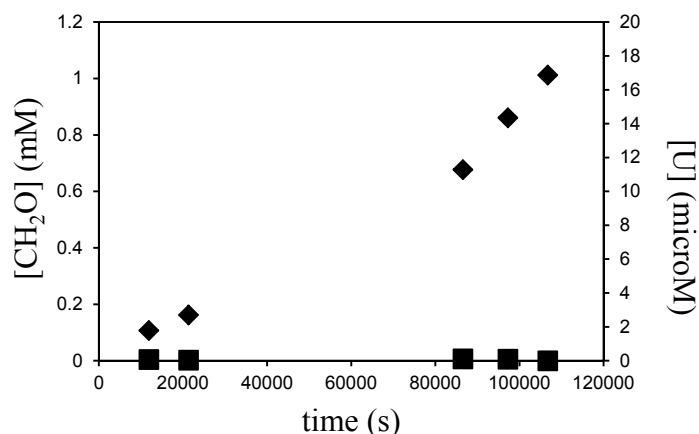
Figure 27. Evolution in the concentrations of U(VI) in solution (■) and CH_2O (♦) during the reaction of H_2O_2 with a SIMFUEL pellet as a function of reaction time at T = 298.15 K. The reaction media consisted of a SIMFUEL pellet in 5 mM H_2O_2, 20 mM Tris-HCl buffer, 1 mM $NaHCO_3$ in 50 ml H_2O.

It is visible in the data shown in Figure 26 and Figure 27 that significant amounts of hydroxyl radicals are formed during the reaction of H_2O_2 with both materials. Though, the amount of hydroxyl radical produced is approximately 50 % lower for SIMFUEL than for UO_2. This observation is in excellent agreement with the difference in overall reactivity of H_2O_2 towards these materials. The dissolution yields for UO_2 and SIMFUEL pellets are 14% and 0.2 %, respectively.[161] Considering the fact that only the HO• formed in the catalytic decomposition is detectable, it is expected that the amount of scavenged HO• parallel the overall H_2O_2 reactivity. The electron transfer process has only a minor impact on the H_2O_2 consumption (14 % for UO_2 and 0.2 % for SIMFUEL). The measured uranium concentrations in this work confirm the previous conclusions on the significant difference in dissolution yield between UO_2 and SIMFUEL. For SIMFUEL the uranium concentration in solution was close to the detection limit throughout the experiment while for the pure UO_2 pellet a significant increase in the concentration of uranium in solution is observed. The ratio between formed HO• and dissolved uranium matches the previously determined dissolution yield. However, the fairly small difference in the amount of HO• scavenged between the two materials supports the idea that the main difference between the materials is the redox reactivity. This is expected because of the inclusion of dopants in SIMFUEL.

4.3 Performance of different density functionals and cluster models in describing the reactivity of H_2O_2, H_2O and $HO^\bullet$ with transition metal oxides.

DFT is a valuable tool for providing a better understanding of the surface chemistry of heterogeneous systems. In this work, the reactivity of H_2O_2, H_2O and $HO^\bullet$ with a multitude of oxide materials was studied using cluster models of the oxides and DFT. For that, various exchange correlation functionals were employed. In this section, the presentation of data (and discussion) is divided in sub-sections by cluster size and degree of surface saturation.

4.3.1 *m-(ZrO₂)₂₆ cluster with B3LYP, B3LYP-D and M06 functionals*

A cluster consisting of 26 units of stoichiometric ZrO_2 was used to evaluate the adsorption energetics of H_2O, H_2O_2 and $HO^\bullet$. The model was constructed by slicing the extended monoclinic crystal (unit cell parameters (a) 5.143, (b) 5.204, and (c) 5.311 Å, Zr-O bond distance 1.771 Å.[109]) and a surface was defined according to the most stable stoichiometric surface of monoclinic zirconia – the ($\bar{1}$11) plane.[166] A top view of the surface of monoclinic ZrO_2 structure sliced according to the ($\bar{1}$11) plane is shown in Figure 28.
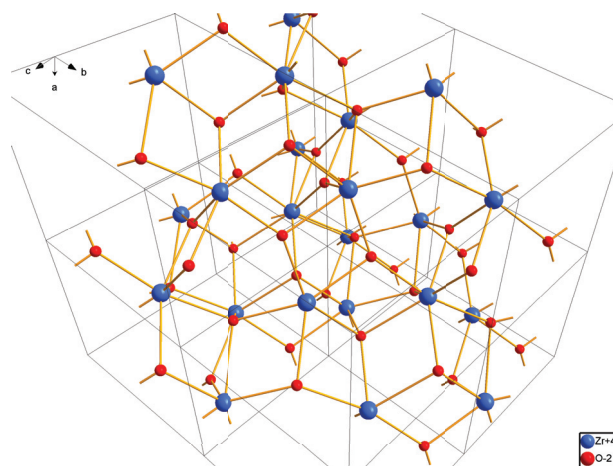
Figure 28. Top view of the single crystal structure of monoclinic ZrO_2 where a surface was defined according to the ($\bar{1}$11) plane. The grids denote the unit cells of the crystal structure. Zr (●), O (●).Reproduced by permission of the PCCP Owner Societies.

For the study of the reactions at its surface, the cluster geometry was constrained, with the exception of the surface atoms directly involved in adsorption and reactivity of the surface species. This model will be denominated *m-(ZrO₂)₂₆*, where *m-* indicates the monoclinic crystal structure. The *m-(ZrO₂)₂₆* with the highlighted reaction site is shown in Figure 29.
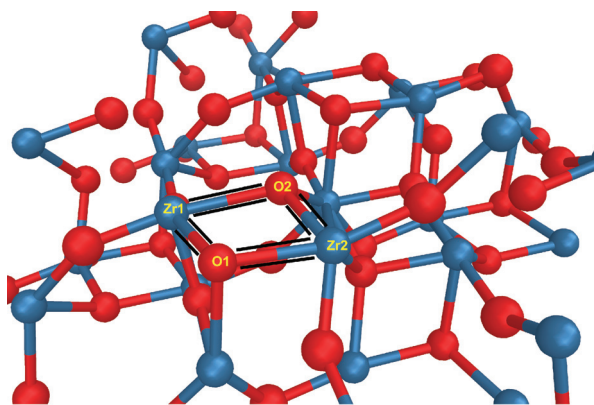
Figure 29. The *m-(ZrO₂)₂₆* cluster used for the study of adsorption of H_2O, H_2O_2 and $HO^\bullet$. The highlighted Zr and O atoms were allowed to relax during geometry optimization of the adsorbed states. Zr (●), O (●).Reproduced by permission of the PCCP Owner Societies.

The choice of this surface site for the study of adsorption was based on preliminary tests that revealed that the adsorption of the species studied here is favored at this surface site when compared to the adsorption at other possible ($\bar{1}11$) surface sites. The adsorption energies calculated using the B3LYP and M06 functionals, and the dispersion corrected B3LYP-D, for dissociative and molecular adsorption of H_2O as well as molecular adsorption of H_2O_2 and its obtained decomposition products (H_2O and $HO^\bullet$) are given in Table 5. The obtained geometries are shown in Figure 30.
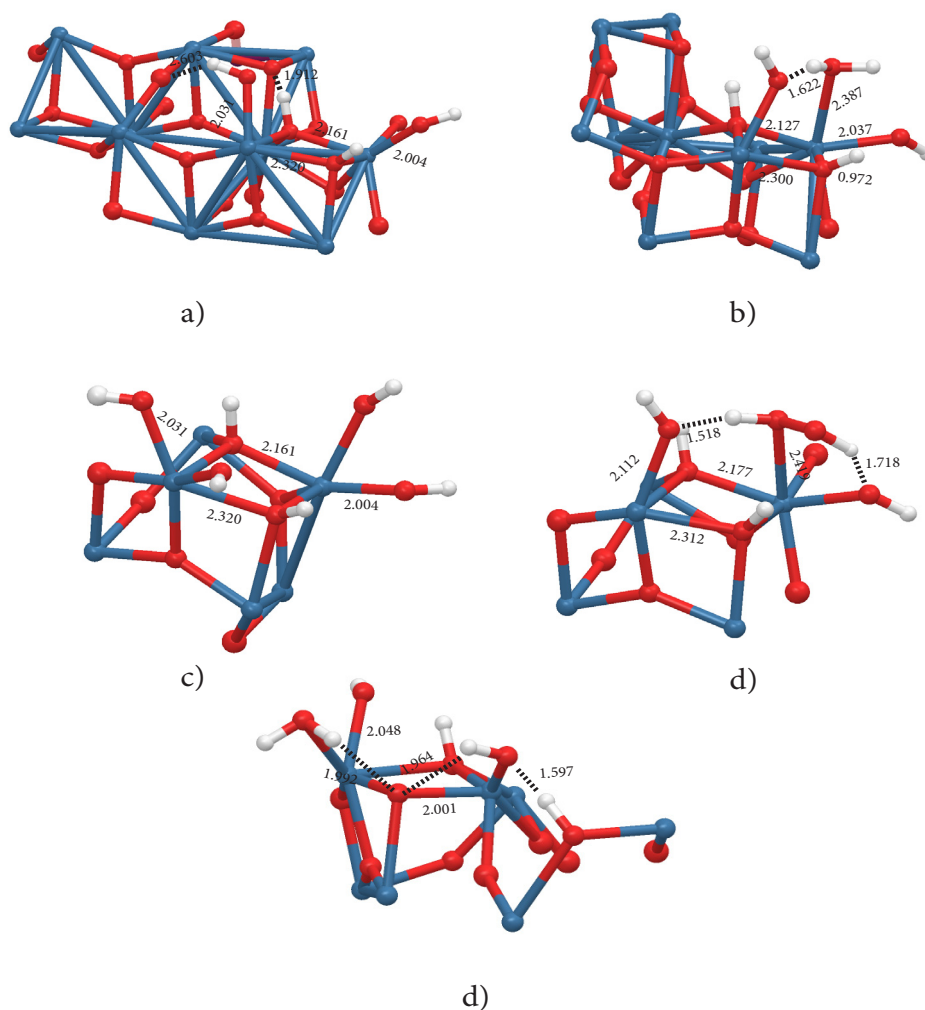
Figure 30. Obtained geometries for the reactions of H_2O_2, H_2O and $HO^{\bullet}$ on the *m-(ZrO$_2$)$_{26}$*. a) Dissociative adsorption of 2 H_2O; b) molecular adsorption of 1 H_2O onto structure a; c) binding of 2 HO radicals onto structure a; d) molecular adsorption of H_2O_2 onto structure a; d) product of the decomposition of H_2O_2. Zr (●), O (●), H (○). Bond lengths in Å. Dashed lines represent hydrogen bonds. *Note: these are zoomed in images of the products formed at the reaction site highlighted on the cluster shown in Figure 27.*

Table 5. ΔE_{ads} for adsorption of H_2O, H_2O_2 and $HO^{\bullet}$ onto a $(ZrO_2)_{26}$ cluster. Reaction energy for decomposition of H_2O_2 (ΔE_r). Values in ($kJ \cdot mol^{-1}$).

Adsorbate	Adsorption energy		
	B3LYP/ LACV3P++**	B3LYP-D/ LACV3P++**	M06/ LACV3P++**
2H_2O *dissociative*	-256	-321	-312
1H_2O *molecular*[a]	-109	-139	-132
2 HO^{\bullet} adsorption	-872	-900	-903
H_2O_2 *molecular*	-143	-180	-166
H_2O_2 decomposition ΔE_r [b]	-523	-513	-520

a – the adsorption of molecular H_2O was studied on the surface of the cluster previously saturated with the products of H_2O dissociative adsorption.

b – the obtained H_2O_2 decomposition products were based in calculations done on smaller sized cluster models where the transition-states obtained for cleavage of the O-O bond in H_2O_2 were relaxed (see section 4.3.2 for details on these calculations). The same primary decomposition products were found for this model.

There is an overall good agreement between the data calculated with M06 and B3LYP-D. The highest difference in energies is 14 $kJ \cdot mol^{-1}$. In general, the "dispersion-corrected" functionals B3LYP-D and M06 predict larger adsorption energies than B3LYP. The pure dispersion effect, taken as the difference between B3LYP-D and B3LYP, is between -14 and -37 $kJ \cdot mol^{-1}$, depending on the adsorbed species (ionic, radical, hydrogen bonding). For molecular adsorption of water, the calculated adsorption energies range from -109 $kJ \cdot mol^{-1}$ (B3LYP) to -139 $kJ \cdot mol^{-1}$ (B3LYP-D), which is larger than previously reported DFT values for low surface coverage (Table 6). This is likely a combined effect of using hybrid DFT and dispersion. The energy for dissociative adsorption of water (-312 $kJ \cdot mol^{-1}$ per two water molecules, leading to -156 $kJ \cdot mol^{-1}$ per water molecule with M06,) is in good agreement with experimental data (Table 6), however, there is a large variation in reported experimental data. This is because the experimentally obtained adsorption enthalpies depend on surface coverage and on the surface geometry – *i.e.* density and type of defects, etc. These in turn depend on the synthetic route used to obtain the surface. Also, the higher exothermicity of the values obtained for adsorption onto this cluster can be attributed to the fact that the clusters terminations are not saturated as in the case of the models that will be discussed next in this work. This causes increased stabilization of the surface atoms of the non-terminated clusters upon

formation of bonds with adsorbates. This is a phenomenon which is known to occur upon formation of bonds with surface sites that are more undercoordinated.[167] Overall, comparisons between computational and experimental data for water adsorption onto metal oxide surfaces have to be done with care. The metal oxide particles used in the determination of the experimental data were in many cases obtained via different synthetic routes, which produces particles with different surface structure, defects, and anisotropic surface energies.[168] These discrepancies can have significant influence on the adsorption energies measured using different particles, and differences of 60 kJ·mol^{-1} have been reported for H_2O adsorption onto two samples of monoclinic ZrO_2 obtained via different synthesis schemes.[169] Furthermore, the computational data referred in Table 6 was obtained for ideal surfaces sliced according to specific Miller planes. Such models do not take into account effects of defects and the multitude of surfaces present in the real systems. The clusters used herein are intended to model adsorption on rough surfaces or surface defects. This might not be representative of the real system, in which a variety of surface defects are present. Nevertheless, the adsorption energies are within the range of values found in the literature shown in Table 6.

Table 6. Literature data for adsorption of H_2O, HO and H_2O_2 onto ZrO_2, TiO_2 and Y_2O_3. (kJ·mol^{-1}).

ZrO$_2$				
Type of data	H$_2$O molecular adsorption	H$_2$O dissociative adsorption	H$_2$O$_2$ molecular adsorption	HO$^\bullet$ Adsorption
Experimental	-(44 − 150)$_a$[170]	-(119; 142)$_a$;[170] -(70 − 94)$_a$[171] -(110 − 170)[169]	–	–
Theoretical	-(42 − 100)$_b$;[172] -(57)$_b$[173]	-(194–208)$_b$;[174] -(91 − 170)$_b$[172]	–	-(498)$_b$[173]
TiO$_2$				
Type of data	H$_2$O molecular adsorption	H$_2$O dissociative adsorption	H$_2$O$_2$ molecular adsorption	HO$^\bullet$ Adsorption
Experimental	-(48 − 68)$_a$[175]	–	–	–
Theoretical	-(71 − 79)$_b$;[176] -(90)$_b$;[177] -(83)$_b$[178]	-(22 − 153)$_b$;[176] -(141)$_b$[177]	-(4 − 78)$_b$[179]	–
Y$_2$O$_3$				
Type of data	H$_2$O molecular adsorption	H$_2$O dissociative adsorption	H$_2$O$_2$ molecular adsorption	HO$^\bullet$ Adsorption
Experimental	–	-(91)$_a$;[180] -(38 − 99)$_a$[181]	–	–
Theoretical	–	–	–	–

a) Refers to an ΔH_{ads}; b) refers to an ΔE_{ads} without zero point energy corrections

4.3.2 m-(ZrO$_2$)$_8$ *cluster with B3LYP, B3LYP-D and M06 functionals*

Another type of cluster to model ZrO$_2$ surfaces is discussed here. A cluster consisting of 8 ZrO$_2$ units was constructed in a similar way as the *m-(ZrO$_2$)$_{26}$* model. The basis for the usage of the saturated cluster model is the fact that it performs good in cases when the cluster sizes are small.[182,183] For implementing the saturated cluster models, the terminal metal atoms were saturated with hydroxide ions (HO$^-$), while terminal oxygen atoms were saturated with protons (H$^+$). All the available terminations were saturated with exception for the reactive site in the ($\bar{1}$11) plane, where dissociative adsorption of water was investigated. The geometry optimizations were done at the B3LYP/LACVP+* level – for the models described further in this section, all the atoms of the clusters and reacting species were allowed to relax during geometry optimizations. This cluster will from now on be denominated *m-(ZrO$_2$)$_8$*. In order to evaluate the effects of dispersion

interactions, adsorption energies were obtained by single-point calculations using the functionals B3LYP, B3LYP-D, and M06. The optimized structure of the m-$(ZrO_2)_8$ cluster is shown in Figure 31.
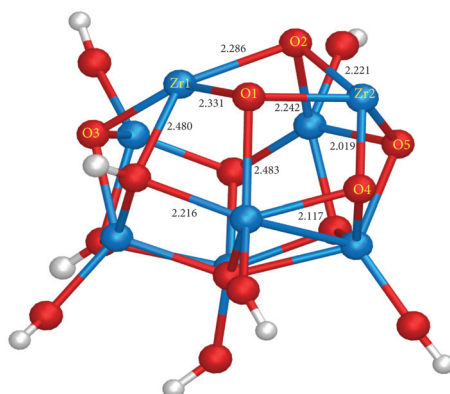
Figure 31. Optimized geometry of the m-$(ZrO_2)_8$ cluster. Zr (●), O (●), H (○).
Reproduced by permission of the PCCP Owner Societies.

The obtained Zr-O bond distances are longer than the experimentally observed distances in the crystalline phase (1.771 Å) but are in good agreement with $(ZrO_2)_4$ clusters optimized at the CCSD(T)/aT and B3LYP/aD levels of theory (~2.1 Å).[184-185] The longer bond distances is due to the lack of a Madelung potential with the same magnitude of the one found in the extended crystal. This causes the bond lengths in the clusters to elongate. Such phenomena also occur upon formation of a surface in a real crystal. A detrimental effect is the one that arises for models such as the m-$(ZrO_2)_{26}$ shown above. The geometry of the whole cluster was not optimized, with the exception of the reactive site. This means that artificial strain can build up in the cluster atoms and have effects on adsorption and reaction energies obtained with such models.[166] These can be more detrimental than the finite size effects introduced by using a smaller terminated model that has been allowed to fully relax.

The first reaction considered was the dissociative adsorption of H_2O. The resulting hydroxylated cluster was used then as the starting point for the study of the reactions with H_2O_2 and $HO^•$. Dissociative adsorption of water onto the m-$(ZrO_2)_8$ model was performed on the atoms: Zr(1), Zr(2), O(1), O(2), O(3), O(4), and O(5) with the resulting HO^- ions binding to the Zr atoms and H^+ binding to the O atoms. Different adsorption modes of the protons and hydroxide ions from the dissociation of two and four water molecules were considered and compared energetically. The resulting structures obtained for the study of water adsorption are shown in Figure 32 and the corresponding energies are given in Table 7.
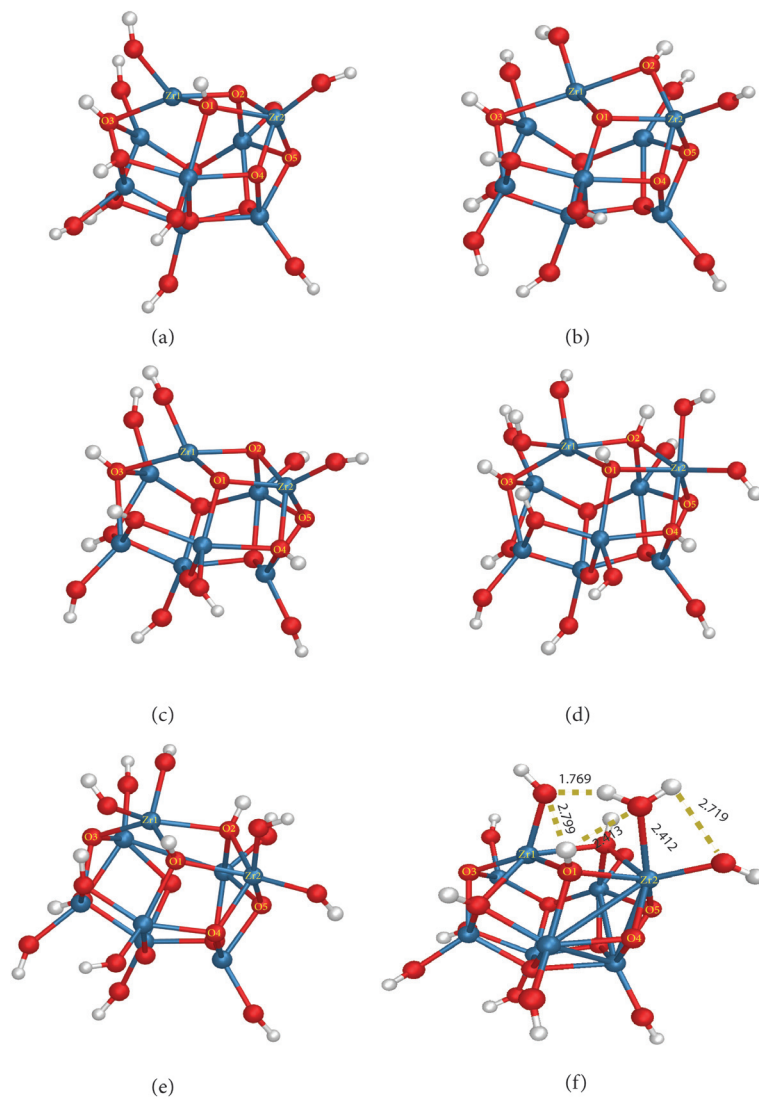
Figure 32. Optimized geometries for adsorption of H₂O and HO radicals into the different available surface sites of the *m*-(ZrO₂)₈ cluster: (a), (b), (c) 2 H₂O molecules, (d) 4 H₂O molecules, (e) 2 H₂O molecules and 2 HO radicals, (f) molecular adsorption of H₂O (dashed lines represent hydrogen bonds). Zr (●), O (●), H (○).The bond lengths are given in Å. Reproduced by permission of the PCCP Owner Societies.

Table 7. ΔE_{ads} for adsorption of H_2O, $HO^.$ and H_2O_2 onto the m-$(ZrO_2)_8$ model. Activation energy for decomposition of H_2O_2, with zero point energy corrections (E_a^{ZPE}). The respective structures are shown in Figure 32 and 31. Values in kJ·mol^{-1}.

Adsorbate	Structure	Adsorption energy		
		B3LYP/ LACV3P++**	B3LYP-D/ LACV3P++**	M06/ LACV3P++**
2 H₂O *dissociative*	Figure 32 (a)	-48	-81	-88
	32 (b)	-77	-107	-120
	32 (c)	-61	-90	-92
4 H₂O *dissociative*	32 (d)	-156	-240	-241
2 HO•	32 (e)	-944	-954	-955
H₂O *molecular*[a]	32 (f)	-71	-85	-78
H₂O₂ *molecular*	Figure 33 (b)	-36	-61	-46
E_a^{ZPE}	Figure 33 (c)	15	12	32

a – the adsorption of molecular H₂O was studied on the surface of the cluster previously saturated with the products of H₂O dissociative adsorption.

For dissociative adsorption of 2 H_2O molecules, as expected, the most exothermic adsorption mode corresponds to the structure that went through the most extensive adsorption site reconstruction (Figure 32b). On this structure, the O(2) atom initially bound to a Zr lattice atom, was dislocated out of the surface plane. The resulting HO group became bi-bridging between two Zr atoms. Such structures have been reported in both experimental and theoretical studies of dissociative adsorption of H_2O in ZrO_2 surfaces.[186,187] The large difference in adsorption energy calculated with B3LYP and B3LYP-D ($\Delta\Delta E_{ads}$=30 kJ·mol^{-1}, Table 7) means that dispersion interactions have an important role in adsorption and are necessary to include in the B3LYP functional to improve the accuracy of this functional for calculations on adsorption. The adsorption energies calculated with B3LYP-D (-107 kJ·mol^{-1}) and M06 (-120 kJ·mol^{-1}), are in reasonable agreement with most experimental data (-70 to -142 kJ·mol^{-1}), although larger values (-170 kJ·mol^{-1}) have been reported (Table 6). As for the case of the *m-(ZrO₂)₂₆* cluster, B3LYP-D and M06 produce similar data for adsorption.

Dissociative adsorption of four H_2O molecules, results in a product where the two hydroxyl groups are bound to the already HO coordinated Zr(1) and Zr(2) atoms (Figure 32d). Due to their proximity caused by their increased surface coverage, hydroxyl groups bound to the same Zr atom are stabilized by hydrogen bonding. A similar situation was found when two HO radicals were adsorbed onto a surface site where two H_2O molecules had previously dissociated (Figure 32e). These observations reveal that the adsorption energies of H_2O can be highly dependent on the degree of surface coverage due to the existence of cooperative effects in adsorption. These cooperative effects in the case of H_2O are to a large extent the result of adsorbate-adsorbate hydrogen bonding. For the adsorption of H_2O, the adsorption of four water molecules (Figure 32d) is the most exothermic. All three functionals predicted this situation, though the adsorption energies obtained with B3LYP-D and M06 are around 85 kJ·mol^{-1} larger than calculated with B3LYP (Table 7). Since the dispersion effect in the adsorption of two water molecules was around -40 kJ·mol^{-1} (Table 7), *i.e.* roughly half the effect in adsorption of four, it can be concluded that the dispersion effect per water molecule is fairly constant with increasing coverage.

The molecular adsorption of a single H_2O molecule occurs via hydrogen bonding and covalent interactions between the oxygen atom of H_2O and the surface Zr(2) atom (Figure 32f). At the B3LYP level, the most stable adsorption mode of two dissociated water molecules (Figure 32b) is only slightly more exothermic than molecular adsorption (Figure 32f, Table 3). On the contrary, the dispersion corrected functionals B3LYP-D and M06 enhances the stability of the dissociative adsorption state significantly, with respect to the state of molecular adsorption. Since the experimental picture is that for ZrO_2 the first water layer dissociates, the dispersion corrected functionals seems to provide a better description. Again, it can be concluded that in these systems, it is necessary to consider the dispersion effects for increasing the accuracy of adsorption data obtained with DFT calculations using B3LYP.

The potential energy surface (PES) for the reaction of decomposition of hydrogen peroxide on the hydroxylated *m-(ZrO₂)₈* cluster, is illustrated in Figure 33.
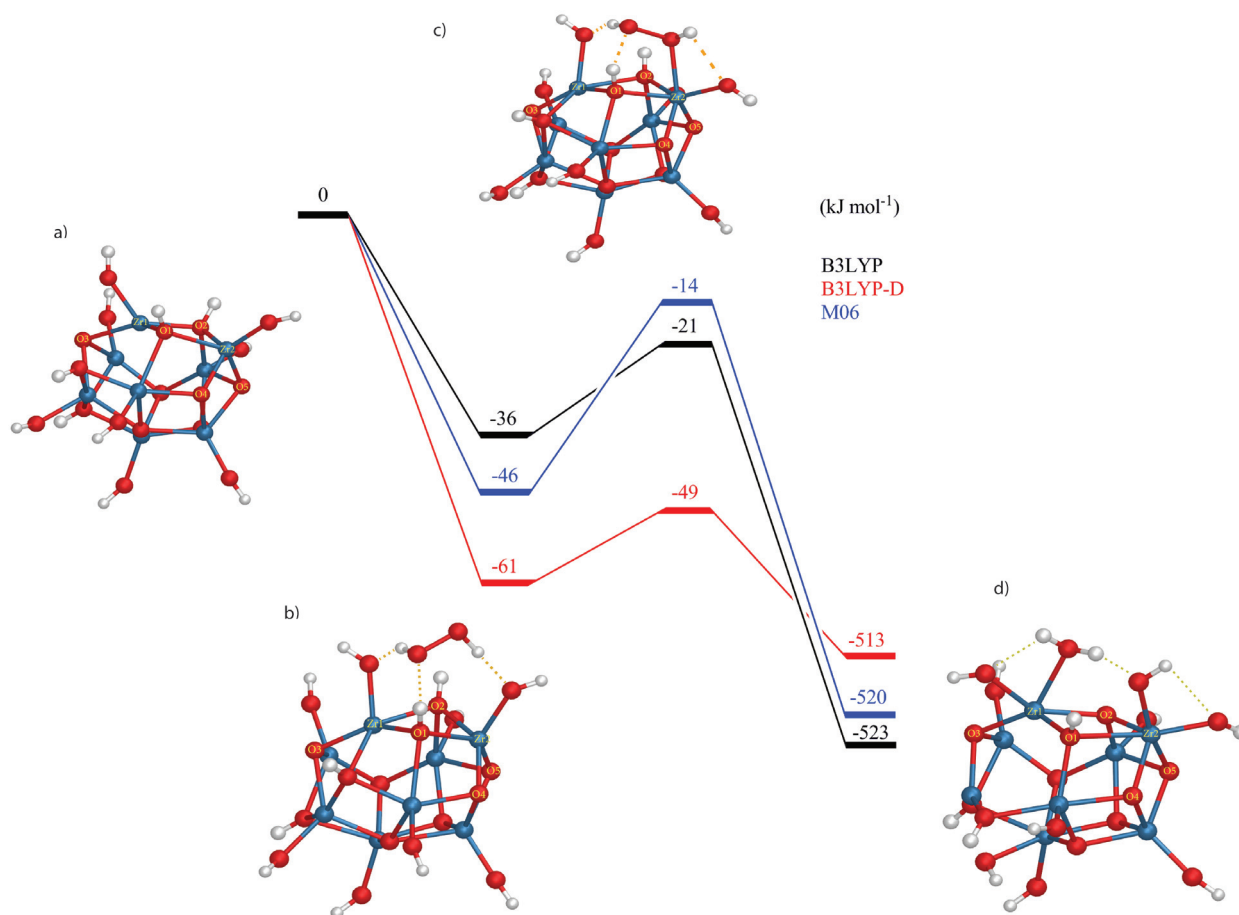
Figure 33. Reaction potential energy diagram and optimized structures for the reaction of H_2O_2 with the surface of the m-$(ZrO_2)_8$ cluster: a) cluster after dissociative adsorption of H_2O, b) molecular adsorption of H_2O_2 onto the surface HO groups, c) transition-state for the cleavage of H_2O_2, d) stable product of the decomposition of H_2O_2. Zr (●), O (●), H (○). Dashed lines represent hydrogen bonds. Reproduced by permission of the PCCP Owner Societies.

When added to the cluster, the H_2O_2 molecule adsorbs molecularly onto the surface (Figure 33b). This is in agreement with the experimental data discussed previously in this work which shows that the adsorption of H_2O_2 is a precedent step to the decomposition. The H_2O_2 molecule adsorbs by hydrogen bonding with surface HO-groups. In addition to the hydrogen bonds, there are dispersion interactions with the surface atoms, but in this case, B3LYP-D and M06 predict slightly different adsorption energies, ΔE_{ads} = -61 kJ·mol^{-1} and ΔE_{ads} = -46 kJ·mol^{-1}, respectively.

In the transition state structure (Figure 33c), one of the HO groups of H_2O_2 is interacting with an exposed Zr cation. When the transition state is relaxed (Figure 33d), the other HO-group of the dissociating H_2O_2 molecule abstracts a hydrogen atom binding to a surface neighboring O atom. This leads to the formation of water and a surface O·. The existence of the water product is

supported by isotope experiments which show that D_2O is formed upon exposure of certain surfaces to $DO^\bullet$.[188] The experimentally obtained activation energy is only 33 ± 1 kJ·mol⁻¹. At the B3LYP level, the activation energy for the cleavage of H_2O_2 is only 15 kJ·mol⁻¹, while the barrier obtained with the M06 functional is 32 kJ·mol⁻¹. Since calculations with B3LYP-D give an activation energy of 12 kJ·mol⁻¹, the difference between B3LYP and M06 cannot be attributed to dispersion interactions only. Here it is clear that the M06 functional outperforms B3LYP in describing the barrier height, in agreement with the concepts behind the development of the M06 functional.[124] Spin density isosurfaces obtained with B3LYP and M06 for the transition state geometries are shown in Figure 34.

a   b
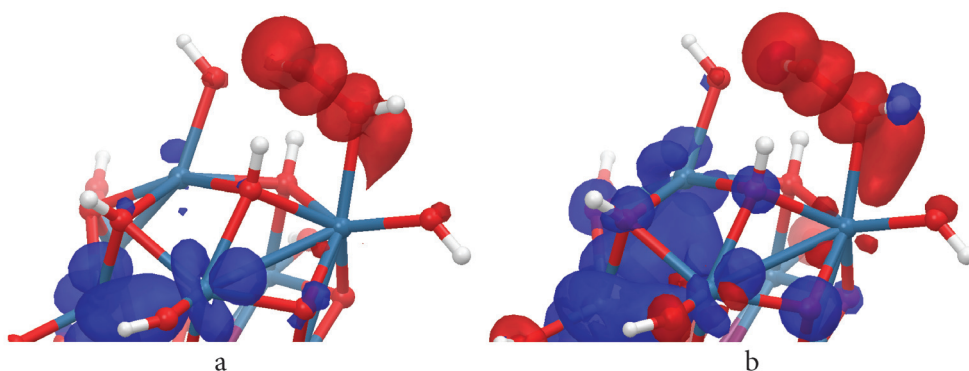
Figure 34. Spin density isosurfaces for the transition state geometries obtained with: a) B3LYP; b) M06 functionals, with LACV3P++** basis set. Alpha-spin density region (■). Beta-spin density region (■). Reproduced by permission of the PCCP Owner Societies.

The M06 functional predicts a more localized spin density in the reactive site where H_2O_2 adsorbs and decomposes. The B3LYP functional predict a more delocalized spin density in comparison. These differences might underlie the explanation for the difference in the activation energies obtained with the two functionals. Since the activation energy obtained with the M06 functional is closer to the experimental value than the B3LYP one, it seems reasonable to believe that in the real system the spin density is more localized.

The transition state and formation of products of the H_2O_2 cleavage is expected to follow a model described by Nilsson and Pettersson[189] for dissociation of molecular species on catalyst surfaces. This model states that a molecular species undergoes cleavage at a surface due to internal (partial) bond breaking which occur when the interactions with the surface are strong enough to drive this process to completion. The binding of products to the surface starts in the transition state with the formation of a *bond-prepared* radical state where the resulting fragments have unpaired electrons that can interact with available electrons on the catalyst surface. Since the O-O bond in H_2O_2 is relatively weak (208 kJ·mol⁻¹)[136], compared to the adsorption

energy of the two HO-radicals (-944 kJ·mol^{-1}, Table 7), it is energetically favorable to break the O-O bond and form HO$^{\bullet}$ The further interaction of the unpaired electron of HO$^{\bullet}$ with the valence electrons of the metal cation leads to formation of bonded states. Besides of incorporating a larger amount of Hartree-Fock exchange (27% in M06, 20 % in B3LYP), the kinetic energy density in M06 is spin dependent,[64] which can lead to better performance of this functional in describing open-shell systems with unpaired electrons. Also, non-covalent interactions such as hydrogen bonding and van der Waals interactions are important in the reaction of H_2O_2 with the metal oxide. Hydrogen bonds are particularly important in the transition-state for H_2O_2 decomposition. It is known that the M06 functional gives improved results over regular hybrid functionals for describing these types of systems where non-covalent interactions are present and dispersion effects are large.[64,190,191]

4.3.3 *(ZrO₂)₂, (TiO₂)₂ and (Y₂O₃) clusters with B3LYP, B3LYP-D, B3LYP*, M06, M06-L, PBE0, PBE and PWPW91 functionals*

The motivation for using the following cluster models of the oxides resides in the fact that for small adsorbates such as the ones studied here, the interactions with a oxide surface are localized.[192] As discussed in the introduction section, in many cases, when defects are present, these defect sites can dictate the overall reactivity of a surface. This means that for such systems, the overall reactivity towards an adsorbate can be determined by localized phenomena. Taking these facts into account, the performance of the minimal possible clusters that retain the stoichiometry of ZrO_2, TiO_2 and Y_2O_3 was investigated. Additionally, the performance of different functionals using these clusters was evaluated. The minimal cluster built for ZrO_2 is shown in Figure 35.
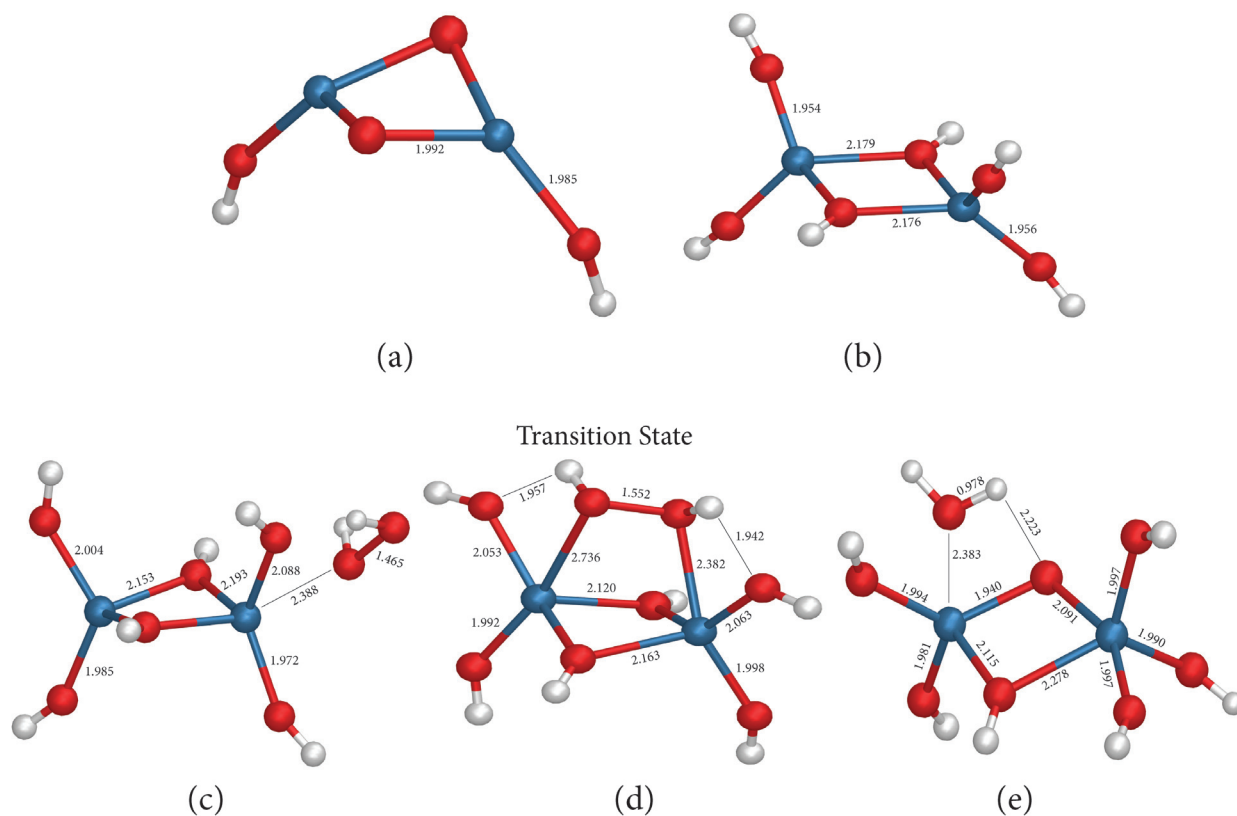
Figure 35. Optimized geometries for adsorption of H_2O and further decomposition of H_2O_2 on a $(ZrO_2)_2$ cluster; (a) bare cluster, (b) dissociative adsorption of two H_2O molecules, (c) molecular adsorption of a H_2O_2 molecule, (d) transition-state for the cleavage of the O-O bond in H_2O_2, (e) product of the decomposition of H_2O_2. Zr (●), O (●), H (○). The bond lengths are given in Å. Reproduced by permission of the PCCP Owner Societies.

Similar clusters were built for TiO_2 and Y_2O_3. Their structures are shown in Figure 36 and Figure 37 respectively.
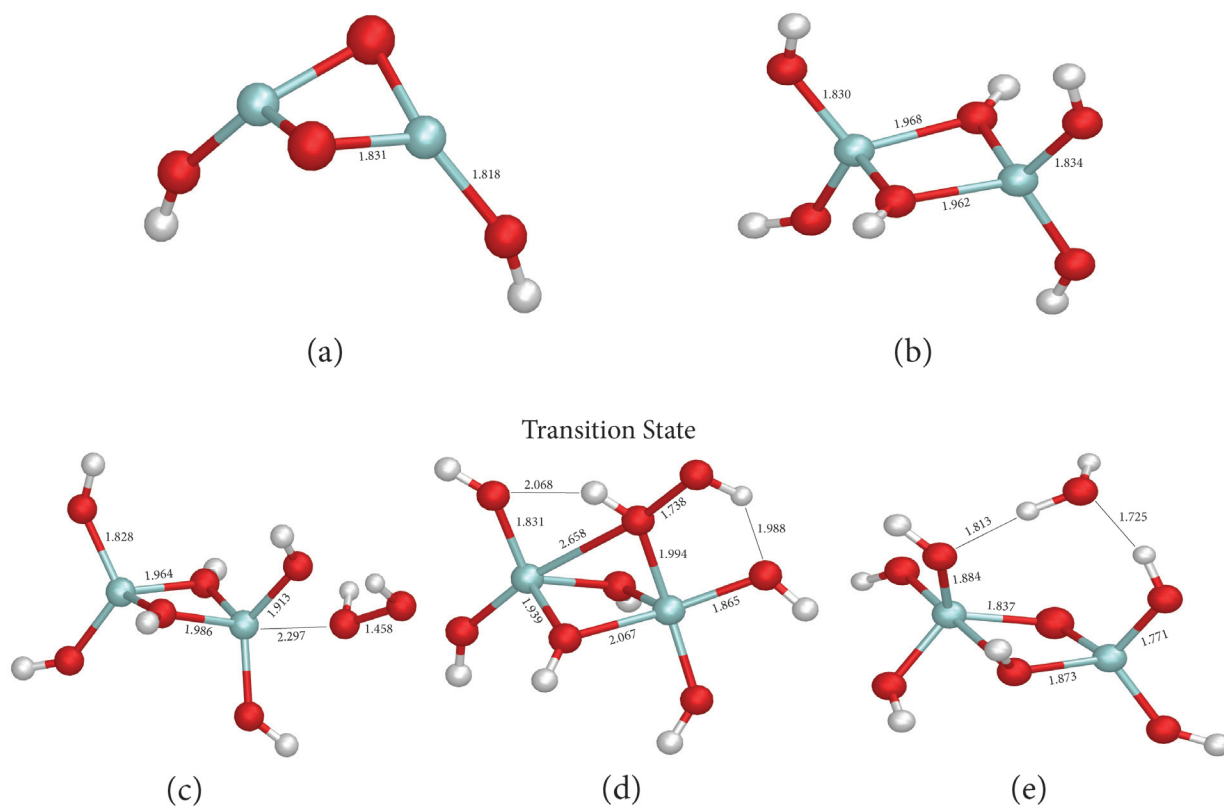
Figure 36. Optimized geometries for adsorption of H₂O and further decomposition of H₂O₂ on a (TiO₂)₂ cluster. (a) bare cluster, (b) dissociative adsorption of two H₂O molecules, (c) molecular adsorption of a H₂O₂ molecule, (d) transition-state for the cleavage of the O-O bond in H₂O₂, (e) product of the decomposition of H₂O₂. Ti (○), O (●), H (○). The bond lengths are given in Å. Reproduced by permission of the PCCP Owner Societies.
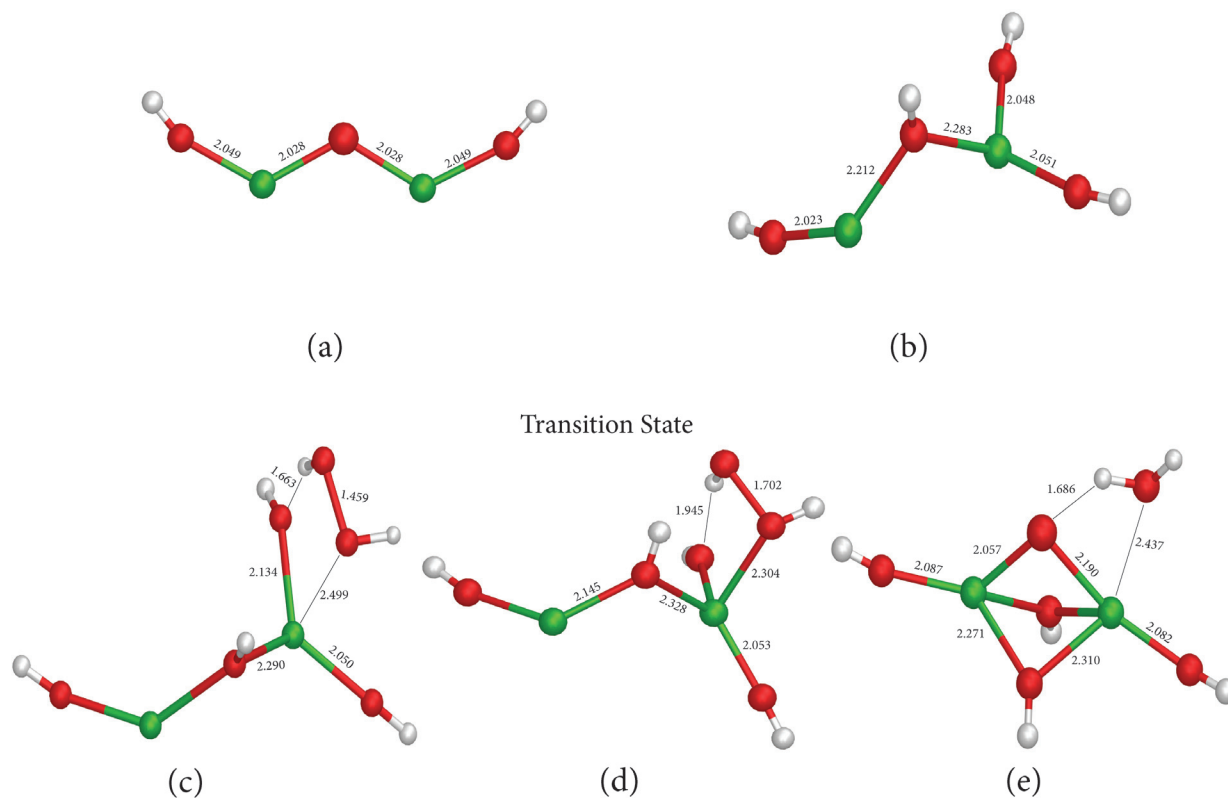
Figure 37. Optimized geometries for adsorption of H₂O and further decomposition of H₂O₂ on a (Y₂O₃) cluster. (a) bare cluster, (b) dissociative adsorption of two H₂O molecules, (c) molecular adsorption of a H₂O₂ molecule, (d) transition-state for the cleavage of the O-O bond in H₂O₂, (e) product of the decomposition of H₂O₂. Y (●), O (●), H (○). The bond lengths are given in Å. Reproduced by permission of the PCCP Owner Societies.

The geometry optimizations were performed with B3LYP and the adsorption and reaction energies were calculated using the functionals B3LYP, B3LYP-D, B3LYP*, M06, PBE0, PBE, PWPW91 and M06-L (Tables 8–10). The geometries for H₂O₂ decomposition were also optimized using the PBE functional. With this functional, while the water adsorption energies deviate from the B3LYP values with an average of 9 kJ·mol⁻¹, the PBE functional predicted a barrierless decomposition of H₂O₂.

Table 8. ΔE_{ads} for adsorption of H_2O, H_2O_2 and $HO^.$ onto a $(ZrO_2)_2$ cluster. Activation energy with zero point energy correction ($E_a{}^{ZPE}$) for the decomposition of H_2O_2 on the surface of the cluster and its respective reaction energy (ΔE_r). Absolute deviation from the experimental value for the activation energy (D_{exp}). Values in (kJ·mol^{-1}).

	B3LYP	B3LYP-D	B3LYP*	PWPW91	PBE	PBE0	M06	M06-L
ΔE_{ads} (2H_2O; *dissociative*)	-229	-261	-230	-218	-209	-233	-258	-231
ΔE_{ads} (H_2O; *molecular*)	-80	-90	-81	-86	-82	-100	-93	-90
ΔE_{ads} (2$HO^{\bullet.}$)	-1005	-1023	-1012	-1027	-1019	-1028	-1027	-1043
ΔE_{ads} (H_2O_2; *molecular*)	-121	-133	-120	-131	-128	-150	-141	-151
$E_a{}^{ZPE}$	38	33	34	–	–	42	36	–
D_{exp}	5	0	1	18	18	9	3	18
ΔE_r	-637	-616	-608	-611	-592	-634	-643	-618

Note: The functionals PBE, PWPW91 and M06-L predict a barrierless decomposition of H_2O_2.

Table 9. ΔE_{ads} for adsorption of H_2O, H_2O_2 and $HO^.$ onto a $(TiO_2)_2$ cluster. Activation energy with zero point energy correction (E_a^{ZPE}) for the decomposition of H_2O_2 on the surface of the cluster and its respective reaction energy (ΔE_r). Absolute deviation from the experimental value for the activation energy (D_{exp}). Values in (kJ·mol^{-1}).

	B3LYP	B3LYP-D	B3LYP*	PWPW91	PBE	PBE0	M06	M06-L
ΔE_{ads} (2H$_2$O; *dissociative*)	-291	-318	-290	-280	-273	-305	-320	-304
ΔE_{ads} (H$_2$O; *molecular*)	-45	-57	-47	-54	-51	-50	-53	-51
ΔE_{ads} (2HO$^\bullet$)	-764	-786	-781	-817	-812	-778	-805	-826
ΔE_{ads} (H$_2$O$_2$; *molecular*)	-58	-75	-55	-69	-65	-68	-81	-80
E_a^{ZPE}	31	32	17	–	–	41	31	–
D_{exp}	6	5	20	59	58	4	6	58
ΔE_r	-494	-525	-498	-500	-501	-490	-489	-513

Note: ... *The*

functionals PBE, PWPW91 and M06-L predict a barrierless decomposition of H_2O_2.

Table 10. ΔE_{ads} for adsorption of H_2O, H_2O_2 and $HO^{\cdot}$ onto a (Y_2O_3) cluster. Activation energy with zero point energy correction (E_a^{ZPE}) for the decomposition of H_2O_2 on the surface of the cluster and its respective reaction energy (ΔE_r). Absolute deviation from the experimental value for the activation energy (D_{exp}). Values in (kJ·mol^{-1}).

	B3LYP	B3LYP-D	B3LYP*	PWPW91	PBE	PBE0	M06	M06-L
ΔE_{ads} (2H_2O; d*issociative*)	-172	-182	-170	-170	-119	-174	-192	-187
ΔE_{ads} (H_2O; *molecular*)	-70	-79	-71	-69	-65	-77	-76	-79
ΔE_{ads} (2$HO^{\bullet}$)	-1081	-1093	-1090	-1098	-1086	-1087	-1099	-1121
ΔE_{ads} (H_2O_2; *molecular*)	-83	-99	-85	-85	-81	-92	-99	-95
E_a^{ZPE}	23	28	19	–	–	45	38	–
D_{exp}	24	19	28	64	58	2	9	49
ΔE_r	-678	-697	-673	-670	-663	-684	-678	-715

Note: The functionals PBE, PWPW91 and M06-L predict a barrierless decomposition of H_2O_2.

Comparing the water adsorption data for the $(ZrO_2)_2$ cluster with the m-$(ZrO_2)_8$, it can be seen that the adsorption of two H_2O molecules on the $(ZrO_2)_2$ cluster is more exothermic than for the m-$(ZrO_2)_8$ cluster, -260 kJ·mol^{-1} (Table 8) and -120 kJ·mol^{-1} (Table 7), respectively at the M06 level. The most exothermic dissociative adsorption of 2 H_2O molecules occurs for adsorption onto the m-$(ZrO_2)_{26}$ model, -312 kJ·mol^{-1}. These discrepancies are explained with basis on the lower degree of coordination of the Zr atoms in the *m*-$(ZrO_2)_{26}$, followed by the $(ZrO_2)_2$ model when compared with the *m*-$(ZrO_2)_8$ cluster. This, as explained before gives the undercoordinated Zr atoms a higher affinity for the HO$^-$ groups which stabilize the shell of the undercoordinated atoms upon adsorption.

Using similar models is possible to compare the differences in adsorption onto the different oxides. The energies for water adsorption onto the ZrO_2, TiO_2 and Y_2O_3 minimal clusters follow the trend: $\Delta E_{ads}(Y_2O_3) < \Delta E_{ads}(ZrO_2) < \Delta E_{ads}(TiO_2)$ (Tables 8–10). It is important to recall that upon dissociative adsorption of water, the adsorbates consist on HO$^-$ and H$^+$ which will bind to the metal cation and exposed surface O atoms respectively. The obtained trend can be explained with basis on the local acidity of the metal cation to which the HO$^-$ binds. The 4s and 4p orbital energies of Zr (2nd row transition metal) are higher than the corresponding 3s and 3p orbital energies of Ti (1st row transition metal) because of the higher effective nuclear charge of Ti. Hence the HO$^-$ anion, acting as a Lewis base – donating an electron pair to the metal cation – will form stringer bonds with Ti^{4+} than Zr^{4+}. In other words, due to its higher ionization energy and smaller ionic radius,[193,194] the Ti^{4+} cation in TiO_2 is a stronger Lewis acid than the Zr^{4+} cation in ZrO_2. The *M*-O bonds are approximately 100 kJ·mol^{-1} stronger in ZrO_2 than in TiO_2.[195,196] Also, the Brønsted acidity of the protonated ZrO_2 surface is greater than for the case of the protonated TiO_2 surface. In the case of Y_2O_3, the lower oxidation state (3+) makes the Y^{3+} ions less Lewis acidic than the *M*$^{4+}$ ions in TiO_2 and ZrO_2. Consequently, the adsorption of a HO$^-$ group is not as exothermic on Y_2O_3 as it is for ZrO_2 and TiO_2. All the functionals used predicted trends for H_2O adsorption in agreement with the acid-base concepts described. (Tables 8–10). The only exception is the data obtained with the PBE functional. This predicted a different trend, and systematically produced the less exothermic values for the dissociative adsorption H_2O. The most exothermic values for dissociative adsorption of water were systematically obtained with the M06 functional. Again, the M06 and B3LYP-D predict very similar dissociative adsorption energies for H_2O. For molecular and dissociative adsorption of H_2O, all functionals used – with one exception – predict the dissociative mode to be thermodynamically preferred. The only exception to this is the data obtained with the PBE functional for Y_2O_3.

As for adsorption on the m-$(ZrO_2)_8$ cluster, the molecular adsorption of H_2O_2 onto the minimal models is stabilized by hydrogen bonds between H_2O_2 and the HO groups binding to the metal atoms (Figure 35c, Figure 36c and Figure 37c). The same trend found for molecular adsorption of H_2O was also found here for H_2O_2 adsorption. This is in increasing order of exothermicity: TiO_2 < Y_2O_3 < ZrO_2. This result is not surprising because the molecular adsorption of both H_2O and H_2O_2 occur via a combination of hydrogen bonding and direct interaction with the metal atoms.

The geometry of the transition-state for decomposition of H_2O_2 in $(ZrO_2)_2$ cluster is slightly different from the corresponding structure obtained in the m-$(ZrO_2)_8$ model. The transition state occurs slightly earlier in the smaller model. This is due to the fact that the interactions between H_2O_2 and the metal cations are less hindered on the smaller model than on the larger model. This could lead to discrepancies on the obtained activation energies. The fact that such effects are also contributing to the reactant structure will cancel to a good extent with the transition-state structure. The obtained E_a^{ZPE} with M06 is 32 kJ·mol^{-1} for the m-$(ZrO_2)_8$ while for the minimal sized cluster is only 4 kJ·mol^{-1} higher.

The computed dissociation pathway of H_2O_2 on the m-$(ZrO_2)_8$ cluster depends on the exchange-correlation functional used: M06 predicts an activation energy in perfect agreement with experimental kinetic data, B3LYP as well as the dispersion corrected B3LYP-D functional, underestimate the activation energy by 15 kJ·mol^{-1}. In order to understand this difference a variety of exchange-correlation functionals of different types where employed for the calculation of the energy barrier using the minimal sized clusters. Although the functionals applied differ in several ways (see further the computational details section) there is a correlation between the amount of HF exchange included in the exchange-correlation functional and the accuracy of the functional for reproducing the experimentally obtained values. For dissociation of H_2O_2 on $(ZrO_2)_2$, the hybrid functionals (B3LYP, B3LYP*, B3LYP-D, M06 and PBE0) predict activation energies between 33 and 42 kJ·mol^{-1} (Table 8), which are in reasonable agreement with the experimental value 33± 1 kJ·mol^{-1} (Table 4). The density functionals that do not incorporate HF exchange (PWPW91, PBE, and M06-L) predict an activation energy of only 15 kJ·mol^{-1}. For dissociation on $(TiO_2)_2$ the results of pure functionals get worse. While the activation energy for decomposition calculated with hybrid functionals (B3LYP, B3LYP-D, M06 and PBE0) deviate from the experimental value (37± 1 kJ·mol^{-1}, Table 4) by 6 kJ·mol^{-1} or less (Table 9), pure density functionals (PBE and M06-L) were unable to predict an energy barrier for decomposition of H_2O_2. The re-parameterized hybrid functional B3LYP*, which incorporates 15 percent HF exchange instead of the 20 percent in the original B3LYP functional, is an outlier in the prediction of

activation energies. Although it predicts an energy barrier for decomposition of H_2O_2, the deviation from the experimental data is larger than for the other hybrid functionals employed (error of 20 kJ·mol^{-1}). Similar trends were obtained for decomposition on Y_2O_3. Here pure DFT also predicted a barrierless reaction (Table 10). Given this, it is plausible to state that in order to correctly describe the energy barrier for H_2O_2 decomposition, the functional used should incorporate an amount of HF exchange of at least 20 percent. Among the three functionals that incorporate HF exchange, the M06 and PBE0 performed better than the B3LYP in terms of reaction energy barriers accuracy. The activation energies calculated with M06 deviate from experiment by 6 kJ·mol^{-1} on average absolute value, while the deviation for PBE0 is 5 kJ·mol^{-1}, and B3LYP deviates with 12 kJ·mol^{-1}. Given the very good agreement between computational and experimental data for the energy barriers for H_2O_2 decomposition, it is possible to state that the minimal models constitute a simple and effective approach for modeling reactivity of particles of these oxides and H_2O_2.

The calculated reaction energies for H_2O_2 decomposition, are in good agreement with the trend verified for the HO$^{\bullet}$ adsorption energies (Table 8–10). The reasoning for this is that the products formed in the decomposition of H_2O_2 consist of a H_2O molecule molecularly adsorbed to the clusters and a HO radical bound to one of the metal atoms. When comparing the reaction energies for the different clusters, the factor that is expected to have more impact on the overall reaction energy is the adsorption of HO$^{\bullet}$ onto the clusters given that this quantity is far larger than the molecular adsorption energy of a H_2O molecule (Tables 8–10). Even though the HO radical binds strongly to all three metal oxides, the formation of H_2O as a product of decomposition of H_2O_2 is supported by experiments which show that HO$^{\bullet}$ can react further at a solid/liquid interface.[197]

Since dispersion interactions occur not only *through bonds* but also *through space*, the cluster size (and geometrical shape) has an impact on the magnitude of the dispersion effect on the calculated adsorption energy. Taking the difference between adsorption energies calculated with B3LYP and B3LYP-D as the dispersion effect, it can be seen that for the molecular adsorption of water on ZrO_2 clusters, the dispersion effect is only 10 kJ·mol^{-1} in the $(ZrO_2)_2$ model (Table 8), while is 14 kJ·mol^{-1} in the m-$(ZrO_2)_8$ model (Table 7) and becomes as large as 30 kJ·mol^{-1} in the m-$(ZrO_2)_{26}$ cluster (Table 5). Differences of similar magnitude are found for the molecular adsorption of H_2O_2.

4.4 Affinity of ZrO₂, TiO₂ and Y₂O₃ for the HO radical

In the mechanistic studies described in section 4.2 there are a multitude of processes which determine the differences in the yield of CH_2O for the

different oxides. To consider, there are: the adsorption of H_2O_2 and Tris onto the surfaces, the reactivity of both species towards the HO radical and the reactivity of the HO radical towards the surfaces. From the properties of the surfaces and the similarities in H_2O_2 adsorption energies (Section 4.3), it is expected that for oxides of transition metals that are neighbors in the periodic table, there should not exist extreme differences in the parameters mentioned above with the exception of the HO radical binding energies (See section 4.6.2). As such, the scavenging capability of the different metal oxides towards HO$^{\bullet}$ present in solution was investigated. This was done by γ-irradiating aqueous powder suspensions of the different oxides in the presence of Tris and determining the amount of CH_2O formed – in a similar way as to what was done for the study of the formation of HO$^{\bullet}$ during the catalytic decomposition of H_2O_2. The competition for HO$^{\bullet}$ between Tris and the surface of the oxides can give a picture of the differences in the abilities of the different oxides to scavenge HO$^{\bullet}$ from solution. The reaction media for the study of the affinity of the oxides for HO$^{\bullet}$, consisted of ZrO_2 (1.5 g, *Sa* = 7.5 m^2) or TiO_2 (0.197 g, *Sa* = 7.5 m^2) or Y_2O_3 (1.678 g, *Sa* = 7.5 m^2) in Tris (20 mM) and a volume of 50 ml. The plots showing the amount of HO$^{\bullet}$ scavenged by Tris, as a function of irradiation time are represented in Figure 38.
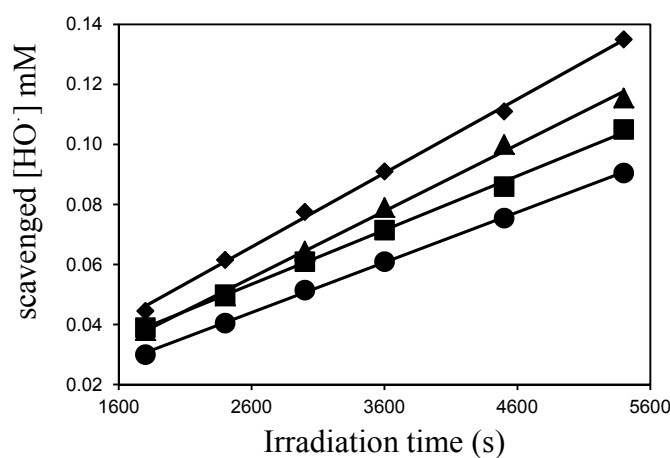
Figure 38. Accumulated [HO$^{\bullet}$] scavenged by Tris in γ-irradiated solutions with and without the presence of different metal oxides. No oxide present ($\blacklozenge$); TiO_2 ($\blacktriangle$); ZrO_2 ($\blacksquare$); Y_2O_3 ($\bullet$). © American Chemical Society.

From Figure 38 it can be seen that the different metal oxides display different yields of scavenged HO$^{\bullet}$. As discussed above, this fact can provide a qualitative measure of the binding energy of HO$^{\bullet}$ to the surfaces of the oxides. The strengths of these bonds are expected to control the relative kinetics for adsorption, desorption and eventual diffusion of HO$^{\bullet}$ on the surface.[198] According to the plots of Figure 38, the HO$^{\bullet}$ binding energies vary in the order of increasing exothermicity: $TiO_2 < ZrO_2 < Y_2O_3$. Also important

to note is that the amount of HO$^•$ scavenged from solution by the metal oxide depends on the (Sa/V) of the metal oxide present in the system. The amount of HO$^•$ scavenged varies inversely with metal oxide (S_a/V).

The DFT obtained geometries for the binding of two HO radicals onto the hydroxylated clusters of $(ZrO_2)_2$, $(TiO_2)_2$ and (Y_2O_3) are shown in Figure 39. The corresponding energetic data are given in Table 8–10. A Mulliken population analysis shows that the adsorption of HO$^•$ causes delocalization of electrons of the metal atoms involved in the bonding with HO$^•$, *i.e.* the metal cation becomes partially oxidized. This could be seen systematically on the Mulliken charges of the metal atoms for all the models studied. The adsorption energies of HO$^•$ can be reasoned in terms of the ionization energy of the metal cation binding with the radicals. The ionization energies of the metal ions present in the oxides vary in the order: $Y^{3+}< Zr^{4+}< Ti^{4+}$.[199] As delocalization of the metal valence electrons has to occur in order to form bonded states with the HO radicals, the strength of the bonds between the metal clusters and the HO radicals is expected to follow the inverse trend as the ionization energies. This because the ionization energy is inversely proportional to the ease of delocalization of electronic density from an atom. This trend was successfully reproduced with all the exchange-correlation functionals used (Table 8–10) and agrees with the experimental data shown in Figure 38. Thus, *the higher the ionization energy of the metal cation present in the cluster, the smaller is the change in Mulliken charge of the metal atom upon adsorption of HO$^•$.*

(a)   (b)   (c)
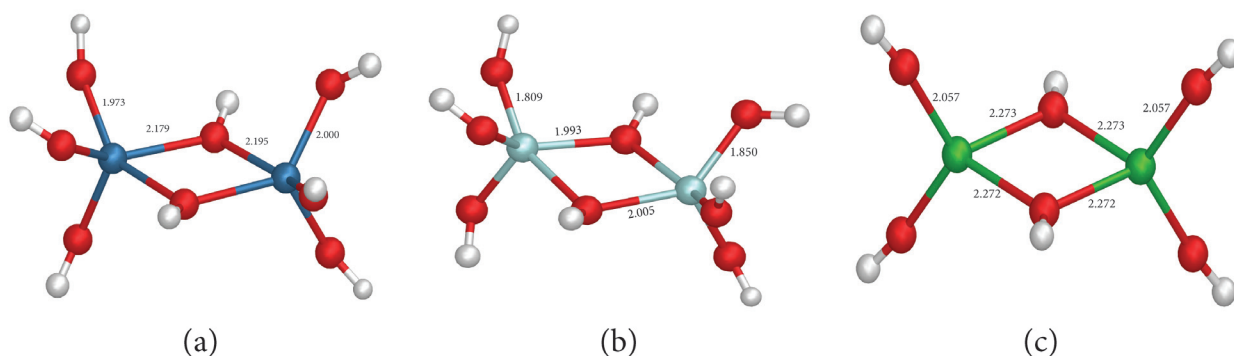
Figure 39. Optimized geometries for the adsorption of two HO radicals onto each of the clusters previously saturated with two H_2O molecules: (a) $(ZrO_2)_2$, (b) $(TiO_2)_2$, (c) (Y_2O_3). Zr (●),Ti (●),Y (●), O (●), H (○). © American Chemical Society.

A similar trend to the one here obtained has been previously reported for adsorption of HO$^•$ onto metallic Au surfaces.[93] The authors found that the lower the oxidation potential of a given Au surface, the stronger the bonds between that surface and HO$^•$. This also indicates that for a metallic surface,

the formation of bonds with HO$^\bullet$ requires delocalization of electron density from the metal atom.

4.5 Effect of HO$^\bullet$ scavengers on the mechanism of decomposition of H$_2$O$_2$

It has been show with the experimental mechanistic data for H$_2$O$_2$ decomposition, with the DFT calculations of the mechanism of decomposition of H$_2$O$_2$ and with the experiments and calculations of the affinity of the oxides for HO$^\bullet$, that this radical might have an important role in the mechanism of decomposition of H$_2$O$_2$.

In surface reactions, changing the amount of an intermediate surface species has consequences on the overall reaction mechanism. Rewriting Reaction (R11) according to the experimental and DFT finds described previously in this work

$$\text{H}_2\text{O}_2 \text{ (ads)} + S_{CA} \longrightarrow \text{H}_2\text{O (ads)} + \text{HO}^\bullet \text{ (ads)} + S_{CA}^\bullet \qquad \text{(R17)}$$
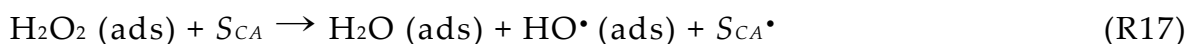
where (ads) represents an adsorbed state and $S_{CA}^\bullet$ is the surface catalytically active site with the unpaired electron at the O atom (Figure 33d, Figure 35e and Figure 37e). The non-adsorbed or weakly adsorbed HO$^\bullet$ can eventually react with H$_2$O$_2$ according to
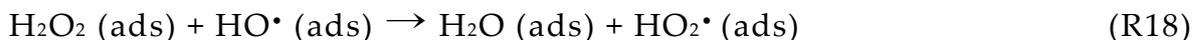
$$\text{H}_2\text{O}_2 \text{ (ads)} + \text{HO}^\bullet \text{ (ads)} \longrightarrow \text{H}_2\text{O (ads)} + \text{HO}_2^\bullet \text{ (ads)} \qquad \text{(R18)}$$

the surface unpaired electron localized at $S_{CA}^\bullet$ is also a possible reaction site for further reactions of H$_2$O$_2$ such as[179]

$$\text{H}_2\text{O}_2 \text{ (ads)} + S_{CA}^\bullet \longrightarrow \text{HO}_2^\bullet \text{ (ads)} + S_{CA}\text{H} \qquad \text{(R19)}$$

where $S_{CA}\text{H}$ represents an H$^\bullet$ bound onto the $S_{CA}^\bullet$ site. Another possible reaction pathway for H$_2$O$_2$ at the surface is
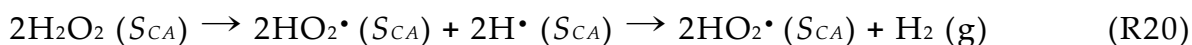
$$2\text{H}_2\text{O}_2 \,(S_{CA}) \longrightarrow 2\text{HO}_2^\bullet \,(S_{CA}) + 2\text{H}^\bullet \,(S_{CA}) \longrightarrow 2\text{HO}_2^\bullet \,(S_{CA}) + \text{H}_2 \text{ (g)} \qquad \text{(R20)}$$

where the state S_{CA} denotes that the corresponding species is adsorbed onto the surface catalytically active site. It has been shown in section 4.3 that H$_2$O$_2$ binds to the S_{CA} site by direct interaction of its O atoms with undercoordinated metal cations at the surface. A similar type of interaction happens for the binding of the HO radicals. These two types of interactions are similar in the sense that both require access to the orbitals of the metal cations in order to form bonded states. So both the H$_2$O$_2$ and HO$^\bullet$ interactions with the surfaces, are more exothermic, the more undercoordinated are the metal cations to which these species bind. As such, the adsorption of H$_2$O$_2$ would be facilitated by the removal of HO$^\bullet$ entities from the system because adsorbed HO$^\bullet$ competes with H$_2$O$_2$ for adsorption

onto exposed surface metal cations. In this section, the effects of HO$^\bullet$ scavengers – Tris and TAPS – on the products of the decomposition of H_2O_2 when catalyzed by ZrO_2, TiO_2 and CuO, are presented and discussed.

In order to correctly evaluate the effects on the mechanism of decomposition of H_2O_2 due to scavenging HO$^\bullet$ by Tris and TAPS, it is necessary to know the adsorption equilibrium constants of these compounds onto the surfaces. This in order to qualitatively know which of these scavengers has a higher surface concentration. The adsorption equilibrium constants for Tris and TAPS were determined for the ZrO_2 system. Upon exposure of a 5 ml solution of varying concentration of Tris or TAPS (100-500 µM, V = 5 ml) to ZrO_2 (2.5 g, Sa = 12.5 m^2) at pH = 7.5, the amount of Tris and TAPS adsorbed onto the surface at equilibrium was determined from the γ-radiation induced bleaching of the methylene blue. This method measures the competition kinetics between methylene blue and Tris or TAPS for the radiation induced produced HO$^\bullet$ radicals. Methylene blue reacts with HO$^\bullet$ radicals with a rate constant of 6.9×10^{10} M^{-1}·s^{-1}.[200] The rate constant for reaction of Tris with HO$^\bullet$ radicals is 1.1×10^9 M^{-1}·s^{-1}.[156] The rate constant for the reaction of TAPS with HO$^\bullet$ radicals has not been precisely determined but based on structural factors – *i.e.* structural similarities between TAPS and other Good's buffers – it is expected to be on the order of 10^9 M^{-1}·s^{-1}.[156] From these rate constants it can be seen that the optimal conditions for the competition kinetics are for a concentration of Tris or TAPS around 10 times higher than the concentration of methylene blue. The resulting data for the percentage of adsorbed Tris and TAPS at equilibrium as a function of their initial concentrations are represented in Figure 40.
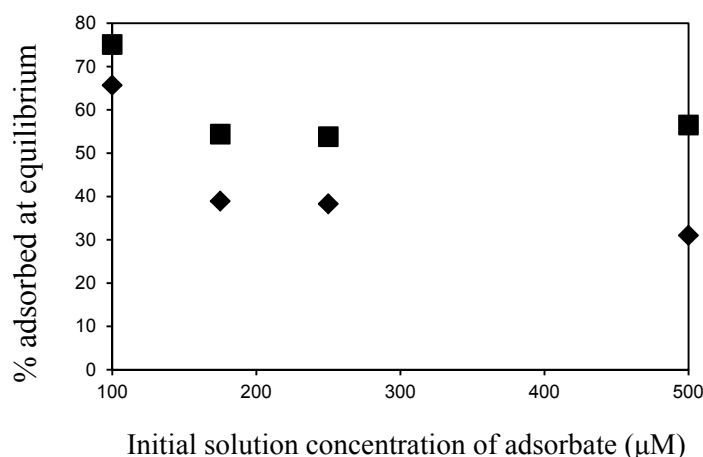

Figure 40. Percentage of Tris (♦) and TAPS (■) adsorbed at equilibrium as a function of their initial concentration in solution at pH = 7.5 for adsorption onto ZrO_2 (2.5 g) at 298 K in a V = 5 ml.

From Figure 40 it can be seen that at equilibrium, TAPS has a higher surface concentration than Tris for the same initial solution concentration. According

to the Langmuir theory of adsorption, the adsorption at equilibrium conditions can be expressed by

$$q_e = \frac{X_m \cdot K \cdot C_e}{1 + KC_e} \tag{15}$$

where q_e is the amount of adsorbate adsorbed per unit weight of adsorbent, X_m is the amount of adsorbate required for a monolayer coverage on the surface of the adsorbent, K is the Langmuir adsorption equilibrium constant and C_e is the equilibrium concentration of adsorbate in solution. The Langmuir adsorption equilibrium constant, K, is defined as k_a/k_d where k_a and k_d are the rate constants of adsorption and desorption. The linearization of Equation (15) has the form

$$\frac{1}{q_e} = \frac{1}{X_m} + \left(\frac{1}{C_e}\right)\left(\frac{1}{K \cdot X_m}\right) \tag{16}$$

the quantity K as defined above can give a comparative picture of the differences in terms of surface coverage and adsorption energies for both molecules and can be obtained by plotting $1/q_e$ as a function of $1/C_e$. The value of K for Tris is 2.5×10^{-3} and for TAPS is 4.6×10^{-4}. Hence, from these data can be seen that the adsorption of TAPS is more exothermic than adsorption of Tris. Translated into the adsorption mechanism, these adsorption data suggests that the area of the surface of ZrO_2 covered, is 4.5 times higher when the adsorbate is TAPS than for the case when the adsorbate is Tris – for the same initial concentration of adsorbate.

To study the effect of $HO^{\bullet}$ scavengers on the mechanism of H_2O_2 decomposition on the surface of ZrO_2, the gaseous products H_2 and O_2 formed upon decomposition of H_2O_2 in the presence of varying amounts of the $HO^{\bullet}$ scavengers Tris or TAPS was measured. During H_2O_2 decomposition, O_2 is formed according to Reaction (R14).[129] According to the Reaction (R20) the eventual formation of H_2 can also take place.

Prior to the measurement of the gaseous products, test experiments were performed to ensure complete consumption of H_2O_2 when the reaction products were measured. Before the analysis of the amount of H_2 and O_2 formed as a function of $HO^{\bullet}$ scavenger concentration, several background experiments were performed. The reaction media for the background experiments consisted of one of the $HO^{\bullet}$ scavengers, either Tris or Taps (200 mM) in a ZrO_2 particle suspension without H_2O_2 present. When H_2O_2 is not present in the reaction media, there is no detectable production of H_2. The amount of H_2 produced was studied for varying concentrations of $HO^{\bullet}$ scavengers and also for different concentrations of H_2O_2 at a fixed concentration (200 mM) of $HO^{\bullet}$ scavenger. The resulting data for the later experiments are shown in Table 11.

Table 11. H_2 detected (mM) after reaction of H_2O_2 in a ZrO_2 particle suspension as a function of the different amounts of H_2O_2 at a fixed concentration (200 mM) of Taps or Tris.

$[H_2O_2]$ (mM)	$[H_2]$ detected (mM) (in Taps (200 mM))	$[H_2]$ detected (mM) (in Tris (200 mM))
0.2	0	0
1.0	1.6×10^{-5}	0
10	2.0×10^{-2}	1.7×10^{-3}

It can be seen (Table 11) that the amount of H_2 formed is dependent on the amount of H_2O_2 present in the system. For the lower concentration of H_2O_2 used (0.2 mM), there is no detectable formation of H_2.

The study of the formation of H_2 as a function of $HO^\bullet$ scavenger concentration was done for a system of ZrO_2 particles (0.4 g; Sa = 1.34 m^2) with H_2O_2 (10 mM) and varying concentrations of Tris and Taps in a volume of 2 ml. The choice of this concentration of H_2O_2 was based on the results of the test experiments shown in Table 11. The data obtained are represented in Figure 41 and Figure 42 for Tris and TAPS, respectively.
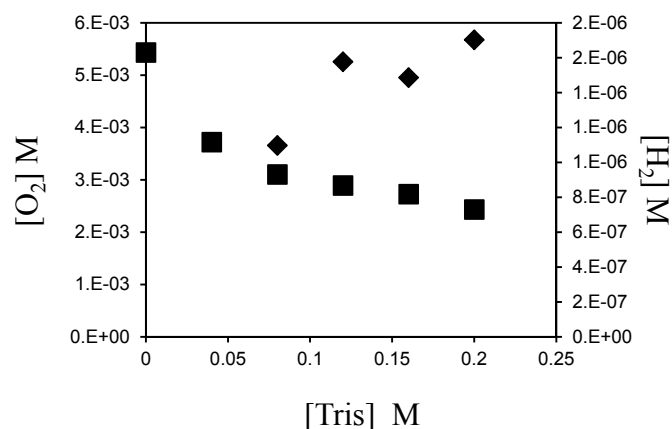

Figure 41. Production of O_2 (■) and H_2 (♦) in the decomposition of H_2O_2 on the surface of ZrO_2 in the presence of different concentrations of the $HO^\bullet$ scavenger Tris (0-0.2 M).
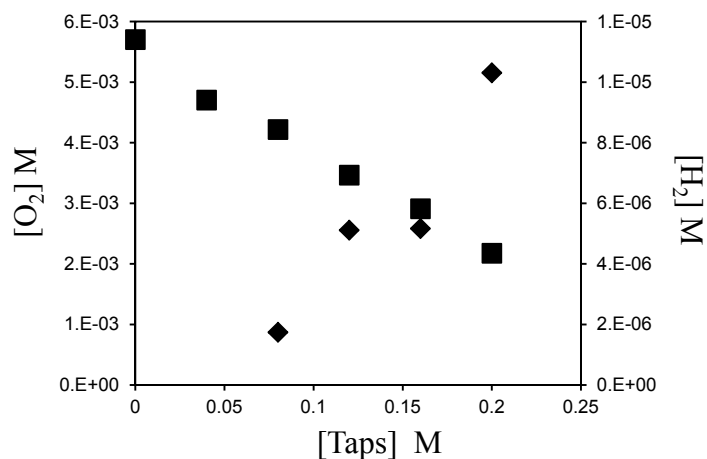
Figure 42. Production of O_2 (∎) and H_2 (♦) in the decomposition of H_2O_2 on the surface of ZrO_2 in the presence of different concentrations of the $HO^•$ scavenger Taps (0-0.2 M).

In the experiments without $HO^•$ radical were detected amounts of O_2 that are in agreement with the proposed stoichiometry for the decomposition of H_2O_2. The amount of O_2 formed is equal to half of the initial amount of H_2O_2,[129] according to Reaction (R14). The results presented in Figure 41 and Figure 42, show that the presence of an $HO^•$ radical scavenger – either Tris or Taps – has an effect on the amounts of O_2 and H_2 produced by the decomposition of H_2O_2. The total amount of O_2 is reduced and that of H_2 is increased. Both the decrease in O_2 and the increase in H_2 are proportional to the amount of $HO^•$ scavenger in the system. For the system where the scavenger is Tris (Figure 41) this is visible for concentrations of Tris higher than 75 mM. The difference in how the two scavengers affect the O_2 yield is noticeable at scavenger concentrations above 0.08 M. For Tris, the decrease in O_2 yield becomes less pronounced for scavenger concentrations higher than 0.08 M, while the O_2 yield decreases linearly up to 0.2 M of TAPS. The changes in the yield of H_2 with increasing concentration of scavenger are also visible. For the same initial solution concentrations, the production of H_2 is higher when TAPS is present than for the case of Tris. According to the adsorption experiments, the surface coverage is 4.5 times higher when TAPS is the adsorbate when compared with the adsorption of Tris, for the same initial solute concentration. This implies that at the surface/interface, TAPS is able to scavenge more $HO^•$ than Tris due to its higher surface/interfacial concentration. This is in agreement with the change in yields of the gaseous products observed Figure 41 and Figure 42 and suggests that the formation of H_2 is a surface process that depends on the presence and on the surface coverage of an $HO^•$ scavenger. This reasoning is further supported by test experiments using TiO_2 and CuO. As for the case of ZrO_2, for these systems,

the presence of Tris or Taps has similar effects on the H_2 and O_2 yields (Table 12).

Table 12. Yields (M) of H_2 and O_2 for the reaction of decomposition of H_2O_2 (10 mM) catalyzed by CuO or TiO_2 in the presence of the $HO^{\bullet}$ scavengers Tris or Taps (0.2 M).

$HO^{\bullet}$ scavenger	$CuO - O_2$	$CuO - H_2$	$TiO_2 - O_2$	$TiO_2 - H_2$
No scavenger	5.0×10^{-3}	0	5.0×10^{-3}	0
Tris (0.2 M)	2.7×10^{-3}	8.4×10^{-6}	1.0×10^{-4}	9.3×10^{-6}
TAPS (0.2 M)	1.2×10^{-3}	1.6×10^{-5}	8.9×10^{-4}	3.0×10^{-5}

When no scavenger is present, the amount of O_2 detected corresponds to the amount of this product predicted by the overall stoichiometry for H_2O_2 decomposition for a system where no $HO^{\bullet}$ scavenger is present – Reaction (R14). For the reaction media where Tris or Taps are present, the yields of both O_2 and H_2 are shown in Table 12. For the same: Sa of solid, $[H_2O_2]_0$ and [Tris or Taps], the yields of H_2 and O_2 for CuO and TiO_2, (Table 12) are different than for the case of ZrO_2, but the same trends are found. The presence of a $HO^{\bullet}$ scavenger enhances the formation of H_2 and decreases the yield of O_2.

   For all oxides, when using TAPS or Tris, the changes in the production of O_2 and H_2 do not seem to obey a specific mass balance. Nevertheless, it is demonstrated that the presence of a $HO^{\bullet}$ scavenger influences the overall H_2O_2 reaction path. The presence of a $HO^{\bullet}$ scavenger favors a reaction which leads to formation of H_2 and at the same time affects the main reaction path that leads to the formation of O_2. This observation further illustrates the importance of the $HO^{\bullet}$ radical as an intermediate reactive species on the decomposition of H_2O_2. As shown in sections 4.2 and 4.3 of this thesis, $HO^{\bullet}$ is a primary product of H_2O_2 decomposition and it competes with H_2O_2 for the same adsorption sites at the surface of the metal oxides. Removal of the $HO^{\bullet}$ from the reaction system has an effect on the relative yields of the products formed. Without the $HO^{\bullet}$ scavenger, H_2O_2 decomposes at the surface of the oxides according to the following stoichiometric relationship stated in Reaction (R14): 1 mole of H_2O_2 forms ½ mole of O_2 and 1 mole of H_2O. The presence of the $HO^{\bullet}$ scavenger changes the overall mechanism to a scheme that can be illustrated by

$$H_2O_2 \xrightarrow{} xO_2 + yH_2O + zH_2 \qquad\qquad (R21)$$

this reaction can be explained in terms of the increase in yield of a side reaction such as the one represented in Reaction (R20). A determination of the coefficients x, y and z is not trivial since their values depend on many parameters besides the solution concentration of an HO$^•$ scavenger.

The removal of HO$^•$ from the S_{CA} site is expected to contribute in two distinctive ways to the formation of H_2. The first is that the increased removal of HO$^•$ from the surface facilitates the adsorption of H_2O_2 through direct interaction of its O atoms with the metal cations. This exchange will lead to a higher H_2O_2 coverage at the S_{CA} sites. According to the stoichiometry of the proposed Reaction (R20), this reaction would benefit from a higher coverage of H_2O_2 at the S_{CA} sites. The other contribution is that the alternative reactive pathway of H_2O_2 decomposition by breaking one of the H-O bonds is also enhanced because there is room at the S_{CA} site to accommodate the resulting products, the HO$_2^•$ and H$^•$ radicals. Surface adsorption of H$^•$ is known to occur for ZnO and the surface migration of adsorbed H$^•$ can have an activation energy as low as 38 kJ·mol^{-1}.[201-203] For metallic surfaces of Cu, H$^•$ adsorbed on neighboring surface metal atoms can easily recombine to form H_2.[204] A similar type of surface adsorbed H radical recombination is expected to occur at the surfaces of the oxides here examined. This recombination has been shown to be possible at surface sites where the adsorbed H atoms are bound to neighboring atoms as reported for TiO$_2$ surfaces.[177,205]

4.6 Application of conceptual DFT to derive catalyst structure-reactivity relationships for the decomposition of H_2O_2

4.6.1 *PBE0 functional study of the decomposition of H_2O_2 on clusters of Fe$_2$O$_3$; Al$_2$O$_3$; CuO; CeO$_2$; HfO$_2$; NiO$_2$; PdO$_2$; TiO$_2$; Y$_2$O$_3$;ZrO$_2$; Gd$_2$O$_3$*

In this section, the DFT calculations for decomposition of H_2O_2 are extended for a total of 9 oxides and the adsorption energies of HO$^•$ radicals onto the hydroxylated clusters of a total of 11 oxides are investigated. The tools of conceptual DFT (Section 2.5) are here applied to experimental data to derive structure-activity relationships for decomposition of H_2O_2 for the oxides: Fe$_2$O$_3$; Al$_2$O$_3$; CuO; CeO$_2$; HfO$_2$; NiO$_2$; PdO$_2$; TiO$_2$; Y$_2$O$_3$; ZrO$_2$; Gd$_2$O$_3$. The same methodologies described in Section 4.3 are applied in this section. Here, the functional PBE0 was used for all geometry optimizations and calculations of the single point energies. This functional revealed faster than the B3LYP and more robust for the location of the transition-states. Also for the lanthanide oxides the B3LYP functional has shown difficulties in locating the transition-states for H_2O_2 decomposition. Due to the very good performance/computational effort ratio, achieved by using these models, the

clusters used for this study were again based on the smallest possible stoichiometric units of the metal oxides described in Section 4.3.3. These are of the type $(M_xO_y)_n$, where M is the metal oxide cation and n is the number of stoichiometric units of the metal oxide. The values of n are 1 or 2 depending on if the oxide is of the type M_2O_3 or MO_2 respectively. These clusters were then further hydroxylated with the products of H_2O dissociative adsorption – (HO^-) and (H^+) binding to the cation and to the O atoms respectively. This procedure decreases the coordinative unsaturation of the models which leads to a more realistic modeling of the surfaces of the oxides in solution.[206] Generally, when exposed to water the surfaces of these oxides are hydroxylated.[207] This phenomenon also leads to a decrease in the coordinative unsaturation of the exposed surface atoms. In order to maintain a charge neutral system, the clusters of the oxides of the type M_2O_3 reacted with the products of dissociation of one water molecule and the clusters of the type MO_2 have reacted with those of two water molecules. The resultant products of these reactions with water are the initial reactants for the study of the reactivity of H_2O_2 and are shown in Figure 43.
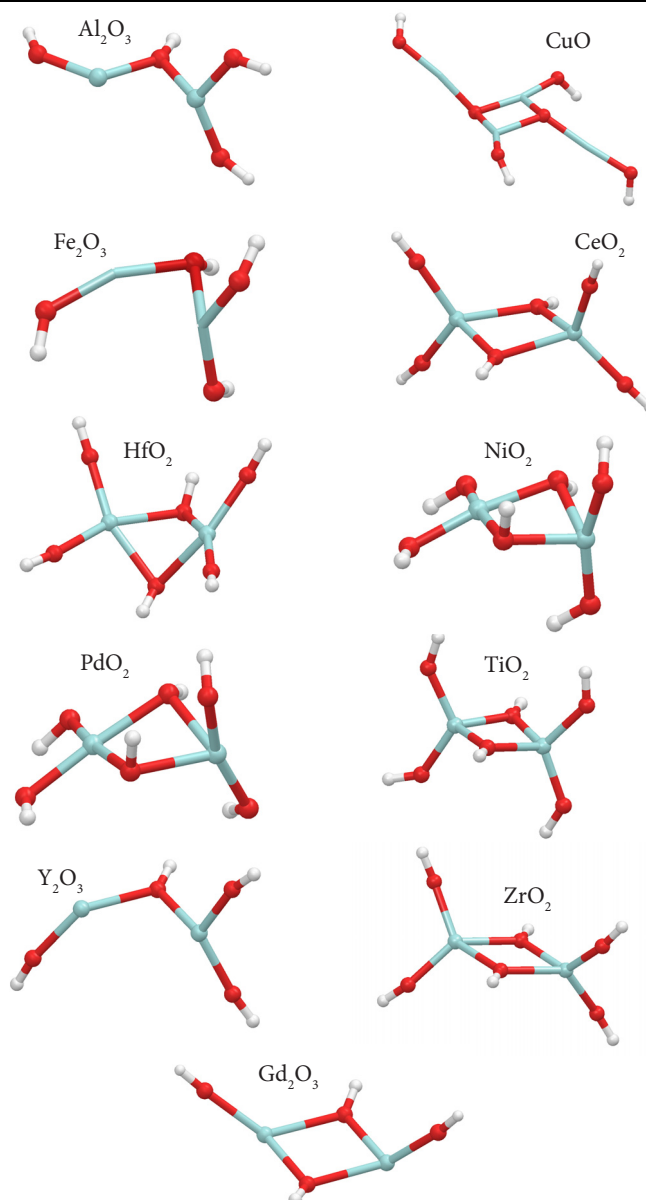
Figure 43. Structures of the hydroxylated clusters used to study the adsorption and further decomposition of H_2O_2. The clusters consist of stoichiometric units of the mentioned oxides, where H_2O has been dissociatively adsorbed. Metal (⬤), O (⬤), H(◯).

The most stable spin states were found to be the singlet, with the exceptions of CuO-quintet and Fe_2O_3-eleventh. During the course of the reactions investigated here, no spin crossover was found for these clusters. In Figure 43 can be seen that the oxides of the transition metal elements belonging to the same periodic table group have a tendency to form similar structures upon dissociative adsorption of H_2O. For example, the hydroxylated clusters of the oxides of Ti(IV), Zr(IV) and Hf(IV) (elements of the group IV) show structural similarities among them in what concerns the way the HO⁻ groups bind to the structures. Ni(IV) and Pd(IV) (elements of the group X) also form similar structures upon the dissociative adsorption of H_2O. For clusters of

different stoichiometry such comparisons on water adsorption geometries are unfeasible.

In the mechanisms described in Section 4.3.3, for ZrO_2, TiO_2 and Y_2O_3, the obtained first step of the decomposition of H_2O_2 is the molecular adsorption. Analogously, for all oxides, a first energy minimum corresponding to the molecular adsorption of H_2O_2 was found. The investigation of the energy barriers for cleavage of H_2O_2 was done only for the oxides for which there are coherent experimental data to compare with. The resulting geometries for adsorption of H_2O_2 onto CeO_2, CuO, Fe_2O_3, HfO_2 and Al_2O_3 are shown in Figure 44. The structures of ZrO_2, TiO_2 and Y_2O_3 are here omitted because there were no significant differences between the PBE0 geometries here obtained and the B3LYP structures shown in Section 4.3.3.
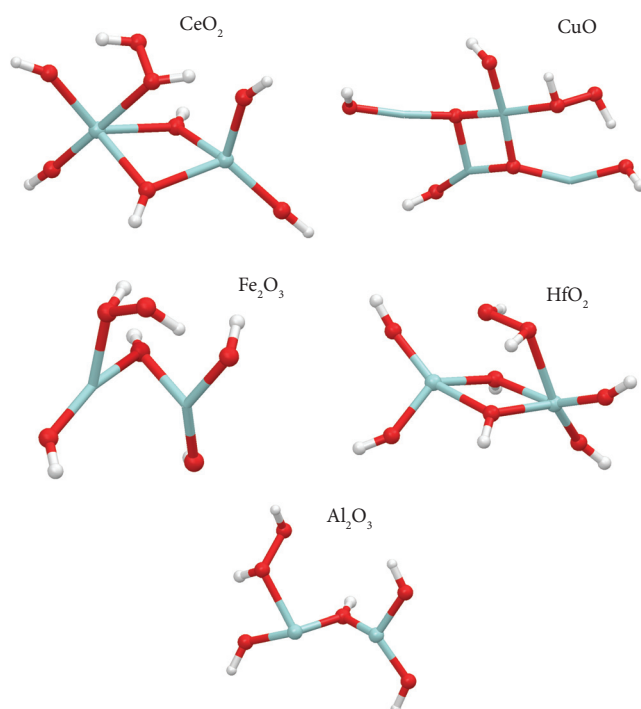
Figure 44. Adsorption of H_2O_2 onto hydroxylated clusters of CeO_2, CuO, Fe_2O_3, HfO_2 and Al_2O_3. Metal cation (●), O (●), H(○).

As described for the previous oxides studied, in order to form the molecular adsorption structure, H_2O_2 binds to the clusters by direct interaction of its O atoms with the oxide metal cation. Another type of interaction present is hydrogen bonding, and for all oxides, H_2O_2 acts both as a donor and acceptor. From these structures (Figure 44), H_2O_2 undergoes decomposition. The obtained structures of the transition-states for the decomposition of H_2O_2 are shown in Figure 45. The reaction energy barriers are given in Table 13.
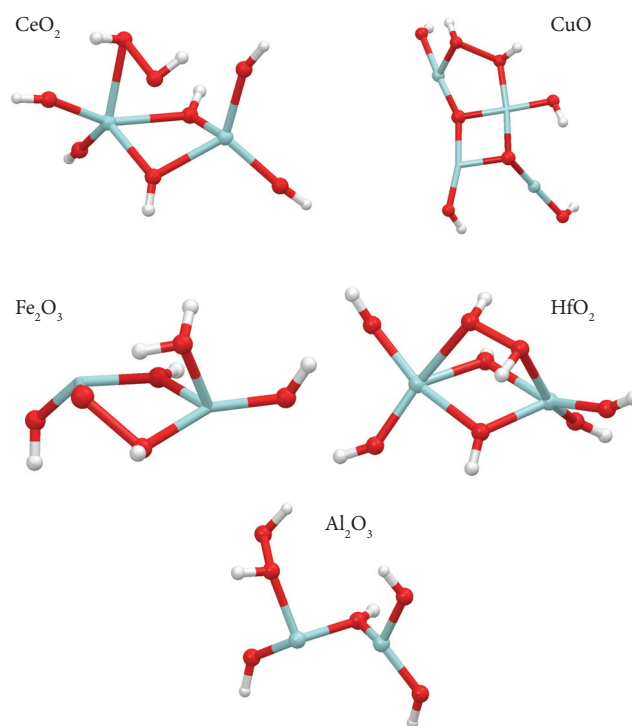
Figure 45. Transition-states for the decomposition of H_2O_2 catalyzed by hydroxylated clusters of CeO_2, CuO, Fe_2O_3, HfO_2, Al_2O_3. Metal cation (●), O (●), H(○).

The transition-states obtained are similar for all the oxides. The decomposition of H_2O_2 consists of a first molecular adsorption step followed by the cleavage of its O-O bond. The only exception is Fe_2O_3. For this cluster, the decomposition of H_2O_2 follows a transition-state involving the cleavage of the H-OOH bond. This reaction has been discussed in the literature as a possible pathway for the decomposition of H_2O_2.[179,208] Though, due to the higher BDE and consequent energy barrier for the cleavage of the H-OOH bond when compared with the O-O bond, this is expected to be a side reaction and not the main reaction path. This was observed for all oxides studied so far with the minimal cluster models, with the exception of Fe_2O_3.

Table 13. Obtained reaction energy barriers with zero point energy correction (E_a^{ZPE}), molecular adsorption energy of H_2O_2 ($\Delta E_{ads}(H_2O_2)$); reaction energy (ΔE_r) for the decomposition of H_2O_2 on the surfaces of some of the clusters shown in Figure 43 and the BEP coefficient obtained from Equation (8) (α_{BEP}). The transition-state structures are shown in Figure 45, Figure 35d-Figure 37d. Energy values are in kJ·mol^{-1}.

Oxide	$\Delta E_{ads}(H_2O_2)$	E_a^{ZPE}	ΔE_r	α_{BEP}
CeO$_2$	-88	60	-435	0.68
CuO	-62	71	-358	1.15
Fe$_2$O$_3$	-150	11	-320	0.07
HfO$_2$	-54	56	-573	1.22
Al$_2$O$_3$	-66	36	-153	0.55
ZrO$_2$	-150	42	-634	0.28
TiO$_2$	-68	41	-490	0.60
Y$_2$O$_3$	-92	45	-684	0.49

From the BEP coefficients shown in Table 13, it is clear that the transition-states for the cleavage of H_2O_2 vary considerably in terms of the BEP classification methodology. For some of the oxides the decomposition of H_2O_2 is more structure sensitive than for others. The decomposition on Fe$_2$O$_3$ is the more structure sensitive and in HfO$_2$ the less structure sensitive. Relaxing the transition-states obtained Figure 45 leads to the formation of the products shown in Figure 46. The corresponding reaction energies are shown in Table 13.
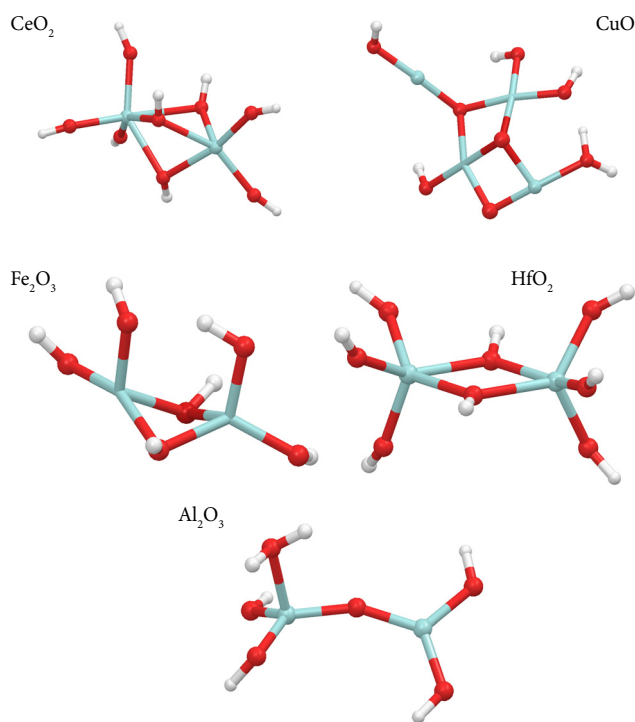
Figure 46. Products of the decomposition of H_2O_2 catalyzed by hydroxylated clusters of CeO_2, CuO, Fe_2O_3, HfO_2 and Al_2O_3. Metal cation (●), O (●), H(○).

The primary stable products of H_2O_2 decomposition consist of both adsorbed HO radical and H_2O. These interact with the clusters by forming bonded states with the metal cations, via the unpaired electron of HO$^\bullet$ and the available non-bonding electrons more localized on the O atom in H_2O. For all cases, the formation of H_2O is due to the abstraction of a structural H atom by the HO$^\bullet$ resultant of the cleavage of the O-O bond in H_2O_2 – the H atom is initially bound to an O atom of the cluster. The only cases where the primary product formed consists of 2 adsorbed HO radicals are Fe_2O_3 and HfO_2. This is interesting since the obtained transition state for H_2O_2 decomposition on Fe_2O_3 is with regard to an H atom transfer from H_2O_2 to a surface HO group which would indicate that water could be the primary product. Though, relaxing this geometry leads to a rearrangement of the structure and the spontaneous formation of 2 HO$^\bullet$ bound to the two cations. This suggests that the H atom transfer mechanism might have a role in the decomposition of H_2O_2. Even if that role is minor when compared to the main reaction pathway which does not involve this process. This evidence is in agreement with the experimental finds reported in Section 4.5 and with the suggested mechanism for H_2 formation according to Reaction (R20). This is triggered by the removal of HO$^\bullet$ from the system where H_2O_2 undergoes decomposition. In the experimental study for H_2O_2 reactivity presented in Sections 4.1.2.2 and 4.2.3 for a series of metal oxides, it can be seen that Fe_2O_3 behaves differently from the other oxides in terms of kinetic parameters and HO$^\bullet$ formation dynamics. The contribution of the Fenton reaction for the

measured experimental energy barrier has to be considered. This would mean that the experimental data for Fe_2O_3 can have a contribution from a redox process. This could explain the discrepancy with the DFT obtained activation energy shown in Table 13.

4.6.2 χ, IP, EA, and ΔE_{ads} (2HO$^\bullet$) as reactivity descriptors for the decomposition of H_2O_2 catalyzed by transition metal, lanthanide and aluminum oxides

In this section, the applicability of reactivity descriptors to the reaction of decomposition of H_2O_2 catalyzed by the oxides: ZrO_2, TiO_2, PdO_2, NiO_2, HfO_2, Fe_2O_3, Y_2O_3, Al_2O_3, Gd_2O_3, CeO_2 and CuO; is discussed. Whenever possible are derived reactivity descriptors whose parameters are values extracted from the experimental and DFT calculations presented in this thesis. Also, literature data is used for the derivation of some descriptors involving the Pauling electronegativity of the metal atoms present in the oxides.

One correlation that was briefly discussed in Section 4.4 is how the ionization potential of the metal cation present in the oxide influences the adsorption energy of the HO radicals. This was discussed based on the fact that upon adsorption of the HO radical, some of the electron density initially localized on the orbitals of the surface exposed metal atom, has to be delocalized in order to form bonded states with the unpaired electron of the HO radical. This causes the partial oxidation of the metal atoms that bind to the HO$^\bullet$. A correlation between the adsorption energy of HO$^\bullet$ and the ionization potentials of Zr^{4+}, Ti^{4+} and Y^{3+} was found. Following this, here is presented and discussed how the changes in the Mulliken charge of the metal cation present in the oxide correlate with the adsorption energy of the HO radicals for the various oxides. The adsorption energies of 2 HO radicals are for the binding of the radicals onto the hydroxylated clusters shown in Figure 43. The resulting plot showing the adsorption energies of the HO radicals as a function of the change in Mulliken charge (*e*) of the cations of the clusters are shown in Figure 47. The values for the change in Mulliken charges (*e*) were obtained as *e = Mp-Mr*. Where *Mp* is the Mulliken charge of the cations in the product, and *Mr* is the Mulliken charge of the cations in the reactant.

Change in Mulliken charge of the metal atom upon adsorption of HO radical. (*e*)
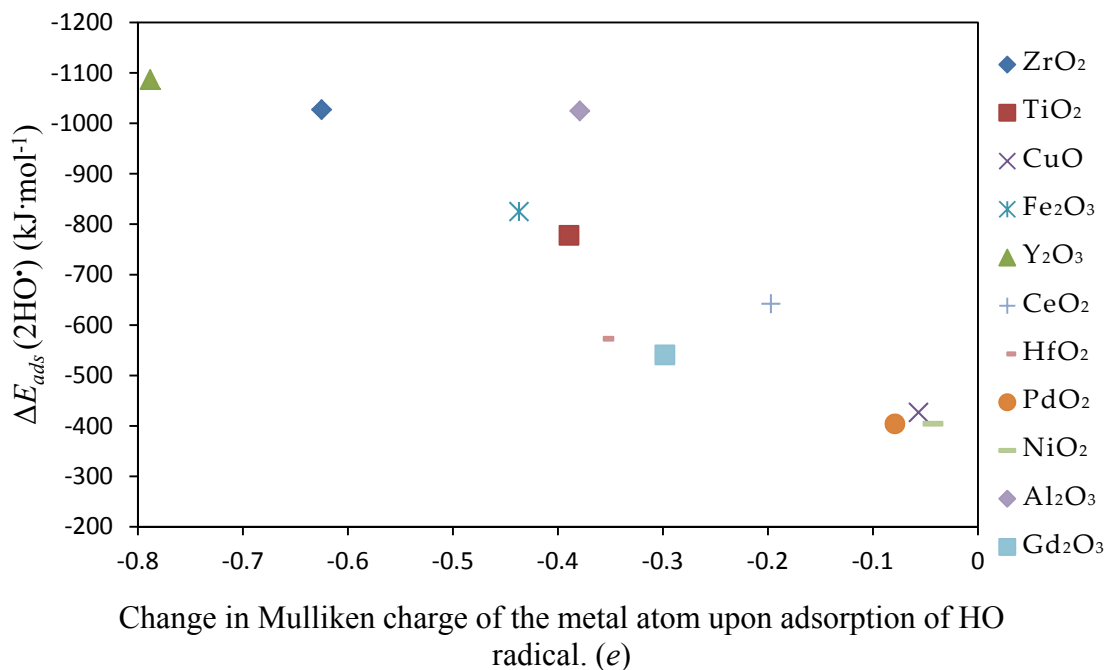
Figure 47. Adsorption energy (ΔE_{ads} (2HO$^\bullet$)) of 2HO radicals as a function of the change in Mulliken charge of the metal cations accommodating the HO radicals (*e*). The value of *e* is an average of the individual *e* of the cations involved in the bonding with the 2HO$^\bullet$.

It can be seen (Figure 47) that there is a fairly linear correlation between the adsorption energies of HO radicals and the values of *e*. From this correlation it can be concluded that upon formation of bonds with HO$^\bullet$, the easier it is to delocalize electron density from the exposed orbitals of metal cation, the stronger the bonds with HO$^\bullet$ will be. The strength of these bonds might have implications on the mechanism of decomposition of H_2O_2 because for the cases where the adsorption of HO$^\bullet$ is stronger than a given threshold, surface poisoning by HO$^\bullet$ might affect the overall reaction mechanism. On the other hand for the cases where the bonds of HO$^\bullet$ with the surface are weaker, the HO$^\bullet$ will probably be able to react further with H_2O_2 to form H_2O and $HO_2^\bullet$. The main outlier in the trend is Al_2O_3. This can be due to the fact that Al does not have *d*-orbitals or *f*-orbitals constituting its valence shell. The more "adsorbate readily available" shape of the 2*p* orbitals accommodating the valence electrons of Al^{3+} might explain why a smaller change in *e* for this cation, leads to a stronger ΔE_{ads} for HO$^\bullet$.[189]

A measure of the tendency of an atom to attract electrons towards itself, is the Pauling electronegativity χ_P.[209] A plot of the ΔE_{ads} of 2 HO$^\bullet$ as a function of χ_P of the atom accommodating the HO$^\bullet$ is shown in Figure 48.
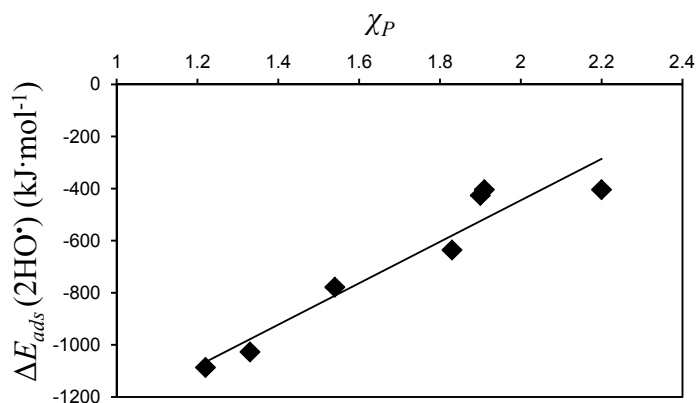
Figure 48. Adsorption energy of 2 HO radicals ($\Delta E_{ads}(2HO^\bullet)$) obtained with DFT calculations using as reactants, the clusters of the transition metals shown in Figure 43, as a function of the Pauling electronegativity of the transition metal atom present in the oxide (χ_P). χ_P are experimental data retrieved from literature.[210]

For the data in Figure 48, the correlation coefficient between the Pauling electronegativity of the metal atom (in oxidation state 0) and the adsorption energy of the HO$^\bullet$ is 0.92. This correlation holds only for the transition metal oxides studied. This can be explained with the following basis: The Pauling electronegativity is determined for the element in oxidation state 0. The removal of electrons to form the cationic species found in the oxides will cause relaxation of the electrons of the cation to minimize the energy of the new electron configuration. This relaxation will be different depending on the type of orbitals occupied in the different cations. Thus is expected that the more different the occupied orbitals are, the more different is the relaxation contribution that influences the shape and energy of the final relaxed orbitals after formation of the cationic species. From Figure 48:

ΔE_{ads} (2HO$^\bullet$) $\approx$ (796 × χ_P - 2036).

The experimental data for the Arrhenius activation energies for decomposition of H_2O_2 on the surfaces of the oxides as well as the DFT data are shown in Table 14.

Table 14. Experimental Arrhenius activation energies (E_a); DFT electronic activation energies with zero-point-energy-corrections (E_a^{ZPE}) for decomposition of H_2O_2 on the surface of different oxides; and adsorption energies of 2 HO radicals onto hydroxylated clusters of the oxides ΔE_{ads} (HO). All values in $kJ \cdot mol^{-1}$.

Material	Experimental	DFT	
	E_a	E_a^{ZPE}	ΔE_{ads} (HO$^\bullet$)
ZrO_2	33 ± 1	42	-1028
TiO_2	37 ± 1	41	-778
Y_2O_3	44 ± 5	45	-1087
Fe_2O_3	51 ± 1	11	-824
CeO_2	40 ± 1	60	-642
CuO	76 ± 1	71	-427
HfO_2	60 ± 1	56	-572
Al_2O_3	38[a]	36	-1025
NiO_2	–	–	-404
PdO_2	–	–	-404
Gd_2O_3	63 ± 1	–	-540

a) Ref.[129]

The DFT obtained energy barriers for H_2O_2 decomposition are in reasonable good agreement with the available experimental data (Table 14). The larger deviation found for CeO_2 and the fact that it was not possible to locate a transition-state for H_2O_2 decomposition on the Gd_2O_3 cluster show the limitations of the DFT methodology in describing the chemistry of lanthanides, especially that of Gd.[211,212] The transition-states for decomposition of H_2O_2 are a challenging system from a computational chemistry perspective. They consist of semi-radical states which are usually difficult to reproduce with DFT.[213] The transition-state for CeO_2 was found and the reaction energy barrier lays 20 $kJ \cdot mol^{-1}$ above the experimentally determined value.

Following the concept by BEP, a plot of the adsorption energy of the HO radicals as a function of the experimental Arrhenius activation energy barriers was done. As discussed in Section 4.3.3, the adsorption of the HO radical contributes the most to the overall reaction energy when compared with the contribution from the molecular adsorption of H_2O.
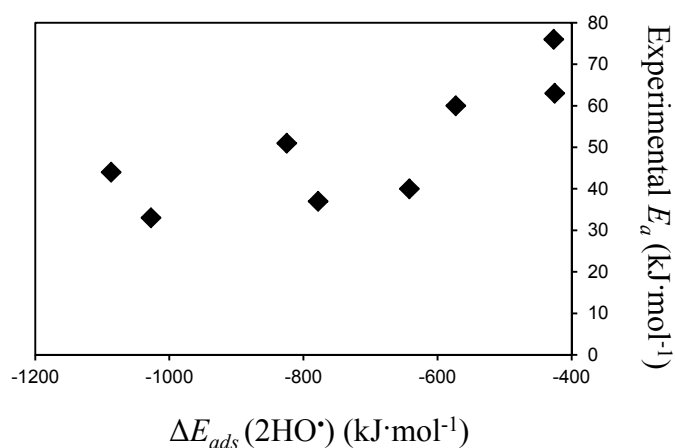
Figure 49. Experimental Arrhenius activation energies for H_2O_2 decomposition (E_a) as a function of the adsorption energies of 2HO radicals (ΔE_{ads} (2HO$^\bullet$)) obtained with DFT calculations using minimal cluster models of the oxides (Figure 43). Data from Table 14.

It is visible (Figure 49) that, following the BEP principle, the more exothermic is the adsorption of the HO radicals, the lower is the activation energy barrier for H_2O_2 decomposition. Worth of a remark is the fact that the experimental energy barriers were determined in solution. The cluster models consist of minimal sized clusters of stoichiometric units of the metal oxides whose terminations were truncated with H atoms and further hydroxylated. As the DFT data is for gas phase and given the good agreement with experiments, it seems plausible that the solvation effects have a small contribution for the energy of the reactions of adsorbed species during H_2O_2 decomposition in the real systems. Nevertheless the extent and stability of the surface hydroxylation have an impact on the activation energy barriers for H_2O_2 decomposition as it will be shown. In order to verify how the local properties of the surface atoms correlate with the experimental activation energies for H_2O_2 decomposition, the experimental data was plotted as a function of the DFT values for IP and Mulliken electronegativities (χ) of the cations present in the oxides (Figure 50 and Figure 51).
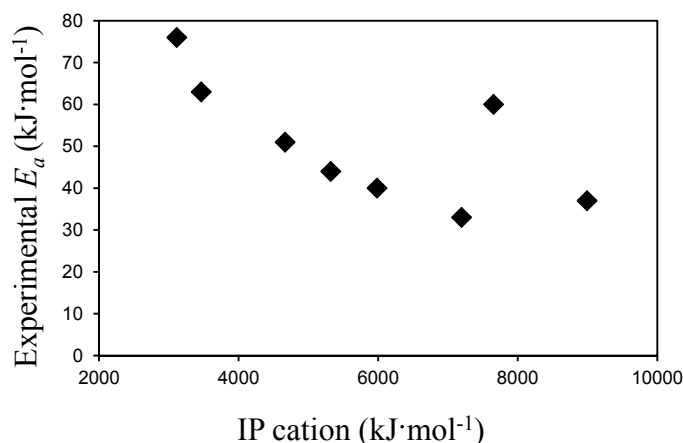
Figure 50. Experimental Arrhenius activation energies (E_a) as a function of the ionization potential of the cation present in the metal oxide.

The IP values (Figure 50) are the HOMO energies of the cations in the oxidation states present in the oxides in gas phase. In a similar way, for the determination of χ (Figure 51), the EA values used are the LUMO energies of the cations, in the oxidation states found in the oxides, in gas phase.
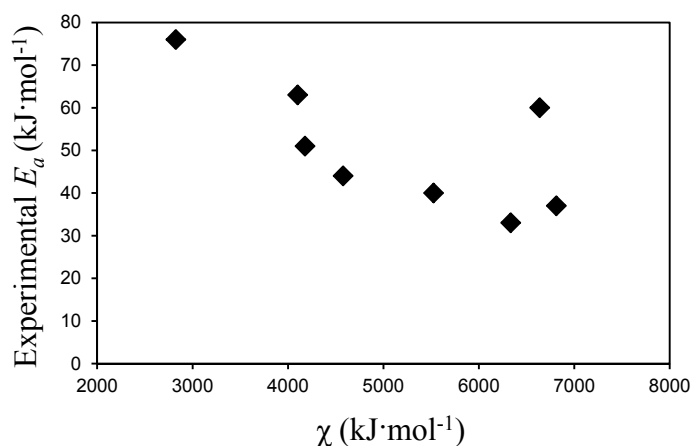
Figure 51. Experimental Arrhenius activation energies (E_a) as a function of the DFT obtained Mulliken electronegativities (χ) of the cations present in the metal oxide.

The trend visible in Figure 50 does not follow a direct BEP relation in the sense that a lower IP of the cation means that the adsorption of HO radical product is more exothermic and as such the energy barrier for the reaction would be lower with decreasing IP. This simple correlation – depending only on the parameter: product adsorption energy – would be true for a reaction occurring on a dry surface (*e.g.* in UHV conditions). It has been discussed previously in this work and in a literature publication that the IP of a metal cation in a metal oxide surface is proportional to the Lewis acidity of the cation present in the oxide.[214,215] As shown in Section 4.3.3, the more Lewis

acidic is the cation, the stronger it will bind the HO⁻ groups resulting from dissociative adsorption of H_2O. The effect of this on the mechanism of decomposition of H_2O_2 is that this will lead to more extensive surface reconstruction and make the reactive surface site less available for accommodating H_2O_2 and its decomposition products, ultimately leading to an increase in the energy barrier for H_2O_2 decomposition at those cations which are more Lewis acidic. This trend is visible in the plot of Figure 50. Also, these different hydroxylation effects will, for the different materials, lead to different contributions – *i.e.* from geometric and electronic effects – to the BEP relation which causes its deviation from linearity.[50] The more extensive the reconstruction of the hydroxylated site, the larger the contribution of a geometric effect to the BEP relation, and vice-versa.

The good correlation between reaction and catalyst properties obtained at a localized level – *i.e.* ΔE_{ads} (2HO•), IP and χ – and the experimental data, indicates that the reaction of H_2O_2 in the real particle systems is determined by local phenomena which is dependent on properties of the cations present in the oxides. This relation is shown here to be valid for a series of 8 oxides, 2 of which are lanthanides. The outlier is HfO_2. This can be explained with the fact that even though hybrid DFT shows good performance for determining the HOMO/LUMO energies even for lanthanides,[216] Hf is a special case in the sense that relativistic effects have to be considered, but the quasirelativistic ECP scheme applied here to Hf, implemented by Cundari and Stevens was parameterized for lanthanides with oxidation states 2+ and 3+.[78] This fact contributes to the deviation in HOMO/LUMO energies prediction for Hf^{4+}.[217]

Even though the cluster models are fairly simplistic representations of the surfaces because they represent only a specific type of coordination site – with the exception of CeO_2 and Fe_2O_3 – the average absolute deviation from the experimental energy barriers (Table 13) is 4 kJ.mol⁻¹. The origin of the discrepancy for CeO_2 can be attributed to the limitations of the KS based DFT in modeling lanthanide reactivity. It is plausible that for Fe_2O_3, the transition-state predicted with DFT does not correspond to the process determining the energy barrier in the real system.

5. Conclusions and summary.

From the experimental studies of the reactions of H_2O_2 with a series of oxides it is possible to conclude that:

- For the same surface to volume ratio of oxide and the same concentration of reactant H_2O_2, the reaction rate laws and rate constants differ widely between the different materials. Also the

heterogeneous rate constants – *i.e.* second order rate constants – are far from diffusion controlled.

- The reactions Arrhenius and enthalpy barriers differ widely for the different materials. The same is observed with the Arrhenius pre-exponential factors.

- The dynamics of formation of HO$^\bullet$ during decomposition of H_2O_2 are in agreement with the fact that HO$^\bullet$ is a primary product of H_2O_2 decomposition. Though, the yield of observed product of the scavenging of HO differs widely between the materials for the same consumption of H_2O_2. This indicates that the relative reactivity of adsorbed species is different for the different materials.

- The formation of HO$^\bullet$ was also observed for decomposition of H_2O_2 on the surface of UO_2 based materials. The mechanistic study indicates that the underlying factor for the differences between UO_2 and SIMFUEL towards reaction with H_2O_2, are differences in the redox reactivity of these materials.

The method for determination of HO$^\bullet$ (implemented with basis in two previously published methods) reveals an effective strategy to observe the dynamics of formation of HO$^\bullet$. This method is quite insensitive to interferences caused by the presence of the oxide. Though, a more in-depth study of the reactivity of the HO$^\bullet$ scavengers Tris and TAPS has to be done in order to determine the effect of the surfaces on the selectivity of the reactions of surface/interfacial HO radicals with the scavengers.

The DFT models implemented for the DFT study are a computationally cheap and effective way of studying the reactivity of H_2O_2 with the particles of the oxides. The density functionals that have shown an overall best performance are the M06 and PBE0. The average absolute deviations from experiments obtained with these functionals are 6 and 5 kJ·mol^{-1} respectively for the energy barriers of the reactions of H_2O_2 with ZrO_2, TiO_2 and Y_2O_3.

In the study of the reactivity descriptors obtained from DFT, using the PBE0 functional, the minimal sized clusters were able to reproduce, the experimental data with an average absolute deviation of 4 kJ·mol^{-1}. This is for a set of 8 oxides. By plotting the experimental data against DFT obtained reactivity descriptors, good correlations which agree with the well-established Brønsted-Evans-Polanyi principle were found. Overall it can be concluded that:

- The adsorption of HO radicals causes delocalization of electron density of the metal cation accommodating those radicals. The more delocalization occurs, the more exothermic is the adsorption of HO$^\bullet$ onto those surface atoms.

- The trend for adsorption energy of HO radicals is inversely proportional to the Pauling electronegativity of the metal atom present in the oxide. This trend was found for transition metal oxides.
- There is a correlation between the adsorption energies of the HO radicals and the energy barrier for H_2O_2 decomposition. The stronger the adsorption of product HO, the lower is the energy barrier for H_2O_2 decomposition, following the BEP principle.
- Both the DFT ionization potential and the Mulliken electronegativity of the bare metal cation (in the same oxidation state as it is present in the oxide) are inversely proportional to the energy barrier for H_2O_2 decomposition. This because the ionization potential is related with Lewis acidity of the cation which in turn determines the extent of its hydroxylation. The Mulliken electronegativity is related with the ease of delocalizing electron density from the metal cation.

All the reactivity descriptors obtained with DFT were calculated using minimal sized clusters consisting of one or two stoichiometric units of the oxides. These clusters represent defective surface sites in which the metal cations are undercoordinated. Given the very good correlations between computational and experimental data, it can be stated that for real oxide materials, the processes that account for the pathway and energetics of the decomposition of H_2O_2 are *very* localized (*i.e.* at the atomic scale) and are highly dependent on the local properties of the cations present in the oxides. This also indicates that the surface defects where the metal cations are more undercoordinated have an important role in determining the reaction kinetic and energetic parameters on the real systems.

6. The contribution of this work to the field of interfacial radiation chemistry

A method was implemented for the detection of HO radicals in solution and interfaces. This is a simple method that can be performed easily in for example, a basic chemistry lab. This method can be applied to many systems such as the study of reactor chemistry, photocatalysis, heterogeneous catalysis, etc. A computationally efficient methodology was developed for the study of the reactions of radiolysis products of water and different metal oxide surfaces. This has brought understanding of the mechanisms of interaction and reactivity of H_2O_2 and HO radical with surfaces. It is demonstrated that the HO radicals formed in solution can be trapped by surfaces. This also raises new questions about the significance of this process in the corrosion of nuclear reactor components. The important role of the interactions of the HO radical with these surfaces is further illustrated by the spontaneous production of H_2 when HO$^\bullet$ scavengers are present in the

system where H_2O_2 undergoes decomposition. Future studies on the interactions of $HO^\bullet$ – and eventually other radicals – with surfaces are necessary. This in order to clearly elucidate the importance of this species in the formation of H_2 at oxide and metallic surfaces and its role in corrosion processes.

Together, the experimental and computational studies lead to surprising results such as the fact that the complex chemistry of H_2O_2 reacting with solid surfaces in liquid phase can actually be described to a good extent by using fairly simple theoretical models of the metal oxides surfaces.

This study lead to the identification of the properties of the oxides surfaces that account for their reactivity towards some radiolysis products. This knowledge, together with the kinetic, energetic and mechanistic data obtained here can be used as a predictive tool for analyzing reactor chemistry and can aid in the design of improved new functional materials to be used within nuclear technology.

7. Supplementary Information: Density Functional Theory

To completely describe the spatial coordinates of an atom, it is necessary to define both where its nucleus is and where the atom's electrons are. The early definition of the atom, much inspired by the planetary motion, considered the atom as being a number of electrons e orbiting a nucleus with charge Ze. From a classical mechanics point of view, defining the spatial coordinates of the atom sounded like a regular many-body problem that could be tackled by using Newton's equations of motion. However, experimental observations were incompatible with this view of the orbiting electrons around a nucleus resembling the solar system. According to the predictions of electromagnetic theory, the electrons in orbital motion, due to the radial acceleration would decelerate and collapse into the nucleus. This would mean that matter would be unstable, clearly an observation far from reality. From the attempts to study the atom and its constituents, Niels Bohr reached a very important conclusion that postulated that the orbits that the electrons occupy have specific energies and spatial radii. In order for the electrons to "jump" in between different orbits, it would be necessary that they absorb or release a *quantum* of energy. The whole set of ideas that surrounded this discovery together with Planck's observations of the blackbody radiation ultimately led to the development of the mathematical tools that became the quantum theory of matter or quantum mechanics.

The energy of a system of quantum bodies is expressed according to the time-independent form of the Schrödinger equation

$$H\Psi = E\Psi \qquad (17)$$

where H is the Hamiltonian operator and Ψ is a set of solutions, or eigenstates, of the Hamiltonian. Each of the solutions Ψ_n of the set Ψ, has an associated eigenvalue, E_n, that satisfies the eigenvalue equation. This equation means that for a system of quantum bodies, there is a wavefunction Ψ over which an operator can be applied and all the properties of the system can be derived by solving the time-independent Schrödinger equation. When applied to electrons, as these particles are fermions, the total electronic wave function must be antisymetric *i.e.* it must change sign; whenever the coordinates of two electrons are exchanged. This is known as *exchange*. If one is interested in obtaining the energy of the system, the operator to apply to the wavefunction is the Hamiltonian operator as stated in Equation (17). The detailed definition of the Hamiltonian depends on the physical system being described by the Schrödinger equation. There are several well-known examples like the particle in a box or the harmonic oscillator where the Hamiltonian has a simple form and the Schrödinger equation can be solved exactly. Though, when applied to the movement of electrons in an atom, the multi-component many-body problem posed by the Schrödinger equation is unsolvable in an exact way for a system more complex than hydrogenoid atoms or the He_2^+ molecule. For more complex systems, the fact that those are many-body systems, plus the existence of Coulomb interactions makes the Schrödinger equation not separable. For describing an atom with Z electrons, it is possible to tackle the multielectronic problem as a product of antisymmetrical one-electron wavefunctions (a Slater determinant). The Hartree-Fock (HF) method assumes that the exact, N-body wave function of a system of fermions can be approximated by a single Slater determinant.[218] This approach however, assumes separability of the Schrödinger equation, implying that the probability of finding an electron at a point in space is essentially independent of the location of the other electrons. This picture does not account for the repulsive electron-electron interactions because an electron located at a region of space r will create an "exclusion zone" where other electrons will not be found (Figure 52). The HF method is computationally cheap but the fact that it neglects correlation produces data with large deviations from experimental results.[219]
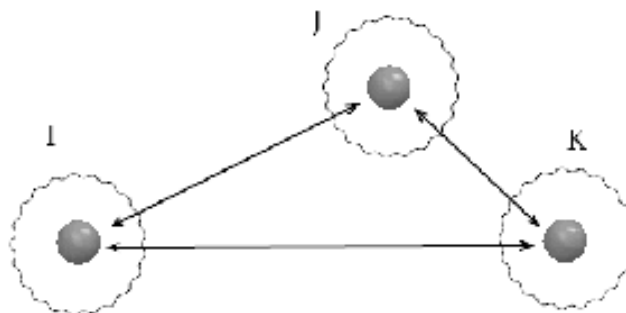
Figure 52. Exclusion zones leading to correlation holes (waving lines) for a system of 3 electrons ($\bullet$). The arrows represent two particle correlation. It is possible to conceptually express the total correlation (X) of this system as: X_{Total} = ij+jk+ik.

Thus, the probability of finding our electron at the point of space r will depend of its interactions with the other Z-1 electrons that constitute the atom – and these interactions depend on the spatial coordinates of the Z-1 electrons. This phenomenon is known as *correlation*. It implies that the many-body wave function must contain terms that depend on two electron coordinates (Figure 52). As such, the approach of the total wave function in terms of one electron wavefunctions is in many cases rough. For a system of M nuclei and N electrons all this means that the Schrödinger equation cannot easily be decoupled into a set of simpler equations, which implies that to solve the Schrödinger equation we have to deal with 3($M+N$) coupled degrees of freedom.

An underlying principle for applying quantum mechanics to atoms resides in the fact that atomic nuclei are much heavier than individual electrons. From a classical mechanics perspective, when this principle is applied to the movement of electrons and nuclei, it means that electrons respond much more rapidly to changes in their surroundings than nuclei do. As a result, under the conditions of applicability of this approximation, it is possible to split the position problem into two parts. First, for fixed positions of the atomic nuclei, we solve the equations that describe the motion of the electrons. It means that for a given set of electrons moving in the field of a set of nuclei, we find the lowest energy configuration, or state, of the electrons. The lowest energy state is known as the ground state of the electrons, and the separation of the nuclei and electrons into distinct mathematical problems is the Born-Oppenheimer approximation. For M nuclei with positions R1, . . . , RM, it is possible to express the ground-state energy, E, as a function of the positions of these nuclei, E(R1, . . . , RM). This

function is the adiabatic potential energy surface of the atoms. And this approximation is known as the adiabatic approximation. Once it is possible to calculate this potential energy surface, it is possible to solve the problem: how does the energy of a material change as we move its atoms in space?

Since the development of the quantum mechanical formulations of matter, there has been a diversity of approaches for approximating a solution to the Schrödinger equation for many-electron systems.[220] One of the most successful approaches is the one developed after two mathematical theorems that were demonstrated by Kohn and Hohenberg,[221] and the further derivation of a set of equations by Kohn and Sham.[222] The Kohn-Hohenberg approach provides an elegant way to approximate electron correlation with resource efficiency similar to that of Hartree-Fock. The first theorem by Kohn and Hohenberg states that: The ground state energy obtained from the Schrödinger equation is a unique functional of the electron density. This means that for an electron system, there is a relation between the ground state wave function and the ground state electron density. This relation is measured by a functional of the electron density. When applied to the energy of a system, the Hohenberg and Kohn's theorem says that the ground state energy E can be expressed as $E[n(r)]$ where $n(r)$ is the density of n electrons at the spatial coordinates r. This is the origin of the term density functional theory (DFT). It implies that the ground state electron density uniquely determines all properties of the system, including the energy and wave function, of the ground state.

DFT marked an enormous progress in the understanding of quantum systems. As an example:[223] "Why is this result important? It means that we can think about "solving the Schrödinger equation" by finding a function of three spatial variables, the electron density, rather than a function of 3N variables, the wave function. Here, by "solving the Schrödinger equation" we mean, to say it more precisely, finding the ground-state energy. So for a nanocluster of 100 Pd atoms the theorem reduces the problem from something with more than 23000 dimensions to a problem with just 3 dimensions."

Although the form of the functional that provides an exact solution for the electronic Schrödinger equation is not known, the second theorem by Hohenberg-Kohn defines a property of the functional that allows its practical application to multi-electronic problems: The electron density that minimizes the energy of the overall functional is the true electron density corresponding to the full solution of the Schrödinger equation. This turns the problem of finding the approximate true electron density, onto a variational problem. A variational principle is used with approximate forms of the functional to determine solutions that satisfy the principles underlying the Schrödinger equation. Over the years, several functional forms have been

developed with the intent of approximating the many-body problem posed by the Schrödinger equation, from the electron density perspective.[224] The simpler case of applicability of the true functional of the electron density – whose existence is shown by the Hohenberg-Kohn theorem but whose form is unknown – is the case where this functional can be derived exactly. This is possible for the uniform electron gas. For a uniform electron gas the density is constant in all points of space. The practical applicability of this approach is somehow limited because chemical properties and chemical bonds are the result of variations in electron density in a molecule or material. Nevertheless for such uniform electron gas, the Kohn-Sham (KS) equations can be applied in a practical way. The concept behind the applicability of the KS equations builds in the fact that the exchange-correlation potential can be set at each position of space to be the known exchange-correlation potential obtained from the uniform electron gas for the electron density observed in that point of space. Because this method uses only the local density to define an approximation of the exchange-correlation functional, it is known as the local density approximation (LDA).[225] The LDA is a tool to define the KS equations but its results are not the exact solution of the Schrödinger equation. This is because the LDA approach is not leading to the true form of the exchange-correlation functional. Recall that the true form of the exchange-correlation functional was demonstrated by Hohenberg-Kohn to provide an exact solution to the Schrödinger equation but from the electron density perspective instead of from a wave-function perspective. The problem of finding accurate approximations to the exact exchange-correlation functional is the biggest challenge of Kohn-Sham DFT. The better we understand the exact functional, the better approximations we can design.

At this point, our intuition as chemists tells us that the LDA functional form as it is presented above should not provide the best description of the physical properties of electron systems, which, are behind chemical properties of molecules and materials. These are: changes in electron density, electronic correlation, spin density gradients, spin-up/spin-down kinetic energy dependence, spin polarizabilities etc. Since the introduction of the LDA concept, there has been published a multitude of different approaches and improvements to the functional forms in order to better describe the chemistry of real systems.

The generalization of LDA that includes electron spin is called local spin density approximation (LSDA) . The energy obtained from LSDA calculations will at each spatial coordinate depend on electron spin $i.e.$ $\alpha(\uparrow)$ or $\beta(\downarrow)$.[226] The next approximation after the LDA and LSDA was the development of a class of functionals that uses information of both the local electron density and the local gradient of the electron density. This is the generalized gradient approximation (GGA).[53] In spite of being also a local

approximation, the inclusion of a gradient dependency of the energy in the GGA lead to improved results when compared with the LSDA approaches for calculations of: total energies,[227] atomization energies,[227,228] energy barriers and structural energy differences.[229-231] One can think directly that the GGA's, because it incorporates more physical information, always performs better than the LDA based approaches. This is not always the case and for example GGA calculations soften chemical bonds, an effect that sometimes corrects[231] and sometimes overcorrects[232] the LSDA predictions. Typically, GGA's favor density inhomogeneity more than LSDA does. Overall the GGA for the exchange-correlation energy are an improvement over the LSDA description of atoms, molecules, and solids. Because there are many ways in which to include the shape of the gradient of the electron density on the functional,[54] there is a large number of types of GGA functionals. Two of the most widely used functionals in calculations involving solids are the Perdew‑Wang functional (PW91)[53] and the Perdew‑Burke‑Ernzerhof functional (PBE).[54] The PBE is a parameter free functional which was constructed by making the functional form to satisfaction some constrains. Further developments after the GGA have been developed and lead to more and more sophisticated classes of functionals which use other pieces of physical information. In fact it is claimed that a hierarchy of functionals can be constructed that gradually include more and more detailed physical information. Because of the different type of information that many of the functionals include, it is difficult to state which are "more correct". According to a recent review,[233] six strategies have been widely employed for designing density functionals: (1) local spin density approximation (LSDA), (2) density-gradient expansion, (3) constraint satisfaction, (4) modeling the exchange-correlation hole, (5) empirical fits, and (6) mixing Hartree–Fock and approximate DFT exchange. Other more sophisticated functionals appeared after the GGA's. The meta-GGA's (MGGA) are the next step in functional improvement as they go beyond the gradient correction. This class of functionals takes into account the second derivative of the density, *i.e*, the Laplacian. Becke and Roussel were the first to proposed an exchange functional (BR) having such dependence.[56] Numerically stable calculations of the Laplacian of the density pose something of a technical challenge, and the somewhat improved performance of MGGA functionals over GGA analogs is balanced by this slight drawback. An alternative MGGA formalism that is more numerically stable is to include in the exchange-correlation potential a dependence on the kinetic-energy density τ. The BR functional includes dependence on τ in addition to its already noted dependence on the Laplacian of the density. Other developers, however, have tended to discard the Laplacian in their MGGA functionals, retaining only a dependence on τ. Various such MGGA functionals for exchange, correlation, or both have been developed including

B95, B98, ISM, KCIS, PKZB, τ HCTH, TPSS, and VSXC. The cost of an MGGA calculation is entirely comparable to that for a GGA calculation, and the former is typically more accurate than the latter for a pure density functional.

Observations that the LDA and GGA trends deviated from the HF results led to the development of a new concept in the implementation of functionals – the inclusion of HF exchange. These functionals involve a DFT correlation with a combination of DFT and HF exchange. This class of functionals is designated by hybrid functionals and their implementation is based on

$$E_{XC}^{hyb} = \alpha E_X^{HF} + (1 - \alpha)E_X^{DFT} + E_C^{DFT} \tag{18}$$

where E_{XC}^{hyb} is the exchange-correlation energy of the hybrid functional, αE_X^{HF} is the HF exchange energy, E_X^{DFT} is the DFT exchange energy, E_C^{DFT} is the DFT correlation energy. α is either chosen to assume a specific value – between 0 and 1 – or is obtained by fitting: in a way that the resulting functional performs the best in predicting the properties of a molecular database. One example of the later type of approach for the determination of the amount of HF exchange to include in the hybrid functional is the B3LYP functional.[58] This functional was optimized to reproduce geometries and binding energies of molecular systems to the same accuracy of low-level quantum chemical methods with the advantage of a significantly lower computational cost. B3LYP can provide accurate molecular geometries even when hydrogen bonds are present.[59] The other approach, that consists in fixing α a priori was behind the development of the PBE0 functional.[60,61] This functional form was obtained by supplying the PBE GGA functional with a predefined amount of exact exchange. The PBE0 functional has shown very good performance for structural, thermodynamic, kinetic and spectroscopic (magnetic, infrared and electronic) properties. The way in which the functional is derived and the lack of empirical parameters fitted to specific properties make the PBE0 model a widely applicable method for both quantum chemistry and condensed matter physics. It has been reported improved performance of the PBE0 functional over the B3LYP for properties of systems containing light and heavy metals.[62,63]

The latest class of functionals developed following the approaches above described are the hybrid-meta-GGA. This type of functionals combine the inclusion of HF exchange with the meta GGA approach. One such functional that has revealed improved performance over some meta and hybrid functionals is the M06 functional.[64] This functional, besides of the Laplacian dependency of the density, includes a dependence on the electronic kinetic-energy density τ. This is up-spin down-spin dependent. This functional was also parameterized to be self-interaction error free (SIE). The SIE is a feature of DFT that results from the fact that the interaction of an electron with itself

is accounted for in the exchange-correlation functionals obtained from the LDA, GGA and MGGA approximations. The hybrid functionals correct the SIE due to the inclusion of HF exchange.[65] The SIE results from a physically unreasonable property that leads to poor performance of the functionals especially in describing systems with non-integer number of electrons.[66] This means that the functionals which are not free from SIE have problems also in describing transition states of chemical reactions (especially those involving homolytic bond cleavage) and charge-transfer complexes. For solids and surfaces, it has been recently show that hybrid DFT functionals that contain a certain amount of Hartree-Fock exchange are necessary to accurately describe the electronic states of nonmetallic solids and the defects in metal oxides.[67-71] In order to properly describe the electronic properties of the defects of TiO_2 surfaces for example, it is necessary to recur to the usage of functionals that incorporate a certain amount of Hartree-Fock exchange.[70] The pure DFT functionals, due to the self-interaction error, fail to give a localized character to trapped electron states and holes in TiO_2 surface defects. When unpaired electronic states are present in the system, this type of functionals will tend do delocalize the electron density in order to minimize the self-interaction error, thus giving results for electron density in surface defects that are poor when compared with experimental data. This situation has been evident whenever pure DFT functionals were used for describing defects in large band gap semiconductors and insulators.[72] Other discrepancies were found in the type of minima for the bonding between $HO^{\bullet}$ and H_2O when these systems were described with pure DFT functionals.[73,74] Although these situations can be improved by using HF exchange in the functionals, the empirical formalisms to correct for the SIE did not lead to good performing functionals for systems where fractional charge behavior is present, polarizabilities of polymers and dissociation of molecules.[75]

In order to solve the electronic structure problem, using HF, post-HF or DFT, it is required that we choose a mathematical representation of the one-electron orbitals. The basis set is the set of mathematical functions from which the electron density or wave function is constructed. In HF theory, each molecular orbital is expressed as a linear combination of basis functions for which the coefficients are determined in an iterative way by finding solutions to the HF self-consistent-field equations. As described above the HF wave function is constructed from individual occupied molecular orbitals. The HF limit is achieved by use of a hypothetical infinite basis set, which would permit the optimal description of the electron probability density within the HF approximation. The one-electron wave functions are expanded in a generic basis set described by a set of orbitals. The Kohn-Sham or Hartree-Fock orbitals are then written as a linear combination of these orbitals in a similar way to the Hückel method. It is thus important to

identify the mathematical functions that allow wave functions to approach the HF limit and at the same time being efficient. There has been a multitude of approaches for constructing basis set depending also on the application that the developers have in mind *i.e.* periodic or molecular systems etc. For molecular systems, the type used is atom-centered basis sets. Within this concept, the most common approach is to expand the one-electron wave functions (molecular orbitals) in terms of atomic orbitals which are centered in the atomic nuclei and are represented in terms of basis functions with different functional forms or can be given numerically on a grid. The tighter or denser this grid is, the easier it is to achieve convergence of the SCF cycle and the more precise is the calculation. A basis set should allow for improvement of its quality when the number of basis functions is incremented. If a single basis function per atomic orbital is used, the basis set is minimal or single-ζ (SZ). These basis sets can be accurate for isolated atoms but have limitations in describing molecular systems where electrons are involved in chemical bonding and the electron density becomes polarized.[234] If one more set of basis functions per orbital is added it becomes a double-ζ (DZ) basis set. More accuracy and flexibility can be achieved by adding more basis functions of the same type, forming the triple-ζ (TZ) basis set. Given that the core states of an atom are rather insensitive to their environment, the usage of multiple basis functions for describing core states is not common. Generally the basis set splitting is applied to the valence orbitals forming the split valence basis sets. The basis sets can be further improved by accounting for polarization effects. These, account for the deformation of atomic orbitals due to the presence of neighboring atoms. Their description requires the introduction of functions of different angular momenta. The presence of polarization functions in a basis set is denoted by "*". For negatively charged systems, the Coulomb repulsion between electrons leads to the spread of the atomic orbitals. To better represent these orbitals – which the standard basis functions are not able to represent – additional basis functions have to be included. These are usually functions with small exponents and are called diffuse functions and are indicated by a "+" sign. One "+" for one diffuse function, "++" for two, etc. These functions are useful for describing non-bonding interactions.[235,236]

A very valuable observation in what concerns optimizing computational resources is that the core electrons in atoms are not involved actively in chemical bonding. As such they don't need to be treated explicitly in terms of a set of orbitals with a corresponding set of functions. The core electrons can then be treated by of using a nodeless pseudo-wave function. This is not an orbital anymore but it is the lowest lying state of an effective pseudo-potential or effective core potential (ECP) which replaces the true potential. This principle is the basis of the design of the ECP basis sets.[76] The number of

electrons treated explicitly is then much smaller and the number of required electronic states and basis set size is reduced significantly. This approach is particularly useful for the study of metals for which the explicit treatment of the core electrons would make the calculations involving these elements computationally prohibitive. Relativistic effects can also be incorporated in ECP basis sets.[77] This is particularly useful for calculations involving heavier transition metals or lanthanide and actinide elements.[78] The design of basis sets based on the ECP approach has expanded to the point where ECP basis sets have been developed for very specific applications such as calculations of properties of specific clusters of certain elements.[237] Tough, some authors claim that such approach is incompatible with the *ab initio* concept.

8. Acknowledgements

I would like to express my sincere gratitude to Prof. Mats Jonsson for giving me the opportunity to work in this project. I want to thank for the motivation and encouragement that I got during these years. Also, I would like to thank his willing to bring a multidisciplinary component to this project. This is truly appreciated.

I want to deeply thank Prof. Tore Brinck for his help and for his collaboration on this project. The opportunity that was given to me, of doing parallel works within experimental and computational chemistry is something that was extremely beneficial for both the project and my development as a scientist.

Johannes Johansson is gratefully acknowledged for his collaboration and for the valuable help with getting me started with the DFT calculations and also for the very interesting scientific discussions we had.

My gratitude to Prof. Jay LaVerne for letting me do experimental work at his laboratory and for helping solving a diversity of unexpected issues related with my stay in Notre Dame.

Mats Jansson is gratefully thanked for his support and precious help with solving innumerous problems during my PhD! Many of them extremely difficult for me such as: properly automating headings in ms word! With him I also acquired knowledge of greatest importance *e.g.* better than LR only LR^2.

Martin Trummer, Reijo Pehrman, Veronica Diesen, Andreas Fischer, Miao Yang and Kristina Nilsson, thank you (!) for our nice collaborations that lead to scientific papers.

A big thank you(!) to all the others at/or formerly at the division: Åsa, Karin, Sara, Sandra, Michael, Anders, Inna, Helena, Johan, Gabor, Susana, Björn, Alex. José Godinho at Stockholm University.

I would like to wholeheartedly thank my family and friends, but especially, my mom, Maria, my sister, Carla and my dad, Artur, for their love, care and support through the years!!! I want to thank my fiancé Isabell for the love, support and motivation!

9. References

(1) R. B. Adamson, P. R. *Dimensional Stability of Zirconium Alloys* Advanced Nuclear Technology International

(2) Deshon, J.; Hussey, D.; Kendrick, B.; McGurk, J.; Secker, J.; Short, M. *Jom* **2011**, *63*, 64.

(3) Center, U. T. T. *Radiation Sources at Nuclear Plants*, USNRC Technical Training Center

(4) G. Hong, W. K., D. Ordway, Zirconium oxide ceramics for surfaces exposed to high temperature water oxidation environments; 1992.

(5) Li, H.; Liang, K.; Mei, L.; Gu, S.; Wang, S. *Journal of Materials Science Letters* **2001**, *20*, 1081.

(6) *Basic Research Needs For Advanced Nuclear Energy Systems* Office of Basic Energy Sciences, U.S. Department of Energy, 2006.

(7) *Radiation Effects in Solids*; Springer Netherlands: Dordrecht, 2007; Vol. 235.

(8) Jonah, C. D. *Radiation Research* **1995**, *144*, 141.

(9) Jonsson, M. In *Recent Trends in Radiation Chemistry* Wishart, J. F., Rao, B. S. M. , Ed.; World Scientific Singapore 2010, p 301.

(10) Keith, J. A.; Anton, J.; Kaghazchi, P.; Jacob, T. In *Modeling and Simulation of Heterogeneous Catalytic Reactions*; Wiley-VCH Verlag GmbH & Co. KGaA: 2011, p 1.

(11) Mozumder, A. In *Fundamentals of Radiation Chemistry*; Academic Press: San Diego, 1999, p 5.

(12) Buxton, G. V., Greenstock, C.L., Helman, W.P. and Ross, A.B., *J. Phys. Chem. Ref. Data* **1988**, *17*, 513.

(13) Mozumder, A. In *Fundamentals of Radiation Chemistry*; Academic Press: San Diego, 1999, p 71.

(14) *Radiation chemistry : From basics to applications in material and life sciences*; Jacqueline Belloni, T. D., Mehran Mostafavi and Mélanie Spotheim-Maurizot, Ed.; EDP Sciences: Les Ulis Cedex 2008.

(15) McNaught, A. D.; Wilkinson, A. *I{UPAC}. Compendium of Chemical Terminology, 2nd ed. (the "Gold Book")*; WileyBlackwell; 2nd Revised edition edition.

(16) Subramanian, H.; Velmurugan, S.; Narasimhan, S. V. *The Canadian Journal of Chemical Engineering* **2013**, *91*, 344.

(17) Sabbe, M. K.; Reyniers, M.-F.; Reuter, K. *Catalysis Science & Technology* **2012**, *2*, 2010.

(18) Do, D. D. *Mathematical Biosciences* **1982**, *61*, 123.

(19) Laidler, K. J.; King, M. C. *The Journal of Physical Chemistry* **1983**, *87*, 2657.

(20) Chorkendorff, I.; Niemantsverdriet, J. W. In *Concepts of Modern Catalysis and Kinetics*; Wiley-VCH Verlag GmbH & Co. KGaA: 2005, p 267.

(21) Chorkendorff, I.; Niemantsverdriet, J. W. In *Concepts of Modern Catalysis and Kinetics*; Wiley-VCH Verlag GmbH & Co. KGaA: 2005, p 23.

(22) Verma, P. K.; Mitra, R. K.; Pal, S. K. *Langmuir* **2009**, *25*, 11336.

(23) Chung, Y.-H.; Xia, J.; Margulis, C. J. *The Journal of Physical Chemistry B* **2007**, *111*, 13336.

(24) Leung, K.; Luzar, A.; Bratko, D. *Phys. Rev. Lett.* **2003**, *90*, 065502.

(25) Grigera, J. R.; Kalko, S. G.; Fischbarg, J. *Langmuir* **1996**, *12*, 154.

(26) Mamatkulov, S. I.; Khabibullaev, P. K.; Netz, R. R. *Langmuir* **2004**, *20*, 4756.

(27) Lum, K.; Chandler, D.; Weeks, J. D. *The Journal of Physical Chemistry B* **1999**, *103*, 4570.

(28) Sendner, C.; Horinek, D.; Bocquet, L.; Netz, R. R. *Langmuir* **2009**, *25*, 10768.

(29) Stewart, P. S. *Journal of Bacteriology* **2003**, *185*, 1485.

(30) Henderson, M. A. *Surface Science Reports* **2002**, *46*, 1.

(31) Law, B. M. *Progress in Surface Science* **2001**, *66*, 159.

(32) Herminghaus, S. *Eur. Phys. J. E* **2012**, *35*, 1.

(33) Kimmel, G. A.; Petrik, N. G.; Dohnalek, Z.; Kay, B. D. *The Journal of Chemical Physics* **2007**, *126*, 114702.

(34) Kimmel, G. A.; Petrik, N. G.; Dohnalek, Z.; Kay, B. D. *The Journal of Chemical Physics* **2006**, *125*, 044713.

(35) Brown Jr, G. E.; Trainor, T. P.; Chaka, A. M. In *Chemical Bonding at Surfaces and Interfaces*; Elsevier: Amsterdam, 2008, p 457.

(36) Jeon, J.; Yu, B. *Journal of the Korean Physical Society* **2013**, *62*, 79.

(37) Woodruff, D. P. In *Chemical Bonding at Surfaces and Interfaces*; Elsevier: Amsterdam, 2008, p 1.

(38) Bérubé, V.; Radtke, G.; Dresselhaus, M.; Chen, G. *International Journal of Energy Research* **2007**, *31*, 637.

(39) Nilsson, A.; Pettersson, L. G. M. In *Chemical Bonding at Surfaces and Interfaces*; Elsevier: Amsterdam, 2008, p 57.

(40) Hammer, B.; Wendt, S.; Besenbacher, F. *Topics in Catalysis* **2010**, *53*, 423.

(41) Kulkarni, A. D.; Pathak, R. K.; Bartolotti, L. J. *The Journal of Physical Chemistry A* **2005**, *109*, 4583.

(42) van Santen, R. A.; Neurock, M. *Principles of Molecular Heterogeneous Catalysis*; Wiley-VCH Verlag GmbH & Co. KGaA, 2007.

(43) Newns, D. M. *Physical Review* **1969**, *178*, 1123.

(44) Anderson, P. W. *Physical Review* **1961**, *124*, 41.

(45) Bronsted, J. N. *Chemical Reviews* **1928**, *5*, 231.

(46) Evans, M. G.; Polanyi, M. *Transactions of the Faraday Society* **1938**, *34*, 11.

(47) Bligaard, T.; Nørskov, J. K.; Dahl, S.; Matthiesen, J.; Christensen, C. H.; Sehested, J. *Journal of Catalysis* **2004**, *224*, 206.

(48) Liu, P.; Kendelewicz, T.; Brown Jr, G. E. *Surface Science* **1998**, *412–413*, 315.

(49) Epling, W. S.; Peden, C. H. F.; Henderson, M. A.; Diebold, U. *Surface Science* **1998**, *412–413*, 333.

(50) Norskov, J. K.; Bligaard, T.; Hvolbaek, B.; Abild-Pedersen, F.; Chorkendorff, I.; Christensen, C. H. *Chemical Society Reviews* **2008**, *37*, 2163.

(51) Spendelow, J. S.; Xu, Q.; Goodpaster, J. D.; Kenis, P. J. A.; Wieckowski, A. *J. Electrochem. Soc.* **2007**, *154*, F238.

(52) Cox., V. E. H. a. P. A. *The Surface Science of Metal Oxides*; Cambridge University Press: Cambridge, UK, 1994.

(53) Perdew, J. P.; Burke, K.; Wang, Y. *Physical Review B* **1996**, *54*, 16533.

(54) Perdew, J. P.; Burke, K.; Ernzerhof, M. *Phys. Rev. Lett.* **1996**, *77*, 3865.

(55) Yang, K.; Zheng, J.; Zhao, Y.; Truhlar, D. G. *The Journal of Chemical Physics* **2010**, *132*, 164117.

(56) Becke, A. D.; Roussel, M. R. *Physical Review A* **1989**, *39*, 3761.

(57) Hao, P.; Sun, J.; Xiao, B.; Ruzsinszky, A.; Csonka, G. I.; Tao, J.; Glindmeyer, S.; Perdew, J. P. *Journal of Chemical Theory and Computation* **2012**, *9*, 355.

(58) Becke, A. D. *The Journal of Chemical Physics* **1993**, *98*, 5648.

(59) Staroverov, V. N.; Scuseria, G. E.; Tao, J.; Perdew, J. P. *The Journal of Chemical Physics* **2003**, *119*, 12129.

(60) Burke, K.; Ernzerhof, M.; Perdew, J. P. *Chemical Physics Letters* **1997**, *265*, 115.

(61) Adamo, C.; Barone, V. *The Journal of Chemical Physics* **1999**, *110*, 6158.

(62) Paier, J.; Marsman, M.; Kresse, G. *The Journal of Chemical Physics* **2007**, *127*, 024103.

(63) Vetere, V.; Adamo, C.; Maldivi, P. *Chemical Physics Letters* **2000**, *325*, 99.

(64) Zhao, Y.; Truhlar, D. G. *Theor. Chem. Acc.* **2008**, *120*, 215.

(65) Polo, V.; Gräfenstein, J.; Kraka, E.; Cremer, D. *Chemical Physics Letters* **2002**, *352*, 469.

(66) Zhang, Y.; Yang, W. *The Journal of Chemical Physics* **1998**, *109*, 2604.

(67) Ammal, S. C.; Heyden, A. *The Journal of Chemical Physics* **2010**, *133*, 164703.

(68) Pacchioni, G. *The Journal of Chemical Physics* **2008**, *128*, 182505.

(69) Da Silva, J. L. F.; Ganduglia-Pirovano, M. V.; Sauer, J.; Bayer, V.; Kresse, G. *Physical Review B* **2007**, *75*, 045121.

(70) Di Valentin, C.; Pacchioni, G.; Selloni, A. *Physical Review Letters* **2006**, *97*, 166803.

(71) Burow, A. M.; Sierka, M.; Dobler, J.; Sauer, J. *The Journal of Chemical Physics* **2009**, *130*, 174710.

(72) Zhang, Y.-f.; Lin, W.; Li, Y.; Ding, K.-n.; Li, J.-q. *The Journal of Physical Chemistry B* **2005**, *109*, 19270.

(73) VandeVondele, J.; Sprik, M. *Physical Chemistry Chemical Physics* **2005**, *7*, 1363.

(74) Chipman, D. M. *The Journal of Physical Chemistry A* **2011**, *115*, 1161.

(75) Mori-Sanchez, P.; Cohen, A. J.; Yang, W. *The Journal of Chemical Physics* **2006**, *125*, 201102.

(76) Blaudeau, J. P.; Brozell, S. R.; Matsika, S.; Zhang, Z.; Pitzer, R. M. *International Journal of Quantum Chemistry* **2000**, *77*, 516.

(77) Roy, L. E.; Hay, P. J.; Martin, R. L. *Journal of Chemical Theory and Computation* **2008**, *4*, 1029.

(78) Cundari, T. R.; Stevens, W. J. *The Journal of Chemical Physics* **1993**, *98*, 5555.

(79) Vektariene, A.; Vektaris, G.; Svoboda, J. *Arkivoc* **2009**, 311.

(80) Martínez, J. *Chemical Physics Letters* **2009**, *478*, 310.

(81) Karelson, M.; Lobanov, V. S.; Katritzky, A. R. *Chemical Reviews* **1996**, *96*, 1027.

(82) Parr, R. G.; Donnelly, R. A.; Levy, M.; Palke, W. E. *The Journal of Chemical Physics* **1978**, *68*, 3801.

(83) Perdew, J. P.; Parr, R. G.; Levy, M.; Balduz, J. L., Jr. *Phys. Rev. Lett.* **1982**, *49*, 1691.

(84) Perdew, J. P.; Levy, M. *Physical Review B* **1997**, *56*, 16021.

(85) Katriel, J.; Davidson, E. R. *Proceedings of the National Academy of Sciences* **1980**, *77*, 4403.

(86) Mulliken, R. S. *The Journal of Chemical Physics* **1934**, *2*, 782.

(87) Parr, R. G.; Pearson, R. G. *Journal of the American Chemical Society* **1983**, *105*, 7512.

(88) Politzer, P.; Abu-Awwad, F. *Theor Chem Acc* **1998**, *99*, 83.

(89) Nørskov, J. K.; Abild-Pedersen, F.; Studt, F.; Bligaard, T. *Proceedings of the National Academy of Sciences* **2011**, *108*, 937.

(90) Logadottir, A.; Rod, T. H.; Nørskov, J. K.; Hammer, B.; Dahl, S.; Jacobsen, C. J. H. *Journal of Catalysis* **2001**, *197*, 229.

(91) Lousada, C. M.; Trummer, M.; Jonsson, M. *Journal of Nuclear Materials.*

(92) Paier, J.; Hirschl, R.; Marsman, M.; Kresse, G. *The Journal of Chemical Physics* **2005**, *122*, 234102.

(93) Pessoa, A. M.; Fajín, J. L. C.; Gomes, J. R. B.; Cordeiro, M. N. D. S. *Journal of Molecular Structure: THEOCHEM* **2010**, *946*, 43.

(94) Andersson, M. P.; Stipp, S. L. S. *The Journal of Physical Chemistry C* **2011**, *115*, 10044.

(95) Tosoni, S.; Sauer, J. *Physical Chemistry Chemical Physics* **2010**, *12*, 14330.

(96) Bailey, C. L.; Mukhopadhyay, S.; Wander, A.; Searle, B. G.; Carr, J. M.; Harrison, N. M. *Physical Chemistry Chemical Physics* **2010**, *12*, 6124.

(97) Evarestov, R.; Bredow, T.; Jug, K. *Physics of the Solid State* **2001**, *43*, 1774.

(98) Zhanpeisov, N. U. *Kinetics and Catalysis* **2010**, *51*, 849.

(99) Matthew, N. In *Studies in Surface Science and Catalysis*; Froment, G. F., Waugh, K. C., Eds.; Elsevier: 1997; Vol. Volume 109, p 3.

(100) Diebold, U.; Li, S.-C.; Schmid, M. *Annual Review of Physical Chemistry* **2010**, *61*, 129.

(101) Dahl, S.; Logadottir, A.; Egeberg, R. C.; Larsen, J. H.; Chorkendorff, I.; Törnqvist, E.; Nørskov, J. K. *Phys. Rev. Lett.* **1999**, *83*, 1814.

(102) Jung, J.; Shin, H.-J.; Kim, Y.; Kawai, M. *Journal of the American Chemical Society* **2011**, *133*, 6142.

(103) Gong, X.-Q.; Selloni, A. *Journal of Catalysis* **2007**, *249*, 134.

(104) Liu, Z.-P.; Hu, P. *Journal of the American Chemical Society* **2003**, *125*, 1958.

(105) Santen, R. A.; Neurock, M. *Russ. J. Phys. Chem. B* **2007**, *1*, 261.

(106) Rendulic, K. D. *Appl. Phys. A* **1988**, *47*, 55.

(107) Scamehorn, C. A.; Harrison, N. M.; McCarthy, M. I. *The Journal of Chemical Physics* **1994**, *101*, 1547.

(108) G. Choppin, J. O. L., J. Rydberg *Radiochemistry and nuclear chemistry* second ed.; Butterworth-Heinemann Ltd: Oxford, 1995; Vol. 46.

(109) Bailey, J. E. *Proceedings of the Royal Society of London. Series A, Mathematical and Physical Sciences* **1964**, *279*, 395.

(110) Howard, C. J.; Sabine, T. M.; Dickson, F. *Acta Crystallographica Section B* **1991**, *47*, 462.

(111) Hanic, F.; Hartmanova, M.; Knab, G. G.; Urusovskaya, A. A.; Bagdasarov, K. S. *Acta Crystallographica Section B* **1984**, *40*, 76.

(112) Hochanadel, C. J. *The Journal of Physical Chemistry* **1952**, *56*, 587.

(113) Ghormley, J. A.; Stewart, A. C. *Journal of the American Chemical Society* **1956**, *78*, 2934.

(114) European Standard,: November 1994; Vol. EN 717-2, 1994.

(115) Academies, C. O. F. C. C. F. A. N. B. I. O. M. O. T. N. *Food Chemicals Codex*; Fifth ed.; The National Academies Press: Washington, D. C., Effective January 1, 2004.

(116) LaVerne, J. A.; Tandon, L.; Knippel, B. C.; Montoya, V. M. *Radiation Physics and Chemistry* **2005**, *72*, 143.

(117) Satoh, A. Y.; Trosko, J. E.; Masten, S. J. *Environmental Science & Technology* **2007**, *41*, 2881.

(118) Deák, P. *physica status solidi (b)* **2000**, *217*, 9.

(119) Schrodinger, LLC New York 2010.

(120) Perdew, J. P.; Chevary, J. A.; Vosko, S. H.; Jackson, K. A.; Pederson, M. R.; Singh, D. J.; Fiolhais, C. *Physical Review B* **1992**, *46*, 6671.

(121)Zhao, Y.; Truhlar, D. G. *The Journal of Chemical Physics* **2006**, *125*, 194101.

(122)Reiher, M.; Salomon, O.; Artur Hess, B. *Theor. Chem. Acc.* **2001**, *107*, 48.

(123)Zhao, Y.; Truhlar, D. *Theoretical Chemistry Accounts: Theory, Computation, and Modeling (Theoretica Chimica Acta)* **2008**, *120*, 215.

(124)Zhao, Y.; Truhlar, D. G. *Accounts of Chemical Research* **2008**, *41*, 157.

(125)Grimme, S. *J. Comput. Chem.* **2006**, *27*, 1787.

(126)Xu, X.; Nakatsuji, H.; Ehara, M.; Lu, X.; Wang, N. Q.; Zhang, Q. E. *Chemical Physics Letters* **1998**, *292*, 282.

(127)Lü, X.; Xu, X.; Wang, N.; Zhang, Q.; Ehara, M.; Nakatsuji, H. *Chemical Physics Letters* **1998**, *291*, 445.

(128)Dunford, H. B. *Coordination Chemistry Reviews* **2002**, *233–234*, 311.

(129)Hiroki, A.; LaVerne, J. A. *The Journal of Physical Chemistry B* **2005**, *109*, 3364.

(130)Suh, M.; Bagus, P. S.; Pak, S.; Rosynek, M. P.; Lunsford, J. H. *The Journal of Physical Chemistry B* **2000**, *104*, 2736.

(131)Sunder, S.; Miller, N. H.; Shoesmith, D. W. *Corrosion Science* **2004**, *46*, 1095.

(132)Lin, C. C.; Smith, F. R.; Ichikawa, N.; Baba, T.; Itow, M. *International Journal of Chemical Kinetics* **1991**, *23*, 971.

(133)E. T. Denisov, T. G. D., T. S. Pokidova *Handbook of Free Radical Initiators*; John Wiley & Sons, Inc: Hoboken, NJ., April 2003.

(134)Takagi Junichi, I. K. *Nuclear science and engineering* **1985**, *89*, 177

(135)Anpo, M.; Che, M.; Fubini, B.; Garrone, E.; Giamello, E.; Paganini, M. *Topics in Catalysis* **1999**, *8*, 189.

(136)McKay, D. J.; Wright, J. S. *Journal of the American Chemical Society* **1998**, *120*, 1003.

(137)Shimanouchi, T.; NSRDS-NBS 5: 1967.

(138)*Handbook of free radical initiators*; Denisov, E. T., Denisova, T. G., & Pokidova, T. S., Ed. Hoboken, NJ, 2003.

(139)Chen, L.; Fleming, P.; Morris, V.; Holmes, J. D.; Morris, M. A. *The Journal of Physical Chemistry C* **2010**, *114*, 12909.

(140)Anders Nilsson, L. G. M. P., Jens K. Nørskov *Chemical Bonding at Surfaces and Interfaces*; Elsevier: Amsterdam, 2008.

(141)Kosmulski, M. *J. Dispersion Sci. Technol.* **2002**, *23*, 529.

(142)Chirita, P. *Chem. Biochem. Eng. Q.* **2009**, *23*, 259.

(143)M. Murphy, D.; W. Griffiths, E.; C. Rowlands, C.; E. Hancock, F.; Giamello, E. *Chemical Communications* **1997**, 2177.

(144)Croiset; E.; Rice; F., S.; Hanush; G., R. *Hydrogen peroxide decomposition in supercritical water*; Wiley-Blackwell: Hoboken, NJ, ETATS-UNIS, 1997; Vol. 43.

(145)Haber, F.; Weiss, J. *Naturwissenschaften* **1932**, *20*, 948.

(146)Henrich, V. E.; Casey, W. H.; Clark, D. L.; Eggleston, C.; Felmy, A.; Goodman, D. W.; Graetzel, M.; Maciel, G.; McCarthy, M. I.; Nealson, K. H.; Sverjensky, D. A.; Toney, M. F.; Zachara, J. M. *Chemical Reviews* **1999**, *99*, 77.

(147)Amorelli, A.; Evans, J. C.; Rowlands, C. C. *Journal of the Chemical Society, Faraday Transactions 1: Physical Chemistry in Condensed Phases* **1988**, *84*, 1723.

(148)Kitajima, N.; Fukuzumi, S.; Ono, Y. *The Journal of Physical Chemistry* **1978**, *82*, 1505.

(149)Giamello, E.; Calosso, L.; Fubini, B.; Geobaldo, F. *The Journal of Physical Chemistry* **1993**, *97*, 5735.

(150)Rhodes, C. J. *Progress in Reaction Kinetics and Mechanism* **2005**, *30*, 145.

(151)Nash, T. *Biochem. J.* **1953**, *55*, 416.

(152) Li, Q.; Sritharathikhun, P.; Motomizu, S. *Analytical Sciences* **2007**, *23*, 413.

(153) Denisova, T.; Denisov, E. *Kinetics and Catalysis* **2006**, *47*, 121.

(154) Busca, G.; Lamotte, J.; Lavalley, J. C.; Lorenzelli, V. *Journal of the American Chemical Society* **1987**, *109*, 5197.

(155) Buxton, G. V.; Greenstock, C. L.; Helman, W. P.; Ross, A. B. *Journal of Physical and Chemical Reference Data* **1988**, *17*, 513.

(156) Hicks, M.; Gebicki, J. M. *FEBS Letters* **1986**, *199*, 92.

(157) Diesen, V.; Jonsson, M. *Journal of Advanced Oxidation Technologies* **2013**, *16*, 16.

(158) Pehrman, R.; Trummer, M.; Lousada, C. M.; Jonsson, M. *Journal of Nuclear Materials* **2012**, *430*, 6.

(159) Ekeroth, E.; Jonsson, M. *Journal of Nuclear Materials* **2003**, *322*, 242.

(160) Jonsson, M.; Ekeroth, E.; Roth, O. 2004; Vol. 807, p 77.

(161) Nilsson, S.; Jonsson, M. *Journal of Nuclear Materials* **2011**, *410*, 89.

(162) Lucuta, P. G.; Verrall, R. A.; Matzke, H.; Palmer, B. J. *Journal of Nuclear Materials* **1991**, *178*, 48.

(163) Casarin, M.; Maccato, C.; Vittadini, A. *Physical Chemistry Chemical Physics* **1999**, *1*, 3793.

(164) Zhao, J.; Zhao, F.; Xu, S.; Ju, X. *The Journal of Physical Chemistry A* **2013**.

(165) Zong, Z.; Ma, Y.; Hu, T.; Cui, G.; Cui, Q.; Zhang, M.; Zou, G. *Solid State Communications* **2011**, *151*, 607.

(166) Christensen, A.; Carter, E. A. *Physical Review B* **1998**, *58*, 8050.

(167) Ahlswede, B.; Homann, T.; Jug, K. *Surface Science* **2000**, *445*, 49.

(168) Lu, A.-H.; Salabas, E. L.; Schüth, F. *Angewandte Chemie International Edition* **2007**, *46*, 1222.

(169) Ushakov, S. V.; Navrotsky, A. *Applied Physics Letters* **2005**, *87*, 164103.

(170) Radha, A. V.; Bomati-Miguel, O.; Ushakov, S. V.; Navrotsky, A.; Tartaj, P. *Journal of the American Ceramic Society* **2009**, *92*, 133.

(171) Raz, S.; Sasaki, K.; Maier, J.; Riess, I. *Solid State Ionics* **2001**, *143*, 181.

(172) Iskandarova, I. M.; Knizhnik, A. A.; Rykova, E. A.; Bagatur'yants, A. A.; Potapkin, B. V.; Korkin, A. A. *Microelectronic Engineering* **2003**, *69*, 587.

(173) Okamoto, Y. *Applied Surface Science* **2008**, *255*, 3434.

(174) Haase, F.; Sauer, J. *Journal of the American Chemical Society* **1998**, *120*, 13503.

(175) Egashira, M.; Kawasumi, S.; Kagawa, S.; Seiyama, T. *Bull. Chem. Soc. Jpn.* **1978**, *51*, 3144.

(176) Vittadini, A.; Selloni, A.; Rotzinger, F. P.; Grätzel, M. *Physical Review Letters* **1998**, *81*, 2954.

(177) Hussain, A.; Gracia, J.; Nieuwenhuys, B. E.; Niemantsverdriet, J. W. *ChemPhysChem* **2010**, *11*, 2375.

(178) Hammer, B.; Wendt, S.; Besenbacher, F. *Topics in Catalysis* **2010**, *53*, 423.

(179) Huang, W. F.; Raghunath, P.; Lin, M. C. *J. Comput. Chem.* **2011**, *32*, 1065.

(180) Zhang, P.; Navrotsky, A.; Guo, B.; Kennedy, I.; Clark, A. N.; Lesher, C.; Liu, Q. Y. *J. Phys. Chem. C* **2008**, *112*, 932.

(181) Gorelov, B. M.; Morozovskaya, D. V.; Pashkov, V. M.; Sidorchuk, V. A. *Tech. Phys.* **2000**, *45*, 1147.

(182) Rittner, F.; Boddenberg, B.; Fink, R. F.; Staemmler, V. *Langmuir* **1998**, *15*, 1449.

(183) Rittner, F.; Fink, R.; Boddenberg, B.; Staemmler, V. *Physical Review B* **1998**, *57*, 4160.

(184) Brugh, D. J.; Suenram, R. D.; Stevens, W. J. *The Journal of Chemical Physics* **1999**, *111*, 3526.

(185)Li, S.; Dixon, D. A. *The Journal of Physical Chemistry A* **2010**, *114*, 2665.

(186)Merle-Méjean, T.; Barberis, P.; Othmane, S. B.; Nardou, F.; Quintard, P. E. *Journal of the European Ceramic Society* **1998**, *18*, 1579.

(187)Korhonen, S. T.; Calatayud, M.; Krause, A. O. I. *The Journal of Physical Chemistry C* **2008**, *112*, 6469.

(188)Weibel, M. A.; Backstrand, K. M.; Curtiss, T. J. *Surface Science* **2000**, *444*, 66.

(189)Nilsson, A.; Pettersson, L. G. M. In *Chemical Bonding at Surfaces and Interfaces*; Elsevier: Amsterdam, 2008, p 57.

(190)Riley, K. E.; Hobza, P. *Wiley Interdisciplinary Reviews: Computational Molecular Science* **2011**, *1*, 3.

(191)Johansson, A. J.; Zuidema, E.; Bolm, C. *Chemistry – A European Journal* **2010**, *16*, 13487.

(192)Casarin, M.; Maccato, C.; Vittadini, A. *Applied Surface Science* **1999**, *142*, 196.

(193)Issa, M. A. A.; Molokhia, N. M.; Dughaish, Z. H. *J. Phys. D-Appl. Phys.* **1983**, *16*, 1109.

(194)Jayaram, G.; Krishnan, V. G. *Physical Review B* **1995**, *51*, 1294.

(195)Balducci, G.; Gigli, G.; Guido, M. *J. Chem. Phys.* **1985**, *83*, 1909.

(196)Murad, E.; Hildenbrand, D. L. *J. Chem. Phys.* **1975**, *63*, 1133.

(197)Brezova, V.; Stasko, A.; Biskupic, S.; Blazkova, A.; Havlinova, B. *J. Phys. Chem.* **1994**, *98*, 8977.

(198)A. van Santen, R.; Neurock, M. *Molecular Heterogeneous Catalysis: A Conceptual and Computational Approach*; WILEY-VCH Verlag GmbH & Co. KGaA: Weinheim, 2006.

(199)Haynes, W. M.; Lide, D. R. *CRC handbook of chemistry and physics : a ready-reference book of chemical and physical data*; CRC Press: Boca Raton, Fla., 2011.

(200)Alpert, S. M.; Knappe, D. R. U.; Ducoste, J. J. *Water Research* **2010**, *44*, 1797.

(201)Becker, T.; Hövel, S.; Kunat, M.; Boas, C.; Burghaus, U.; Wöll, C. *Surface Science* **2001**, *486*, L502.

(202)Doh, W. H.; Roy, P. C.; Kim, C. M. *Langmuir* **2010**, *26*, 16278.

(203)Bang, J.; Chang, K. J. *Applied Physics Letters* **2008**, *92*, 132109.

(204)Johansson, A. J.; Lilja, C.; Brinck, T. *The Journal of Chemical Physics* **2011**, *135*, 084709.

(205)Menetrey, M.; Markovits, A.; Minot, C. *Surface Science* **2003**, *524*, 49.

(206)Johnson, J. R. T.; Panas, I. *Inorganic Chemistry* **2000**, *39*, 3181.

(207)Ahdjoudj, J.; Minot, C. *Surface Science* **1998**, *402-404*, 104.

(208)Thetford, A.; Hutchings, G. J.; Taylor, S. H.; Willock, D. J. *Proceedings of the Royal Society A: Mathematical, Physical and Engineering Science* **2011**, *467*, 1885.

(209)Jensen, W. B. *Journal of Chemical Education* **1996**, *73*, 11.

(210)*CRC, Handbook of Chemistry and Physics*; 78 ed.; CRC Press: Cleveland, OH, 1997.

(211)Eisenstein, O.; Maron, L. *Journal of Organometallic Chemistry* **2002**, *647*, 190.

(212)Luo, Y.; Selvam, P.; Koyama, M.; Kubo, M.; Miyamoto, A. *Chemistry Letters* **2004**, *33*, 780.

(213)Bassan, A.; Blomberg, M. R. A.; Siegbahn, P. E. M.; Que, L. *Journal of the American Chemical Society* **2002**, *124*, 11056.

(214)van Santen, R. A.; Neurock, M. *Catalysis by Oxides and Sulfides*; Wiley-VCH Verlag GmbH & Co. KGaA, 2007.

(215)*Phys. Chem. Chem. Phys., DOI:10.1039/C3CP44559C.*

(216)Xiaoyan, C.; Michael, D. *Molecular Physics* **2003**, *101*, 2427.

(217)Pantazis, D. A.; Neese, F. *Journal of Chemical Theory and Computation* **2009**, *5*, 2229.

(218)Szabo, A. O., N. S. *Modern Quantum Chemistry*; Drover: Mineola, New York, 1996.

(219)Meadows, J. H.; Schaefer, H. F. *Journal of the American Chemical Society* **1976**, *98*, 4383.

(220)Cramer, C. J. *Essentials of Computational Chemistry: Theories and Models*; 2nd ed.; Wiley: West Sussex, UK, 2004.

(221)Hohenberg, P.; Kohn, W. *Physical Review* **1964**, *136*, B864.

(222)Kohn, W.; Sham, L. J. *Physical Review* **1965**, *140*, A1133.

(223)Sholl, D. S.; Steckel, J. A. In *Density Functional Theory*; John Wiley & Sons, Inc.: 2009, p i.

(224)Capelle, K.

(225)Ceperley, D. M.; Alder, B. J. *Phys. Rev. Lett.* **1980**, *45*, 566.

(226)Perdew, J. P.; Ruzsinszky, A.; Tao, J.; Staroverov, V. N.; Scuseria, G. E.; Csonka, G. I. *The Journal of Chemical Physics* **2005**, *123*, 062201.

(227)Shi, J. M.; Peeters, F. M.; Hai, G. Q.; Devreese, J. T. *Physical Review B* **1991**, *44*, 5692.

(228)Becke, A. D. *The Journal of Chemical Physics* **1992**, *96*, 2155.

(229)Hammer, B.; Scheffler, M. *Phys. Rev. Lett.* **1995**, *74*, 3487.

(230)Philipsen, P. H. T.; te Velde, G.; Baerends, E. J. *Chemical Physics Letters* **1994**, *226*, 583.

(231)Ozoliņš, V.; Körling, M. *Physical Review B* **1993**, *48*, 18304.

(232)Filippi, C.; Singh, D. J.; Umrigar, C. J. *Physical Review B* **1994**, *50*, 14947.

(233)Scuseria, G. E.; Staroverov, V. N. In *Theory and Applications of Computational Chemistry*; Clifford, E. D., Gernot, F., Kwang, S. K., Gustavo E. ScuseriaA2 - Clifford E. Dykstra, G. F. K. S. K., Gustavo, E. S., Eds.; Elsevier: Amsterdam, 2005, p 669.

(234)Moskowitz, J. W.; Topiol, S.; Snyder, L. C.; Ratner, M. A. *International Journal of Quantum Chemistry* **1981**, *19*, 131.

(235)Sahu, P. K.; Chaudhari, A.; Lee, S.-L. *Chemical Physics Letters* **2004**, *386*, 351.

(236)Sahu, P. K.; Chaudhari, A.; Lee, S.-L. *Chemical Physics Letters* **2004**, *393*, 284.

(237)Schultz, N. E.; Truhlar, D. G. *Journal of Chemical Theory and Computation* **2004**, *1*, 41.

I

Kinetics, Mechanism, and Activation Energy of H₂O₂ Decomposition on the Surface of ZrO₂

Cláudio M. Lousada* and Mats Jonsson

KTH Chemical Science and Engineering, Nuclear Chemistry, Royal Institute of Technology, SE-100 44 Stockholm, Sweden

The kinetics, mechanism, and activation energy of H_2O_2 decomposition in ZrO_2 particle suspensions were studied. The obtained first-order and second-order rate constants for the decomposition of H_2O_2 in the presence of ZrO_2 at $T = 298.15$ K produced the values $k_1 = (6.15 \pm 0.04) \times 10^{-5}$ s^{-1} and $k_2 = (2.39 \pm 0.09) \times 10^{-10}$ m·s^{-1}, respectively. The dependency of the reaction first-order rate constant with temperature was studied; consequently, the activation energy for the reaction was obtained in the temperature interval 294.15–353.15 K having yielded the value $E_a = 33 \pm 1.0$ kJ·mol^{-1}. The dependency of the zeroth-order reaction rate constant with pH was investigated and discussed. A mechanistic study encompassing the investigation of the dynamics of formation of hydroxyl radicals during the course of the reaction was performed. A version of the modified Hantzsch method was applied for this purpose, and it was verified that the dynamics of formation of hydroxyl radicals during the reaction are in good agreement with the proposed reaction mechanism.

1. Introduction

Zirconium dioxide, mostly known as zirconia, is one of the most versatile ceramic materials known. Its physical and chemical properties make it suitable for a wide range of applications including nanotechnology,[1] catalysis and synthesis,[2-5] medicine,[6] electronics and sensors,[7] and the manufacture of a diversity of materials.[8] The fact that its radiation stability is good,[9] it has a low neutron cross section, and it has low solubility in water at high temperatures[10] makes it presently a main favored candidate to be a component of the inert fuel matrix in nuclear reactors.[11] The presence of zirconium dioxide in nuclear systems is not only restricted to its incorporation into the fuel matrix. The fuel material in a nuclear reactor is protected by cladding pipes made of alloyed zirconium. In contact with water near and above its critical temperature, a corrosion layer of hydrated zirconium dioxide $ZrO_2 \cdot nH_2O$ is formed and has implications on the chemistry of the reactor.[12-14] One of the most important water radiolysis products to concern about in reactor chemistry is hydrogen peroxide.[15] Hydrogen peroxide is an important compound that has found innumerous uses such as a bleaching agent,[16] disinfectant,[17] oxidizer,[18] or as a nontoxic monopropellant in rocket fuel.[19] Hydrogen peroxide is the main oxidizing molecular product formed during the radiolysis of water. It is formed primarily by combination reactions of HO radicals produced in the radiolytic decomposition of water. Its importance due to an increase in its concentration is augmented under conditions subjected to radiation with high linear energy transfer, as in an operating nuclear power plant,[20] where ~2% of the total fast neutrons and γ-ray energy released in the core of an operating nuclear reactor is deposited in the cooling water[21] or under conditions of storage of spent nuclear fuel.[22] The importance of the system ZrO_2/H_2O_2 lead us to develop a study on the dynamics, energetics, and mechanism of the reaction between these two chemical species.

It was previously reported that the reaction of H_2O_2 on the surface of ZrO_2 in liquid water consists of the decomposition of H_2O_2 to produce water and oxygen. Given that the zirconium in ZrO_2 is in its highest oxidation state, no redox reactions are involved in the process. This metal-oxide-catalyzed reaction is proposed to follow the scheme[23]

$$H_2O_2 + M \rightarrow 2HO^{\cdot} + M \quad \text{(R1)}$$

$$HO^{\cdot} + H_2O_2 \rightarrow HO_2^{\cdot} + H_2O \quad \text{(R2)}$$

$$2HO_2^{\cdot} \rightarrow H_2O_2 + O_2 \quad \text{(R3)}$$
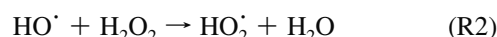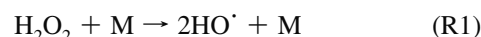
where M represents an undefined site located at the oxide surface. The decomposition of hydrogen peroxide on a solid surface is a spontaneous process at temperatures that range from room temperature to 286 °C, and its reported activation energy ranges from 20.93 to 96.30 kJ·mol^{-1}, depending on the surface type and on factors such as the oxidation state of the metal, among others.[24] Reaction R3 corresponds to the chain termination and occurs via the disproportionation of two hydroperoxyl radicals as represented. When reaction R3 occurs with pure water as a solvent, the activation energy is 25.0 kJ·mol^{-1} in the temperature range 274–316 K.[25]

The evaluation of the effect of zirconium dioxide on the kinetics and energetics of decomposition of hydrogen peroxide has to be done at a temperature and pH range where the spontaneous uncatalyzed decomposition of hydrogen peroxide is negligible when compared with the rate of decomposition of hydrogen peroxide on the surface of the oxide itself. In neutral water, from the species involved in the reactions mentioned above, only dissociation of $HO_2^{\cdot}$ needs to be considered because the pK_a values for H_2O_2, $HO^{\cdot}$, and $HO_2^{\cdot}$ are 11.8, 11.9, and 4.88, respectively.[26] The $HO_2^{\cdot}$ hydroperoxyl radical is a weak acid and is also the protonated form of the superoxide radical anion which is easily formed and sorbed at the surface of the zirconium dioxide according to the following reaction[27]

$$HO_2^{\cdot} \xrightarrow{ZrO2} H^+ + O_2^{-\cdot} \quad \text{(R4)}$$
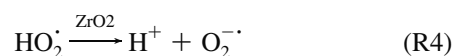
The superoxide anion radical is stabilized by adsorption on the surface of the zirconium dioxide and has been used

* To whom correspondence should be addressed. Tel: (46) 8 790 87 89. Fax: (46) 8 790 87 72. E-mail: cmlp@kth.se.

H$_2$O$_2$ Decomposition on the Surface of ZrO$_2$

J. Phys. Chem. C, Vol. 114, No. 25, 2010 **11203**

previously as a probe for surface cationic fields. The superoxide radical adsorbs to the surface exclusively by coordination with exposed Zr^{4+} surface sites.[27] The superoxide radical anion is in many cases a precursor of the highly reactive hydroxyl radical following a Fenton-type mechanism in systems where the metal cation can undergo further stages in oxidation.[28] The formed superoxide anion radical is an active reductive species and can reduce ions in the higher valence state, for example[25]

$$O_2^{-\cdot} + Fe^{3+} \rightarrow O_2 + Fe^{2+} \qquad (R5)$$
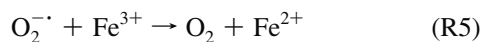
The rate constant for the reaction of the hydroxyl radical with organic molecules ranges from $\sim 4 \times 10^6$ to 2×10^{11} M$^{-1}\cdot$s^{-1}.[29] The surface of the oxide is capable of stabilizing the intermediary radical species formed during the decomposition of H$_2$O$_2$ by means of interactions of the formed radicals with the oxide lattice.[27,30] As shown above, the proposed mechanism of the reaction of decomposition of hydrogen peroxide on the surface of an oxide that cannot undergo further oxidation is rather complex and has not been clearly elucidated. In this work, the reaction of H$_2$O$_2$ in the presence of ZrO$_2$ was studied at different temperatures and pH values. A mechanistic study was also performed and consisted of developing a method to study the dynamics of formation of the intermediary radical species during the decomposition of H$_2$O$_2$ at the surface of ZrO$_2$. A study involving water radiolysis in the presence of tris/HCl buffer allowed us to calibrate the method cited above and consequently to quantify the rate of formation of HO radicals during the reaction of H$_2$O$_2$ in the presence of ZrO$_2$.

2. Experimental Details

Instrumentation. Specific surface areas of the powders were determined using the BET method of isothermal adsorption and desorption of a gaseous mixture consisting of 30% N$_2$ and 70% He on a Micrometrics Flowsorb II 2300 instrument. γ-Irradiation was performed using a MDS Nordion 1000 Elite Cs-137 γ-source with a dose rate of 0.15 Gy$\cdot$s^{-1}; this value was determined by Fricke dosimetry.[31] X-ray powder diffractograms (XRD) were obtained at 293 K using Cu Kα radiation, on a PANanalytical X'pert instrument. Powders were encapsulated on Lindemann capillaries. The data was collected over the range $3 \leq 2\theta \leq 80°$ with a step size of 0.033° (2θ). Data evaluation was done using The High Score Plus software package, and the PDF-2 database was used for matching the experimentally obtained diffractograms. The samples were weighted to $\pm 10^{-5}$ g, in a Mettler Toledo AT261 Delta Range microbalance. The reactions were performed under an inert atmosphere with a constant flux of N$_2$ gas (AGA Gas AB) with a flow rate of 0.21 L$\cdot$min^{-1} that was also used for stirring the solutions. We kept the temperature constant throughout the experiments by using a Huber CC1 or a Lauda E100 thermostat calibrated against a Therma 1 thermometer coupled to a submersible K-type (NiCrNi) temperature probe with a precision of ± 0.1 K. UV/vis spectra were collected using a WPA Lightwave S2000 or a WPA Biowave II UV/vis spectrophotometer. Trace elemental analysis were performed using the technique of inductively coupled plasma spectroscopy on a Thermo Scientific iCAP 6000 series ICP spectrometer. The analysis for Zr was performed at the wavelength of 343.823 nm.

Reagents and Experiments. All solutions used in this study were prepared using water from a Millipore Milli-Q system.

Zirconium dioxide (CAS[1314-23-4], Aldrich 99%, particle size <5 μm) was used without further purification. The powder pattern was indexed as monoclinic. A Rietveld refinement using ICSD-26488 as a starting model was performed yielding the

following cell parameters: (a) 5.1458(2), (b) 5.2083(3), and (c) 5.3124(3) Å. These values are in good agreement with (a) 5.143, (b) 5.204, and (c) 5.311 Å attributed to the monoclinic phase and published in a previous work.[32] The specific surface area of the ZrO$_2$ powder, measured by the BET method produced the value of 5.0 ± 0.2 m$^2\cdot$g^{-1}. This value is the average of three measurements, each one consisting of a sorption and a desorption isotherm whose values were also averaged. The ZrO$_2$ particle suspensions, where the reaction with H$_2$O$_2$ (CAS[7722-84-1]) took place, consisted of 0.5–4.5 g of ZrO$_2$ in 50 mL of H$_2$O$_2$ solution with a H$_2$O$_2$ concentration that varied from 0.5 mM to 6 mM. The H$_2$O$_2$ solutions were prepared from a 30% standard solution (Merck). After extraction of the sample from the reaction vessel, the sample was filtered through a Gamma Medical 0.45 μm to 25 mm cellulose acetate syringe filter. Subsequently a sample volume of 0.2 mL was used for the measurement of hydrogen peroxide concentration. The concentration of hydrogen peroxide as a function of reaction time was then determined by the Ghormley triiodide method. In this method, I$^-$ is oxidized to I$_3^-$ by the H$_2$O$_2$.[33,34] The absorbance of the product I$_3^-$ was measured spectrophotometrically at the wavelength of 360 nm. A calibration curve where the absorbance of I$_3^-$ was plotted as a function of the concentration of hydrogen peroxide was obtained in the range of concentrations 0.02 to 0.8 mM in H$_2$O$_2$, resulting in a linear correlation between absorbance and concentration. A mechanistic study of the decomposition of H$_2$O$_2$ on the surface of ZrO$_2$ was carried out and involved verifying the presence and quantifying the rate of production of hydroxyl radicals as intermediate product in the reaction of decomposition of H$_2$O$_2$ on the surface of ZrO$_2$. This was done by means of the reaction between tris(hydroxymethyl)aminomethane (tris buffer) (CAS[77-86-1], BDH Chemicals 99%) and the hydroxyl radicals to produce formaldehyde.[35] In this study, the reaction between ZrO$_2$ particle suspensions and H$_2$O$_2$ was performed at temperatures that ranged from 293.15 to 313.15 K at the midpoint of the buffering range of the tris buffer. The reaction mixture consisted of 0.5–4.5 g of ZrO$_2$ in 50 mL solution of 0.5–6.0 mM in H$_2$O$_2$ and 0.5–20 mM in tris buffer at a pH of 7.5; the pH was adjusted with HCl. The formaldehyde produced was then quantified spectrophotometrically at 368 nm using a modified version of the Hantzsch reaction.[36] In this method, the formaldehyde reacted with acetoacetanilide AAA (CAS[102-01-2], Alfa Aesar >98%) in the presence of ammonium acetate (CAS[631-61-8], Lancaster 98%) to form a dihydropyridine derivative, which has the maximum absorption wavelength at 368 nm. A calibration curve plotting the absorbance of the dihydropyridine derivative as a function of formaldehyde concentration was obtained at 368 nm, giving a linear correlation between absorbance and concentration in the concentration range 0.15 μM to 1 mM in formaldehyde. The plotting of the calibration curve for formaldehyde required the preparation of several solutions of CH$_2$O with different rigorously known concentrations in the concentration range mentioned above. It was then necessary to proceed to the accurate determination of the concentration of formaldehyde in the solution used initially (CAS[50-00-0], Aldrich 37 wt % in H$_2$O) using the iodometric method.[37] The solutions and respective standardizations necessary to follow the iodometric method procedure were prepared as stated in the cited paper[37] and as described elsewhere.[38] The error associated with the determination of the concentration of formaldehyde in the initial solution was <2%.
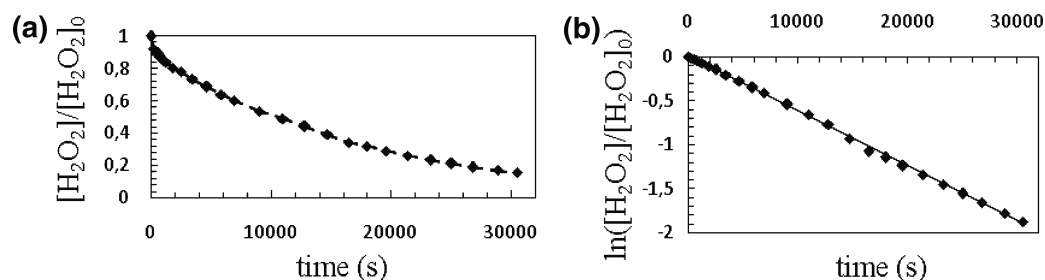
Figure 1. (a) Concentration of hydrogen peroxide as a function of reaction time at $T = 298.15$ K. Initially, 0.5 mM in H_2O_2 and 1.5 g of ZrO_2 in 50 mL of H_2O. (b) $\ln([H_2O_2]/[H_2O_2]_0)$ as a function of reaction time for $T = 298.15$ K.

3. Results and Discussion

Kinetics of H_2O_2 Decomposition on the Surface ZrO_2. It has been previously reported that the catalytic decomposition of hydrogen peroxide follows first-order kinetics with respect to H_2O_2.[39−41] In the presence of a solid, the reaction can be approached to a pseudo-first-order when an excess of solid substance is present. Given this fact, and considering reaction R1, one can expect that the concentration of H_2O_2 evolves as a function of time according to

$$\frac{-d[H_2O_2]}{dt} = k_1[H_2O_2], \quad \text{which in its integrated form,}$$

$$\ln\left(\frac{[H_2O_2]}{[H_2O_2]_o}\right) = -k_1 t \quad (6)$$

where t is the reaction time, k_1 is the pseudo-first-order rate constant at a given temperature, $[H_2O_2]$ is the concentration of H_2O_2 at a time, t, and $[H_2O_2]_o$ is the concentration of H_2O_2 at $t = 0$.

The set of data obtained for the variation in the concentration of hydrogen peroxide at $T = 298.15$ K as a function of reaction time is represented in Figure 1a. Previous test reactions with concentrations in hydrogen peroxide ranging from 0.5−6.0 mM in H_2O_2 and 0.5−4.5 g of ZrO_2, in 50 mL of solution showed that the concentration in H_2O_2 and the amount of ZrO_2 that provided better conditions for error minimization caused by too short reaction time or by a large number of dilutions for further concentration measurement was the value of 0.5 mM in H_2O_2 and 1.5 g of ZrO_2. The first-order rate constant obtained from the slope in Figure 1b for the temperature $T = 298.15$ K is $k_1 = (6.15 \pm 0.04) \times 10^{-5}$ s^{-1}. We determined the second-order rate constant by studying the pseudo-first-order rate constant as a function of solid-surface-area-to-solution volume ratio. The second-order rate expression is given by

$$\frac{-d[H_2O_2]}{dt} = k_2\left(\frac{SA_{ZrO_2}}{V}\right)[H_2O_2] \quad (7)$$

where SA_{ZrO_2} denotes the surface area of the zirconium dioxide powder, V is the volume of the solution where the reaction takes place, and k_2 is the second-order rate constant. The first-order rate constant is plotted against surface-area-to-solution volume ratio in Figure 2. The second-order rate constant obtained from the slope of Figure 2 for the reaction at 293.15 K is $k_2 = (2.39 \pm 0.09) \times 10^{-10}$ m·s^{-1}. As expected, this value is very far from a diffusion controlled reaction for which the rate constant is on the order of 10^{-5} m·s^{-1} for particles of this size.[42]

The variation of the rate constant with temperature generally follows the Arrhenius equation

$$k_1 = Ae^{-E_a/RT} \quad (8)$$

where E_a is the activation energy for the reaction, A is the pre-exponential or the frequency factor, R is the gas constant, and
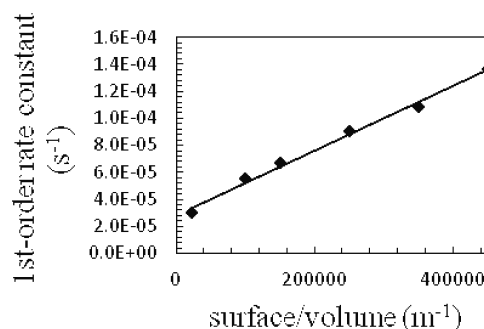

Figure 2. First-order rate constant as a function of the ZrO_2 surface-area-to-solution volume ratio obtained at a temperature of 298.15 K and with a initial concentration of 0.5 mM in H_2O_2 in a volume of 50 mL.
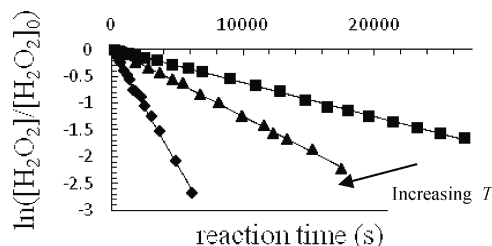

Figure 3. $\ln([H_2O_2]/[H_2O_2]_0)$ as a function of reaction time for $T = 298.15$, 313.15, and 353.15 K.

T is the absolute temperature. To determine the activation energy for the reaction, we obtained the rate constants as a function of temperature in the temperature interval $T = [294.15−353.15]$ K with a temperature step of 5 K. Some of the resulting first-order plots are represented in Figure 3. The plots of $\ln([H_2O_2]/[H_2O_2]_0)$ as a function of reaction time show good agreement with first-order kinetic behavior; the order of the reaction with respect to H_2O_2 was confirmed by obtaining initial rates with different initial concentrations of H_2O_2 while keeping the amount of ZrO_2 constant. A plot of $\ln$(initial reaction rate) as a function of $\ln$(concentration of H_2O_2) was obtained at $T = 313.15$ K, for a mass of ZrO_2 equal to 1.5 g and concentrations in H_2O_2 that ranged from 0.5 to 6 mM. A linear regression of the obtained data yielded a slope of 0.98 ± 0.04. Considering the experimental error associated with this value, it is possible to say that the reaction is first-order with respect to H_2O_2. Because the intercept of this plot is equal to $\ln k_1$, this value corresponds to a k_1 value of $(2.02 \pm 0.09) \times 10^{-4}$ s^{-1}, which differs by less than a factor of two from the first-order rate constant obtained at this same temperature by the standard method, $k_1 = (1.22 \pm 0.13) \times 10^{-4}$ s^{-1}.

For each temperature value, three experiments were performed, and the resulting rate constants were averaged for the calculation of the activation energy. The logarithm of the rate constants as a function of the inverse of the temperature, obtained in the temperature interval mentioned above, are
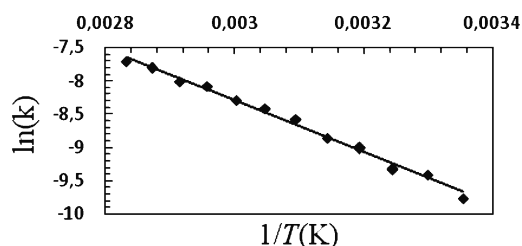
Figure 4. $\ln(k)$ as a function of $1/T$ (K) for $T = [294.15-353.15]$ K with a temperature step of 5 K.

represented in Figure 4. As can be seen, the rate constant is largely affected by the temperature, displaying Arrhenius behavior. The rate constant varied from $(5.670 \pm 0.003) \times 10^{-5}$ to $(4.50 \pm 0.01) \times 10^{-4}$ s^{-1}, when the temperature varied from 298.15 to 353.15 K, respectively. The half-life varied from 198.0 min for the reaction at 298.15 K to 26.3 min for the reaction at 353.15 K. The determined activation energy for the decomposition reaction of hydrogen peroxide at the surface of zirconium dioxide in the temperature range $T = [298.15-353.15]$ K is 33 $\pm$ 1.0 kJ·mol^{-1}. This value is in good agreement with previously published values for similar systems.[24] When comparing this value with the energy necessary for the cleavage of the O—O bond in H₂O₂,[43] 208 kJ·mol^{-1}, it is obvious that the oxide—liquid interface lowers the energy barrier for its cleavage substantially.

To verify the fact that zirconium dioxide acts only as a catalytic support for the decomposition of the hydrogen peroxide and has no further involvement in the reaction, a study of possible changes in the surface area of the powder was performed prior to immersion in water, after immersion in water during a time interval equal to the reaction time and after reaction with hydrogen peroxide. Prior to the BET specific surface area determination, the solid was dried in vacuum at $T = 353.15$ K and $P = 0.1$ Pa; the data obtained are summarized in Table 1. As can be seen, no changes occurred in the specific surface area of the solid during the reaction with hydrogen peroxide. We studied a possible change in the crystal structure of the powder by obtaining XRD diffractograms before and after reaction. Prior to the collection of the XRD diffractogram, the reaction between ZrO₂ and H₂O₂ was performed in 50 mL of H₂O with 0.5 mM H₂O₂ at $T = 298.15$ K until complete consumption of H₂O₂, which implied a reaction time of around 13 h. The obtained cell parameters (a) 5.1497(7), (b) 5.2123(7), and (c) 5.3164(8) Å are in excellent agreement with the ones obtained before the reaction took place. This is an indicator that no change occurred in the crystal structure of the powder in the course of the reaction. We investigated the possible reduction of Zr(IV) in the powder by means of the O₂$^{-\cdot}$ according to reaction R5 and the subsequent release of zirconium in the solution where the reaction took place by measuring possible traces of elemental zirconium in solution using inductively coupled plasma spectroscopy (ICP). A blank measurement was previously performed on a sample from a suspension consisting of 1.5 g of zirconium dioxide in 50 mL of water and from which the solid particles were filtered after a time of exposure in the solution that matched the reaction

time. The measurement to track the amount of zirconium released during reaction was made after the reaction with H₂O₂ reached the end point, corresponding to complete consumption of the hydrogen peroxide initially present. The ICP spectroscopic measurement was performed after filtration of the solid particles from the reactant solution, following a similar procedure and the same conditions as the blank experiment. The measured increase in concentration of Zr in solution after the reaction was $(9.1 \pm 0.2) \times 10^{-8}$ mol·dm^{-3}. When comparing the amount of zirconium in solution and the amount of hydrogen peroxide present that had reacted, one can conclude that the obtained value for the concentration of zirconium in solution is negligible, and reaction R5, even if it would occur as a side reaction, would have very little importance to the overall process in this system. However, the occurrence of reaction R5 causing a change in the oxidation state of Zr(IV) to other state besides Zr(0) could be thought to occur. The implication of the occurrence of this reaction in the crystal structure of the solid would be to create a defect in the lattice by the replacement of a Zr(IV) atom by a Zr atom in a different oxidation state and consequent rearrangement of oxygen atoms to compensate for the non-neutrality in terms of the overall charge of the new created lattice. This would translate in different cell parameters before and after reaction. This is not observed, and so the reduction of zirconium by superoxide anion radical is not detectable in this system.

In general, a continuously cycling surface catalyzed reaction can be broken down into a short sequence of steps as follows:[44]

SCHEME 1: Steps Involved in a Continuously Cycling Surface Catalyzed Reaction

(1a) diffusion of adsorptive reactants to the active site on the solid surface; (2a) adsorption of one or more reactants (adsorbates) onto the surface: if molecule A is chemically adsorbed onto one of the active sites, then a surface complex (S—A) is formed; (3a) surface reaction: A reacts forming the products (B + C); (4a) desorption of products from the surface: (B + C) escapes the site, thus regenerating site S; and (5a) diffusion of products away from the surface.

The overall surface chemical reaction represents the sum of the elementary steps mentioned above, each of them occurring with different rate constants. When in the presence of a large amount of active adsorbing sites when compared with the total amount of adsorbate, the initial steep part of the curve representing the concentration of H₂O₂ as a function of reaction time corresponds to a process dominated by the steps 1a and 2a of Scheme 1, diffusion and adsorption of H₂O₂ into the surface of ZrO₂, until an equilibrium of adsorbate in the surface is reached. The period of time during which steps 1a and 2a dominate the overall process can be reduced to a very short period that is negligible when compared with the total time of the reaction. A behavior very close to zeroth-order kinetics can then be obtained when the amount of H₂O₂ present is in large excess compared with the number of adsorption sites available initially on the powder surface. In this way, it is possible to fit the data to zeroth-order kinetics minimizing the error of such

TABLE 1: Specific Surface Areas of the Fresh Powder Determined by the BET Method after Immersion in Water at 80 °C and after Reaction with H₂O₂ at 80 °C

		specific surface area (m²·g^{-1})
ZrO₂ powder (grain size <5 μm)	fresh powder	5.0 ± 0.2
	after immersion in water at 80 °C	5.0 ± 0.2
	after reaction with H₂O₂ in aqueous media at 80 °C	5.0 ± 0.3

11206 *J. Phys. Chem. C, Vol. 114, No. 25, 2010*

Lousada and Jonsson

approximation. The lower limit of Zirconium mass, where the reaction changes from pseudo-first-order to zeroth-order, which implies that the reaction rate constant will be independent of the initial concentration of H_2O_2, was ~0.5 g, which corresponds to a surface area of 2.5 m². When the mass of zirconium was <0.5 g in 50 mL of 0.5 mM H_2O_2 solution, zeroth-order kinetics was approached. The zeroth-order rate constant obtained at T = 298.15 K with 0.224 g ZrO_2 in 50 mL of 0.5 mM H_2O_2 solution was $k_0 = (2.0 \pm 0.1) \times 10^{-5}$ M·s⁻¹.

The pH plays an important role in surface processes specifically in the rate of uptake of an adsorbate by a surface.[45] In the case of a system where hydrogen-bonded structures are possible to form, the pH effect becomes even more important. Hydrogen peroxide is capable of forming stable cyclic hydrogen-bonded structures.[46] At low pH values, metal oxide and hydroxide surfaces tend to be positively charged, with an excess of protons bound to the surface, and thus these surfaces tend to repel positively charged ions and attract negatively charged ions. In the specific case of the system studied in this work, this environment can trigger the formation of stable hydrogen-bonded clusters of hydrogen peroxide in solution and on the surface, having the effect of stabilizing the hydrogen peroxide. At some intermediate pH value, the surface becomes charge neutral. At the pH of the point of zero charge, which in the case of ZrO_2 is ~6.5,[47] electrostatic repulsion of a positively or negatively charged ion would be minimized. At pH above the point of zero charge, the surface becomes negatively charged because of the predominance of hydroxo (OH^-) or oxo (O^{2-}) groups on the surface. Under these conditions, a positively charged ion in solution would be attracted to the surface, but a negatively charged ion would be repelled. Anions show the opposite behavior, with strong electrostatic attraction to metal oxide particle surfaces at low pH values and repulsion at high pH values. According to the proposed mechanism of the decomposition of H_2O_2 on the surface of a solid, one of the intermediate species formed is the superoxide radical (pK_a = 4.88). A change in the pH of the solution where the reaction takes place can have the effect of altering the concentration of superoxide radical trapped on the surface by affecting the attractive/repulsive forces between the superoxide radical and the surface and by promoting or slowing down the rate of decomposition of the former according to reaction R4. To evaluate the effect of pH changes on the rate of decomposition of H_2O_2 by affecting the stability of intermediate species, the zeroth-order rate was determined for different pH values. The data obtained are represented in Figure 5. As can be seen, the zeroth-order rate constant is linearly dependent on the pH of the solution. When considering the zeroth-order rate constant, where as described above the processes 3a and 4a are rate-determining, one can have a picture of what is the effect in the reaction rate of the amount of superoxide radical present. Because at the range of studied pH values the deprotonation of H_2O_2 and HO˙ radical are not to be considered because of their higher pK_a values, the pH effect translates mostly in the amount of superoxide present on the surface. As expected when considering the amount of superoxide radical present on the surface as an important factor affecting the reaction rate, the zeroth-order rate is higher the less superoxide is present on the surface. Reaction R1 is dependent on the number of available sites on the surface where H_2O_2 can adsorb. The amount of superoxide accommodated on the surface has an impact on the overall reaction rate. This fact occurs probably by alterations in the interactions between H_2O_2 and the active sites in the surface due to the occupancy of the latter by the superoxide anion radical. Besides this, the fact that hydrogen peroxide forms stabilizing hydrogen-bonded clusters at lower pH
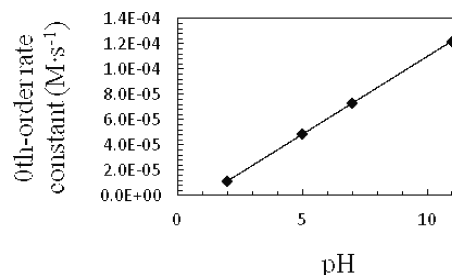

Figure 5. Zeroth-order rate constant as a function of pH obtained at 298.15 K for 50 mL of solution, 0.5 mM in H_2O_2, and 0.5 g ZrO_2. The obtained correlation coefficient for the least-squares fit is equal to 1, and the associated error is equal to 5.16×10^{-8}.

values will increase the potential energy barrier for the reaction to occur. This means that the rate at which the hydrogen peroxide reaches catalytic active surface sites will be diminished, causing the rate constant to decrease. These two effects, hydrogen peroxide stabilization and superoxide presence in the surface, have to be considered when analyzing the dynamics of the reaction at different pH values.

Mechanistic Study of the Decomposition of H_2O_2 on the Surface of ZrO_2. A mechanistic study on the production of HO radicals as intermediate species formed in the decomposition of H_2O_2 in the presence of ZrO_2 according to reaction R1 was performed. An assessment of the amount of hydroxyl radicals produced as intermediate species in the decomposition of hydrogen peroxide was carried out. These studies involved determining the rate of formation of hydroxyl radicals and compare its dynamics with the rate of consumption of hydrogen peroxide. The chemical yield for the formation of formaldehyde upon reaction of the hydroxyl radicals with tris buffer was determined by quantifying the amount of formaldehyde produced when a known amount of hydroxyl radicals are present in the system. For that, a calibration curve was obtained by performing an experiment where a known amount of hydroxyl radicals was produced by radiolysis of water under γ radiation and where tris buffer was present triggering the formation of formaldehyde according to Scheme 2.

The method based on the Hantzsch reaction, introduced by Nash[48] for the spectrophotometric detection of formaldehyde, has been used frequently in previous works. In this work, however, it was necessary to use a modified version of this method.[36] The use of acetoacetanilide instead of acetylacetone or 2,4-pentadione avoids interferences with H_2O_2, which made this technique possible to apply with good sensitivity to the system studied in this work.

Water radiolysis occurs when the water is exposed to ionizing radiation. Upon radiolysis of water, HO˙, H_2O_2, $H_2O˙$, e_{aq}^-, H˙, and H_2 are formed.[49] The main products formed in water radiolysis are e_{aq}^- and HO˙, which are formed in equal amounts. When the solution is saturated with N_2O, the solvated electrons produced are converted to HO˙ according to the following reactions[50]

$$e_{aq}^- + N_2O \rightarrow N_2 + O^{˙-} \quad k = 9.1 \times 10^9 \text{ L·mol}^{-1}\text{·s}^{-1}$$
(R9)

$$O^{˙-} + H_2O \rightarrow HO^˙ + OH^- \quad k = 1.8 \times 10^6 \text{ L·mol}^{-1}\text{·s}^{-1}$$
(R10)
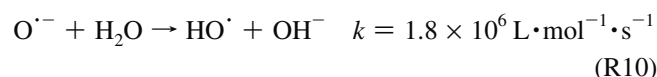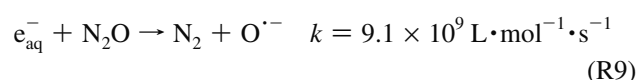
The amount of hydroxyl radicals produced in water radiolysis can be quantified from the dose rate of the radiation source and

H$_2$O$_2$ Decomposition on the Surface of ZrO$_2$

J. Phys. Chem. C, Vol. 114, No. 25, 2010 **11207**
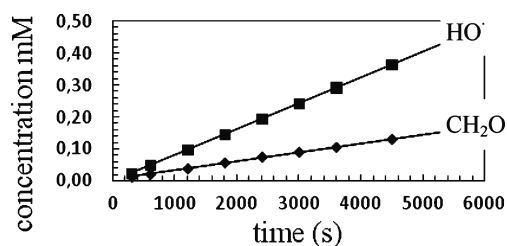
Figure 6. Comparison between the rate of formation of hydroxyl radicals in water radiolysis and the corresponding concentration of formaldehyde, obtained using the modified Hantzsch method.

SCHEME 2: Formation of Formaldehyde by Means of the Reaction of Tris(hydroxymethyl)aminomethane with Hydroxyl Radical to Form Amongst Other Products, Formaldehyde and a Radical Species, Which Can Further React to Form a More Stable Species
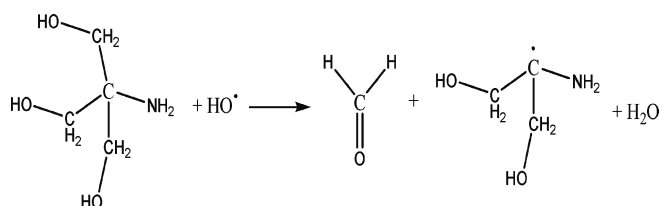
the *G* value (radiation chemical yield) for the hydroxyl radical according to

$$\dot{C}(OH^{\cdot}) = \dot{D} \times G \times \rho \qquad (11)$$

Where $\dot{C}(OH^{\cdot})$ is the amount of OH radicals produced in mol·dm^{-3}·s^{-1}, $\dot{D}$ is the dose rate of the radiation source and in this case is equal to 0.15 Gy·s^{-1}, G is the G value for the production of hydroxyl radicals and ρ is the density of the solvent which in this case is 1 as the solvent is water. Given that the solution was purged with N$_2$O gas, the G value for the production of hydroxyl radicals is equal to 5.5×10^{-7} mol·J^{-1}.[51] From eq 11, one can obtain the amount of hydroxyl radicals produced as a function of irradiation time $C(HO^{\cdot})_t$, where $C(HO^{\cdot})_t$ has the units of mol·dm^{-3}. The set of data obtained for comparison of the amount of formaldehyde produced with the amount of hydroxyl radicals present in solution upon irradiation of a solution 20 mM in tris/HCl buffer, pH = 7.5 in 50 mL of H$_2$O at $T = 293.25$ K, are represented in Figure 6. The yield of the method when comparing the concentration of formaldehyde produced with a given concentration of hydroxyl radicals present is 35%. This means that 35% of the hydroxyl radicals present in the system react with tris buffer to produce formaldehyde. A result well below 100% would be expected because according to Scheme 2, the reaction of the hydroxyl radical with tris buffer can take place in other positions besides the α-hydrogen atom of the alcohol group that results in the formation of formaldehyde. Consequently, the reaction can follow different pathways producing different compounds not detectable by the modified Hantzsch method. However, the limit of detection obtained in this work for the detection of formaldehyde was 0.5 μM, which corresponded to a concentration in HO radicals equal to 1.43 μM. When comparing the limit of detection of the method, obtained in this work for the detection of formaldehyde, with a previously published value where no solid was present, 0.1 μM,[36] it can be asserted that this method can be applied to systems similar to the one studied in this work without major changes in the detection limits caused by interferences due to the presence of H$_2$O$_2$ and the solid oxide. On the basis of the data from Figure 6, a study involving
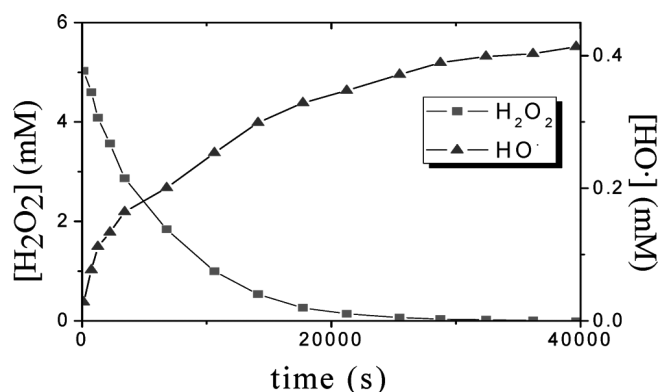

Figure 7. Evolution in the concentrations of H$_2$O$_2$ and HO$^{\cdot}$ as a function of reaction time, in the reaction of H$_2$O$_2$ with ZrO$_2$.

determining the amount of formaldehyde and consequently the amount of hydroxyl radicals produced during the course of the reaction between H$_2$O$_2$ and ZrO$_2$ was performed. The reaction was carried out in a suspension of 4.5 g ZrO$_2$ at a temperature of 293.25 K in 50 mL of H$_2$O with 20 mM tris buffer and 5 mM H$_2$O$_2$. The pH was adjusted to 7.5 with HCl. Samples were collected at different time intervals and filtered. Subsequently, 1.5 mL of reactant solution was diluted in 2.5 mL of 4 M solution of ammonium acetate and 1 mL of 0.2 M solution of acetoacetanilide in ethanol. The modified Hantzsch reaction was left to react during 15 min at a temperature of 313.15 K. The obtained set of data is represented in Figure 7.

According to the proposed reaction mechanism, the overall stoichiometry of the reaction of H$_2$O$_2$ in the surface of ZrO$_2$ states that for each mol of H$_2$O$_2$ consumed, two moles of hydroxyl radicals are produced. The determined concentration of hydroxyl radical represented in Figure 7 lies around 1/10 of the concentration predicted by the reaction mechanism. This is due to the competition between tris buffer and H$_2$O$_2$ to react with the hydroxyl radical. The energetics of the bonds involved in both reactions are approximately of the same magnitude, the cleavage of the O−H bond in tris buffer requires around[52] 431 kJ·mol^{-1} of energy, the cleavage of the C−H bond requires 393 kJ mol^{-1}, whereas the cleavage of the O−H bond in H$_2$O$_2$ requires[43] 429 kJ·mol^{-1}. Although the method used for the study of the evolution of hydroxyl radicals with reaction time does not allow discriminating if the hydroxyl radicals are on the surface of the powder or in solution when scavenged by the tris, previous studies show that for similar systems the hydroxyl radicals can be trapped and stabilized on the surface of the metal oxide powder.[53] The rate constant for H$_2$O$_2$ consumption obtained with the presence of tris/HCl buffer at pH 7.5 was compared with the rate constant obtained under normal conditions, no buffering system present, pH 7.0. The first-order rate constant obtained for 313.15 K under normal conditions produced the value $k_1 = (1.22 \pm 0.13) \times 10^{-4}$ s^{-1}, and the first-order rate constant obtained with the presence of tri/HCl buffer at pH 7.5 produced the value $k_1 = (1.13 \pm 0.70) \times 10^{-4}$ s^{-1}. When taking the associated errors into account, the obtained values are in good agreement, and it is possible to state that the buffering system tris/HCl with a pH 7.5 is not affecting the reaction rate when compared with the reaction where no buffer is present.

4. Conclusions

The obtained activation energy for the reaction agrees with previously published values for similar systems where different techniques were used for its determination. The mechanism of

the reaction of decomposition of H_2O_2 in the presence of ZrO_2, although not completely elucidated, is confirmed to involve the formation of hydroxyl radicals as intermediate species, most likely sorbed to the surface of the solid. The dynamics of the formation of the HO radicals during the course of the reaction of decomposition of H_2O_2 was found to be in good agreement with the predicted by the proposed reaction mechanism. The modified Hantzsch method has proven an easy and sensitive method for the determination of the concentration of HO radicals produced as a byproduct of the decomposition of H_2O_2. Because the system is complex because of the possibility of innumerous surface phenomena that could cause interferences with the reaction of production of formaldehyde and further with the modified Hantzsch reaction, one could expect that the sensitivity of this method would be reduced when applied to this type of system. This was not verified, and the limit of detection obtained in this work for the detection of formaldehyde is in the same order of magnitude of the limit of detection of the method previously published and where no solid was present. It can be asserted that the modified Hantzsch method can be applied to systems similar to the one studied in this work without major changes in the detection limits caused by interferences due to the presence of H_2O_2 or the solid metal oxide.

References and Notes

(1) Li, H. H.; Liu, S. Q.; Dai, Z. H.; Bao, J. C.; Yang, X. D. *Sensors* **2009**, *9*, 8547.

(2) Ozawa, M. *J. Alloys Compd.* **1998**, *275*, 886.

(3) Li, Q.; Yuan, L.; Ye, T.; Chen, Y. (University of China Science & Technology). Patent CN101306370-A, 2009.

(4) Wulff-Doering, J.; Stichert, W.; Schueth, F. (BASF). Patent 849224, 1998.

(5) Fukunaga, T. (Idemitsu Kosan Co., Ltd. (IDEK)). Patent 1093852, 1999.

(6) Andreiotelli, M.; Wenz, H. J.; Kohal, R. J. *Clin. Oral Implant. Res.* **2009**, *20*, 32.

(7) Niinisto, L.; Paivasaari, J.; Niinisto, J.; Putkonen, M.; Nieminen, M. *Phys. Status Solidi A-Appl. Res.* **2004**, *201*, 1443.

(8) Comte, M. J. M.; Comte, M. (Eurokera SNC). Patent 1957421, 2007.

(9) Sickafus, K. E.; Minervini, L.; Grimes, R. W.; Valdez, J. A.; Ishimaru, M.; Li, F.; McClellan, K. J.; Hartmann, T. *Science* **2000**, *289*, 748.

(10) Qiu, L. Y.; Guzonas, D. A.; Webb, D. G. *J. Solution Chem.* **2009**, *38*, 857.

(11) *Radiation Effects in Solids*; Sickafus, Kurt E., Kotomin, E. A., Uberuaga, B. P., Eds.; Springer: Dordrecht, The Netherlands, 2007; Vol. 235.

(12) Medek, J.; Weishauptová, Z. *J. Nucl. Mater.* **2009**, *393*, 306.

(13) Cox, B. *J. Nucl. Mater.* **2005**, *336*, 331.

(14) Motta, A. T.; Yilmazbayhan, A.; da Silva, M. J. G.; Comstock, R. J.; Was, G. S.; Busby, J. T.; Gartner, E.; Peng, Q.; Jeong, Y. H.; Park, J. Y. *J. Nucl. Mater.* **2007**, *371*, 61.

(15) Wada, Y.; Uchida, S.; Nakamura, M.; Akamine, K. *J. Nucl. Sci. Technol.* **1999**, *36*, 169.

(16) Dishman, M. V.; Covey, D. A.; Baughan, L. W. *Dent. Mater.* **1994**, *10*, 33.

(17) Penna, T. C. V.; Ferraz, C. A. M. *Infect. Control Hosp. Epidemiol.* **2000**, *21*, 499.

(18) Brodrecht, D. J.; Rusek, J. J. *Appl. Energy* **2003**, *74*, 113.

(19) Hurlbert, E.; Applewhite, J.; Nguyen, T.; Reed, B.; Zhang, B. J.; Wang, Y. *J. Propul. Power* **1998**, *14*, 676.

(20) Pastina, B.; LaVerne, J. A. *J. Phys. Chem. A* **1999**, *103*, 1592.

(21) Loveland, W. D.; Morrissey, D. J.; Seaborg, G. T. *Modern Nuclear Chemistry*; John Wiley & Sons: New York, 2006.

(22) Jonsson, M.; Nielsen, F.; Roth, O.; Ekeroth, E.; Nilsson, S.; Hossain, M. M. *Environ. Sci. Technol.* **2007**, *41*, 7087.

(23) Hiroki, A.; LaVerne, J. A. *J. Phys. Chem. B* **2005**, *109*, 3364.

(24) Lin, C. C.; Smith, F. R.; Ichikawa, N.; Baba, T.; Itow, M. *Int. J. Chem. Kinet.* **1991**, *23*, 971.

(25) Denisov, E. T.; Denisova, T. G.; Pokidova, T. S. *Handbook of Free Radical Initiators*; John Wiley & Sons: Hoboken, NJ, 2003.

(26) Takagi Junichi, I. K. *Nucl. Sci. Eng.* **1985**, *89*, 177.

(27) Anpo, M.; Che, M.; Fubini, B.; Garrone, E.; Giamello, E.; Paganini, M. *Top. Catal.* **1999**, *8*, 189.

(28) Wardman, P.; Ross, A. B. *Free Radical Biol. Med.* **1991**, *10*, 243.

(29) Anbar, M.; Neta, P. *Int. J. Appl. Radiat. Isot.* **1967**, *18*, 493.

(30) Bahnemann, D. W.; Hoffmann, M. R. *J. Electrochem. Soc.* **1987**, *134*, C463.

(31) G. Choppin, J.-O. L.; Rydberg, J. *Radiochemistry and Nuclear Chemistry*, 2nd ed.; Butterworth-Heinemann: Oxford, U.K., 1995; Vol. 46.

(32) Bailey, J. E. *Proc. R. Soc. London, Ser. A* **1964**, *279*, 395.

(33) Hochanadel, C. J. *J. Phys. Chem.* **1952**, *56*, 587.

(34) Ghormley, J. A.; Stewart, A. C. *J. Am. Chem. Soc.* **1956**, *78*, 2934.

(35) Shiraishi, H.; Kataoka, M.; Morita, Y.; Umemoto, J. *Free Radical Res.* **1993**, *19*, 315.

(36) Li, Q.; Sritharathikhun, P.; Motomizu, S. *Anal. Sci.* **2007**, *23*, 413.

(37) *EN 717-2*; European Committee for Standardization, Brussels, 1994.

(38) *Food Chemicals Codex*, 5th ed.; National Academy Press: Washington, D.C., 2003.

(39) Chirita, P. *Chem. Biochem. Eng. Q.* **2009**, *23*, 259.

(40) Croiset, E.; Rice, F. S.; Hanush, G. R. *Hydrogen Peroxide Decomposition in Supercritical Water*; Wiley-Blackwell: Hoboken, NJ, 1997; Vol. 43.

(41) Murphy, M. D.; Griffiths, W. E.; Rowlands, C. C.; Hancock, E. F.; Giamello, E. *EPR Study of the H_2O_2 Interaction with TIO_2: Evidence for a Novel S = 1 Surface Radical Pair*; Royal Society of Chemistry: Cambridge, U.K., 1997.

(42) Jonsson, M. In *Recent Trends in Radiation Chemistry*; Wishart, J. F., Rao, B. S. M., Eds.; World Scientific: Singapore, 2010; p *301*.

(43) McKay, D. J.; Wright, J. S. *J. Am. Chem. Soc.* **1998**, *120*, 1003.

(44) Erbil, H. Y. *Surface Chemistry Of Solid and Liquid Interfaces*, 1st ed.; Blackwell Publishing: Oxford, U.K., 2006.

(45) Nilsson, A.; Pettersson, L. G. M.; Nørskov, J. K. *Chemical Bonding at Surfaces and Interfaces*; Elsevier: Amsterdam, 2008.

(46) Kulkarni, A. D.; Pathak, R. K.; Bartolotti, L. J. *J. Phys. Chem. A* **2005**, *109*, 4583.

(47) Kosmulski, M. *J. Dispersion Sci. Technol.* **2002**, *23*, 529.

(48) Nash, T. *Biochem. J.* **1953**, *55*, 416.

(49) Jacqueline Belloni, T. D. In *Radiation Chemistry: From Basics to Applications in Material and Life Sciences*; Mostafavi, M., Spotheim-Maurizot, M., Eds.; EDP Sciences: Les Ulis Cedex, France, 2008.

(50) Buxton, G. V.; Greenstock, C. L.; Helman, W. P.; Ross, A. B. *J. Phys. Chem. Ref. Data* **1988**, *17*, 513.

(51) Tabata, Y. *Pulse Radiolysis of Irradiated Systems*; CRC Press: Tokyo, 1991.

(52) Denisova, T.; Denisov, E. *Kinet. Catal.* **2006**, *47*, 121.

(53) Giamello, E.; Calosso, L.; Fubini, B.; Geobaldo, F. *J. Phys. Chem.* **1993**, *97*, 5735.

JP1028933

Reactivity of H$_2$O$_2$ towards different UO$_2$-based materials: The relative impact of radiolysis products revisited

Cláudio M. Lousada, Martin Trummer, Mats Jonsson *

KTH Chemical Science and Engineering, Nuclear Chemistry, Royal Institute of Technology, SE-100 44 Stockholm, Sweden

ARTICLE INFO

ABSTRACT

The reactivity of doped UO$_2$ such as SIMFUEL towards H$_2$O$_2$ has been shown to be fairly similar to that of pure UO$_2$. However, the oxidative dissolution yield, i.e. the ratio between the amount of dissolved uranium and the amount of consumed H$_2$O$_2$ is significantly lower for doped UO$_2$. In this work we have studied the mechanistic difference between SIMFUEL and pure UO$_2$. H$_2$O$_2$ can be catalytically decomposed on UO$_2$ in competition with the redox process in which U(IV) is oxidized. The latter process leads to the dissolution of oxidized uranium. The first step in the catalytic decomposition is the formation of hydroxyl radicals. The presence of hydroxyl radicals was verified using Tris buffer as a radical scavenger. For both UO$_2$ and SIMFUEL pellets, significant amounts of hydroxyl radicals were formed. The results also show that the difference in dissolution yield between the two materials can mainly be attributed to differences in the redox reactivity. Based on this, the rate constants for electron transfer were revised and the relative impact of the radiolytic oxidants in oxidative dissolution of UO$_2$ and SIMFUEL pellets were calculated. The impact of H$_2$O$_2$ is shown to be slightly reduced.

© 2011 Elsevier B.V. All rights reserved.

1. Introduction

Deep geological repositories have been put forward by several countries that make use of nuclear power for electricity production as the leading technology for handling the spent nuclear fuel. The safety of these repositories relies on multiple natural and man-made barriers protecting both, the fuel from the surrounding groundwater, and the environment from the highly radiotoxic radionuclides present in the fuel. In order to predict risks and estimate the effects on the surroundings, existing experimental data need to be projected. In the case of the innermost barrier, the fuel itself, the mechanism and kinetics of reactions affecting its dissolution constitute key-data.

Dissolution of the uranium dioxide matrix is generally considered to be negligible under the reducing conditions expected in some deep geological depositories [1]. Due to radiolysis caused by the ionizing radiation from the spent nuclear fuel, these conditions will be altered, and oxidants, as well as reductants are formed [2]. It has been shown that in a deep repository, where the uranium accessible for reaction with radiolysis products is mostly reduced, oxidation of the sparingly soluble U(IV) [3–5] to the significantly more soluble U(VI) is kinetically favored. In presence of HCO$_3^-$, the solubility increases further by complex formation [6–9]. The oxidative dissolution is shown in the following reactions.

$$UO_{2(s)} + Ox \rightarrow UO_{2(s)}^{2+} + Red \qquad (1)$$

$$UO_{2(s)}^{2+} \rightarrow UO_{2(aq)}^{2+} \qquad (2)$$

After barrier failure, relatively high concentrations of H$_2$ will be present in the groundwater surrounding the fuel. It is produced in both the reaction of the groundwater with the iron part of the container, in which the fuel is stored (reaction (3)) [10], and the radiolysis of water [2]. The effect of the former process is larger.

$$3Fe(s) + 4H_2O(l) \rightarrow Fe_3O_4(s) + 4H_2(g) \qquad (3)$$
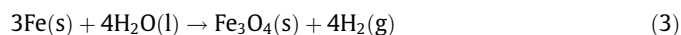
Hydrogen has been shown to decrease the dissolution in the case of spent nuclear fuel, SIMFUEL, and α- and Pd-doped UO$_2$ [11–15]. The impact of H$_2$ on the dissolution of spent nuclear fuel has been discussed extensively in several papers [16–18].

Real spent nuclear fuel can often not be used to elucidate the kinetics and mechanisms of reactions affecting the dissolution of the uranium oxide matrix, directly due to its inherent complexity and radiotoxicity. Instead, simpler and less toxic systems can be studied. Usually, the simplest possible system, pure UO$_2$, is a good starting point for such investigations. An extensive number of studies on the oxidation and dissolution of UO$_2$ has been carried out [1]. In consecutive experiments, the complexity of the system can be raised gradually by including more properties of real fuel. By these means, information about the effect of different solid alterations and other physical properties on the oxidative dissolution of the fuel matrix can be obtained. Systems with different levels of complexity have been studied in both dissolution and electrochemical experiments: UO$_2$ with a single dopant (Pd parti-

* Corresponding author.
   E-mail address: matsj@kth.se (M. Jonsson).

cles, Y_2O_3 particles) [11,12,19], multiple dopants (SIMFUEL and combined Pd- and Y_2O_3 particle doping) [18–20], and ultimately real spent nuclear fuel [16,21].

Experiments and simulations performed by Ekeroth et al. on the relative impact of the different radiolysis products show that the only oxidant that has to be considered in the case of radiation induced dissolution of pure UO_2, and in conditions similar to the ones in a deep repository, is hydrogen peroxide [22]. The analysis was based on the kinetics for oxidation taking the rate constants and concentrations into account. It should be noted that the relative impact of the radiolysis products could be different for real spent nuclear fuel, SIMFUEL or otherwise doped pellets, as the dopants could affect the surface reactivity towards H_2O_2 (i.e. the rate constant). Recently, it has been shown that, while the surface reactivity towards H_2O_2 remains virtually unaltered (within a factor of 2), the ratio between dissolved U(VI) and consumed H_2O_2 is significantly reduced for doped UO_2 compared to pure UO_2 [19,23]. To understand the effect of doping, we must consider the mechanism for the reaction between H_2O_2 and UO_2. In addition to the electron transfer reaction between H_2O_2 and UO_2, H_2O_2 can also be catalytically decomposed at the UO_2 surface (reaction (4)).

$$H_2O_2 \xrightarrow{M} 2HO^{\cdot} \tag{4}$$

The hydroxyl radical formed at the catalytic active site M can react further according to reactions (5) and (6) resulting in the overall reaction (7).

$$HO^{\cdot} + H_2O_2 \rightarrow H_2O + HO_2^{\cdot} \tag{5}$$
$$2HO_2^{\cdot} \rightarrow H_2O_2 + O_2 \tag{6}$$
$$2H_2O_2 \rightarrow O_2 + 2H_2O \tag{7}$$

Catalytic decomposition of H_2O_2 has been demonstrated for several metal oxides where electron transfer is not possible [24]. The mechanism involving the intermediate formation of hydroxyl radicals during this type of reaction was recently confirmed by experiments on ZrO_2 [25]. For UO_2 powder, the dissolution yield, reflecting the ratio between electron transfer and catalytic decomposition of H_2O_2, has been reported to be 80% [26]. Hence, electron transfer is four times faster than catalytic decomposition on this particular material. The observed reduction in dissolution yield upon doping implies that the ratio between electron transfer and catalytic decomposition is changed in favor of catalytic decomposition. However, it is not clear if the change in ratio can be attributed to a change in redox reactivity or a change in the catalytic properties of the surface. Nevertheless, this change will influence the relative impact of the radiolysis products.

In this work, the proposed mechanism for catalytic decomposition of H_2O_2 on UO_2 was investigated. Dissolution experiments with pure UO_2 powder and pellets and SIMFUEL pellets were performed and the production of $HO^{\cdot}$ was studied. The relative impact of the radiolytic oxidants for doped UO_2 was revised employing recent kinetic data and dissolution yields.

2. Experimental details

2.1. Instrumentation

γ-Irradiation was performed using a MDS Nordion 1000 Elite Cs-137 γ-source with a dose rate of 0.15 Gy s^{-1}, this value was determined by Fricke dosimetry [27]. The powder samples were weighted to $\pm 10^{-5}$ g, in a Mettler Toledo AT261 Delta Range microbalance. The reactions were performed under inert atmosphere with a constant flux of N_2 gas (AGA Gas AB) with a flow rate of 0.21 L min^{-1} that was also used for stirring the solutions. The temperature was kept constant throughout the experiments by using a

Huber CC1 or a Lauda E100 thermostat, calibrated against a Therma 1 Thermometer coupled to a submersible K-type (NiCrNi) temperature probe, with a precision of ± 0.1 K. UV/Vis spectra were collected using a WPA Lightwave S2000 or a WPA Biowave II UV/Vis Spectrophotometer. Trace elemental analysis were performed using the technique of inductively coupled plasma spectroscopy, on a Thermo Scientific iCAP 6000 series ICP spectrometer. The analyses for U were performed at the wavelengths of 367.0 and 385.9 nm. For the determination of the concentration of U in solution the values obtained from both wavelengths were averaged.

2.2. Reagents and experiments

All the solutions used in this study were prepared using water from a Millipore Milli-Q system.

Uranium dioxide pellets and powder provided by Westinghouse Atom AB and SIMFUEL pellets provided by Atomic Energy of Canada Limited were used in the experiments after being washed with a solution 10 mM $NaHCO_3$ (Merck, p.a.) for 14 h. The specific surface area of the UO_2 powder was obtained by using the B.E.T. method of isothermal adsorption and desorption of a gaseous mixture consisting of 30% N_2, 70% He on a Micrometrics Flowsorb II 2300 instrument. The obtained surface area was 5.4 ± 0.2 m^2 g^{-1}. The powders average particle size is 16 μm with a size distribution 99.9% < 100 μm. The total impurities present on the UO_2 powder correspond to 48 μg/gU. The surface area of the pellets was calculated by using a geometrical approach and produced the values of 352 mm^2 for the Westinghouse pellet and 471 mm^2 for the SIMFUEL pellet. The mass of the pellets was determined to be 5.3 g for the Westinghouse pellet and 7.9 g for the SIMFUEL pellet. The composition of the SIMFUEL pellet expressed as weight ratios to uranium is as follows: Sr (2.74×10^{-3}), Y (6.46×10^{-4}), Zr (5.72×10^{-3}), Mo (5.24×10^{-3}), Ru (3.80×10^{-3}), Rh (6.25×10^{-3}), Pd (2.93×10^{-3}), Ba (3.68×10^{-3}), La (8.77×10^{-3}), Ce (8.77×10^{-3}), Nd (1.00×10^{-2}). A mechanistic study of the decomposition of H_2O_2 on the surface of the pellets and on the UO_2 powder was carried out and involved verifying the presence and quantifying the rate of production of hydroxyl radicals as intermediate product in the reaction of H_2O_2 on the surface of these materials. This was done by means of the reaction between Tris(hydroxymethyl)aminomethane (Tris buffer) (BDH Chemicals 99%) and the hydroxyl radicals formed as intermediate products of the reaction of H_2O_2 with the pellets or the powder to produce formaldehyde as previously described in a similar study from our group [25]. It was then verified that this method has a yield of 35% (formaldehyde formed per total amount of hydroxyl radical present in the system). In this present study, the reaction between UO_2 pellets, SIMFUEL pellets, UO_2 powder and H_2O_2 was performed at 293.15 K, at the midpoint of the buffering range of the Tris. The reaction mixture consisted of one of the mentioned pellets or 0.1 g of UO_2 powder, in 50 mL solution 5 mM H_2O_2 (Sigma–Aldrich, 30% standard solution, p.a.), 10 mM $NaHCO_3$ and 20 or 80 mM Tris at a pH of 7.5, the pH was adjusted with HCl. In the case of the UO_2 powder, after extraction of a sample from the reaction vessel, this was filtered through a Gamma Medical 0.45 μm Cellulose Acetate syringe filter. For all materials studied, a sample volume of 1.5 mL was used for the determination of formaldehyde. The formaldehyde produced was then quantified spectrophotometrically at 368 nm. This method consists on the reaction of formaldehyde with acetoacetanilide AAA (Alfa Aesar > 98%) in the presence of ammonium acetate (Lancaster 98%) to form a dihydropyridine derivative which has the maximum absorption wavelength at 368 nm. A calibration curve plotting the absorbance of the dihydropyridine derivative as a function of formaldehyde concentration was obtained at 368 nm, giving a linear correlation between absorbance and concentration, in the concentration range 3.0–0.5 mM in formaldehyde. In the

case of the reaction with the UO_2 powder, the evolution in the concentration of H_2O_2 with reaction time was also studied. After extraction of a sample aliquot from the reaction vessel the sample was filtered, subsequently a sample volume of 0.2 mL was used for the measurement of hydrogen peroxide concentration. The concentration of hydrogen peroxide was then determined by the Ghormley triiodide method. In this method I^- is oxidized to I_3^- by the H_2O_2 [28,29]. The absorbance of the product I_3^- was measured spectrophotometrically at the wavelength of 360 nm. A calibration curve where the absorbance of I_3^- was plotted as a function of the concentration of hydrogen peroxide was obtained in the range of concentrations 5–20 mM in H_2O_2 resulting in a linear correlation between absorbance and concentration.

2.3. Numerical simulations details

Numerical simulations were performed using MAKSIMA-CHEMIST [30] on α- and γ-irradiated systems. The reaction rate constants for the reactions involved in the radiolysis of water used in the simulations were taken from the NDRL/NIST Solution Kinetics Database [31]. The systems were treated as homogeneous and UO_2-surface reactions were not included. The impact of the surface reactions on the radiolysis product concentrations has been shown to be negligible [22]. The simulations were run for time periods of 6 h. The dose rate used was 0.15 Gy s^{-1}. The relative impact which different oxidants have on the oxidation of UO_2 in systems subjected to γ-irradiation were calculated with the following expression.

$$\text{Relative impact} = \frac{k[\text{ox}]}{\sum_i k_i[\text{ox}]_i} \quad (8)$$

where ox represents a given oxidant and k is the rate constant for the oxidation of UO_2 by the oxidant ox.

3. Results and discussion

3.1. UO_2-powder experiments

In order to validate the mechanistic assumptions made for the reaction of H_2O_2 with UO_2 which involve the formation of hydroxyl radicals as intermediate species according to reaction (4), we studied the evolution of the H_2O_2 and HO$^\cdot$ concentrations during the reaction of H_2O_2 with a UO_2 powder suspension. The reaction media consisted of 5 mM H_2O_2, 20 mM Tris–HCl buffer, 1 mM NaHCO$_3$ and 0.1 g UO_2 in 50 mL H_2O. The results from the UO_2 powder experiment are represented in Fig. 1.
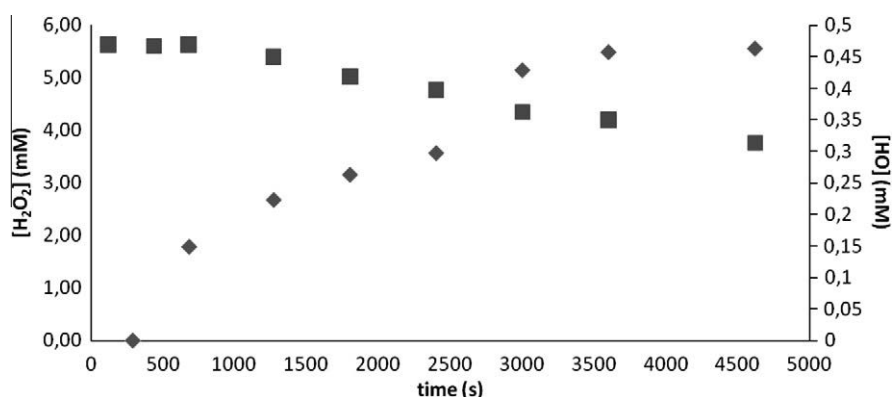
In a previous work where we performed similar mechanistic studies for a system where the H_2O_2 decomposes catalytically on the surface of ZrO_2, we concluded that the validation of the mechanism for this type of reaction can be done by studying the dynamics of formation of HO$^\cdot$ and comparing it with the dynamics of disappearance of H_2O_2 from solution [25].

For ZrO_2, where the decomposition of H_2O_2 can only occur due to the metal oxide surface catalyzed reaction, the dynamics of HO$^\cdot$ formation agrees with the dynamics of H_2O_2 consumption and the curves relative to the concentrations of these species as a function of reaction time show a high symmetry [25]. However, in the present case the reaction of H_2O_2 with UO_2 powder will to a large extent be governed by a Fenton type of mechanism. Judging from previously reported dissolution yields, about 80% of the consumed H_2O_2 will react in this way, with oxidation of U(IV) to U(VI). Hydroxyl radicals will be formed as an intermediate species of this reaction. The remaining 20% of the consumed H_2O_2 will react by catalytic decomposition as previously described in other works also leading to the formation of HO$^\cdot$ [32]. The plausible coexistence of different oxidation states of uranium at the surface and the participation of these species on the catalytic decomposition of H_2O_2 was discussed in a review by Shoesmith [33]. The HO$^\cdot$ produced in the oxidation of U(IV) to U(V) is not expected to be scavenged by the Tris since the reaction of HO$^\cdot$ with U(V) is very rapid [34]. Hence, the scavenged HO$^\cdot$ are expected to come from the fraction of H_2O_2 that decomposes catalytically on the surface of UO_2 powder. From Fig. 1 we can see that a significant amount of hydroxyl radicals are scavenged. The amount of formaldehyde produced corresponds to about 6% of the amount of the H_2O_2 consumed in the course of the reaction. Taking into account the yield of the method it is possible to determine the amount of H_2O_2 that reacts by decomposition. The resulting fraction of H_2O_2 that reacts by decomposition is around 17% while the other 83% will react by electron transfer. These values are in excellent agreement with previously published work where the estimation of the percentage of H_2O_2 that reacted by decomposition and by electron transfer was based on the ratio between the amount of dissolved uranium and the amount of consumed H_2O_2 [32]. The theory that the radicals formed in the oxidation process cannot be scavenged by the Tris is also supported by these results.

3.2. UO_2 and SIMFUEL pellet experiments

In a very recent work it was demonstrated that the dissolution yield (the ratio between dissolved uranium and consumed H_2O_2) differs significantly between pure UO_2-pellets and SIMFUEL pellets [23]. H_2O_2 can react with these materials via a redox process which


Fig. 1. Evolution in the concentrations of H_2O_2 (■) and scavenged HO$^\cdot$ (◆) during the reaction of H_2O_2 with a UO_2 powder suspension as a function of reaction time at $T = 298.15$ K. The reaction media consisted of 5 mM H_2O_2, 20 mM Tris–HCl buffer, 1 mM NaHCO$_3$ and 0.1 g UO_2 in 50 mL H_2O.

leads to the oxidation of U(IV) to U(VI) and further dissolution of the latter or via catalytic decomposition which does not lead to the dissolution of the catalyst. It was verified in the above mentioned work [23] that SIMFUEL displays a much lower dissolution yield which indicates that a larger fraction of the H_2O_2 is consumed by catalytic decomposition. The overall reactivity of H_2O_2 was found to be 50% lower on SIMFUEL compared to pure UO_2. To clarify the mechanistic reasons behind the observed differences between UO_2 and SIMFUEL we measured the concentrations of hydroxyl radicals (accumulated) and dissolved uranium as a function of reaction time. The amount of H_2O_2 consumed in the reaction with the pellets can be determined indirectly. This quantity is related to the amount of uranium in solution (corresponding to the fraction of H_2O_2 consumed in oxidation reactions) plus half of the $HO^{\cdot}$ produced (corresponding to the fraction of H_2O_2 consumed by catalytic decomposition).

It should be noted that the surface-to-volume ratio is significantly lower in the pellet experiments than in the powder experiment discussed above. Hence, the rate of oxidant consumption will be much lower in the pellet experiment.

The results of the pellet experiments are presented in Fig. 2 for the pure UO_2 pellet, and in Fig. 3 for the SIMFUEL pellet.

As can be seen, significant amounts of hydroxyl radicals are formed in both cases. Interestingly, the hydroxyl radical production rate is approximately 50% lower for SIMFUEL than for UO_2. This is in excellent agreement with the difference in overall reactivity of H_2O_2 towards these materials. As the dissolution yields for UO_2 and SIMFUEL pellets have been shown to be 14% and 0.2%, respectively [23], it is not surprising that the hydroxyl radical production rates parallel the overall H_2O_2 reactivity. The electron transfer process has only a minor impact on the H_2O_2 consumption (14% for UO_2 and 0.2% for SIMFUEL). The measured uranium concentrations in the present work confirm the previous conclusions on the significant difference in dissolution yield between UO_2 and SIMFUEL. For SIMFUEL the uranium concentration was close to the detection limit throughout the experiment while for the pure UO_2 pellet a significant increase in uranium concentration is observed. The ratio between produced hydroxyl radical and dissolved uranium provides the same information as the previously determined dissolution yield. However, the fairly small difference in hydroxyl radical production rate between the two materials supports the idea that the main difference between the materials is the redox reactivity.

3.3. The relative impact of radiolytic oxidants

From the results presented above it is obvious that the contribution of H_2O_2 to oxidation of UO_2 in SIMFUEL will decrease in comparison with pure UO_2. Hence, the relative impact of the different radiolytic oxidants produced in groundwater in contact with spent nuclear fuel in a deep geological repository can change. The relative impact of an oxidant is given by the rate of oxidative dissolution of U(IV) attributed to one specific oxidant compared to the total rate of radiation induced oxidation [22]. The total rate of oxidation of U(IV) can be calculated using the following equation:

$$\text{rate} = A_{UO_2} \sum_{ox=1}^{n} k_{ox}[ox]\frac{n_{e^-}}{2} \tag{9}$$

In this equation, ox corresponds to the different oxidants, n_{e^-} to the number of electrons involved in the redox process, k_{ox} represents the reaction rate constant and A_{UO_2} is the BET surface area. For a pellet the BET surface is estimated to be three times the geometrical surface area [35]. In a previous work [22], the rate constants for the different oxidants were used to calculate the rates of oxidation and relative impact of oxidants for pure UO_2 powder in various atmospheres. In order to adapt these values to the UO_2 and SIMFUEL pellets, differences in rate constant for the electron transfer process between H_2O_2 and the UO_2-based material must be considered. From previous experiments we know, the rate of oxidation decreases by a factor of 400 from pure UO_2 powder to the SIMFUEL pellet, and by a factor of ≈ 6 regarding the UO_2 pellet. This fact will reduce the relative impact of H_2O_2 and increase the relative impact of other oxidants. In this work the rate constants used in the numerical simulations of radiation induced oxidation of UO_2 based materials were adjusted by the factors mentioned above. The values for the relative impact of the radiolytic oxidants on pure UO_2 and the new values for the SIMFUEL pellet during α- and γ-radiolysis in 10 mM HCO_3^- are shown in Table 1.

As can be seen, the difference between UO_2 powder and UO_2 and SIMFUEL pellets is larger during γ-irradiation. This is expected, since the impact of the radicals in comparison with the molecular oxidants is already larger in the case of pure UO_2 powder and γ-irradiation. The simulations show that, during α-irradiation, radicals are not of major importance in the oxidative dissolution, even for the case of SIMFUEL where the rate constant for oxidation by H_2O_2 is reduced by a factor of 400 compared to the UO_2 powder.
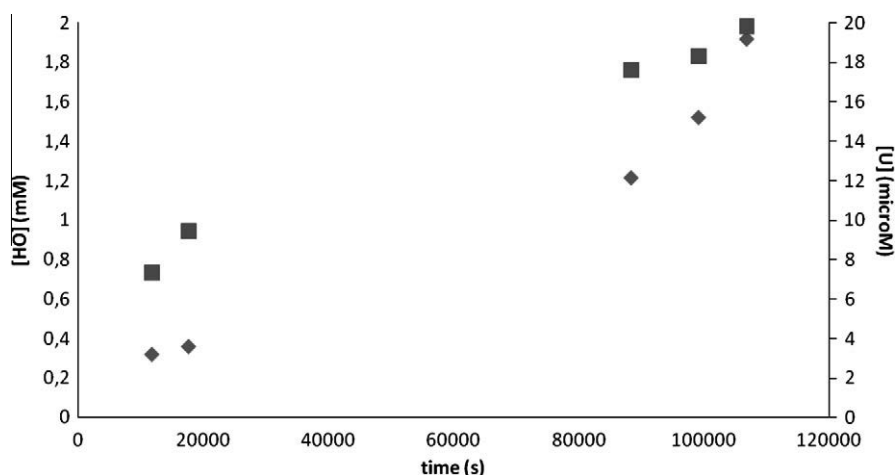

Fig. 2. Evolution in the concentrations of U(VI) in solution (■) and $HO^{\cdot}$ (◆) during the reaction of H_2O_2 with a UO_2 pellet as a function of reaction time at T = 298.15 K. The reaction media consisted of a UO_2 pellet in 5 mM H_2O_2, 20 mM Tris–HCl buffer, 1 mM $NaHCO_3$ in 50 mL H_2O.
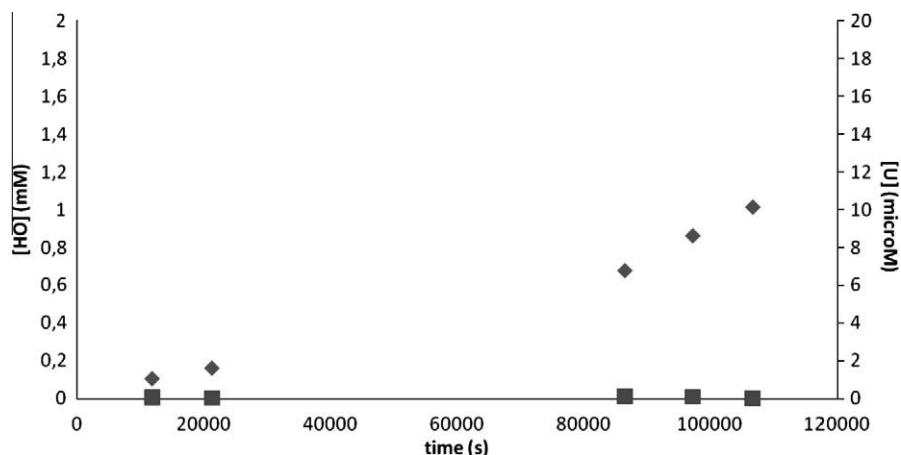
Fig. 3. Evolution in the concentrations of U(VI) in solution (■) and scavenged HO· (◆) during the reaction of H_2O_2 with a SIMFUEL pellet as a function of reaction time at $T = 298.15$ K. The reaction media consisted of a SIMFUEL pellet in 5 mM H_2O_2, 20 mM Tris–HCl buffer, 1 mM $NaHCO_3$ in 50 mL H_2O.

Table 1
Impact of the radiolytic oxidants.

	α-Radiolysis			γ-Radiolysis		
	UO_2 powder (%)	UO_2 pellet (%)	SIMFUEL (%)	UO_2 powder (%)	UO_2 pellet (%)	SIMFUEL (%)
H_2O_2	99.90	99.27	65.97	72.47	26.92	0.52
O_2	0.09	0.65	30.10	1.71	4.53	6.16
CO_3^-	0.00	0.02	0.77	24.25	64.37	87.62
HO·	0.00	0.00	0.00	0.00	0.00	0.01
O_2^-	0.00	0.03	1.58	0.03	0.08	0.11
HO_2^-	0.00	0.03	1.58	1.54	4.10	5.58
Sum	100	100	100	100	100	100

It should be noted that the second molecular oxidant, oxygen, is no longer negligible. During γ-irradiation, with the UO_2 and SIMFUEL pellets, the role of CO_3^- becomes dominant. However, the simulated time is only four hours and it has previously been shown that the relative impact of radicals decreases with time [22]. When increasing the simulated γ-irradiation time to 99 h using the same rate constants as in this work, the relative impact of H_2O_2 increases and the relative impact of radicals is significantly reduced [23].

4. Conclusions

The results presented in this work clearly show that the previously observed reduction in oxidative dissolution yield for SIMFUEL pellets compared to pure UO_2 pellets can be attributed to a difference in the redox reactivity of the solid. The experimental results also confirm the previously proposed mechanism for catalytic decomposition of H_2O_2. Taking the change in redox reactivity towards H_2O_2 into account we can conclude that the relative impact of H_2O_2 in the oxidative dissolution of SIMFUEL is significantly lower than in the oxidative dissolution of pure UO_2. For longer irradiation time this difference becomes less obvious.

Acknowledgements

References

[1] O. Roth, M. Jonsson, Cent. Eur. J. Chem. 6 (2008) 1–14.
[2] J.W.T. Spinks, R.J. Woods, An Introduction to Radiation Chemistry, John Wiley and Sons Inc., New York, 1964.
[3] R.L. Segall, R.S.C. Smart, J. Nowotny, Surface and Near-surface Chemistry of Oxide Materials, Elsevier Science Publishers B.V., Amsterdam, 1988.
[4] D. Rai, A.R. Felmy, J.L. Ryan, Inorg. Chem. 29 (1990) 260.
[5] I. Casas, J. de Pablo, J. Giménez, M.E. Torrero, J. Bruno, E. Cera, R.J. Finch, R.C. Ewing, Geochim. Cosmochim. Acta 62 (1998) 2223.
[6] I. Grenthe, D. Ferri, F. Salvatore, G. Riccio, Dalton Trans. (1984) 2439–2443.
[7] J.d. Pablo, I. Casas, J. Giménez, M. Molera, M. Rovira, L. Duro, J. Bruno, Geochim. Cosmochim. Acta 63 (1999) 3097–3103.
[8] D.E. Grandstaff, Econ. Geol. 71 (1976) 1493–1506.
[9] E.M. Pierce, J.P. Icenhower, R.J. Serne, J.G. Catalano, J. Nucl. Mater. 345 (2005) 206–218.
[10] N.R. Smart, D.J. Blackwood, L. Werme, Swedish Nucelar Fuel and Waste Management Company in, SKB Tech. Rep. TR-01-22, 2001.
[11] M. Trummer, S. Nilsson, M. Jonsson, J. Nucl. Mater. 378 (2008) 55–59.
[12] M. Trummer, O. Roth, M. Jonsson, J. Nucl. Mater. 383 (2009) 226–230.
[13] B. Muzeau, C. Jégou, F. Delaunay, V. Broudic, A. Brevet, H. Catalette, E. Simoni, C. Corbel, J. Alloy. Compd. 467 (2009) 578–589.
[14] A. Loida, V. Metz, B. Kienzler, H. Geckeis, J. Nucl. Mater. 346 (2005) 24–31.
[15] K. Ollila, Y. Albinsson, V. Oversby, M. Cowper, Swedish Nucelar Fuel and Waste Management Company in, SKB Tech. Rep. TR-03-13, 2003.
[16] P. Carbol, J. Cobos-Sabate, J.P. Glatz, C. Ronchi, V. Rondinella, D.H. Wegen, T. Wiss, Swedish Nucelar Fuel and Waste Management Company in, SKB Tech. Rep. TR-05-09, 2005.
[17] E. Cera, J. Bruno, L. Duro, T.E. Eriksen, Swedish Nucelar Fuel and Waste Management Company in, SKB Tech. Rep. TR-06-07, 2006.
[18] M.E. Broczkowski, J.J. Noël, D.W. Shoesmith, J. Nucl. Mater. 346 (2005) 16–23.
[19] M. Trummer, B. Dahlgren, M. Jonsson, J. Nucl. Mater. 407 (2010) 195–199.
[20] H. He, P.G. Keech, M.E. Broczkowski, J.J. Noel, D.W. Shoesmith, Can. J. Chem. 85 (2007) 702–713.
[21] K. Spahiu, L. Werme, U.B. Eklund, Radiochim. Acta 88 (2000) 507–511.
[22] E. Ekeroth, O. Roth, M. Jonsson, J. Nucl. Mater. 355 (2006) 38–46.
[23] S. Nilsson, M. Jonsson, J. Nucl. Mater. 410 (2011) 89–93.
[24] A. Hiroki, J.A. LaVerne, J. Phys. Chem. B 109 (2005) 3364–3370.
[25] C.M. Lousada, M. Jonsson, J. Phys. Chem. C 114 (2010) 11202–11208.
[26] M. Jonsson, E. Ekeroth, O. Roth, Proc. Mater. Res. Soc. Sym. 807 (2004) 77–82.
[27] J.-O.L.G. Choppin, J. Rydberg, Radiochemistry and Nuclear Chemistry, second ed., Butterworth-Heinemann Ltd., Oxford, 1995.
[28] C.J. Hochanadel, J. Phys. Chem. 56 (1952) 587–594.
[29] J.A. Ghormley, A.C. Stewart, J. Am. Chem. Soc. 78 (1956) 2934–2939.

[30] M.B. Carver, D.V. Hanley, K.R. Chaplin, MAKSIMA-CHEMIST a program for mass action kinetics simulation by automatic chemical equation manipulation and integration using stiff techniques, in: AECL-6413, Atomic Energy of Canada Limited, Ontario, 1979.

[31] A.B. Ross, B.H.J. Bielski, G.V. Buxton, D.E. Cabelli, C.L. Greenstock, W.P. Helman, R.E. Huie, J. Grodkowski, P. Neta, NDRL/NIST Solution Kinetics Database, in: National Institute of Standards and Technology, 1992.

[32] M. Jonsson, E. Ekeroth, O. Roth, Dissolution of UO_2 by one- and two-electron oxidants, in: V.M. Oversby, L.O. Werme (Eds.), Scientific Basis for Nuclear Waste Management Xxvii, Materials Research Society, Warrendale, 2004, pp. 77–82.

[33] D.W. Shoesmith, J. Nucl. Mater. 282 (2000) 1–31.

[34] E. Ekeroth, M. Jonsson, J. Nucl. Mater. 322 (2003) 242–248.

[35] I. Casas, J. Giménez, V. Marti, M.E. Torrero, J.d. Pablo, Proc. Mater. Res. Soc. Sym. 294 (1993) 61–66.

III

On the redox reactivity of doped UO_2 pellets – Influence of dopants on the H_2O_2 decomposition mechanism

Reijo Pehrman [a], Martin Trummer [b], Cláudio M. Lousada [b], Mats Jonsson [b,*]

[a] *Laboratory of Radiochemistry, University of Helsinki, A.I. Virtasen aukio 1 (PL 55), 00014 Helsingin yliopisto, Finland*
[b] *KTH Chemical Science and Engineering, Nuclear Chemistry, Royal Institute of Technology, SE-100 44 Stockholm, Sweden*

ARTICLE INFO

ABSTRACT

The reactivity of doped UO_2 such as SIMFUEL, Y_2O_3 doped UO_2 and Y_2O_3/Pd doped UO_2 towards H_2O_2 has been shown to be fairly similar to that of pure UO_2. However, the oxidative dissolution yield, i.e. the ratio between the amount of dissolved uranium and the amount of consumed H_2O_2 is significantly lower for doped UO_2. The rationale for the observed differences in dissolution yield is a difference in the ratio between the rates of the two possible reactions between H_2O_2 and the doped UO_2. In this work we have studied the effect of doping on the two possible reactions, electron-transfer and catalytic decomposition. The catalytic decomposition was studied by monitoring the hydroxyl radical production (the primary product) as a function of time. The redox reactivity of the doped pellets was studied by using MnO_4^- and $IrCl_6^{2-}$ as model oxidants, only capable of electron-transfer reactions with the pellets. In addition, the activation energies for oxidation of UO_2 and SIMFUEL by MnO_4^- were determined experimentally. The experiments show that the rate of catalytic decomposition of H_2O_2 varies by 30% between the most and least reactive material. This is a negligible difference compared to the difference in oxidative dissolution yield. The redox reactivity study shows that doping UO_2 influences the redox reactivity of the pellet. This is further illustrated by the observed activation energy difference for oxidation of UO_2 and SIMFUEL by MnO_4^-. The redox reactivity study also shows that the sensitivity to dopants increases with decreasing reduction potential of the oxidant. These findings imply that the relative impact of radiolytic oxidants in oxidative dissolution of spent nuclear fuel must be reassessed taking the actual fuel composition into account.

© 2012 Elsevier B.V. All rights reserved.

1. Introduction

The long term release of radionuclides from spent nuclear fuel in a geological repository is expected to be largely controlled by the dissolution of the matrix component of the fuel, UO_2 [1]. The redox conditions in deep geological repositories are expected to be reducing and, due to the low solubility of U(IV) [2–4], the release of radionuclides is expected to be very slow under these conditions [5]. However, radiolysis of groundwater in contact with the spent fuel can create local oxidizing conditions, leading to the oxidation of uranium to U(VI) and a notable increase in matrix solubility. Both the solubility and the dissolution rate are further enhanced by the presence of carbonate, which forms strong water soluble complexes with UO_2^{2+} [6–9] and prevents the formation of secondary solid uranyl phases.

The oxidizing species produced in radiolysis of water are HO·, H_2O_2, O_2 and $HO_2^·$ [10] as well as CO_3^- produced in the presence of carbonate. All these species are oxidants strong enough to oxidize UO_2 to U(V) or U(VI). For fuel ages of interest in the safety assessment, alpha radiation will dominate the dose contribution at

the fuel surface. For alpha radiolysis of water the radiation chemical yields for molecular products are higher than for radical products [10]. However, some of the radical oxidants display much higher reactivity towards the UO_2 matrix than H_2O_2 and O_2. Based on experimental kinetic studies and numerical simulations of aqueous radiation chemistry it has been shown that H_2O_2 is the most important oxidant, responsible for virtually 100% of the UO_2 oxidation [11]. It should be noted that this conclusion is based on kinetic data for pure and unirradiated UO_2-powder. Furthermore, for UO_2-powder it has been shown that the oxidative dissolution yield upon reaction with H_2O_2 is approximately 80%, i.e. the amount of dissolved U(VI) corresponds to 80% of the consumed H_2O_2 [12]. The remaining 20% of the H_2O_2 was assumed to react by catalytic decomposition on the UO_2 surface. The two reaction pathways for H_2O_2 are given below:

$$H_2O_2 + UO_2(s) \rightarrow UO_2^{2+}(aq) + 2OH^- \qquad (1)$$

$$H_2O_2 \rightarrow 1/2O_2 + H_2O \qquad (2)$$

The formation of HO· as the first step of the decomposition of H_2O_2 on metal oxides (reaction (2)) was previously suggested, but not experimentally verified [13,14]. Recently, it was shown that the dynamics of formation of HO· during the decomposition of

H_2O_2 on a transition metal oxide surface agrees with the fact that $HO^{\cdot}$ is formed as a primary product of the reaction [15]. In a recent study, a similar phenomenon was found also for UO_2 [16]. In previous studies where EPR and ESR techniques were used to study reactions of H_2O_2 with metal oxides [14,17], the authors were able to detect $HO_2^{\cdot}$ and $O_2^{\cdot-}$ on the surface of the oxides after reaction of H_2O_2 with these materials. It was claimed that these radical species are the result of a chain reaction where the initially formed $HO^{\cdot}$ is involved. However, the extent to which such reactions occur is not known and the role of the hydroxyl radical in this type of reactions is still not clear. It is possible though to conjecture on what concerns the role of the surface on this type of reactions and expect that the surface will have a stabilizing effect on the radicals produced as intermediate species of the decomposition of H_2O_2.

The properties of spent nuclear fuel differ significantly from pure UO_2 powder. A fuel pellet consists of pressed and sintered powder. During the use of UO_2 fuel in a nuclear reactor, cracks, as well as changes in grain structure and porosity are introduced. In addition, fission products and transuranium elements are produced [18]. These changes can alter the surface reactivity considerably.

The effect of doping UO_2 with fission products soluble in the matrix, mainly lanthanides, on the oxidation rate in air has been studied and it has been noted that in solid UO_2–M_2O_3-solutions ($M = Y$, La, Gd) there is an increase in kinetic resistance towards U_3O_8 formation with increasing doping level. Also U_4O_9 is stabilized and U_3O_7 is not formed as intermediate [19–21]. For aqueous systems, kinetic data on oxidation of doped UO_2 is scarce. It has been shown that the rate of U(VI) dissolution from SIMFUEL is significantly lower than that from pure UO_2 [22]. In recent studies it was demonstrated that the reactivity of SIMFUEL towards H_2O_2 in HCO_3^- containing aqueous solution is very similar to that of UO_2 while the rate of U(VI) dissolution differs by more than two orders of magnitude [16,23]. Hence, there is a considerable difference in the oxidative dissolution yield. The same trend was observed when comparing pure UO_2 pellets and UO_2 pellets doped with Y_2O_3 [24]. Obviously, doping alters the ratio between the rate constant for oxidation of UO_2 and the rate constant for catalytic decomposition of H_2O_2. However, it is not clear whether dopants influence one of the possible reactions or both. It should also be noted that the oxidative dissolution yield for a pure UO_2 pellet is significantly lower than that for UO_2 powder [23].

The influence of noble metal inclusions (ε-particles) on the redox reactivity of UO_2 pellets has been studied quite extensively using Pd particles as a model for the ε-particles [25,26]. These studies have, in addition to previous electrochemical studies on SIMFUEL [27], clearly shown that noble metal inclusions catalyze the reduction of surface bound U(VI) to U(IV) by H_2. This process is the main route for inhibition of oxidative dissolution in the presence of H_2 [28]. It has also been shown that the oxidation of UO_2 is catalyzed by Pd inclusions [25]. Redox experiments using UO_2 doped with Y_2O_3 and Pd particles show that the rate of uranium dissolution is significantly reduced [24].

In this work we have studied the catalytic decomposition of H_2O_2 on UO_2, SIMFUEL and Y_2O_3/Pd doped UO_2 pellets by monitoring the formation of hydroxyl radicals. The redox reactivity (i.e. the kinetics for UO_2 oxidation) of the pellets was studied using MnO_4^- and $IrCl_6^{2-}$, two oxidants that cannot undergo catalytic decomposition.

2. Experimental

2.1. Instrumentation

The reactions were performed under inert atmosphere with a constant flux of N_2 gas (AGA Gas AB) with a flow rate of 0.21 L min^{-1} that was also used for the purpose of stirring the solutions. The temperature was kept constant throughout the experiments by using a Huber CC1 or a Lauda E100 thermostat, calibrated against a Therma 1 Thermometer coupled to a submersible K-type (NiCrNi) temperature probe, with a precision of ±0.1 K. UV/Vis spectra were collected using a WPA Lightwave S2000 or a WPA Biowave II UV/Vis Spectrophotometer. The U analysis was performed with an ICP-OES (Thermo Scientific iCAP 6000 series) at 367.0 nm and 385.9 nm. The values obtained with both wavelengths were averaged.

2.2. Reagents and experiments

All the solutions used in this study were prepared using water from a Millipore Milli-Q system.

In this work, a uranium dioxide pellet (Westinghouse) and a SIMFUEL pellet (AECL) were used. Furthermore, four in-house UO_2 pellets were manufactured from UO_2 powder (Westinghouse) according to the method described in [25]. The pellets were doped with 0.3 wt.% Y_2O_3, with 0.3 wt.% Y_2O_3 and 0.1 wt.% Pd, or with 0.1 wt.% Pd. All the pellets were placed in a 10 mM NaHCO$_3$ (Merck, p.a.) solution for a period of 14 h prior to the experiments. The specific surface area of the UO_2 powder used for the in-house pellets was obtained from the B.E.T. isotherm (30% N_2, 70% He) on a Micrometrics Flowsorb II 2300 instrument. The obtained surface area is 5.4 ± 0.2 m^2 g^{-1}. The average particle size of the powder is 16 μm, with a size distribution of 99.9% < 100 μm. The total impurities present in the UO_2 powder have a concentration of 48 μg/g U. The geometrical surface areas of the pellets are 352 mm^2 for the Westinghouse pellet, 471 mm^2 for the SIMFUEL pellet and 372 mm^2 for the doped UO_2 pellets. The mass of the pellets are 5.3 g for the Westinghouse pellet, 7.9 g for the SIMFUEL pellet and 3.5 g for the doped UO_2 pellets. The composition of the SIMFUEL pellet expressed as weight ratios to uranium is as follows: Sr(2.74×10^{-3}), Y(6.46×10^{-4}), Zr(5.72×10^{-3}), Mo(5.24×10^{-3}), Ru(3.80×10^{-3}), Rh(6.25×10^{-3}), Pd(2.93×10^{-3}), Ba(3.68×10^{-3}), La(8.77×10^{-3}), Ce(8.77×10^{-3}), Nd(1.00×10^{-2}).

2.3. Catalytic decomposition of H_2O_2 on UO_2-based pellets

A mechanistic study of the decomposition of H_2O_2 on the surface of the pellets was carried out. In this study the hydroxyl radicals produced as an intermediate product of the decomposition of H_2O_2 were measured. This was done by measuring the formaldehyde produced in the reaction between tris(hydroxymethyl)aminomethane (Tris buffer) (BDH Chemicals 99%) and the hydroxyl radicals. This method has been described in a previous work [15]. In this study, the reaction between the pellets and H_2O_2 was performed at 298.15 K, at the midpoint of the buffering range of the Tris buffer. The reaction mixture consisted of one of the above mentioned pellets, in 5 mM in H_2O_2 (Sigma–Aldrich, 30% standard solution, p.a.) aqueous solution with a volume of 50 mL. These solutions also contained 10 mM NaHCO$_3$ and 20 or 80 mM Tris buffer at pH 7.5. The pH was adjusted with HCl (VWR BDH Prolabo, 30%). For all materials studied a sample volume of 1.5 ml was used for the determination of formaldehyde. The formaldehyde produced was then quantified spectrophotometrically at 368 nm. This method is based on the reaction of formaldehyde with acetoacetanilide AAA (Alfa Aesar >98%) in the presence of ammonium acetate (Lancaster 98%) to form a dihydropyridine derivative which has the maximum absorption wavelength at 368 nm. A calibration curve plotting the absorbance of the dihydropyridine derivative as a function of formaldehyde concentration was obtained at 368 nm giving a linear correlation between absorbance and concentration in the range 0.05–3.0 mM in formaldehyde.

2.4. Redox reactions of MnO_4^- and $IrCl_6^{2-}$ with UO_2-based pellets

For the study of the redox reactions of the pellets with MnO_4^- and $IrCl_6^{2-}$, we followed the evolution in the concentrations of these oxidants as a function of reaction time. The concentrations were measured directly with UV/visible spectroscopy. The absorbance of MnO_4^- was measured at $\lambda = 525$ nm and the one of $IrCl_6^{2-}$ at $\lambda = 488$ nm. After the measurements, the solutions were poured back into the reaction vessel. The reaction media for the reactions of the pellets with MnO_4^- consisted of 10 mL aqueous solution with 0.6 mM MnO_4^- and 10 mM $NaHCO_3$. For the reactions with $IrCl_6^{2-}$, the reaction media contained 0.3 mM $IrCl_6^{2-}$ and 10 mM $NaHCO_3$. The reactions were performed under inert atmosphere with a constant flow of N_2.

The activation energies for the reactions between MnO_4^- and UO_2 and between MnO_4^- and SIMFUEL were determined from Arrhenius plots based on kinetic experiments performed in the temperature interval 303.15–343.15 K.

3. Results and discussion

It was shown in previous studies that the rate constant for H_2O_2 consumption is fairly insensitive to doping [23,24]. The rate constant varies by a factor of two between SIMFUEL and pure UO_2 (Westinghouse) [23]. As mentioned above, the oxidative dissolution yield displays a strong dependence on dopants. The yields are summarized in Table 1.

The yields presented in Table 1 are based on the ratio between dissolved U(VI) and consumed H_2O_2. As can be seen, there are significant differences between the data obtained with the powder and the pellets and between pure and doped UO_2 pellets. These dissimilarities are attributed to differences in the ratio between electron-transfer and catalytic decomposition upon reaction between H_2O_2 and the solid surface. However, based on the dissolution yields alone it is not possible to determine whether doping influences the redox reactivity or the catalytic ability of the surface. To be able to assess this, further information is required. In a very recent work we studied the consumption of H_2O_2 from solution and its relation with the production of hydroxyl radicals on UO_2 powder [16]. The results clearly showed that hydroxyl radicals are formed in the process of H_2O_2 consumption. Interestingly, the dissolution yield calculated from the hydroxyl radical production and the hydrogen peroxide consumption is in almost perfect agreement with the previously reported dissolution yield [12,16]. For the UO_2 powder used in the experiment, the dominating reaction path is uranium oxidation.

The accumulated hydroxyl radical production normalized to surface area upon reaction between H_2O_2 and the UO_2 based pellets studied in this work is presented as a function of reaction time in Fig. 1.

It is obvious that hydroxyl radicals are formed during reaction of H_2O_2 with all the UO_2-based pellets. The rate of hydroxyl radical production differs by approximately 30% between the most and

least reactive pellet, i.e. the rate is virtually independent of doping. Given the fact that the dissolution yield varies by more than two orders of magnitude, this strongly indicates that the redox reactivity of the pellet is influenced to a greater extent by doping than is its catalytic ability. The uranium concentration was also measured as function of reaction time in the same experiments. The results are displayed in Fig. 2.

There is a significant difference in the rate of uranium dissolution between the pellets. While almost no uranium was detected in solution in the reaction with SIMFUEL, a significant amount was dissolved in the reaction with the Westinghouse UO_2 pellet. This difference is far too large to be attributed to a difference in the overall H_2O_2 reactivity or rate of catalytic H_2O_2 decomposition.

3.1. Reactivity of different oxidants

Since differences in the ability to catalyze the decomposition of H_2O_2 cannot explain the observed differences in dissolution yield, the rationale for this must be differences in the redox reactivity of the doped materials. In order to elucidate this possibility we performed experiments using pure oxidants that cannot undergo catalytic decomposition. In addition to H_2O_2, which has already been studied quite extensively, we used $IrCl_6^{2-}$ and MnO_4^- to monitor the redox reactivity of the doped UO_2 materials. In Fig. 3 the MnO_4^- concentration as a function of reaction time is presented for the reactions of this species with Westinghouse UO_2 and SIMFUEL.

The plot clearly shows that UO_2 is more reactive than SIMFUEL towards MnO_4^-. In addition, the activation energy for oxidation of UO_2 by MnO_4^- is lower than the activation energy for oxidation of SIMFUEL by MnO_4^-. The measured activation energies were extracted from the Arrhenius plots represented in Fig. 4.

The obtained activation energies are (7.4 ± 0.6) kJ mol^{-1} for the reaction with UO_2 and (13 ± 2) kJ mol^{-1} for the reaction with SIMFUEL. This confirms that the observed difference in reactivity is not the result of a difference in number of reactive sites. The difference in activation energy reflects a difference in the energy barrier for oxidation, i.e. a difference in redox reactivity. The activation energy for oxidation of UO_2 by O_2 is reported to vary between 67 and 126 kJ mol^{-1}. These data refer to the dry oxidation of UO_2 by oxygen [29]. Recently a quantum chemical study revealed the important role of the presence of water on the surface of UO_2 in what concerns the oxidation of this material [30]. The authors reported a lowering in the energy barrier for reaction of O_2 with the surface of UO_2 in aqueous solution when compared to the equivalent gas phase process. In this work, we measured the energy barrier for oxidation of UO_2 with stronger oxidants than O_2. Both factors are expected to lower the energy barrier considerably. The difference in the release of U(VI) into solution between undoped and doped UO_2 pellets can be rationalized with the fact that the inclusion of dopants alters the corrosion resistance of the doped pellets by causing changes in the structural parameters and surface energies of the oxides. It was previously demonstrated [31] that doping a metal oxide can increase its surface energy and this stabilizes the surface. These new types of surfaces can have altered reactivity and improved mechanical and chemical resistance. For the case of UO_2, this fact was shown in a previously published work where it was demonstrated that the inclusion of Y^{3+} into UO_2 pellets increases the corrosion resistance of the latter when oxidized in air at high temperatures, $T = [1375–1750]$ °C [20]. This fact is explained in a review by McEachern and Taylor [32] where the authors attribute the increased corrosion resistance to the enhanced surface stability of the doped material when compared to the undoped UO_2. This will cause a change in the corrosion mechanism between the undoped and doped materials according to the authors. A similar phenomenon can be expected to cause the

Table 1
Dissolution yields expressed as % of [U(VI)] in solution per [H_2O_2] consumed for different UO_2 based materials.

| Material	Dissolution yield (%)
UO_2 powder	80 [12]
UO_2 pellet (Westinghouse)	14 [23]
SIMFUEL pellet	0.2 [23]
UO_2 pellet (in house)	6 [24]
UO_2/Y_2O_3 pellet (in house)	2.5 [24]
$UO_2/Y_2O_3/Pd$ pellet (in house)	0.9
UO_2/Pd pellet (in house)	11.5 [25]
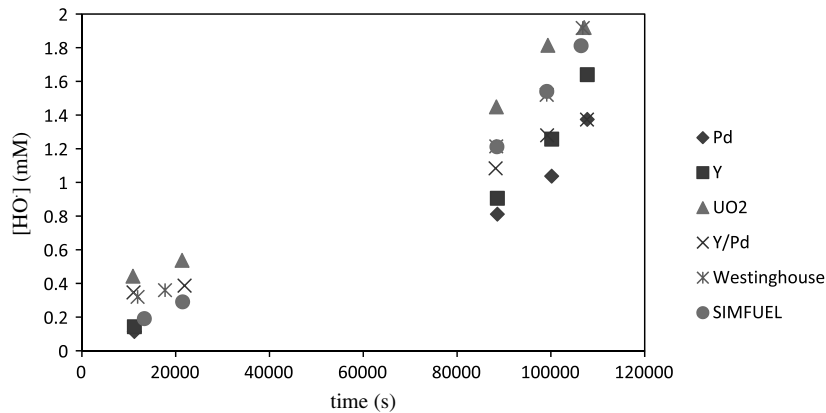
Fig. 1. Accumulated hydroxyl radical concentration (normalized to pellet surface area) as a function of reaction time for the different UO_2 based pellets studied in this work. $\sigma_e = \pm 25 \times 10^{-3}$ mM.
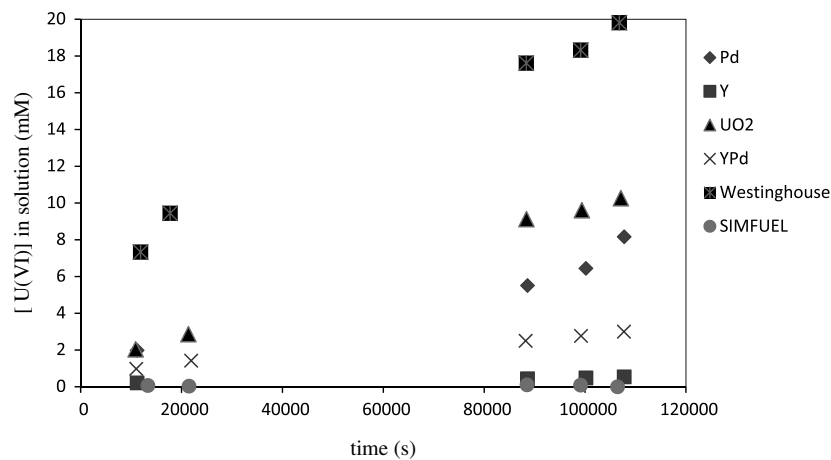

Fig. 2. [U(VI)] in solution (normalized to pellet surface area) as a function of reaction time for the reaction of H_2O_2 with the different UO_2 based pellets. $\sigma_e = \pm 25 \times 10^{-3}$ mM.
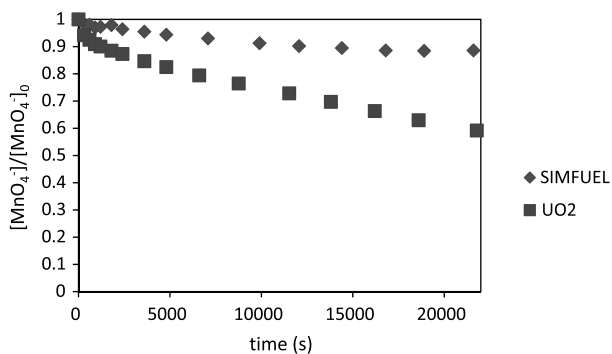

Fig. 3. Evolution in the concentration of MnO_4^- in the reaction with UO_2 and SIMFUEL pellets ($\sigma_e = \pm 0.05$).
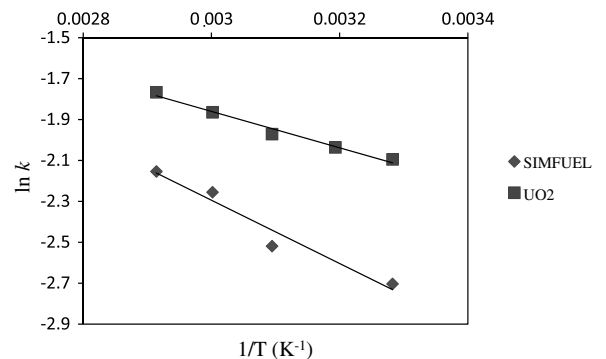

Fig. 4. Arrhenius plots for the reactions between MnO_4^- and UO_2 (Westinghouse) and SIMFUEL pellets for $T = [303.15–343.15]$ K with a temperature step of 10 K. The experimental uncertainty in the rate constant is $\pm 10\%$.

differences visible in the plots of Fig. 2. By increasing the stability of the doped UO_2 and consequently changing the mechanism through which this material will react with oxidants when compared to the undoped UO_2, one can expect different redox reactivity and a possible reduction in the amount of U(VI) released into solution. The first-order rate constants (based on initial rates normalized to exposed surface area) for reactions of H_2O_2, MnO_4^- and $IrCl_6^{2-}$ with the pellets used in this study are summarized in Table 2. The rate constant for H_2O_2 was extracted from the overall reactivity towards the pellets taking the oxidative dissolution yield (Table 1) into account.

It can clearly be seen that the redox reactivity of the doped materials differ significantly for the weaker oxidant (MnO_4^-) while the reaction with the stronger oxidant ($IrCl_6^{2-}$) in general is much faster and the difference in reactivity between the doped materials is insignificant. For H_2O_2, the redox reactivity towards the pellets is lower and the difference between the pellet reactivities is also more pronounced than for MnO_4^-. Judging from these data, the rate constant for matrix oxidation increases with increasing reduction potential of the oxidant as was also previously observed for pure

Table 2
First-order rate constants for reactions of H_2O_2, MnO_4^- and $IrCl_6^{2-}$ with the different UO_2 based pellets studied in this work (uncertainty ±10%).

Pellet	$k\ (H_2O_2)/(s^{-1})$	$k\ (MnO_4^-)/(s^{-1})$	$k\ (IrCl_6^{2-})/(s^{-1})$
UO_2 (Westinghouse)	2.5×10^{-6}	5.5×10^{-5}	3.3×10^{-4}
SIMFUEL	2.3×10^{-8}	1.0×10^{-5}	2.8×10^{-4}
UO_2	7.2×10^{-7}	1.0×10^{-4}	3.3×10^{-4}
UO_2/Y_2O_3	2.2×10^{-7}	8.8×10^{-5}	3.5×10^{-4}
$UO_2/Y_2O_3/Pd$	7.2×10^{-8}	7.7×10^{-5}	3.8×10^{-4}
UO_2/Pd	1.1×10^{-6}	1.3×10^{-4}	3.7×10^{-4}

Table 3
Rate constants for oxidation of UO_2 (Westinghouse) and SIMFUEL by radiolytic oxidants calculated from extrapolation of Fig. 5.

Oxidants	E^o(V vs SHE)	k_{ox} (UO_2) m s^{-1}	k_{ox} (SIM) m s^{-1}
O_2	-0.15 [34]	2.7×10^{-11}	1.3×10^{-15}
H_2O_2	0.46 [35]	1.0×10^{-8}	9.5×10^{-11}
CO_3^-	1.59 [36]	1.7×10^{-5}	1.7×10^{-5}
$OH\cdot$	1.9 [35]	1.7×10^{-5}	1.7×10^{-5}

UO_2 powder [33]. The results indicate that the sensitivity to doping increases with decreasing reduction potential of the oxidant. The results presented above clearly show that the redox reactivity is significantly influenced by doping. To further illustrate the trend presented in Table 2, we have plotted the logarithm of the ratio between the rate constants for oxidation of SIMFUEL and UO_2 (Westinghouse), reflecting the difference in activation energy between the two pellets, against the reduction potential of the oxidant in Fig. 5.

If we apply a linear extrapolation from Fig. 5 (keeping in mind that the plot in Fig. 5 is NOT expected to be linear as the logarithm of the ratio between the rate constants is expected to asymptotically approach 0 for oxidants with higher standard potentials) we can roughly estimate the relative rate constant for oxidation of SIMFUEL by O_2 to be at least 21,000 times lower than for a UO_2 pellet. For oxidants stronger than $IrCl_6^{2-}$ (i.e. $OH\cdot$ and CO_3^-) for which the activation energies approach 0, the rate constants are expected to be similar for UO_2 and SIMFUEL (diffusion controlled). To illustrate the trends discussed above we have calculated the rate constants for oxidation of UO_2 (Westinghouse) and SIMFUEL by the most common radiolytic oxidants. The resulting rate constants are summarized in Table 3.

Similar trends are observed for the Y_2O_3 and Y_2O_3/Pd doped UO_2 pellets. The relative impact of radiolytic oxidants has previously been used to assess the relative importance of the oxidants in oxidative dissolution of spent nuclear fuel [11]. From the data presented in Table 3 we can conclude that, while the impact of the strongly oxidizing radicals is the same for both pellets, the impact of H_2O_2 is more than 100 times lower for SIMFUEL than for UO_2 (Westinghouse). For O_2 the impact is 21,000 times lower than for UO_2. How these changes will influence the relative impact of each oxidant depends on the relative oxidant concentrations. Hence, doping of UO_2 will change the relative impact of the radiolysis products. The relative impact of radicals will increase as the relative impact of molecular oxidants decreases. These findings are important to keep in mind when employing data obtained from pure UO_2-systems for modelling radiation induced spent nuclear fuel dissolution.

4. Conclusions

In this work we have studied the catalytic decomposition of H_2O_2 on doped UO_2 pellets. The redox reactivity of the pellets was studied using MnO_4^- and $IrCl_6^{2-}$ as oxidants. From these experiments the following conclusions can be drawn.

Hydroxyl radicals are produced upon catalytic decomposition of H_2O_2 on pure UO_2 pellets as well as on doped UO_2 pellets. The rate of hydroxyl radical production varies by 30% between the most and least reactive pellet. Hence, the activation energy for catalytic decomposition of H_2O_2 is very similar for all the pellets. This is the major reaction pathway for the reaction between H_2O_2 and the spent nuclear fuel surface and should be accounted for in the safety analysis.

The redox reactivity study shows that the main effect of doping is a decrease in the redox reactivity. This is confirmed by differences in rate constants for oxidation as well as differences in activation energy. Consequently, the level of doping (depending on fuel burn-up) must be accounted for in the safety analysis.

References

[1] D.W. Shoesmith, J. Nucl. Mater. 282 (2000) 1–31.
[2] R.L. Segall, R.S.C. Smart, J. Nowotny, Surface and Near-Surface Chemistry of Oxide Materials, Elsevier Science Publishers BV, Amsterdam, 1988.
[3] I. Casas, J. de Pablo, J. Giménez, M.E. Torrero, J. Bruno, E. Cera, R.J. Finch, R.C. Ewing, Geochim. Cosmochim. Acta 62 (1998) 2223.
[4] D. Rai, A.R. Felmy, J.L. Ryan, Inorg. Chem. 29 (1990) 260.
[5] O. Roth, M. Jonsson, Cent. Eur. J. Chem. 6 (2008) 1–14.
[6] I. Grenthe, D. Ferri, F. Salvatore, G. Riccio, Dalton Trans. (1984) 2439–2443.
[7] J.d. Pablo, I. Casas, J. Giménez, M. Molera, M. Rovira, L. Duro, J. Bruno, Geochim. Cosmochim. Acta 63 (1999) 3097–3103.
[8] D.E. Grandstaff, Econ. Geol. 71 (1976) 1493–1506.
[9] E.M. Pierce, J.P. Icenhower, R.J. Serne, J.G. Catalano, J. Nucl. Mater. 345 (2005) 206–218.
[10] G. Choppin, J.O. Liljenzin, J. Rydberg, Radiochemistry and Nuclear Chemistry, second ed., Butterworth-Heinemann Ltd., Oxford, 1995.
[11] E. Ekeroth, O. Roth, M. Jonsson, J. Nucl. Mater. 355 (2006) 38–46.
[12] M. Jonsson, E. Ekeroth, O. Roth, Dissolution of UO_2 by one- and two-electron oxidants, in: V.M. Oversby, L.O. Werme (Eds.), Scientific Basis for Nuclear Waste Management Xxvii, Materials Research Society, Warrendale, 2004, pp. 77–82.
[13] M. Suh, P.S. Bagus, S. Pak, M.P. Rosynek, J.H. Lunsford, J. Phys. Chem. B 104 (2000) 2736–2742.
[14] M. Anpo, M. Che, B. Fubini, E. Garrone, E. Giamello, M. Paganini, Top. Catal. 8 (1999).
[15] C.M. Lousada, M. Jonsson, J. Phys. Chem. C 114 (2010) 11202–11208.
[16] C.M. Lousada, M. Trummer, M. Jonsson, doi: http://dx.doi.org/10.1016/j.jnucmat.2011.06.003.

Fig. 5. Logarithm of the ratio between the rate constants for oxidation of SIMFUEL and Westinghouse pellets as a function of the reduction potential of the oxidant (H_2O_2, MnO_4^- and $IrCl_6^{2-}$).

[17] C.J. Rhodes, Prog. React. Kinet. Mech. 30 (2005) 145–213.
[18] H. Kleykamp, J. Nucl. Mater. 131 (1985) 221–246.
[19] J.-G. Kim, Y.-K. Ha, S.-D. Park, K.-Y. Jee, W.-H. Kim, J. Nucl. Mater. 297 (2001) 327–331.
[20] W.B. Wilson, C.A. Alexander, A.F. Gerds, J. Inorg. Nucl. Chem. 20 (1961) 242–251.
[21] L.E. Thomas, R.E. Einziger, H.C. Buchanan, J. Nucl. Mater. 201 (1993) 310–319.
[22] V.M. Oversby, Uranium Dioxide, SIMFUEL, and Spent Fuel Dissolution Rates – A Review Of Published Data, SKB, Tech. Rep. TR-99-22, 1999.
[23] S. Nilsson, M. Jonsson, J. Nucl. Mater. 410 (2011) 89–93.
[24] M. Trummer, B. Dahlgren, M. Jonsson, J. Nucl. Mater. 407 (2010) 195–199.
[25] M. Trummer, S. Nilsson, M. Jonsson, J. Nucl. Mater. 378 (2008) 55–59.
[26] M. Trummer, O. Roth, M. Jonsson, J. Nucl. Mater. 383 (2009) 226–230.

[27] M.E. Broczkowski, J.J. Noël, D.W. Shoesmith, J. Nucl. Mater. 346 (2005) 16–23.
[28] M. Trummer, M. Jonsson, J. Nucl. Mater. 396 (2010) 163–169 (189–198).
[29] Z. Chernia, Phys. Chem. Chem. Phys. 11 (2009) 1729–1739.
[30] F.N. Skomurski, L.C. Shuller, R.C. Ewing, U. Becker, J. Nucl. Mater. 375 (2008) 290–310.
[31] Z. Zong, Y. Ma, T. Hu, G. Cui, Q. Cui, M. Zhang, G. Zou, Solid State Commun. 151 (2011) 607–609.
[32] R.J. McEachern, P. Taylor, J. Nucl. Mater. 254 (1998) 87–121.
[33] E. Ekeroth, M. Jonsson, J. Nucl. Mater. 322 (2003) 242–248.
[34] A.J. Bard, R. Parsons, J. Jordan, Standard Potentials in Aqueous Solution, Marcel Dekker, New York, 1985.
[35] P. Wardman, J. Phys. Chem. Ref. Data 18 (1989) 1637–1755.
[36] R.E. Huie, C.L. Clifton, P. Neta, Radiat. Phys. Chem. 38 (1991) 477–481.

IV

Mechanism of H$_2$O$_2$ Decomposition on Transition Metal Oxide Surfaces

Cláudio M. Lousada,* Adam Johannes Johansson, Tore Brinck, and Mats Jonsson

Applied Physical Chemistry, School of Chemical Science and Engineering, KTH Royal Institute of Technology, SE-100 44 Stockholm, Sweden

ABSTRACT: We performed an experimental and density functional theory (DFT) investigation of the reactions of H$_2$O$_2$ with ZrO$_2$, TiO$_2$, and Y$_2$O$_3$. In the experimental study we determined the reaction rate constants, the Arrhenius activation energies, and the activation enthalpies for the processes of adsorption and decomposition of H$_2$O$_2$ on the surfaces of nano- and micrometer-sized particles of the oxides. The experimentally obtained enthalpies of activation for the decomposition of H$_2$O$_2$ catalyzed by these materials are 30 ± 1 kJ·mol^{-1} for ZrO$_2$, 34 ± 1 kJ·mol^{-1} for TiO$_2$, and 44 ± 5 kJ·mol^{-1} for Y$_2$O$_3$. In the DFT study, cluster models of the metal oxides were used to investigate the mechanisms involved in the surface process governing the decomposition of H$_2$O$_2$. We compared the performance of the B3LYP and M06 functionals for describing the adsorption energies of H$_2$O$_2$ and HO$^\bullet$ onto the oxide surfaces as well as the energy barriers for the decomposition of H$_2$O$_2$. The DFT models implemented can describe the experimental reaction barriers with good accuracy, and we found that the decomposition of H$_2$O$_2$ follows a similar mechanism for all the materials studied. The average absolute deviation from the experimental barriers obtained with the B3LYP functional is 6 kJ·mol^{-1}, while with the M06 functional it is 3 kJ·mol^{-1}. The differences in the affinity of the different surfaces for the primary product of H$_2$O$_2$ decomposition, the HO radical, were also addressed both experimentally and with DFT. With the experiments we found a trend in the affinity of HO$^\bullet$ toward the surfaces of the oxides, depending on the type of oxide. This trend is successfully reproduced with the DFT calculations. We found that the adsorption energy of HO$^\bullet$ varies inversely with the ionization energy of the metal cation present in the oxide.
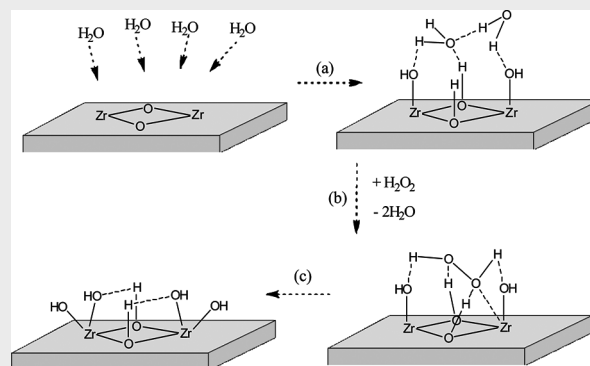
1. INTRODUCTION

Reactions of H$_2$O$_2$ with metal and metal oxide surfaces have been studied to some extent[1-7] mainly due to their importance in areas ranging from catalysis to geo- and environmental chemistry and nuclear technology. Due to the complexity of the systems involved, which is dominated by the heterogeneity caused by the introduction of a solid phase, several mechanistic details remain to be understood. Furthermore, effects such as solution pH, type of oxide, temperature, and oxide particle size have profound effects on the kinetics and energetics of this type of reactions.[8-10] The reactivity of H$_2$O$_2$—an aqueous radiolysis product—toward metal and metal oxide surfaces is important in the context of nuclear technology.[11] The knowledge of the mechanistic details that govern this type of reactions is of the utmost importance for allowing a rigorous assessment of the chemistry of nuclear technological systems which is determinant for sensitive issues such as the reliability, stability, and safety of an operating nuclear power plant or of a repository for spent nuclear fuel.[12,13] In spite of their importance in a variety of contexts, radiation-induced processes at solid−liquid interfaces are often poorly understood. To better understand these processes, the mechanisms and kinetics of reactions between radiolysis products in solution and the solid surfaces must be known.[14]

Besides being able to react through a redox path,[15] H$_2$O$_2$ also reacts via catalytic decomposition.[16,17] The latter type of reaction is typical of systems where the metal present in the oxide cannot undergo further oxidation. Nevertheless, the presence of catalytic decomposition of H$_2$O$_2$ in systems where the metal atoms have the possibility to undergo oxidation has been reported.[18] Since H$_2$O$_2$ can act both as an oxidant and as a reductant, reduction of Ti^{4+} to Ti^{3+} by reaction of H$_2$O$_2$ with TiO$_2$ has also been proposed based on experimental studies.[19] The initial step of the catalytic decomposition of H$_2$O$_2$ on metal oxide surfaces has been proposed to be the homolytic cleavage of the O−O bond in H$_2$O$_2$ to form two HO radicals.[19,20] We previously reported a study in which we followed the dynamics of formation of HO radicals during the course of H$_2$O$_2$ decomposition on the surface of ZrO$_2$. Our findings show that the HO radical is a primary product of this type of reaction.[21] The further reactions of the HO radicals formed in this process are still a matter that is not completely understood. It has been suggested that these radicals can react further with H$_2$O$_2$ to form HO$_2^\bullet$ and O$_2^{\bullet-}$.[7,22,23] In previous

studies of this type of reaction, EPR/ESR measurements revealed the presence of $HO_2^{\cdot}$, $O_2^{\cdot-}$, and peroxyl radical species on the surface of different oxides. These normally short-lived and reactive species had become long-lived due to the stabilization imparted by their adsorption onto the oxide surface.[20,24] It was also demonstrated that the possible existence of such chemical species is a factor that depends on the solution pH. Kinetic studies on these systems have shown that for the catalytic decomposition of H_2O_2 on different metal oxide surfaces similar activation energies are involved, while the pre-exponential factors differ widely. Consequently, the rate constants differ substantially depending on the type of oxide.[25] This indicates that different surface processes might be involved in the reactions of H_2O_2 with the different metal oxides.

In this paper, we report a combined theoretical and experimental effort aimed at providing an understanding of the mechanisms and surface processes involved in the reactions of H_2O_2 with different metal oxides. We performed a comprehensive experimental investigation of the reactions between H_2O_2 and ZrO_2, TiO_2 and Y_2O_3. We studied the kinetics of such reactions, and some mechanistic aspects were addressed. The affinity of HO radicals for the different metal oxides was also studied. Density functional theory (DFT) calculations were used to study the reactions of the different oxide surfaces with H_2O_2 and $HO^{\bullet}$. The potential for using molecular cluster models to describe these systems was explored using the DFT functionals B3LYP (refs 26−29) and M06 (ref 30).

The surface processes studied in this work are represented in Figure 1. The adsorption of H_2O onto metal oxide surfaces can
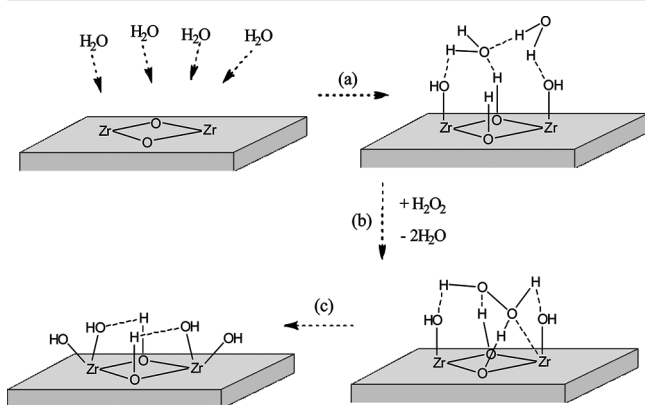

Figure 1. Surface processes studied in this work: (a) adsorption of H_2O; (b) reaction with H_2O_2—initial adsorption of H_2O_2 with desorption of H_2O; and (c) formation of products of the decomposition of H_2O_2 and their adsorption to the surface.

occur via two pathways which are molecular adsorption or dissociative adsorption.[31] It has been reported that the mode of adsorption of the first layer of water onto a metal oxide surface is in general dissociative.[32] However, for certain defective metal oxide surfaces, the cleavage of water occurs spontaneously only on specific surface defects.[32−34] The first reaction step investigated in this work by DFT was the adsorption of H_2O_2 onto the surfaces of the clusters in which H_2O had been previously dissociatively adsorbed. The energies of H_2O adsorption obtained in an undergoing work where we study the performance of similar cluster models to describe a diversity of surface processes[35] are compared with the available data in

the literature. These values are used as benchmarks for the performance of our cluster models. A comparison between our experimentally obtained activation enthalpies for the decomposition of H_2O_2 on the surface of the different metal oxides and the values calculated with DFT allowed us to conclude that we can, to a good extent, describe the complex chemistry of the surface reactions involved, by using small clusters comprised of $(M_xO_y)_2$ where M is the metal atom. This indicates that on the real particle surfaces, due to the dominance of surface defects, localized properties of the surface are decisive in determining the mechanism of the reaction and its kinetics and energetics.

2. EXPERIMENTAL AND COMPUTATIONAL METHODS

2.1. Instrumentation. Specific surface areas of the powders were determined using the BET method of isothermal adsorption and desorption of a gaseous mixture consisting of 30% N_2 and 70% He on a Micrometrics Flowsorb II 2300 instrument. γ-Irradiation was performed using an MDS Nordion 1000 Elite Cs-137 γ-source with a dose rate of 0.15 Gy·s^{-1}. This value was determined by Fricke dosimetry.[36] X-ray powder diffractograms (XRDs) were obtained at 293.15 K, using Cu K$_{\alpha}$ radiation, on a PANanalytical X'pert instrument. For all samples, the default setup with the X'Celerator was used. The data were collected over the range $10° \leq 2\theta \leq 100°$, with a step size of $0.033°$ (2θ). Data evaluation was done using The High Score Plus software package, and the PDF-2 database was used for matching the experimentally obtained diffractograms. The reactions were performed under an inert atmosphere with a constant flux of N_2 gas (AGA Gas AB) with a flow rate of 0.21 L·min^{-1} that was also used for stirring the solutions. The temperature was kept constant throughout the experiments by using a Huber CC1 or a Lauda E100 thermostat, calibrated against a Therma 1 Thermometer coupled to a submersible K-type (NiCrNi) temperature probe, with a precision of ±0.1 K. For the γ-irradiations, the samples were purged with N_2O with a flow rate of 0.7 L·min^{-1}. UV/vis spectra were collected using a WPA Biowave II UV/vis spectrophotometer.

2.2. Reagents and Experiments. All the solutions used in this study were prepared using water from a Millipore Milli-Q system.

ZrO_2 (CAS[1314-23-4], Aldrich 99%), TiO_2 (CAS[13463-67-7], Alfa Aesar, 99.9%), and Y_2O_3 (CAS[1314-36-9], Alfa Aesar, 99.9%) were used without further purification. A Rietveld refinement using ICSD-26488 as a starting model was performed yielding the following cell parameters for ZrO_2: (a) 5.1458(2) Å, (b) 5.2083(3) Å, (c) 5.3124(3) Å. These values are in good agreement with the cell parameters attributed to the monoclinic phase.[37] For TiO_2, the Rietveld refinement yielded a composition of 88.5% anatase and 11.5% rutile. The obtained cell parameters for TiO_2 are: (a = b) 3.7856(2) Å, (c) 9.5058(5) Å for the anatase phase, and (a = b) 4.5914(8) Å, (c) 2.9539(10) Å for the rutile phase.[38] The obtained cell parameters for Y_2O_3 are: (a) 10.60398(9) Å, attributed to the bixbyite-type structure.[39] The specific surface areas of the powders were found to be 5.0 ± 0.2 m^2·g^{-1} for ZrO_2, 38.9 ± 0.2 m^2·g^{-1} for TiO_2, and 4.48 ± 0.03 m^2·g^{-1} for Y_2O_3. These values are the average of three measurements, each consisting of a sorption and a desorption isotherm whose values were also averaged. The particle suspensions where the reactions with H_2O_2 took place consisted of TiO_2 (0.146−0.341 g) or Y_2O_3 (1.269−2.961 g) in 50 mL of H_2O_2 (0.5−6 mM) solution. The H_2O_2 solutions were prepared from a 30% standard solution (Merck). After extraction of the sample from

9534

dx.doi.org/10.1021/jp300255h | J. Phys. Chem. C 2012, 116, 9533−9543

the reaction vessel, the sample was filtered through a Gema Medical 0.45 μm−25 mm Cellulose Acetate syringe filter. Subsequently, a sample volume of 0.2 mL was used for the measurement of the H_2O_2 concentration. The concentration of H_2O_2 was determined using the Ghormley triiodide method. In this method, I^- is oxidized to I_3^- by H_2O_2.[40,41] The absorbance of the product I_3^- is measured spectrophotometrically at the wavelength of 350 nm. A calibration curve where the absorbance of I_3^- was plotted as a function of the concentration of H_2O_2 was obtained in the range 0.02−0.8 mM resulting in a linear correlation between absorbance and concentration. A mechanistic study of the decomposition of H_2O_2 on the surface of the metal oxides was carried out and involved verifying the presence and quantifying the rate of production of $HO^\bullet$ as intermediate product in H_2O_2 decomposition on TiO_2 and Y_2O_3. This was done by means of the reaction between tris(hydroxymethyl)aminomethane (Tris) (CAS[77-86-1], BDH Chemicals, 99%) and the HO radicals to produce formaldehyde. The formaldehyde produced was then quantified spectrophotometrically at 368 nm, by using a modified version of the Hantzsch reaction. We reported this method to detect the HO radicals in a previous work,[21] and the same procedure was followed in this study. The reaction media for $HO^\bullet$ detection during decomposition of H_2O_2 consisted of TiO_2(0.197 g) or Y_2O_3, (1.678 g) in 50 mL of solution H_2O_2 (5 mM) with Tris (20 mM) at a pH of 7.5. The pH was adjusted with HCl. The study of the scavenging capacities of the oxides toward $HO^\bullet$ consisted initially of γ-irradiating samples of the oxides in the presence of Tris. The reaction media used was ZrO_2 (1.5 g) or TiO_2 (0.197 g) or Y_2O_3 (1.678 g) in 50 mL of Tris (20 mM) solution at pH 7.5. The pH was adjusted with HCl. The detection of the amount of HO radicals scavenged by Tris followed the same procedure as described above.

2.3. Computational Details. DFT calculations were performed using the Molecular Cluster Model (MCM)[42] approach and the software package Jaguar 7.7.[43] Cluster geometries were optimized using the hybrid functional B3LYP (refs 26−29) with the LACVP+* basis set. B3LYP can provide accurate molecular geometries even when hydrogen bonds are present.[44] The basis set LACVP+* is a combination of the split valence basis set 6-31+G(d) and the Los Alamos effective core potential for the transition metals Zr, Ti, and Y. Single-point evaluations of the energies were performed at the B3LYP/LACV3P++** and M06 (ref 30)/LACV3P++** levels of theory. The basis set LACV3P++** is triple-ζ in the valence space and is supplemented with polarization and diffuse functions on all atoms. Tight SCF convergence criteria were used for all calculations. Transition states were located using the quadratic synchronous transit (QST) method implemented in Jaguar 7.7. To characterize the stationary points and make zero-point energy corrections, a frequency analysis was done for all stationary points. All transition states were found to have one imaginary frequency.

The adsorption energies reported herein were calculated as

$$\Delta E_{ads} = E_{adsorbate/cluster} - (E_{adsorbate} + E_{cluster}) \tag{1}$$

were $E_{adsorbate/cluster}$, $E_{adsorbate}$, and $E_{cluster}$ represent the optimized electronic energies in the gas phase for the adsorbate binding to the cluster, free adsorbate, and bare cluster, respectively. This means that the more negative the electronic adsorption energy, the stronger is the adsorption.

Corrections to obtain the thermodynamic potential enthalpy (H) were calculated from a Hessian matrix of harmonic force constants using the partition functions of an ideal-/non-interacting gas at T = 298.15 K and P = 1 atm. The vibrational frequencies obtained from the Hessian matrix were also used to verify the first-order saddle point nature of the transition states.

3. RESULTS AND DISCUSSION

3.1. Experimental Results. *3.1.1. Kinetics of Decomposition of H_2O_2 on ZrO_2, TiO_2, and Y_2O_3.* The reaction of H_2O_2 with a solid catalyst which in this case is a metal oxide of the type M_xO_y consists of a series of steps characteristic of cycling surface-catalyzed reactions. The first step is the diffusion and adsorption of H_2O_2 to the surface followed by its cleavage to form $HO^\bullet$. One can write these two processes as

$$H_2O_2(aq) \underset{k_{a''}}{\overset{k_{a'}}{\rightleftharpoons}} H_2O_2(ads) \tag{R1}$$

$$H_2O_2(ads) \overset{k_b}{\to} 2HO(ads)/(aq) \tag{R2}$$
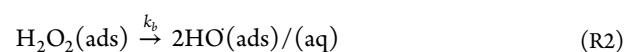
where reaction R1 represents the adsorption of H_2O_2 onto the oxide surface and R2 represents the cleavage of H_2O_2 catalyzed by the oxide surface to form HO radicals. $k_{a'}$ is the rate constant of adsorption of H_2O_2; $k_{a''}$ is the rate constant of desorption; and k_b is the rate constant for the cleavage of H_2O_2 on the surface of the metal oxide. When the surface is saturated with adsorbate, the rate of disappearance of H_2O_2 from solution will be governed by k_b of reaction R2. Hence, a quasi-equilibrium state is reached.[45]

It has been reported that the catalytic decomposition of H_2O_2 follows first-order kinetics.[46−48] However, the observed reaction order is strongly dependent on the solid-surface-area-to-solution-volume-ratio (S_A/V) and other experimental conditions.[21] When the available surface area of the catalyst is in excess, first-order kinetics are observed. Zeroth-order kinetics are observed when the available surface area is too small. In this work, using the same S_A/V as we used to obtain first-order kinetics in the case of ZrO_2,[21] it was verified that the reactions of H_2O_2 with TiO_2 and Y_2O_3 deviated from first-order kinetic behavior, and two different trends can be observed in the plots of Figure 2 where $[H_2O_2]_t$ is the concentration of H_2O_2 at time t and $[H_2O_2]_0$ is the concentration of H_2O_2 at t = 0. In both cases, after a fast initial consumption of H_2O_2, the reaction is slowed down significantly. To extract the rate constants, we considered the two visible trends for each reaction in Figure 2
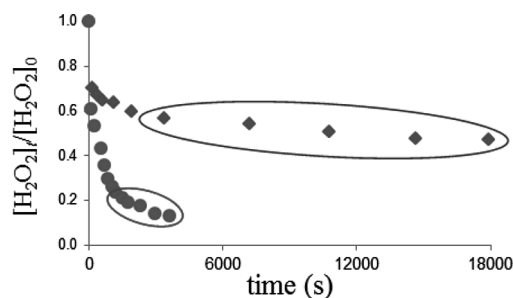

Figure 2. Normalized concentration of H_2O_2 as a function of reaction time in the reaction of H_2O_2 with TiO_2 (blue diamond) and Y_2O_3 (red circle) at T = 298.15 K with $[H_2O_2]_0$ = 0.5 mM. The highlighted areas denote the regions where the kinetics start to be controlled by the decomposition of H_2O_2 after the initial adsorption process.

to be the result of two different processes governing the kinetics. The nature of the two different kinetic trends of this reaction were investigated by performing the reaction in the presence of Tris buffer and tracking the formation of CH_2O with reaction time. Verifying if $HO^\bullet$ is formed during the stage of initial fast disappearance of H_2O_2 from solution is essential to make valid statements regarding the surface process involved. The process can be either molecular adsorption of H_2O_2 onto the surface or decomposition of H_2O_2 or a mixed adsorption/decomposition phenomenon. The reaction of H_2O_2 (5 mM) with TiO_2 (0.537 g) was performed in a volume of 50 mL of Tris (200 mM) solution at pH 7.5. The pH was adjusted with HCl.

It can be seen in Figure 3 that the initial disappearance of H_2O_2 from solution is not accompanied by the formation of a
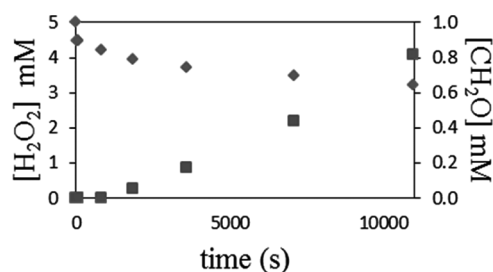

Figure 3. Evolution in the concentrations of H_2O_2 (blue diamond) and CH_2O (red square) during the reaction of H_2O_2 with a particle suspension of TiO_2 at T = 298.15 K.

detectable amount of HO radicals. From the calibration experiments, a consumption of the equivalent amount of H_2O_2 (0.5 mM) that disappeared from solution in the initial process would produce ~0.18 mM CH_2O. From Figure 3, we can see that this is not the case. Hence, we can conclude that the initial fast disappearance of H_2O_2 can be attributed to molecular adsorption of this species onto the surface of the TiO_2. We can attribute the two different kinetic trends represented in Figure 2 and Figure 3 to the following processes: an initial adsorption step followed by a second process that consists of the cleavage of H_2O_2 on the surface of the oxide. By extracting the rate constants from these plots, taking into account the fact that the two processes, adsorption and decomposition of H_2O_2, occur on different time scales, it is possible to obtain the kinetics of decomposition of H_2O_2 with minimal errors associated.

The kinetic experiments were performed using H_2O_2 (0.5 mM) with TiO_2 (0.197 g) or Y_2O_3 (1.67 g) in 50 mL of H_2O. The zeroth-order rate constants (k_0) obtained at T = 298.15 K, with a (S_A/V) = 1.4×10^5 m^{-1} for TiO_2 and 1.5×10^5 m^{-1} for Y_2O_3 are k_0 = $(5.9 \pm 0.6) \times 10^{-6}$ $M \cdot s^{-1}$ for the decomposition of H_2O_2 on TiO_2 and k_0 = $(4.5 \pm 0.4) \times 10^{-5}$ $M \cdot s^{-1}$ for the decomposition of H_2O_2 on Y_2O_3. The rate constants for adsorption under the same conditions were extracted from the initial parts of the plots. The obtained first-order rate constants (k_1) for this process are k_1 = 3×10^{-3} s^{-1} for adsorption of H_2O_2 on TiO_2 and k_1 = 6×10^{-3} s^{-1} for adsorption of H_2O_2 on Y_2O_3.

The variation of the rate constant with temperature generally follows the Arrhenius equation

$$k = Ae^{-E_a/RT} \tag{2}$$

where E_a is the Arrhenius activation energy for the reaction; A is the pre-exponential or the frequency factor; R is the gas constant; and T is the absolute temperature. The respective reaction enthalpies of activation were obtained by means of a linearization of the Eyring equation

$$\ln\left(\frac{k}{T}\right) = -\frac{\Delta H^{o,\ddagger}}{RT} + \frac{\Delta S^{o,\ddagger}}{R} + \ln\left(\frac{k_B}{h}\right) \tag{3}$$

where k is the reaction rate constant; T is the absolute temperature; $\Delta H^{o,\ddagger}$ is the enthalpy of activation; R is the gas constant; k_B is the Boltzmann constant; h is the Planck constant; and $\Delta S^{o,\ddagger}$ is the entropy of activation. To determine the Arrhenius activation energies and the activation enthalpies for the reactions of decomposition of H_2O_2 on TiO_2 and Y_2O_3, we obtained the zeroth-order rate constants as a function of temperature in the temperature intervals T = [298.15−348.15] K for TiO_2 and T = [293.15−308.15] K for Y_2O_3. The respective Arrhenius plots are represented in Figure 4. The
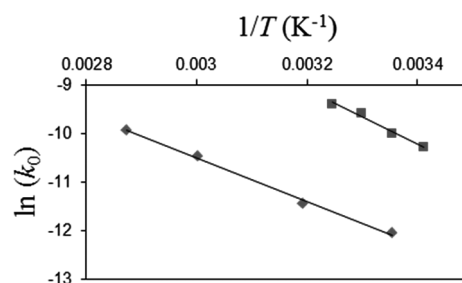

Figure 4. Arrhenius plots for the reaction of decomposition of H_2O_2 on TiO_2 (blue diamond) and Y_2O_3 (red square).

resulting activation energies for decomposition of H_2O_2 on TiO_2 and Y_2O_3 are 37 ± 1 $kJ \cdot mol^{-1}$ and 47 ± 5 $kJ \cdot mol^{-1}$, respectively. The pre-exponential factors are 18 ± 2 $M \cdot s^{-1}$ for TiO_2 and 6228 ± 6 $M \cdot s^{-1}$ for Y_2O_3. The activation enthalpies $\Delta H^\ddagger$ for H_2O_2 decomposition are 34 ± 1 $kJ \cdot mol^{-1}$ for TiO_2 and 44 ± 5 $kJ \cdot mol^{-1}$ for Y_2O_3.

The activation energies of adsorption $E_{a,ads}$ were calculated from plots of the logarithm of the first-order rate constants as a function of the inverse of the temperature. The activation enthalpies of adsorption $\Delta H_{ads}^\ddagger$ were determined by using the same first-order rate constants. The first-order rate constants for adsorption were extracted from the initial parts of the plots of $\ln([H_2O_2]_t/[H_2O_2]_0)$ as a function of reaction time. The resulting activation energies for adsorption are $E_{a,ads}$ = 23 ± 1 $kJ \cdot mol^{-1}$ for adsorption of H_2O_2 on TiO_2 and $E_{a,ads}$ = 32 ± 3 $kJ \cdot mol^{-1}$ for adsorption of H_2O_2 on Y_2O_3. The frequency factors are A = 21 ± 2 s^{-1} for the adsorption on TiO_2 and A = 2625 ± 3 s^{-1} for the adsorption on Y_2O_3. The activation enthalpies of adsorption are $\Delta H_{ads}^\ddagger$ = 21 ± 2 $kJ \cdot mol^{-1}$ for adsorption of H_2O_2 onto TiO_2 and $\Delta H_{ads}^\ddagger$ = 29 ± 3 $kJ \cdot mol^{-1}$ for adsorption of H_2O_2 onto Y_2O_3.

The second-order rate constants for the process of adsorption were determined by studying the variation of the pseudo first-order rate constants as a function of solid-surface-area-to-solution-volume-ratio. The rate expression for the adsorption process is given by

$$-\frac{d[H_2O_2]}{dt} = k_2\left(\frac{S_{A_{MxOy}}}{V}\right)[H_2O_2] \tag{4}$$

where $S_{A_{M_xO_y}}$ denotes the surface area of the metal oxide powder; V is the volume of the solution where the reaction takes place; and k_2 is the second-order rate constant. The second-order rate constants for adsorption of H_2O_2 onto the surfaces of TiO_2 and Y_2O_3 were obtained from experiments in which the first-order rate constants were determined for different oxide S_A values. The resulting data are represented in Figure 5. The second-order rate constants extracted from the
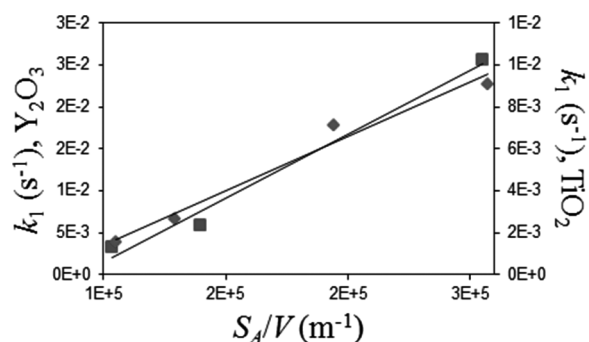

Figure 5. First-order rate constants as a function of solid-surface-area-to-solution-volume-ratio (S_A/V) for the adsorption of H_2O_2 onto Y_2O_3 (red square) and TiO_2 (blue diamond) at T = 298.15 K.

plots of Figure 5 obtained at T = 298.15 K are k_2 = (5.2 ± 0.6) × 10^{-8} m·s^{-1} for adsorption of H_2O_2 onto TiO_2 and k_2 = (1.5 ± 0.2) × 10^{-7} m·s^{-1} for adsorption of H_2O_2 onto Y_2O_3. These values are far from the diffusion limit of systems containing particle suspensions within this size range.[14] A plot of the variation of the zeroth-order rate constant for decomposition of H_2O_2 as a function of S_A/V gives the rate constant k which represents the catalytic capacity of the surface. The rate constants extracted from the plots of Figure 6, obtained at T =
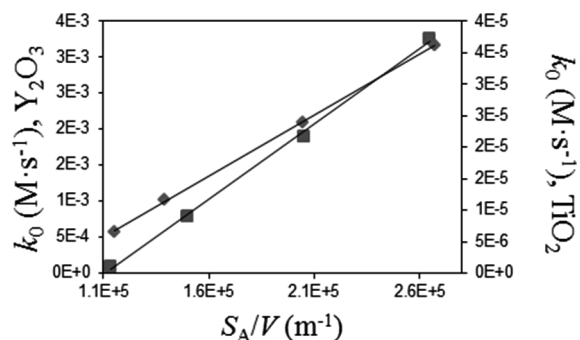

Figure 6. Zeroth-order rate constants as a function of solid-surface-area-to-solution-volume-ratio (S_A/V) for the reactions of decomposition of H_2O_2 with Y_2O_3 (red square) and TiO_2 (blue diamond) at T = 298.15 K.

298.15 K, are k = (1.93 ± 0.02) × 10^{-13} mol·m^{-2}·s^{-1} for reaction with TiO_2 and k = (2.08 ± 0.06) × 10^{-11} mol·m^{-2}·s^{-1} for reaction with Y_2O_3.

In the plots of Figure 1, it can be seen that it is possible to distinguish between the adsorption and the decomposition processes because the latter process is slower than the former. This allows us to determine the amount of H_2O_2 removed from solution during the adsorption process which is directly dependent on the number of adsorption sites on the surface of the oxides that can accommodate H_2O_2. By determining the amount of H_2O_2 removed from solution due to adsorption as a

function of the oxide surface area, we can estimate the number of adsorption sites per unit surface area of the oxide. Increasing the surface area of oxide increases the amount of H_2O_2 removed from solution by adsorption. The proportionality coefficient between these two quantities gives the number of adsorption sites available to accommodate H_2O_2 per unit surface area. The amount of H_2O_2 removed from solution as a function of TiO_2 and Y_2O_3 surface areas is represented in Figure 7. The number of adsorption sites that can
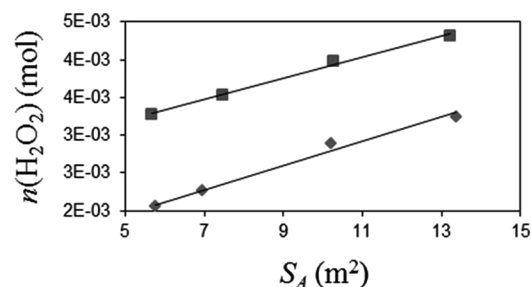

Figure 7. Variation in the amount (n) of H_2O_2 molecules removed from solution by adsorption onto TiO_2 (blue diamond) and Y_2O_3 (red square) as a function of the surface area of solid present in the reaction system.

accommodate H_2O_2, extracted from the slopes of the plots, is 2 × 10^{-4} mol·m^{-2} for TiO_2 and 1 × 10^{-4} mol·m^{-2} for Y_2O_3. These values correspond to 1.2 (adsorption sites)/Å^2 for TiO_2 and 0.6 (adsorption sites)/Å^2 for Y_2O_3.

3.1.2. Study of the Affinity of HO• for Metal Oxide Surfaces. Water radiolysis and the products formed therein are well documented in the literature. During the process of water radiolysis induced by γ radiation, for times greater than 10^{-6} s after energy deposition, the radiation chemical yields for the solvated electrons (e_{aq}^-) and HO• are the same.[49] Upon saturation of the aqueous phase with N_2O before and during irradiation, e_{aq}^- is quantitatively converted to HO•.[50]

We investigated the scavenging capabilities of the different metal oxides toward HO• present in solution. This was done by γ-irradiating aqueous powder suspensions of the different oxides in the presence of Tris. The competition for HO• between Tris and the surface of the oxides can give us a picture of the differences in the abilities of the different oxides to scavenge HO• from solution. A background plot was obtained to determine the yield of the method in a similar way as described in a previous work.[21] To obtain the background, the reaction media consisted of a solution of Tris (20 mM) at pH 7.5 adjusted with HCl in 50 mL of H_2O, continuously purged with N_2O. The yield of the method—CH$_2$O formed per total amount of HO• formed—is ≈35%. In the scavenging capability experiments, ZrO_2 (1.5 g, S_A = 7.5 m^2) or TiO_2 (0.197 g, S_A = 7.5 m^2) or Y_2O_3 (1.678 g, S_A = 7.5 m^2) were added to a solution with the same volume and composition as described above. Plots showing the amount of HO• detected as a function of irradiation time are represented in Figure 8. After irradiating the system for 1600 s, the different scavenging capacities of the different metal oxides toward HO• start to become evident. This fact can provide a qualitative measure of the affinity of HO• toward the surfaces of the oxides. The affinity of HO• toward the surfaces of the oxides is expected to control the relative kinetics for adsorption, desorption, and eventual diffusion of HO• on the surface.[51] According to the plots, the HO• affinity toward the surfaces vary in the order: $TiO_2 < ZrO_2$
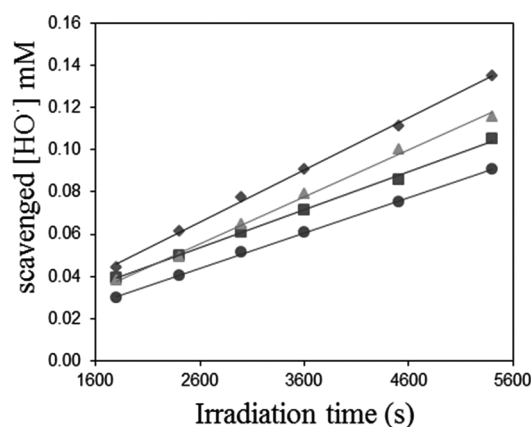
Figure 8. [HO•] measured in γ-irradiated solutions with and without the presence of different metal oxides. No oxide (blue diamond); TiO_2 (green triangle); ZrO_2 (red square); and Y_2O_3 (purple circle).

< Y_2O_3. The amount of HO• scavenged from solution by the metal oxide depends on the (S_A/V) of the metal oxide present in the system. Consequently, the amount of HO• detected varies inversely with metal oxide (S_A/V).

3.2. Computational Results. In this section, we discuss results of DFT calculations on the reactions of H_2O, H_2O_2, and HO• with stoichiometric clusters of ZrO_2, TiO_2, and Y_2O_3. The clusters studied are of the type $(ZrO_2)_2$, $(TiO_2)_2$, and (Y_2O_3). The choice for using these model sizes is based on an undergoing work where we verified that the type of reactions studied here can be modeled using minimal sized clusters for describing the metal oxides (work to be published).[35] There are several examples in the literature where it is shown that energy

barriers for reactions catalyzed by surface sites where the metal atoms are undercoordinated can be much lower than the energy barriers for equivalent reactions catalyzed by non-defective surfaces.[52−54] Consequently, for defective surfaces, the overall reaction rate is often determined by processes occurring at defect sites.[55] The physical-chemical properties of the defects and consequently the chemical reactivity of such surface sites are the result of the local properties of the defect and not so much dependent on the properties of the extended surface.

In our cited work,[35] the performance of the models used here is compared with the performance of larger clusters. The clusters used in this work can reproduce with small deviation the data obtained with clusters composed of 8 and 12 units of (M_xO_y) where M is the metal present in the oxide. The cluster performance in reproducing adsorption energies was evaluated by benchmarking the water adsorption energies against experimental and computational data found in the literature. The data can be found in Table 1. The overall performance of our models for describing water adsorption energies is good. The adsorption of water, both molecular and dissociative, can be modeled with good agreement between experimental and computational data using our minimal sized clusters to represent the metal oxides. The same clusters are used in this work to study the surface processes involved in the catalytic decomposition of H_2O_2 catalyzed by metal oxide particles. It should be noted that these particle surface topologies are dominated by defects. As H_2O adsorption is dissociative in most of the metal oxide defective surface sites,[31] the clusters where the reaction with H_2O_2 was performed had previously been saturated with the products of H_2O adsorption. These products are HO⁻ and H⁺ which bind to a surface metal and

Table 1. ΔE_{ads} Obtained with DFT Calculations for the Adsorption Reactions Represented in Figures 9−12 and Data Found in the Literature for Comparison[a]

data	H_2O molecular adsorption	H_2O dissociative adsorption	H_2O_2 molecular adsorption	HO• adsorption
		ZrO_2		
B3LYP	−80	−115	−121	−503
M06	−93	−129	−141	−514
literature - experimental	−(44)[b,60]	−(119; 142)[b,60] −(70−94)[b,61]	−−	−−
literature - theoretical	−(42−100)[c,62] −(57)[c,63]	−(194−208)[c,64] −(91−170)[c,62]	−−	−(498)[c,63]
		TiO_2		
data	H_2O molecular adsorption	H_2O dissociative adsorption	H_2O_2 molecular adsorption	HO• adsorption
B3LYP	−45	−146	−58	−382
M06	−52	−160	−81	−403
literature - experimental	−(48−68)[b,65]	−−	−−	−−
literature - theoretical	−(71−79)[c,66] −(90)[c,67] −(83)[c,68]	−(22−153)[c,66] −(141)[c,67]	−(4−78)[c,69]	−−
		Y_2O_3		
data	H_2O molecular adsorption	H_2O dissociative adsorption	H_2O_2 molecular adsorption	HO• adsorption
B3LYP	−70	−86	−83	−541
M06	−76	−96	−99	−550
literature - experimental	−−	−(91)[b,70] −(38−99)[b,71]	−−	−−
literature - theoretical	−−	−−	−−	−−

[a]All values in kJ·mol⁻¹—per mole of adsorbate. [b]Refers to an ΔH_{ads}. [c]Refers to an ΔE_{ads} without zero-point energy corrections.
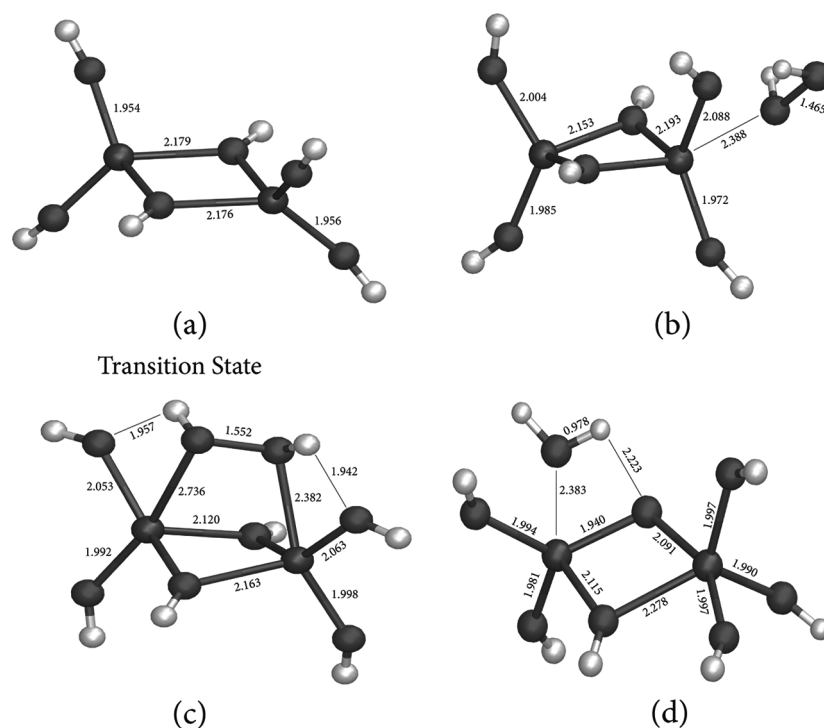
Figure 9. Optimized geometries for adsorption and further decomposition of H_2O_2 on a $(ZrO_2)_2$ cluster: (a) bare cluster, (b) chemisorption of a H_2O_2 molecule, (c) transition-state for the cleavage of the O—O bond in H_2O_2, (d) product of the decomposition of H_2O_2. Zr (blue); O (red); H (white).
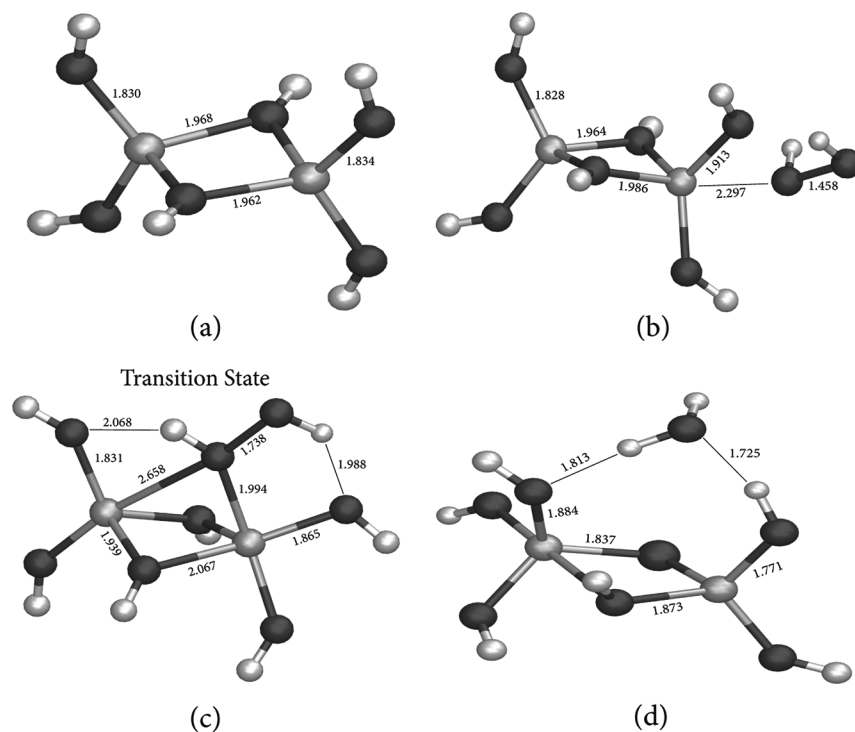
Figure 10. Optimized geometries for the study of adsorption and further decomposition of H_2O_2 in reaction with a $(TiO_2)_2$ cluster: (a) bare cluster, (b) chemisorption of a H_2O_2 molecule, (c) transition-state for the cleavage of the O—O bond in H_2O_2, (d) product of the decomposition of H_2O_2. Ti (cyan); O (red); H (white).

oxygen atoms, respectively. The structures of the resulting products are represented in Figures 9(a), 10(a), and 11(a).

To study the reactions of our clusters with H_2O_2, we investigated the molecular adsorption of this species as being the first step of the reaction of decomposition of H_2O_2 on the surface of the metal oxides. Energy minima geometries corresponding to the molecular adsorption of H_2O_2 onto the surface of the clusters were found for the three materials studied. The corresponding structures are depicted in Figures 9(b), 10(b), and 11(b). The obtained adsorption energies are

9539

dx.doi.org/10.1021/jp300255h | J. Phys. Chem. C 2012, 116, 9533–9543
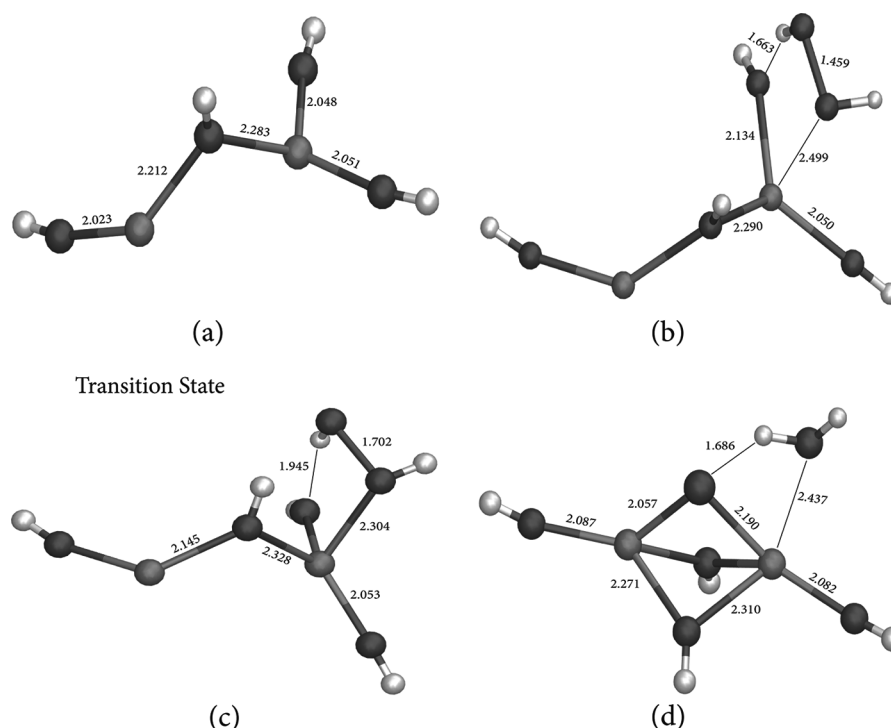
Figure 11. Optimized geometries for the study of adsorption and further decomposition of H_2O_2 in reaction with a (Y_2O_3) cluster: (a) bare cluster, (b) chemisorption of a H_2O_2 molecule, (c) transition-state for the cleavage of the O–O bond in H_2O_2, (d) product of the decomposition of H_2O_2. Y (green); O (red); H (white)

given in Table 1. The molecular adsorption energies obtained for H_2O_2 lie in the range of the molecular adsorption energies reported for H_2O, the adsorption of the former being slightly more exothermic than that of H_2O. This was expected given that these two chemical species adsorb onto the cluster surfaces through a similar process which is largely mediated by hydrogen bonding. The fact that H_2O_2 adsorbs to the metal oxides stronger than H_2O is an explanation for the fact that in the kinetic experiments represented in Figure 2 it is possible to observe an adsorption process that precedes the decomposition. The existence of molecular adsorption of H_2O_2 as the first step of the reaction of its decomposition on the surfaces of the metal oxides studied can be inferred also from the experiments reported above where the consumption of H_2O_2 and the formation of $HO^\bullet$ were tracked simultaneously and are represented in Figure 3. As already described above, the initial process responsible for the disappearance of H_2O_2 from solution is molecular adsorption according to the experimental results. The energy minima geometries corresponding to adsorption, found with the DFT calculations, agree well with this experimental evidence. Both the M06 and B3LYP functionals are able to describe these adsorption energies following a similar trend. For all the materials studied, the molecular adsorption of H_2O_2 is slightly more exothermic—up to 23 kJ·mol^{-1}—when computed with the M06 functional. Given the scarcity of literature data for molecular adsorption of H_2O_2 onto the materials studied, we cannot benchmark the performance of the two functionals in describing this process.

The transition state geometries for the cleavage of the O–O bond in H_2O_2 are represented in Figures 9 (c), 10(c), and 11(c). The enthalpy barriers for the decomposition of H_2O_2 can be found in Table 2. The reactants for these reactions have the structures shown in Figures 9(b), 10(b), and 11(b), where H_2O_2 is molecularly adsorbed to the surface of the clusters.

Table 2. Experimental $\Delta H^{\ddagger}$ and DFT Obtained $\Delta H^{\ddagger}$ and $\Delta E^{\ddagger}$ for the Decomposition of H_2O_2[a]

	experimental	DFT $\Delta H^{\ddagger}$		DFT $\Delta E^{\ddagger}$	
material	$\Delta H^{\ddagger}$	B3LYP	M06	B3LYP	M06
ZrO_2	30 ± 1[b]	37	33	38	36
TiO_2	34 ± 1	29	29	31	31
Y_2O_3	44 ± 5	23	38	23	38

[a]The DFT barriers were obtained using the LACV3P++** basis set and clusters of the type $(ZrO_2)_2$, $(TiO_2)_2$, and (Y_2O_3) represented in Figures 9, 10, and 11, respectively. Values in kJ·mol^{-1} in the gas phase. [b]Value recalculated from reference 21.

There is a very good agreement between the experimentally obtained enthalpy barriers and the DFT obtained ones, especially with the M06 functional. The larger discrepancy between experimental and DFT values is for the reaction barrier calculated with the B3LYP functional in the case of Y_2O_3. In this case, the B3LYP functional underestimated the reaction barrier by 21 kJ·mol^{-1}. The M06 functional could reproduce this barrier with better accuracy, only 6 kJ·mol^{-1} lower than the experimental value. This leads us to conclude that our models, in spite of their small size, are able to reproduce with good accuracy the processes responsible for the apparent reaction energy barriers that exist in the real systems. Overall, M06 performs better than B3LYP for the reaction barriers. This can be attributed to that noncovalent interactions such as hydrogen bonding play an important role in the obtained geometries of reactants and transition-states; the latter are mediated by multiple hydrogen bondings between H_2O_2 and the surface HO groups. The M06 functional performs better in describing these types of systems where noncovalent interactions are present and dispersion effects are large.[56−58] The products of H_2O_2 decomposition are represented in

Figures 9(d), 10(d), and 11(d). The products consist of HO radicals in all the cases. This is in agreement with the experimental results shown above in Figure 3 and with the results published in a previous work by our group that point toward the existence of HO radicals as a primary product of the decomposition of H_2O_2 when catalyzed by the surface of transition metal oxides.[21] The two HO radicals initially formed can have different fates. From the products of the reaction of H_2O_2, it can be seen that one HO radical can adsorb to the surface by bonding with a metal atom, while the other can remove a surface $H^\bullet$ initially bound to a surface oxygen atom, to form physisorbed H_2O. The formation of H_2O due to the reaction of a $HO^\bullet$ with the surface of the wet clusters is in agreement with the experimental evidence that D_2O is formed upon exposure of DO saturated surfaces to DO radicals.[59] The obtained reaction enthalpies for decomposition of H_2O_2 are shown in Table 3.

Table 3. ΔH and ΔE for the Reactions of Decomposition of H_2O_2 on the Surface of $(ZrO_2)_2$, $(TiO_2)_2$, and (Y_2O_3) Clusters Obtained with the B3LYP and M06 Functionals[a]

cluster	B3LYP ΔH	M06 ΔH	B3LYP ΔE	M06 ΔE
$(ZrO_2)_2$	−617	−605	−613	−608
$(TiO_2)_2$	−493	−488	−494	−485
(Y_2O_3)	−679	−681	−678	−678

[a]Values in kJ·mol^{-1} in the gas phase.

The large exothermicity of the reaction of cleavage of the O−O bond in H_2O_2 and formation of adsorbed HO radicals can be attributed to the process of adsorption of the later species. Both B3LYP and M06 reaction enthalpies differ very little for all the metal oxides with the largest difference for the case of ZrO_2 which is 12 kJ·mol^{-1}. The reaction of two HO radicals with the metal oxide clusters was also studied and leads to the formation of stable species. The obtained geometries are represented in Figure 12.

The energies for adsorption of $HO^\bullet$ onto the surfaces of $(ZrO_2)_2$, $(TiO_2)_2$, and (Y_2O_3) presented in Table 1 are of similar magnitude. The only value found in the literature for which first-principles molecular dynamics with periodic boundary conditions was used to calculate the adsorption energy of $HO^\bullet$ onto the surface of ZrO_2 is in good agreement with the values obtained in this work. The adsorption energies of $HO^\bullet$ vary in the order of decreasing exothermicity $Y_2O_3 > ZrO_2 > TiO_2$. This is in excellent agreement with our

experimentally obtained trends for $HO^\bullet$ adsorption energies onto the surface of these materials which are visible in Figure 8. The good agreement between experimental and DFT data is also relevant to note that the ionization energies of the metal cations present in the metal oxides studied vary in the order: $Y^{3+} < Zr^{4+} < Ti^{4+}$. Clearly the $HO^\bullet$ adsorption exothermicity varies inversely with the ionization energies of the metal ions present in the oxides. The higher the ionization energy of the metal cation present in the oxide, the weaker is the adsorption of $HO^\bullet$ onto that metal oxide; this is because the $HO^\bullet$ adsorbs onto the metal oxide by forming bonding states with the metal atom.

Overall, there is a good agreement between the data obtained with our minimal sized cluster models and the literature and experimental values. Whereas to describe a perfect surface of a conductor or semiconductor a large model is necessary to correctly account for the delocalized electronic states of the material, a smaller model can be a good descriptor to describe a defective surface like the case of our particles. This is because the electronic states of the metal oxides are not as delocalized on the surface defective sites as they are on a perfect surface. This makes the local properties of the defect, such as the type of metal atom present and its intrinsic properties, the factors that will have a larger contribution to the adsorption energies and reaction energy barriers. Furthermore, on defective surfaces, effects such as diffusion of adsorbates across the plane of the surface will be hindered when compared to the same phenomena occurring on a perfect surface.

4. CONCLUSIONS

The kinetic experiments on the decomposition of H_2O_2 together with the experiments on $HO^\bullet$ detection show the existence of an adsorption step prior to decomposition. This type of process is also predicted with the DFT calculations. The decomposition of H_2O_2 follows a similar mechanism for the three metal oxides studied. The obtained transition states are largely mediated by hydrogen bonding between H_2O_2 and surface HO groups. Nevertheless, direct interaction between the oxygen atoms of H_2O_2 and the metal atoms present in the oxide was also observed in the geometries of the transition states. The formation of two HO radicals as the primary product of the decomposition of H_2O_2 is confirmed with both the DFT calculations and the experiments. One of these radicals can further abstract a H atom initially bound to a surface O and form H_2O. The other HO radical can adsorb to the surface by forming bonding states with the metal cation
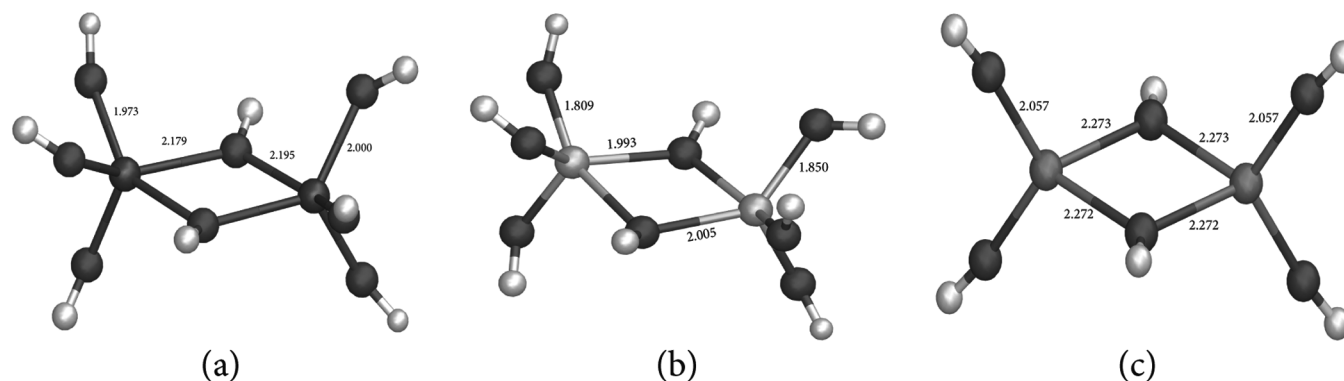

Figure 12. Optimized geometries for the adsorption of two HO radicals onto each of the clusters previously saturated with two H_2O molecules: (a) $(ZrO_2)_2$, (b) $(TiO_2)_2$, and (c) (Y_2O_3).

present in the oxides. The experimental method used for the study of the scavenging capacities of the metal oxides toward $HO^\bullet$ formed during γ radiolysis of H_2O gave us a qualitative measure of the affinity of $HO^\bullet$ toward the metal oxide surfaces present in the system undergoing radiolysis. The obtained trend for adsorption energies of $HO^\bullet$ onto the different metal oxides is inversely proportional to the variation in ionization potential of the metal cation. The trend obtained in these experiments was reproduced successfully with the DFT calculations.

The overall performance of our theoretical models, especially at the M06/LACV3P++** level, is very good. The local properties of the defects are crucial for the surface reaction of decomposition of H_2O_2 catalyzed by metal oxide particles. The extended surface effects are minimized, and these types of systems which have surfaces dominated by defects can be described by small model systems. Given the reduced coordination of the metal atoms in the clusters and since these models could describe with good accuracy the barriers for reactions catalyzed by real particles, in the real systems, catalysis by the defects where the exposed metal atoms are under-coordinated is expected to be of importance in determining the apparent reaction energy barrier. Nevertheless the type of metal atom present in a surface defect on the oxide and its stoichiometry are the most important factors that will determine the height of the barrier for the reaction catalyzed by the surface defect.

■ AUTHOR INFORMATION

Corresponding Author
*Phone: (46) 8 790 87 89. Fax: (46) 8 790 87 72. E-mail: cmlp@kth.se.

Notes
The authors declare no competing financial interest.

■ ACKNOWLEDGMENTS

■ REFERENCES

(1) Soleymani, M.; Moheb, A.; Babakhani, D. *Chem. Eng. Technol.* **2011**, *34*, 49.
(2) Rasti, N.; Toyserkani, E.; Ismail, F. *Mater. Lett.* **2011**, *65*, 951.
(3) Pehrman, R.; Amme, M.; Roth, O.; Ekeroth, E.; Jonsson, M. *J. Nucl. Mater.* **2010**, *397*, 128.
(4) Park, J. N.; Shon, J. K.; Jin, M.; Hwang, S. H.; Park, G. O.; Boo, J. H.; Han, T. H.; Kim, J. M. *Chem. Lett.* **2010**, *39*, 493.
(5) Mooi, J.; Selwood, P. W. *J. Am. Chem. Soc.* **1952**, *74*, 1750.
(6) Yamaguchi, K.; Yoshida, C.; Uchida, S.; Mizuno, N. *J. Am. Chem. Soc.* **2004**, *127*, 530.
(7) Kitajima, N.; Fukuzumi, S.; Ono, Y. *J. Phys. Chem.* **1978**, *82*, 1505.
(8) Zhao, Y.; Aoki, K. *Chem. Phys. Lett.* **2006**, *430*, 117.
(9) Anders Nilsson, L. G. M. P.; Nørskov, J. K. *Chemical Bonding at Surfaces and Interfaces*; Elsevier: Amsterdam, 2008.
(10) Erbil, H. Y. *Surface Chemistry Of Solid and Liquid Interfaces*, 1st ed.; Blackwell Publishing Ltd.: Oxford, 2006.
(11) Wada, Y.; Uchida, S.; Nakamura, M.; Akamine, K. *J. Nucl. Sci. Technol.* **1999**, *36*, 169.
(12) Tipping, P. *Int. J. Pressure Vessels Piping* **1996**, *66*, 17.
(13) Ekeroth, E.; Roth, O.; Jonsson, M. *J. Nucl. Mater.* **2006**, *355*, 38.
(14) Jonsson, M. In *Recent Trends in Radiation Chemistry*; Wishart, J. F., Rao, B. S. M., Ed.; World Scientific: Singapore, 2010; p 301.

(15) Haber, F.; Weiss, J. *Naturwissenschaften* **1932**, *20*, 948.
(16) Spear, E. B. *J. Am. Chem. Soc.* **1908**, *30*, 195.
(17) Satterfield, C.; Stein, T. *Ind. Eng. Chem.* **1957**, *49*, 1173.
(18) Trummer, M.; Dahlgren, B.; Jonsson, M. *J. Nucl. Mater.* **2010**, *407*, 195.
(19) Suh, M.; Bagus, P. S.; Pak, S.; Rosynek, M. P.; Lunsford, J. H. *J. Phys. Chem. B* **2000**, *104*, 2736.
(20) Anpo, M.; Che, M.; Fubini, B.; Garrone, E.; Giamello, E.; Paganini, M. *Top. Catal.* **1999**, *8*, 189.
(21) Lousada, C. M.; Jonsson, M. *J. Phys. Chem. C* **2010**, *114*, 11202.
(22) Amorelli, A.; Evans, J. C.; Rowlands, C. C. *J. Chem. Soc., Faraday Trans. 1: Phys. Chem. Condens. Phases* **1988**, *84*, 1723.
(23) Giamello, E.; Calosso, L.; Fubini, B.; Geobaldo, F. *J. Phys. Chem.* **1993**, *97*, 5735.
(24) *Progress React. Kinet. Mech.* **2005**, *30*, 145.
(25) Hiroki, A.; LaVerne, J. A. *J. Phys. Chem. B* **2005**, *109*, 3364.
(26) Becke, A. D. *Phys. Rev. A* **1988**, *38*, 3098.
(27) Lee, C.; Yang, W.; Parr, R. G. *Phys. Rev. B* **1988**, *37*, 785.
(28) Becke, A. D. *J. Chem. Phys.* **1993**, *98*, 5648.
(29) Stephens, P. J.; Devlin, F. J.; Chabalowski, C. F.; Frisch, M. J. *J. Phys. Chem.* **1994**, *98*, 11623.
(30) Zhao, Y.; Truhlar, D. *Theor. Chem. Acc.: Theory, Comput., Model. (Theor. Chim. Acta)* **2008**, *120*, 215.
(31) Henderson, M. A. *Surf. Sci. Rep.* **2002**, *46*, 1.
(32) Ahdjoudj, J.; Minot, C. *Surf. Sci.* **1998**, *402–404*, 104.
(33) Gong, X.-Q.; Selloni, A.; Batzill, M.; Diebold, U. *Nat. Mater.* **2006**, *5*, 665.
(34) Brookes, I. M.; Muryn, C. A.; Thornton, G. *Phys. Rev. Lett.* **2001**, *87*, 266103.
(35) Lousada, C. M.; Johannson, A. J.; Brinck, T.; Jonsson, M., to be published.
(36) Choppin, G.; J.-O. L., Rydberg, J. *Radiochemistry and nuclear chemistry*, 2nd ed.; Butterworth-Heinemann Ltd: Oxford, 1995; Vol. 46.
(37) Bailey, J. E. *Proc. R. Soc. London Ser. A, Math. Phys. Sci.* **1964**, *279*, 395.
(38) Howard, C. J.; Sabine, T. M.; Dickson, F. *Acta Crystallogr., Sect. B* **1991**, *47*, 462.
(39) Hanic, F.; Hartmanova, M.; Knab, G. G.; Urusovskaya, A. A.; Bagdasarov, K. S. *Acta Crystallogr., Sect. B* **1984**, *40*, 76.
(40) Hochanadel, C. J. *J. Phys. Chem.* **1952**, *56*, 587.
(41) Ghormley, J. A.; Stewart, A. C. *J. Am. Chem. Soc.* **1956**, *78*, 2934.
(42) Deák, P. *Physica Status Solidi B* **2000**, *217*, 9.
(43) *Jaguar*, version 7.7; Schrödinger, LLC: New York, 2011.
(44) Staroverov, V. N.; Scuseria, G. E.; Tao, J.; Perdew, J. P. *J. Chem. Phys.* **2003**, *119*, 12129.
(45) Santen, R. A. v.; Neurock, M.; Shetty, S. G. *Chem. Rev.* **2009**, *110*, 2005.
(46) Chirita, P. *Chem. Biochem. Eng. Q.* **2009**, *23*, 259.
(47) M. Murphy, D.; W. Griffiths, E.; C. Rowlands, C.; E. Hancock, F.; Giamello, E. *Chem. Commun.* **1997**, 2177.
(48) Croiset, E.; Rice, F. S.; Hanush, G., R. *Hydrogen peroxide decomposition in supercritical water*; Wiley-Blackwell: Hoboken, NJ, ETATS-UNIS, 1997; Vol. 43.
(49) *Radiation chemistry: From basics to applications in material and life sciences*; Belloni J., T. D., Mostafavi, M., Spotheim-Maurizot, M., Eds.; EDP Sciences: Les Ulis Cedex, 2008.
(50) Buxton, G. V.; Greenstock, C. L.; Helman, W. P.; Ross, A. B. *J. Phys. Chem. Ref. Data* **1988**, *17*, 513.
(51) A. van Santen, R.; Neurock, M. *Molecular Heterogeneous Catalysis: A Conceptual and Computational Approach*; WILEY-VCH Verlag GmbH & Co. KGaA: Weinheim, 2006.
(52) Jung, J.; Shin, H.-J.; Kim, Y.; Kawai, M. *J. Am. Chem. Soc.* **2011**, *133*, 6142.
(53) Gong, X.-Q.; Selloni, A. *J. Catal.* **2007**, *249*, 134.
(54) Liu, Z.-P.; Hu, P. *J. Am. Chem. Soc.* **2003**, *125*, 1958.
(55) Bailey, C. L.; Mukhopadhyay, S.; Wander, A.; Searle, B. G.; Carr, J. M.; Harrison, N. M. *Phys. Chem. Chem. Phys.* **2010**, *12*, 6124.
(56) Zhao, Y.; Truhlar, D. G. *Theor. Chem. Acc.* **2008**, *120*, 215.

(57) Riley, K. E.; Hobza, P. *Wiley Interdiscip. Rev.: Comput. Mol. Sci.* **2011**, *1*, 3.

(58) Johansson, A. J.; Zuidema, E.; Bolm, C. *Chem.—Eur. J.* **2010**, *16*, 13487.

(59) Weibel, M. A.; Backstrand, K. M.; Curtiss, T. J. *Surf. Sci.* **2000**, *444*, 66.

(60) Radha, A. V.; Bomati-Miguel, O.; Ushakov, S. V.; Navrotsky, A.; Tartaj, P. *J. Am. Ceram. Soc.* **2009**, *92*, 133.

(61) Raz, S.; Sasaki, K.; Maier, J.; Riess, I. *Solid State Ionics* **2001**, *143*, 181.

(62) Iskandarova, I. M.; Knizhnik, A. A.; Rykova, E. A.; Bagatur'yants, A. A.; Potapkin, B. V.; Korkin, A. A. *Microelectron. Eng.* **2003**, *69*, 587.

(63) Okamoto, Y. *Appl. Surf. Sci.* **2008**, *255*, 3434.

(64) Haase, F.; Sauer, J. *J. Am. Chem. Soc.* **1998**, *120*, 13503.

(65) Egashira, M.; Kawasumi, S.; Kagawa, S.; Seiyama, T. *Bull. Chem. Soc. Jpn.* **1978**, *51*, 3144.

(66) Vittadini, A.; Selloni, A.; Rotzinger, F. P.; Gr; auml; tzel, M. *Phys. Rev. Lett.* **1998**, *81*, 2954.

(67) Hussain, A.; Gracia, J.; Nieuwenhuys, B. E.; Niemantsverdriet, J. W. *ChemPhysChem* **2010**, *11*, 2375.

(68) Hammer, B.; Wendt, S.; Besenbacher, F. *Top. Catal.* **2010**, *53*, 423.

(69) Huang, W. F.; Raghunath, P.; Lin, M. C. *J. Comput. Chem.* **2011**, *32*, 1065.

(70) Zhang, P.; Navrotsky, A.; Guo, B.; Kennedy, I.; Clark, A. N.; Lesher, C.; Liu, Q. Y. *J. Phys. Chem. C* **2008**, *112*, 932.

(71) Gorelov, B. M.; Morozovskaya, D. V.; Pashkov, V. M.; Sidorchuk, V. A. *Tech. Phys.* **2000**, *45*, 1147.

"Reactivity of metal oxide clusters with hydrogen peroxide and water – a DFT study evaluating the performance of different exchange–correlation functionals"
Cláudio M. Lousada, Adam Johannes Johansson, Tore Brinck and Mats Jonsson, *Physical Chemistry Chemical Physics*, **2013**, DOI: 10.1039/c3cp44559c

V

PAPER

Reactivity of metal oxide clusters with hydrogen peroxide and water – a DFT study evaluating the performance of different exchange–correlation functionals†

Cláudio M. Lousada,* Adam Johannes Johansson, Tore Brinck and Mats Jonsson

We have performed a density functional theory (DFT) investigation of the interactions of H_2O_2, H_2O and HO radicals with clusters of ZrO_2, TiO_2 and Y_2O_3. Different modes of H_2O adsorption onto the clusters were studied. In almost all the cases the dissociative adsorption is more exothermic than molecular adsorption. At the surfaces where H_2O has undergone dissociative adsorption, the adsorption of H_2O_2 and the transition state for its decomposition are mediated by hydrogen bonding with the surface HO groups. Using the functionals B3LYP, B3LYP-D and M06 with clusters of 26 and 8 units of ZrO_2, the M06 functional performed better than B3LYP in describing the reaction of decomposition of H_2O_2 and the adsorption of H_2O. Additionally, we investigated clusters of the type $(ZrO_2)_2$, $(TiO_2)_2$ and (Y_2O_3) and the performance of the functionals B3LYP, B3LYP-D, B3LYP*, M06, M06-L, PBE0, PBE and PWPW91 in describing H_2O_2, H_2O and $HO^\bullet$ adsorption and the energy barrier for decomposition of H_2O_2. The trends obtained for $HO^\bullet$ adsorption onto the clusters are discussed in terms of the ionization energy of the metal cation present in the oxide. In order to correctly account for the existence of an energy barrier for the decomposition of H_2O_2, the functional used must include Hartree–Fock exchange. Using minimal cluster models, the best performance in describing the energy barrier for H_2O_2 decomposition was obtained with the M06 and PBE0 functionals – the average absolute deviations from experiments are 6 kJ mol^{-1} and 5 kJ mol^{-1} respectively. With the M06 functional and a larger monoclinic $(ZrO_2)_8$ cluster model, the performance is in excellent agreement with experimental data. For the different oxides, PBE0 was found to be the most effective functional in terms of performance and computational time cost.

1. Introduction

The interactions of metal oxide surfaces with hydrogen peroxide in aqueous solution are important in areas such as catalysis, energy production, geo-chemistry and biological processes.[1–7] Despite the importance of these systems, and except for the existence of some experimental literature, little is known about these reactions at the molecular scale. In principle, hydrogen peroxide can react with metal oxide surfaces *via* three different pathways: one-electron oxidation (R1), two-electron oxidation (R2), and catalytic decomposition (reactions (R3)–(R5)).[8–10]

Applied Physical Chemistry, School of Chemical Science and Engineering, KTH Royal Institute of Technology, SE-100 44 Stockholm, Sweden. E-mail: cmlp@kth.se; Fax: +46 8 790 87 72; Tel: +46 8 790 87 89

† Electronic supplementary information (ESI) available. See DOI: 10.1039/c3cp44559c

One-electron oxidation: $H_2O_2 + M^x \rightarrow M^{x+1} + HO^- + HO^\bullet$ (R1)

Two-electron oxidation: $H_2O_2 + M^x \rightarrow M^{x+2} + 2HO^-$ (R2)

Catalytic decomposition:

$$H_2O_2 + M^y \rightarrow 2HO^\bullet + M^y \quad (R3)$$

$$HO^\bullet + H_2O_2 \rightarrow HO_2^\bullet + H_2O \quad (R4)$$

$$2HO_2^\bullet \rightarrow H_2O_2 + O_2 \quad (R5)$$
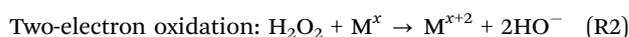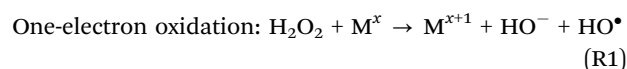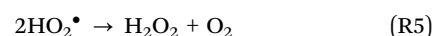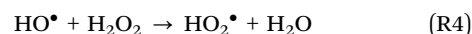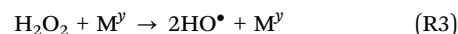
for which the overall known stoichiometry is

$$H_2O_2 \rightarrow H_2O + 1/2O_2 \quad (R6)$$
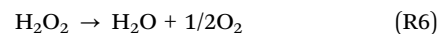
here, M represents a metal atom in the metal oxide and x and y its oxidation states.

In metal oxides where the metal atom can undergo further oxidation, any of these reactions can occur in principle.[11] For metal oxides in which the metal is present in its highest oxidation state, catalytic decomposition involving breaking of the O–O bond in H_2O_2 is the major reaction pathway. The decomposition of H_2O_2 involving the breaking of the H–OOH bond is also possible, but given the strength of this bond and the low exothermicity for this process, the contribution of this reaction to the total reactivity of H_2O_2 should be minor.[8,9] Also, reduction of the metal atoms in the oxide by H_2O_2 has been reported but it represents a minor reactive path for H_2O_2 when compared with the catalytic decomposition.[10] It has been suggested that the first step of the reaction (R3) is the molecular adsorption of H_2O_2 onto the oxide surface followed by the homolytic cleavage of its O–O bond to form two HO radicals,[10–12] $HO^•$ is then a primary product of this reaction.[13] There are experimental studies which show that after exposure of metal oxide surfaces to H_2O_2, radical species are stabilized and can be detected on the surface of the oxides after the complete disappearance of H_2O_2 from the system.[7,14,15] Due to their interaction with the metal oxide surfaces, these radicals can acquire half-lives which are very long (in the order of days) when compared to their half-lives in solution.[11,16,17]

Interactions between molecules and surfaces can be described theoretically recurring to a diversity of methods. Perhaps the most commonly applied method for investigating adsorption and reactivity is the use of density functional theory (DFT) and periodic boundary conditions (PBC). Another approach is to use a finite cluster model of the surface. Both approaches have their advantages and disadvantages. While PBC provides a physically sound treatment of the periodicity of extended surfaces, surface defects can be a hard task to model with PBC due to the interactions of artificial periodicity of the defects introduced. Even though this can be overcome by using very large unit cells, it increases the computational time and cost significantly.[18] Besides the restricted offer of codes[19,20] using the PBC approach which permits the access to wave function methods and consequently also to the hybrid Hartree–Fock/DFT,[21] the usage of hybrid functionals with PBC requires computational power which is prohibitively expensive for many users. In general, the major source of error when using the PBC approach is due to limitations in the electronic structure methods used, *i.e.* pure DFT.[22]

For molecules (*i.e.* non-solids), it has been known since the early 1990s that mixing Hartree–Fock exchange (exact exchange for a non-interacting system), with density dependent functionals (*e.g.* local density approximation) in the exchange–correlation functional, improves the performance of DFT calculations.[23,24] For solids, it has recently been shown that it is necessary to include a certain amount of Hartree–Fock exchange in order to describe the electronic states of non-metallic solids and the defects in metal oxide surfaces.[18,25–28] Due to the self-interaction error (SIE),[29–32] pure DFT fails to give a localized character to trapped states of electrons or holes in TiO_2 surface defects for example.[25] When unpaired electrons are present in the system, pure density functionals tend to delocalize the electron density, which minimizes the artificial Coulomb self-repulsion that

appears due to the SIE. This situation has been evident whenever pure DFT was used to model defects in large band-gap semiconductors and insulators.[33]

The cluster approach has the advantage that one can make use of the vast array of quantum chemical methods that have been developed and implemented.[21] Quantum chemical methods such as hybrid density functionals, double hybrid density functionals or higher-order wave function methods are available tools for modeling surfaces using cluster models.[22,34] The cluster approach is best suited for describing local phenomena such as interactions on catalytically active sites. Due to its low computational cost, the cluster approach is efficient for modeling the reactivity of surface defects, which can be crucial for understanding experimentally observed kinetics.[35] On the other hand, finite size effects can be detrimental for obtaining reliable data for properties of extended surfaces.[36] Such problems can be overcome by increasing the cluster size or by using the embedded cluster model approach.[37] For the modeling of adsorption on ideal/perfect surfaces, the cluster approach becomes inefficient due to the size of the cluster required to accurately represent the system.[38] Nevertheless, in real applications of engineered or natural materials, ideal surfaces are rarely present. Instead, solid surfaces are typically polycrystalline and display a rough surface-structure.[39,40]

Effects of cluster size and edge geometry on calculated adsorption energies, were recently investigated in a work where cluster models were used in combination with hybrid and double hybrid exchange–correlation functionals.[22] Accurate adsorption energies onto mineral surfaces were obtained with two layer thickness clusters that retained the correct stoichiometry and charge of the surfaces. The authors calculated adsorption energies as a function of cluster size and concluded that beyond size-convergence, the maximum error introduced was 16 kJ mol^{-1} for adsorption from the gas phase. Convergence was achieved with clusters only large enough to include the surface atoms and groups involved in the binding of the adsorbate.

In this paper we present the results of DFT calculations of interactions of H_2O_2, H_2O and $HO^•$ with ZrO_2, TiO_2 and Y_2O_3 clusters of different size. Since water is an important molecular probe for surface reactivity,[41] the first reaction step investigated was the adsorption of H_2O onto the available surface sites of the clusters. In this way it is possible to validate the cluster models, as there are previously published data for water adsorption onto metal oxide surfaces to compare with. The two modes of H_2O adsorption onto metal oxide surfaces[42–44] – molecular and dissociative adsorption – were modeled and compared energetically. The adsorption of the first layer of water onto a metal oxide surface generally occurs through the dissociative path.[45] However, for some metal oxides, the cleavage of water occurs only on specific surface defects.[45–47] The computed adsorption energies of H_2O are used to evaluate the performance of the applied functionals, and as a probe for the Lewis acidity of the clusters. We consider a variety of exchange–correlation functionals and the calculated activation energies for the decomposition of H_2O_2 on the cluster surfaces are

compared with previously published experimental kinetic data from our group.[12,13]

2. Methods

DFT calculations were performed using the molecular cluster model[48] approach and the software package Jaguar 7.7.(ref. 49). Cluster geometries were optimized at the B3LYP/LACVP*+ level of theory,[46–49] which is known to provide accurate molecular geometries even when hydrogen bonds are present.[50] The basis set LACVP*+ is a combination of the split valence basis set 6-31+G(d) and the Los Alamos effective core potential for the transition metals Zr, Ti, and Y. Single-point evaluations of energies were performed using exchange–correlation functionals built on the generalized gradient approximation (GGA), namely the pure density functionals PBE[51–53] and PWPW91;[54] the pure meta functional M06-L,[55] the hybrid functionals PBE0,[54,55] B3LYP, and B3LYP*;[56] and the hybrid meta functional M06.[57] The M06 functional has shown improved accuracy for describing transition metal chemistry and medium range attractive dispersion interactions.[58] In addition, we have investigated the effects of adding an empirical attractive dispersion term $(-f(R)C_6 R^{-6})$ to the B3LYP functional according to the method of Grimme.[59] The functionals used are further described in Table 1 in terms of the amount of Hartree–Fock exchange (E_{HF}^{XC}) incorporated and whether or not the electronic kinetic energy density depends on the spin.

Single point calculations were performed with the split valence triple-ζ basis set LACV3P**++, which is supplemented with polarization and diffuse functions on all atoms. The following convergence criteria were used for all geometry calculations (atomic units): rms gradient $< 3 \times 10^{-4}$; maximum gradient $< 4.5 \times 10^{-4}$; rms step $< 1.2 \times 10^{-3}$; maximum step $< 1.8 \times 10^{-3}$; maximum change in total energy between two consecutive steps $< 5 \times 10^{-5}$.

Our cluster models conform to the three principles proposed to model metal oxides using clusters.[60,61] These principles are the neutrality principle, the stoichiometry principle and the coordination principle.

The adsorption energies reported herein were calculated as

$$\Delta E_{ads} = E_{adsorbate/cluster} - (E_{adsorbate} + E_{cluster}) \quad (1)$$

were $E_{adsorbate/cluster}$, $E_{adsorbate}$, $E_{cluster}$, represent the electronic energies in the gas-phase for the adsorbate binding to the cluster, free adsorbate and bare cluster respectively. This means that the more negative the adsorption energy, the stronger is the adsorption.

Transition states were located using the quadratic synchronous transit (QST) method implemented in Jaguar 7.7. Corrections to obtain zero-point vibrational effects and the thermodynamic potential enthalpy (H) were calculated from a Hessian matrix of harmonic force constants using the partition functions of an ideal/non-interacting gas at $T = 298.15$ K and $P = 1$ atm. The vibrational frequencies obtained from the Hessian matrix were also used to verify the first-order saddle point nature of the transition states.

3. Results and discussion

The surface reactivity of ZrO_2 (s), TiO_2 (s), and Y_2O_3 (s) with hydrogen peroxide, has been modeled using cluster models and DFT using various exchange–correlation functionals. Adsorption of water and hydroxyl radicals is also considered. The discussion is divided into sub-sections by cluster size and degree of surface saturation.

m-$(ZrO_2)_{26}$ cluster with B3LYP, B3LYP-D and M06 functionals

A cluster consisting of 26 units of stoichiometric ZrO_2 was used to evaluate the adsorption energetics of H_2O, H_2O_2 and $HO^\bullet$. The model was constructed by slicing the extended monoclinic crystal (unit cell parameters (a) 5.143, (b) 5.204, and (c) 5.311 Å, Zr–O bond distance 1.771 Å)[62] and a surface was defined according to the ($\bar{1}11$) Miller index. This crystallographic plane was chosen since it is the most stable stoichiometric surface of monoclinic zirconia.[62] The cluster geometry was constrained, with the exception of the surface atoms directly involved in adsorption (i.e. the reaction site). This model will from now on be denoted m-$(ZrO_2)_{26}$, where m- indicates the monoclinic crystal structure. The surface reaction site is highlighted in Fig. 1a, and a top view of the ($\bar{1}11$) surface sliced on the monoclinic structure of ZrO_2 can be seen in Fig. 1b. Our initial tests have shown that the adsorption is favored at this site when compared to other ($\bar{1}11$) surface sites.

The calculated adsorption energies for dissociative and molecular adsorption of water as well as molecular adsorption of H_2O_2 and its decomposition products (H_2O and $HO^\bullet$) are given in Table 2. Overall there is a good agreement between the energies calculated with M06 and B3LYP-D. At most, the adsorption energies differ by 14 kJ mol^{-1}. In general, the
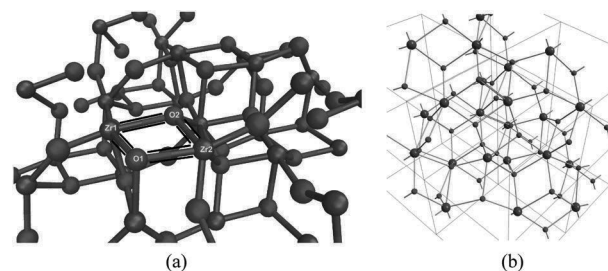
Fig. 1 (a) m-$(ZrO_2)_{26}$ cluster used for the study of adsorption of H_2O, H_2O_2 and $HO^\bullet$. The highlighted Zr and O atoms were allowed to relax during geometry optimization of the adsorbed states. (b) Top view of the single crystal structure of monoclinic ZrO_2 with a surface defined according to the ($\bar{1}11$) plane. The grids denote the unit cells of the crystal structure. Zr (●), O (●), H (○).

Table 1 Density functionals used in this work described in terms of: the percentage of Hartree–Fock exchange (E_{XC}^{HF}); up-spin and down-spin electronic kinetic energy density (ρ_{Te})

	B3LYP	B3LYP*	M06	M06-L	PBE0	PBE	PWPW91
E_{XC}^{HF}(%)	20	15	27	0	25	0	0
ρ_{Te}	No	No	Yes	Yes	No	No	No

Table 2 ΔE_{ads} for adsorption of H_2O, H_2O_2 and $HO^{\bullet}$ onto a $(ZrO_2)_{26}$ cluster. Reaction energy for decomposition of H_2O_2 (ΔE_r). Values in (kJ mol^{-1})

Adsorbate	Adsorption energy		
	B3LYP/ LACV3P++**	B3LYP-D/ LACV3P++**	M06/ LACV3P++**
2 H_2O-dissociative	−256	−321	−312
1 H_2O-molecular[a]	−109	−139	−132
2 $HO^{\bullet}$ adsorption	−872	−900	−903
H_2O_2-molecular	−143	−180	−166
H_2O_2 decomposition ΔE_r	−523	−513	−520

[a] The adsorption of molecular H_2O was studied on the surface of the cluster previously saturated with the products of H_2O dissociative adsorption.

"dispersion-corrected" functionals B3LYP-D and M06 predict larger adsorption energies than B3LYP. The pure dispersion effect, taken as the difference between B3LYP-D and B3LYP, is between −14 and −37 kJ mol^{-1}, depending on the adsorbed species (ionic, radical, hydrogen bonding). For molecular adsorption of water, our calculated adsorption energies range from −109 kJ mol^{-1} (B3LYP) to −139 kJ mol^{-1} (B3LYP-D), which are larger than previously reported DFT values for low surface coverage (Table 4). This is likely a combined effect of using hybrid DFT and dispersion. The calculated energy for dissociative adsorption of water (−312 kJ mol^{-1} per two water molecules, leading to −156 kJ mol^{-1} per water molecule with M06) is in good agreement with experimental data (Table 4), however, there is a large variation in reported experimental data. This is because the experimentally obtained adsorption enthalpies depend on surface coverage and on the synthetic route used to obtain the surface.

$(ZrO_2)_8$ cluster with B3LYP, B3LYP-D and M06 functionals

A cluster model consisting of 8 ZrO_2 units was constructed by slicing the monoclinic crystal structure and a surface was defined according to the ($\bar{1}11$) Miller plane. In previous works of adsorption of molecular species onto TiO_2, it was found that hydrogen saturated model clusters (or using similar approaches such as the pseudo hydrogens) produced good results especially in the cases when the cluster sizes were small.[63,64] A similar approach was followed in this work for the smaller sized clusters. Terminal metal atoms were saturated with hydroxide ions (HO^-), while terminal oxygen atoms were saturated with protons (H^+). All the available terminations were saturated with exception for the reactive site on the ($\bar{1}11$) surface where water adsorption was modeled. The geometry of the cluster model was fully relaxed and optimized at the B3LYP/LACVP+* level. This cluster will from now on be denominated m-$(ZrO_2)_8$. In order to evaluate the effects of dispersion interactions, adsorption energies were obtained by single-point calculations using the functionals B3LYP, B3LYP-D, and M06. The optimized structure of the m-$(ZrO_2)_8$ cluster is shown in Fig. 2. The obtained Zr–O bond distances are longer than the experimentally observed distances in the crystalline phase (1.771 Å) but are in good agreement with $(ZrO_2)_4$ clusters
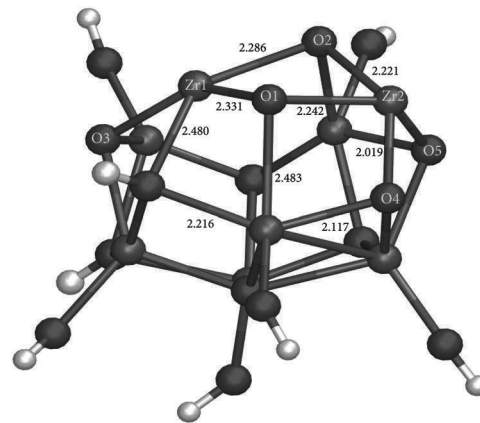
Fig. 2 Optimized structure of the m-$(ZrO_2)_8$ cluster used as the starting point for the study of the surface reactions with H_2O, H_2O_2 and $HO^{\bullet}$. Zr (●), O (●), H (○). The bond lengths are given in Å.

optimized at the CCSD(T)/aT and B3LYP/aD levels of theory ($\sim$2.1 Å).[65,66] The effects of this difference on the Zr–O bond distance between finite clusters and the crystal will be discussed at the end of this section. The m-$(ZrO_2)_8$ cluster was used initially to model the adsorption of water on ZrO_2. Dissociative adsorption of water was performed on the atoms: Zr(1), Zr(2), O(1), O(2), O(3), O(4), and O(5) with the resulting HO^- ions binding to the Zr atoms and H^+ binding to the O atoms. Different adsorption modes of the protons and hydroxide ions from the dissociation of two and four water molecules were considered and compared energetically. The adsorption of two HO radicals onto a surface which had previously adsorbed two H_2O molecules dissociatively was also considered in order to model the dissociative adsorption of hydrogen peroxide on a surface in aqueous solution (Fig. 3, Table 3). The most exothermic dissociative adsorption mode for two H_2O molecules was also the structure that went through the most extensive adsorption site reconstruction (Fig. 3b). As a result of protonation, the O(2) atom lost one of its bonds to a Zr-atom in the lattice, and was dislocated out of the surface plane. The resulting hydroxyl group is better described as a bi-bridging surface adsorbed hydroxyl group than a protonated lattice oxygen atom (Fig. 3b), which is interesting since other theoretical as well as experimental studies have reported similar results.[67,68] The large difference in adsorption energy calculated with B3LYP and B3LYP-D ($\Delta\Delta E_{ads} = 30$ kJ mol^{-1}, Table 3) shows that dispersion interactions are important to make a quantitatively correct description of adsorption, and in fact the adsorption energies calculated with B3LYP-D (−107 kJ mol^{-1}) and M06 (−120 kJ mol^{-1}), are in reasonable agreement with most experimental data (−70 to −142 kJ mol^{-1}), although larger values (−170 kJ mol^{-1}) have been reported (Table 4). Once again, B3LYP-D and M06 make very similar predictions.

Dissociative adsorption of four H_2O molecules, results in a product where the two hydroxyl groups are bound to the already HO coordinated Zr(1) and Zr(2) atoms (Fig. 3d). Due to their proximity, hydroxyl groups bound to the same Zr atom are stabilized by hydrogen bonding. Another interesting aspect of
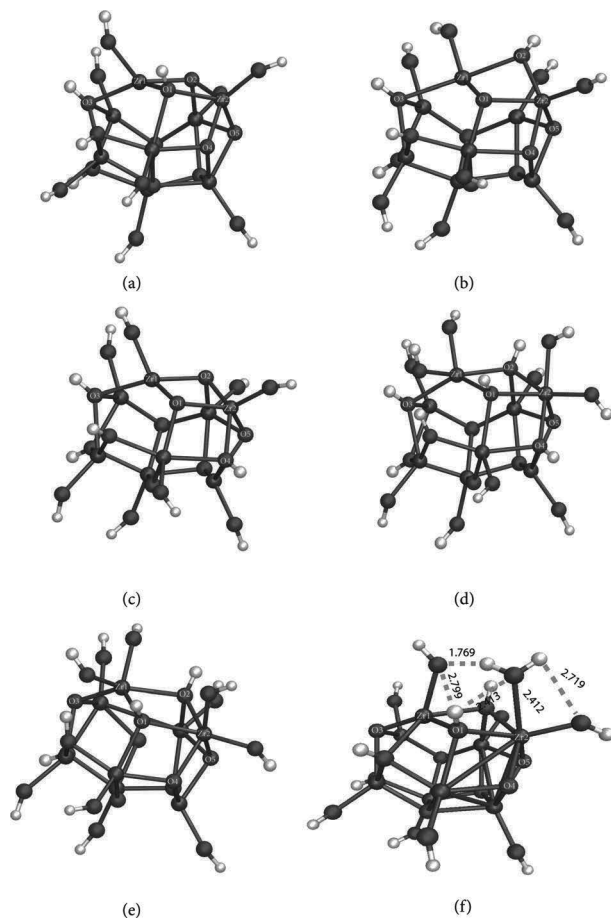
Fig. 3 Optimized geometries for adsorption of H_2O and HO radicals into the different available surface sites of the m-$(ZrO_2)_8$ cluster: (a), (b), (c) $2H_2O$ molecules, (d) $4H_2O$ molecules, (e) $2H_2O$ molecules and 2HO radicals, (f) molecular adsorption of H_2O (dashed lines represent hydrogen bonds). Zr (●), O (●), H (○). The bond lengths are given in Å.

Table 3 ΔE_{ads} (kJ mol^{-1}) for adsorption of H_2O, HO$^\bullet$ and H_2O_2 onto the m-$(ZrO_2)_8$ model. The respective structures are shown in Fig. 3 and 4

		Adsorption energy		
Adsorbate	Structure	B3LYP/ LACV3P++**	B3LYP-D/ LACV3P++**	M06/ LACV3P++**
2 H_2O-dissociative	3(a)	−48	−81	−88
	3(b)	−77	−107	−120
	3(c)	−61	−90	−92
4 H_2O-dissociative	3(d)	−156	−240	−241
2 HO$^\bullet$	3(e)	−944	−954	−955
H_2O molecular[a]	3(f)	−71	−85	−78
H_2O_2 molecular	4(b)	−36	−61	−46

[a] The adsorption of molecular H_2O was studied on the surface of the cluster previously saturated with the products of H_2O dissociative adsorption.

structure (3d) is the fact that the protonated O(1) and O(2) atoms each remain coordinated to three Zr atoms, on the contrary to what was found in structure (3b). The explanation is that the Zr(1) and Zr(2) atoms in structure (3d) have a higher degree of coordinative saturation than the corresponding Zr atoms in structure (3b), and thus possess weaker affinity for the

Table 4 Literature data for adsorption of H_2O, HO and H_2O_2 onto ZrO_2, TiO_2 and Y_2O_3. (kJ mol^{-1})

Type of data	H_2O molecular adsorption	H_2O dissociative adsorption	H_2O_2 molecular adsorption	HO$^\bullet$ adsorption
ZrO_2				
Experimental	−(44–150)[a 88]	−(119; 142)[a 88] −(70–94)[a 43] −(110–170)[70]	—	—
Theoretical	−(42–100)[b 89] −(57)[b 84]	−(194–208)[b 90] −(91–170)[b 89]	—	−(498)[b 84]
TiO_2				
Experimental	−(48–68)[a 91]	—	—	—
Theoretical	−(71–79)[b 92] −(90)[b 93] −(83)[b 94]	−(22–153)[b 92] −(141)[b 93]	−(4–78)[b 95]	—
Y_2O_3				
Experimental	—	−(91)[a 96] −(38–99)[a 97]	—	—
Theoretical	—	—	—	—

[a] Refers to an ΔH_{ads}. [b] Refers to an ΔE_{ads} without zero point energy corrections.

HO groups formed by the protonation of surface O-atoms. A similar situation was found when two HO radicals were adsorbed onto a surface site where two H_2O molecules had previously dissociated (Fig. 3e). Among the different adsorption modes of H_2O, the adsorption of four water molecules (Fig. 3d) is the most exothermic. All three functionals predicted this situation, though the adsorption energies obtained with B3LYP-D and M06 are around 85 kJ mol^{-1} larger than those calculated with B3LYP (Table 3). Since the dispersion effect in the adsorption of two water molecules was around −40 kJ mol^{-1} (Table 3), i.e. roughly half the effect in the adsorption of four water molecules, it can be concluded that the dispersion effect per water molecule is fairly constant.

The molecular adsorption of a single H_2O molecule occurs via hydrogen bonding and interactions between the oxygen atom of H_2O and the surface Zr(2) atom (Fig. 3f). At the B3LYP level, the most stable adsorption mode of two dissociated water molecules (3b) is only slightly more exothermic than molecular adsorption (Fig. 3f, Table 3). On the contrary, the dispersion corrected functionals B3LYP-D and M06 enhance the stability of the dissociative adsorption state significantly, with respect to the state of molecular adsorption. Because the experimental picture is that for ZrO_2 the first water layer dissociates, the dispersion corrected functionals seem to provide a better description. Again, it can be concluded that dispersion effects are necessary to be included in order to make correct predictions about adsorption by DFT calculations.

Experimental and computational data found in the literature for the above mentioned processes are summarized in Table 4. A comparison between computational and experimental data for water adsorption onto metal oxide surfaces has to be done carefully. The metal oxide particles used in the determination of the experimental data are in many cases obtained via different synthetic routes, which produce particles with different surface structures, defects, and anisotropic surface energies.[69] These discrepancies can have a significant

influence on the adsorption energies measured using different particles, and differences of 60 kJ mol^{-1} have been reported for H_2O adsorption onto two samples of monoclinic ZrO_2 obtained *via* different synthesis schemes.[70] Furthermore, the computational data referred in Table 4 was obtained for ideal surfaces sliced according to specific Miller planes. Such models do not take into account effects of defects and the multitude of surfaces present in the real systems. The clusters used herein are intended to model adsorption on rough surfaces or surface defects. This might not be representative of the real system as well, in which a variety of surface defects are present. Nevertheless, our computed adsorption energies are within the range of values found in the literature shown in Table 4.

The decomposition of hydrogen peroxide on the m-$(ZrO_2)_8$ cluster, after the dissociative adsorption of four water molecules, is illustrated by the potential energy surface (PES) in Fig. 4. As a first step, the H_2O_2 molecule adsorbs molecularly onto the cluster surface and attaches through three (donating two, accepting one) hydrogen bonds with surface HO-groups. At the B3LYP level ΔE_{ads} equals -36 kJ mol^{-1}, this is expected since 12 kJ mol^{-1} ($\Delta E_{ads}/3$) is the normal strength of a single hydrogen bond. In addition to the hydrogen bonds, there are dispersion interactions with the surface atoms, but in this case, B3LYP-D and M06 predict slightly different adsorption energies, $\Delta E_{ads} = -61$ kJ mol^{-1} and $\Delta E_{ads} = -46$ kJ mol^{-1}, respectively.

Already in the transition state for the dissociation of H_2O_2 (Fig. 4), one of the resulting HO-groups starts to form a bond with Zr(2). When the transition state is relaxed, the other HO-group of the dissociating H_2O_2 molecule abstracts a hydrogen atom from the protonated surface O(2)-atom, which leads to the

formation of water. The reason for water formation seems to be that the HO-group that abstracts a surface H atom interacts with the same H atom through hydrogen bonding already in the reactant geometry. The stability of the water product is supported by isotope experiments which show that D_2O is formed upon exposure of certain surfaces to $DO^{\bullet}$.[71] In a previous paper we reported experimental kinetic data for the decomposition of hydrogen peroxide on ZrO_2.[15] The experimentally obtained Arrhenius activation energy is only 33 ± 1 kJ mol^{-1}, meaning that the decomposition is rapid. At the B3LYP level, the activation energy for the cleavage of H_2O_2 is only 15 kJ mol^{-1}, while the barrier obtained with the M06 functional is 32 kJ mol^{-1}. Since calculations with B3LYP-D give an activation energy of 12 kJ mol^{-1}, the difference between B3LYP and M06 cannot be attributed to dispersion interactions only. Here it is clear that the M06 functional outperforms B3LYP in describing the barrier height, in agreement with the concepts behind the development of the M06 functional.[58] The spin density isosurfaces for the transition state geometries are shown in Fig. 5. The different distributions of spin density in the reactive sites are evident. The M06 functional predicts a more localized spin density in the reactive site where H_2O_2 adsorbs and undergoes decomposition. For the same cluster geometry, B3LYP calculations give a more delocalized spin density that seems to be distributed over the entire cluster. These differences could underlie the explanation for the difference in the activation energies obtained with the two functionals. Since the activation energy obtained with the M06 functional is very close to the experimental value, it seems reasonable to believe that in the real system the spin density is more localized.
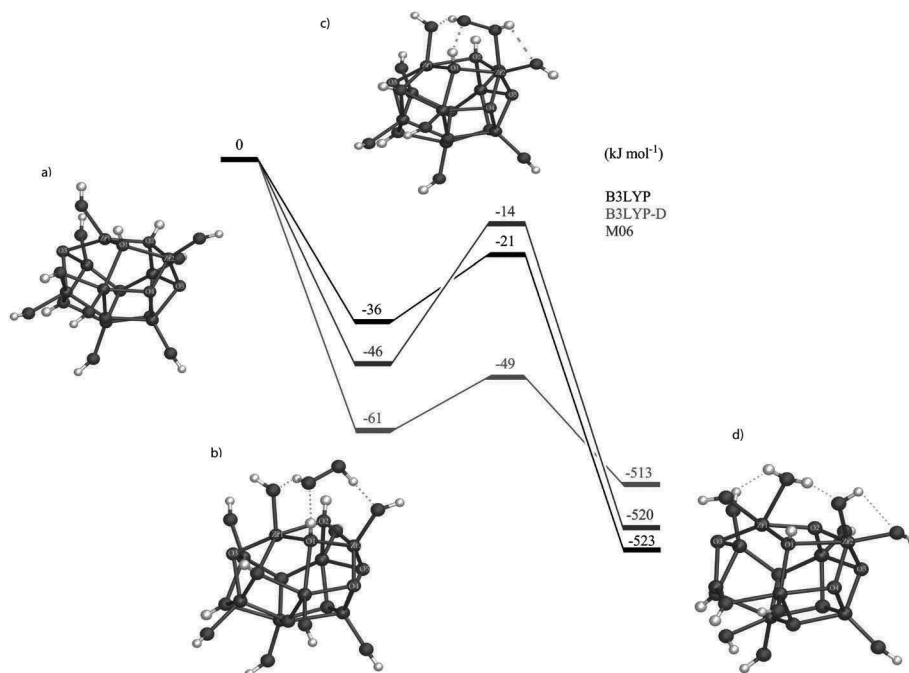
Fig. 4 Reaction potential energy diagram and corresponding optimized structures for the reaction of H_2O_2 with the surface of the m-$(ZrO_2)_8$ cluster: (a) cluster after dissociative adsorption of H_2O, (b) molecular adsorption of H_2O_2 onto the surface HO groups, (c) transition-state for the cleavage of H_2O_2, (d) stable product of the decomposition of H_2O_2. Zr (●), O (●), H (○). The bond lengths are given in Å. (More detailed figures can be found in the ESI†).
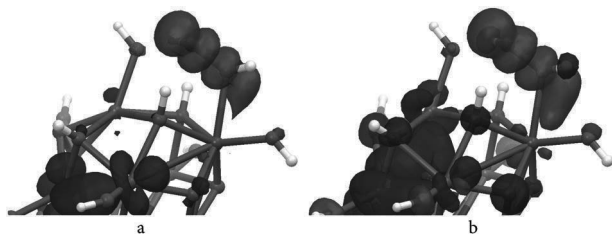
Fig. 5 Spin density isosurfaces for the transition state geometries obtained with: (a) B3LYP; (b) M06 functionals with a LACV3P++** basis set. Alpha-spin density region (■). Beta-spin density region (■).

The rationale for the fact than M06 performs better than B3LYP can be based on the fact that the transition-state for the cleavage of H_2O_2 is expected to follow the model discussed by Nilsson and Pettersson[72] for dissociation of molecular species on catalyst surfaces. According to the model, for a molecular adsorbate, a *bond-prepared* radical state is obtained upon internal (partial) bond-breaking where the resulting fragments have unpaired electrons that can interact with available electrons on the catalyst surface. Since the O–O bond in H_2O_2 is relatively weak (208 kJ mol^{-1}),[73] compared to the adsorption energy of the two HO-radicals (−944 kJ mol^{-1}, Table 3), it is energetically favorable to fully break the O–O bond and further interaction of the unpaired electron of HO$^{\bullet}$ with the valence electrons of the metal atom occurs, giving rise to bonding states. Besides incorporating a larger amount of Hartree–Fock exchange (27% in M06, 20% in B3LYP, Table 1), the kinetic energy density in M06 is spin dependent,[74] which could lead to better performance of this functional in describing open-shell systems with unpaired electrons. An important feature of the systems studied in this work is that non-covalent interactions such as hydrogen bonding and Van der Waals interactions play important roles in the reaction of H_2O_2 with the metal oxide. In particular, hydrogen bonds are important in the transition-state for H_2O_2 decomposition, in which multiple hydrogen bonding between H_2O_2 and the surface HO groups are present. The M06 functional, in agreement with previous findings, performed better in describing these types of systems where non-covalent interactions are present and dispersion effects are large.[74–76]

The water adsorption energies obtained for the m-$(ZrO_2)_{26}$ cluster are systematically more exothermic than the equivalent obtained for the m-$(ZrO_2)_8$ cluster (Tables 2 and 3). A possible cause for this is the fact that the surface atoms in the m-$(ZrO_2)_{26}$ cluster are more under-coordinated than the atoms on the m-$(ZrO_2)_8$ cluster and as such, the bonding with adsorbates adds more stabilization onto the more under-coordinated surface atoms of the m-$(ZrO_2)_{26}$ cluster.

$(ZrO_2)_2$, $(TiO_2)_2$ and (Y_2O_3) clusters with B3LYP, B3LYP-D, B3LYP*, M06, M06-L, PBE0, PBE and PWPW91 functionals

There are several examples in the literature showing that defective surface sites, displaying coordinatively unsaturated metal atoms, can enhance the reactivity of a material.[77–79] Jung and coworkers reported that the presence of surface defects in

MgO films lower the activation energies for reactions with water by as much as 60%.[77] The same authors found that a reaction which has considerable activation energy on an ideal surface, can occur without energy barrier when the surface has defects. Consequently, for non-ideal surfaces, the overall reaction rate is often determined by interactions with defective sites.[35] The physico-chemical properties of surface defects and the chemical reactivity of such sites are mainly the results of local structural and electronic properties, and less dependent on the properties of the extended surface.[40] The properties of surface defects are above all dependent on the types of atom exposed at the defects, their oxidation states, their coordination/ligand field and their Lewis acidity. Bearing these facts in mind we investigated if minimal sized metal oxide clusters could be used to describe the adsorption of H_2O and H_2O_2 on metal oxide surfaces. The clusters were built following the approach where (H^+) and (HO^-) are used to truncate the cluster terminations in an analogous way to the m-$(ZrO_2)_8$ model. As mentioned above, it has been reported previously that this approach has shown very good performance for small clusters.[63,64]

The minimal possible clusters that retain the stoichiometry of the crystals were constructed for ZrO_2, TiO_2 and Y_2O_3 (Fig. 6–9). Cluster optimizations were performed with B3LYP and adsorption energies were calculated using the functionals B3LYP, B3LYP-D, B3LYP*, M06, PBE0, PBE, PWPW91 and M06-L (Tables 5–7). We also optimized the cluster geometries for H_2O adsorption, H_2O_2 decomposition and HO radical adsorption using the PBE functional. The water adsorption energies for clusters optimized with PBE deviate from the ones optimized with B3LYP by 2 kJ mol^{-1} for molecular adsorption and by 18 kJ mol^{-1} for dissociative adsorption. PBE was able to find a structure for the transition state for the decomposition of H_2O_2, but the obtained energy barrier is 0. Based on the physically unreasonable results for H_2O_2 reactivity obtained when PBE was used for optimizing geometries, we proceeded the study using the B3LYP geometries.

Adsorption of two H_2O molecules on the $(ZrO_2)_2$ cluster is more exothermic than for the m-$(ZrO_2)_8$ cluster, −260 kJ mol^{-1} (Table 5) and −120 kJ mol^{-1} (Table 3), respectively, at the M06 level. The main reason for this discrepancy is the lower degree of coordination of the Zr atoms in the smaller cluster, which gives Zr a higher affinity for HO-groups.

The general trend in the calculated adsorption energy for water is that $\Delta E_{ads}(Y_2O_3) < \Delta E_{ads}(ZrO_2) < \Delta E_{ads}(TiO_2)$ (Tables 5–7). The trend can be explained by the local acidity of the metal atom adsorbing the hydroxide ion formed upon the heterolytic cleavage of water. The 4s and 4p orbital energies of Zr (2nd row transition metal) are higher than the corresponding 3s and 3p orbital energies of Ti (1st row transition metal) because of the higher effective nuclear charge of Ti. Hence the HO^- anion, acting as a Lewis base donating an electron pair to the metal cation, will be more strongly adsorbed on Ti^{4+} than Zr^{4+}. In other words, due to its higher ionization energy and smaller ionic radius,[80,81] the Ti^{4+} cation in the $(TiO_2)_2$ cluster is a stronger Lewis acid than the Zr^{4+} cation in $(ZrO_2)_2$. The M–O bonds are approximately 100 kJ mol^{-1} stronger in ZrO_2 than in TiO_2.[82,83] Also, the Bronsted acidity of the
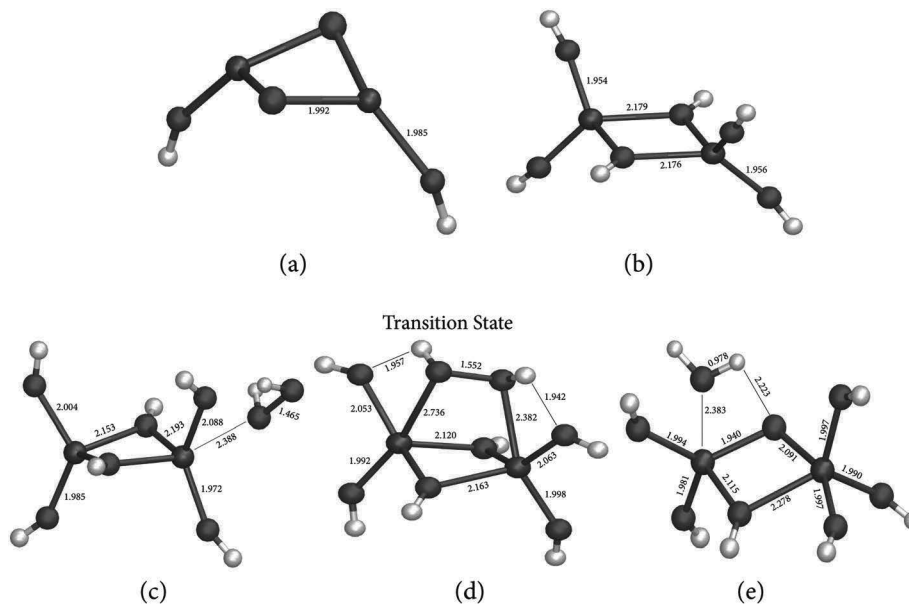
Fig. 6 Optimized geometries for adsorption of H_2O and further decomposition of H_2O_2 on a $(ZrO_2)_2$ cluster; (a) bare cluster, (b) dissociative adsorption of two H_2O molecules, (c) molecular adsorption of a H_2O_2 molecule, (d) transition-state for the cleavage of the O–O bond in H_2O_2, (e) product of the decomposition of H_2O_2. Zr (●), O (●), H (○). The bond lengths are given in Å.
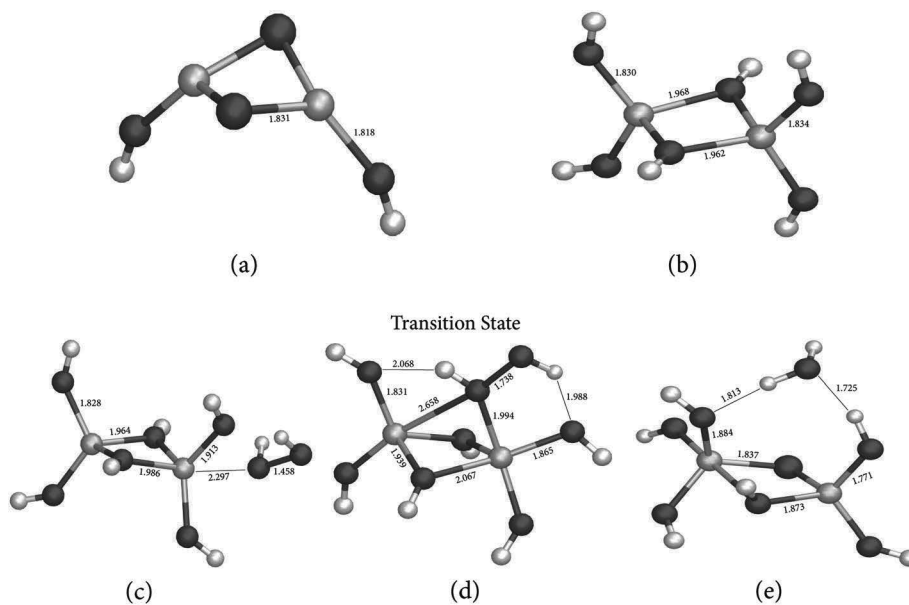
Fig. 7 Optimized geometries for adsorption of H_2O and further decomposition of H_2O_2 on a $(TiO_2)_2$ cluster. (a) Bare cluster, (b) dissociative adsorption of two H_2O molecules, (c) molecular adsorption of a H_2O_2 molecule, (d) transition-state for the cleavage of the O–O bond in H_2O_2, (e) product of the decomposition of H_2O_2. Ti (●), O (●), H (○). The bond lengths are given in Å.

protonated ZrO_2 surface is greater than for the protonated TiO_2 surface. In the case of Y_2O_3, the lower oxidation state (3+) makes the Y^{3+} ions less Lewis acidic than the M^{4+} ions in TiO_2 and ZrO_2. Consequently, the adsorption of a HO^- group is not as exothermic on Y_2O_3 as it is for ZrO_2 and TiO_2. The trend for the dissociative adsorption energies of H_2O obtained in this work with the B3LYP, M06, M06-L, PBE0 and PWPW91 functionals, agrees with the principles described above,

i.e. $\Delta E_{ads}(Y_2O_3) < \Delta E_{ads}(ZrO_2) < \Delta E_{ads}(TiO_2)$ (Tables 5–7). However, the PBE functional predicted a different trend, and for all the three materials, PBE was the functional that gave the least exothermic values for the dissociative adsorption of H_2O. The most exothermic values for dissociative adsorption of water were systematically obtained with the M06 functional. The M06 and B3LYP-D predict very similar dissociative adsorption energies for H_2O.
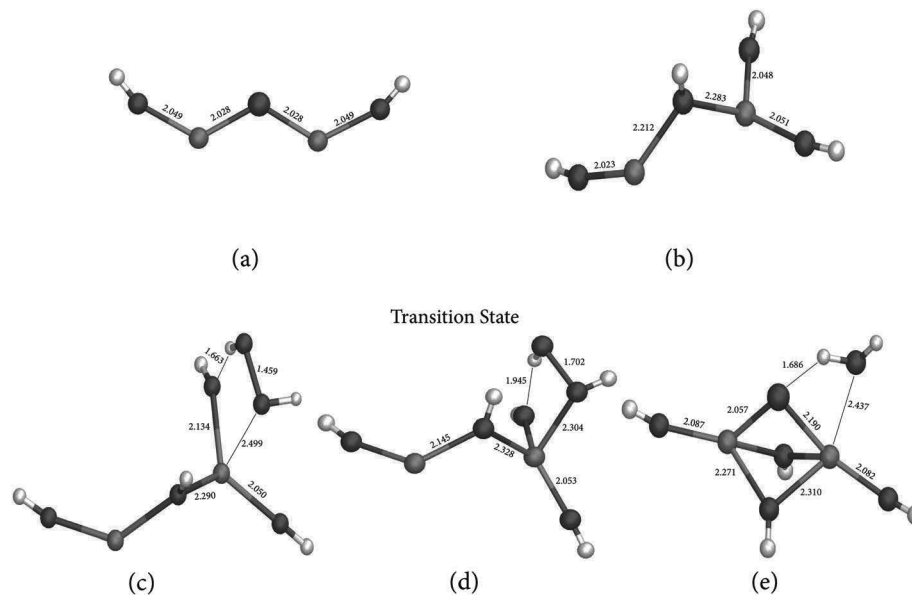
Fig. 8 Optimized geometries for adsorption of H_2O and further decomposition of H_2O_2 on a (Y_2O_3) cluster. (a) Bare cluster, (b) dissociative adsorption of two H_2O molecules, (c) molecular adsorption of a H_2O_2 molecule, (d) transition-state for the cleavage of the O–O bond in H_2O_2, (e) product of the decomposition of H_2O_2. Y (●), O (●), H (○). The bond lengths are given in Å.
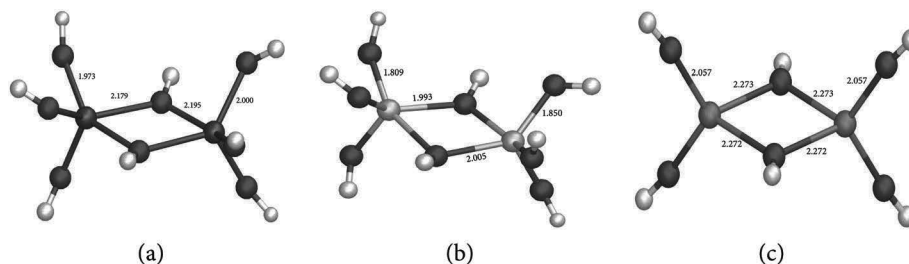

Fig. 9 Optimized geometries for adsorption of 2 HO radicals onto each of the clusters previously saturated with 2 H_2O molecules: (a) $(ZrO_2)_2$, (b) $(TiO_2)_2$, (c) (Y_2O_3). Zr (●), Ti (●), Y (●), O (●), H (○). The bond lengths are given in Å.

Table 5 ΔE_{ads} for adsorption of H_2O, H_2O_2 and $HO^{\bullet}$ onto a $(ZrO_2)_2$ cluster. Activation energy with zero point energy correction (E_a^{ZPE}) for the decomposition of H_2O_2 on the surface of the cluster and its respective reaction energy (ΔE_r). Absolute deviation from the experimental value for the activation energy (D_{exp}). Values in (kJ mol^{-1})

	B3LYP	B3LYP-D	B3LYP*	PWPW91	PBE	PBE0	M06	M06-L
ΔE_{ads} (2H_2O; dissociative)	−229	−261	−230	−218	−209	−233	−258	−231
ΔE_{ads} (H_2O; molecular)	−80	−90	−81	−86	−82	−100	−93	−90
ΔE_{ads} (2$OH^{\bullet}$)	−1005	−1023	−1012	−1027	−1019	−1028	−1027	−1043
ΔE_{ads} (H_2O_2; molecular)	−121	−133	−120	−131	−128	−150	−141	−151
E_a^{ZPE}	38	33	34	—^{a}	—^{a}	42	36	—^{a}
D_{exp}	5	0	1	18	18	9	3	18
ΔE_r	−637	−616	−608	−611	−592	−634	−643	−618

^{a} The functionals PBE, PWPW91 and M06-L predict a barrierless decomposition of H_2O_2.

The energy for molecular adsorption of H_2O was also calculated, which allowed thermodynamic comparison with dissociative adsorption. A very consistent picture emerges, as all functionals applied, with only one exception, predicted the dissociative to be the thermodynamically preferred adsorption mode. The only exception to this is the data obtained with the PBE functional for Y_2O_3.

As for adsorption on the m-$(ZrO_2)_8$ cluster, the molecular adsorption of H_2O_2 onto the smaller clusters is stabilized by hydrogen bonds between the H_2O_2 molecule and the surface

Table 6 ΔE_{ads} for adsorption of H_2O, H_2O_2 and $HO^\bullet$ onto a $(TiO_2)_2$ cluster. Activation energy with zero point energy correction (E_a^{ZPE}) for the decomposition of H_2O_2 on the surface of the cluster and its respective reaction energy (ΔE_r). Absolute deviation from the experimental value for the activation energy (D_{exp}). Values in (kJ mol^{-1})

	B3LYP	B3LYP-D	B3LYP*	PWPW91	PBE	PBE0	M06	M06-L
ΔE_{ads} (2H_2O; dissociative)	−291	−318	−290	−280	−273	−305	−320	−304
ΔE_{ads} (H_2O; molecular)	−45	−57	−47	−54	−51	−50	−53	−51
ΔE_{ads} (2$OH^\bullet$)	−764	−786	−781	−817	−812	−778	−805	−826
ΔE_{ads} (H_2O_2; molecular)	−58	−75	−55	−69	−65	−68	−81	−80
E_a^{ZPE}	31	32	17	—^{b}	—^{b}	41	31	—^{b}
D_{exp}	6	5	20	59	58	4	6	58
ΔE_r	−494	−525	−498	−500	−501	−490	−489	−513

^{b} The functionals PBE, PWPW91 and M06-L predict a barrierless decomposition of H_2O_2.

Table 7 ΔE_{ads} for adsorption of H_2O, H_2O_2 and $HO^\bullet$ onto a (Y_2O_3) cluster. Activation energy with zero point energy correction (E_a^{ZPE}) for the decomposition of H_2O_2 on the surface of the cluster and its respective reaction energy (ΔE_r). Absolute deviation from the experimental value for the activation energy (D_{exp}). Values in (kJ mol^{-1})

	B3LYP	B3LYP-D	B3LYP*	PWPW91	PBE	PBE0	M06	M06-L
ΔE_{ads} (2H_2O; dissociative)	−172	−182	−170	−170	−119	−174	−192	−187
ΔE_{ads} (H_2O; molecular)	−70	−79	−71	−69	−65	−77	−76	−79
ΔE_{ads} (2$OH^\bullet$)	−1081	−1093	−1090	−1098	−1086	−1087	−1099	−1121
ΔE_{ads} (H_2O_2; molecular)	−83	−99	−85	−85	−85	−92	−99	−95
E_a^{ZPE}	23	28	19	—^{c}	—^{c}	45	38	—^{c}
D_{exp}	24	19	28	64	58	2	9	49
ΔE_r	−678	−697	−673	−670	−663	−684	−678	−715

^{c} The functionals PBE, PWPW91 and M06-L predict a barrierless decomposition of H_2O_2.

HO groups (Fig. 6c, 7c and 8c). All functionals applied predicted that H_2O_2 adsorbs to the clusters in the order of increasing exothermicity: $TiO_2 < Y_2O_3 < ZrO_2$. This same trend was found for the molecular adsorption of H_2O. Not surprisingly, since the molecular adsorption of both H_2O and H_2O_2 occur *via* a combination of hydrogen bonding and direct interaction with the metal atoms.

In the transition state for decomposition on the $(ZrO_2)_2$ cluster, the O–O bond distance in H_2O_2 is considerably shorter (1.552 Å, Fig. 6) than what was obtained for the larger m-$(ZrO_2)_8$ cluster (1.655 Å, Fig. 4), meaning that the transition-state occurs earlier in the smaller model. While only one of the oxygen atoms of H_2O_2 coordinate to Zr in the transition state in the m-$(ZrO_2)_8$ cluster (Fig. 4), both oxygen atoms of H_2O_2 are coordinated by Zr atoms in the $(ZrO_2)_2$ cluster (Fig. 6). In other words, the transition state in the m-$(ZrO_2)_8$ cluster is mono-coordinated, while the transition state in the $(ZrO_2)_2$ cluster is bi-coordinated. The latter situation gives rise to a stronger interaction between H_2O_2 and the metal oxide cluster leading to a weakening of the O–O bond in H_2O_2, and consequently to an earlier transition-state. The reason for the bi-coordinated transition state in the $(ZrO_2)_2$ cluster is to be found in the Zr–Zr bond length, which is 0.244 Å shorter in the $(ZrO_2)_2$ cluster, than in m-$(ZrO_2)_8$.

As discussed above, the computed dissociation pathway of H_2O_2 on the m-$(ZrO_2)_8$ cluster depends on the exchange–correlation functional used. While M06 predicts an activation energy in perfect agreement with experimental kinetic data, B3LYP as well as the dispersion corrected B3LYP-D functional, underestimate the activation energy with roughly 15 kJ mol^{-1}. In order to understand this difference, we tried a variety of exchange–correlation functionals of different types (a table showing the computational time cost for the different functionals can be found in the ESI†). Although the functionals applied differ in several ways (see further the Computational Details section) there seems to be a correlation between the amount of Hartree–Fock exchange included in the exchange–correlation functional and the height of the reaction barrier on the potential energy surface. For dissociation of H_2O_2 on $(ZrO_2)_2$, the hybrid functionals (B3LYP, B3LYP*, B3LYP-D, M06 and PBE0) predict activation energies between 33 and 42 kJ mol^{-1} (Table 5), which is in reasonable agreement with the experimental value of 33 ± 1 kJ mol^{-1} (Table 8). On the other hand, the pure density functionals applied (PWPW91, PBE, and M06-L) predict a barrierless decomposition of H_2O_2. For dissociation on $(TiO_2)_2$ the results of pure DFT are similar. While the activation energy calculated with hybrid

Table 8 Experimental $\Delta H^\ddagger$ and corresponding Arrhenius activation energies (E_a) for the decomposition of H_2O_2. Data retrieved from ref. 14 and 15. Values in kJ mol^{-1}

Material	$\Delta H^\ddagger$	E_a
ZrO_2	30 ± 1	33 ± 1
TiO_2	34 ± 1	37 ± 1
Y_2O_3	44 ± 5	47 ± 5

functionals incorporating 20 percent Hartree–Fock exchange or more (B3LYP, B3LYP-D, M06 and PBE0) deviates from the experimental value (37 ± 1 kJ mol^{-1}, Table 8) with 6 kJ mol^{-1} or less (Table 6), pure density functionals (PBE, PWPW91 and M06-L) predict a barrierless decomposition of H_2O_2. The re-parametrized hybrid functional B3LYP*, which incorporates 15 percent Hartree–Fock exchange instead of the 20 percent in the original B3LYP functional, is an outlier in the prediction of activation energies. Although it predicts an energy barrier for decomposition of H_2O_2, the deviation of the calculated value from the experimental data is larger than for the other hybrid functionals applied (error of -20 kJ mol^{-1}, Tables 6 and 8). Similar trends were obtained for decomposition on Y_2O_3, and pure DFT predicted a barrierless reaction (Table 7). It thus seems like the optimum amount of Hartree–Fock exchange is at least 20 percent, which is the lower amount of the other hybrid functionals applied. It should be remembered though, that these functionals differ in other aspects besides the amount of Hartree–Fock exchange incorporated (Table 1). Among the three functionals that incorporate Hartree–Fock exchange, M06 and PBE0 outperform B3LYP in predicting accurate reaction energy barriers. The activation energies calculated with M06 deviate from the experiments by 6 kJ mol^{-1} on average absolute value, while the deviation for PBE0 is 5 kJ mol^{-1}, and B3LYP deviates with 12 kJ mol^{-1}. For the adsorption of HO radicals on $(ZrO_2)_2$, the correlation to the amount of Hartree–Fock exchange is less apparent and all the density functionals used predicted adsorption energies that deviate less than 24 kJ mol^{-1} (per HO radical) from the only literature value found (-498 kJ mol^{-1}).[84] The dispersion effect, taken as the difference between B3LYP-D and B3LYP, is 9 kJ mol^{-1} (per HO radical).

A Mulliken population analysis showed that the adsorption of HO$^\bullet$ causes some delocalization of the d electrons of the metal atoms involved in the bonding with HO$^\bullet$, i.e. the metal atom becomes slightly oxidized. This can be seen systematically on the Mulliken charges of the metal atoms for all the models studied (data provided as ESI†). Consider the adsorption of the HO radical onto the $(ZrO_2)_2$, $(TiO_2)_2$ and (Y_2O_3) clusters (Fig. 9). The ionization energies of the metal ions present in these metal oxides vary in the order: $Y^{3+} < Zr^{4+} < Ti^{4+}$.[85] Since delocalization of the metal valence electrons has to occur in order to form bonding states with the HO radicals, the strength of the bonds between the metal clusters and the HO radicals is expected to follow the inverse trend as the ionization energies. This trend was successfully reproduced with all the exchange–correlation functionals used (Tables 5–7). Thus, *the higher the ionization energy of the metal cation present in the cluster, the smaller is the change in Mulliken charge of the metal atom upon adsorption of* HO$^\bullet$.

The adsorption of HO$^\bullet$ follows the trend for adsorption of HO$^\bullet$ onto metallic Au surfaces reported in a work by Pessoa et al.[21] The authors found that the higher the reactivity of a given Au surface towards oxidation, the stronger the HO radical will bind to that surface. For H_2O_2 decomposition, the calculated reaction energies are in good agreement with the trend

verified for the HO$^\bullet$ adsorption energies (Tables 5–7). The reasoning for this is that the products formed in the decomposition of H_2O_2 consist of a H_2O molecule molecularly adsorbed on the clusters and a HO radical bound to one of the metal atoms. When comparing the reaction energies for the different clusters, the factor that is expected to have more impact on the overall reaction energy is the adsorption of HO$^\bullet$ onto the clusters given that this quantity is far larger than the molecular adsorption energy of a H_2O molecule (Tables 5–7). In what concerns the decomposition of H_2O_2, it can be seen by comparison of the products formed in the reaction with the different clusters (Fig. 6e, 7e, and 8e), that the structure that undergoes the most extensive geometry change upon reaction is the (Y_2O_3) cluster. This structural change might provide an explanation for the larger exothermicity of reaction with the (Y_2O_3) cluster. It is difficult to say whether the (Y_2O_3) cluster is a fair model of the solid Y_2O_3 surface, since the structural flexibility of the solid could be lower than for the cluster. Nevertheless, the reaction energy for the Y_2O_3 case agrees with the trends in adsorption energies of the HO radical mentioned above.

Finally, it is worth mentioning that although the HO$^\bullet$ radical binds strongly to all three metal oxides, the formation of H_2O as a product of decomposition of H_2O_2 is supported by experiments showing that adsorbed HO$^\bullet$ can react further at the solid/liquid interface.[86] Also, since dispersion interactions occur not only *through bonds* but *through space* as well, the cluster size (and geometrical shape) has an impact on the magnitude of the dispersion effect on the calculated adsorption energy. Taking the difference between adsorption energies calculated with B3LYP and B3LYP-D as the dispersion effect, it can be seen that for the molecular adsorption of water on ZrO_2 clusters, the dispersion effect is only 10 kJ mol^{-1} in the $(ZrO_2)_2$ model (Table 5), while it is 14 kJ mol^{-1} in the medium sized m-$(ZrO_2)_8$ model (Table 3) and becomes as large as 30 kJ mol^{-1} in the large m-$(ZrO_2)_{26}$ cluster (Table 2). Differences of similar magnitude are found for the molecular adsorption of hydrogen peroxide (Tables 2 and 3). Similar effects have been reported previously.[87]

4. Conclusions

Two types of interactions responsible for the adsorption of H_2O_2 onto the surfaces of the metal oxides were observed: direct interaction between the O-atoms of H_2O_2 and the exposed metal atoms of the surfaces; and also hydrogen bonding between the surface HO groups and H_2O_2. The former type of interaction leads to stronger adsorption. Both types of interaction coexist in solution, depending on the density of surface HO groups. The transition state for decomposition of H_2O_2 is largely mediated by hydrogen bonding with the surface HO groups. In all cases studied here, the primary product of H_2O_2 decomposition, the HO radical, adsorbs to the surfaces by forming bonding states with the surface exposed metal atoms. The adsorption energy (ΔE_{ads}) depends on the ionization energy of the metal cation accommodating the HO radical, the higher

the ionization energy of the metal cation, the weaker the adsorption of HO radical.

For all materials studied, and all models and DFT methods applied, the thermodynamic product of H_2O_2 decomposition is HO and H_2O. The latter product is formed through abstraction of an H atom from a surface HO group.

The overall performance of the cluster models using the hybrid DFT functionals M06, PBE0 and B3LYP is very good, with an average absolute deviation from the experimental barriers of 7.5 kJ mol^{-1}. The inclusion of Hartree–Fock exchange in the functional is essential to properly describe the reactions studied here. The density functionals that do not incorporate Hartree–Fock exchange (PBE, PWPW91 and M06-L) failed to predict the existence of an energy barrier for the decomposition of H_2O_2. From the hybrid functionals used (B3LYP, M06 and PBE0) the best overall performance was achieved with the M06 and PBE0. For the smaller clusters, PBE0 barriers deviate from the experimental values by 5 kJ mol^{-1} in absolute average, while the deviation from experiments obtained with the M06 functional is 6 kJ mol^{-1}. In the larger m-$(ZrO_2)_8$ model, the M06 value is in excellent agreement with the experimental value, while B3LYP underestimates the activation energy at 18 kJ mol^{-1}. Since empirical correction of dispersion (B3LYP-D) gave a slightly lower barrier than B3LYP, it can be concluded that the better performance of M06 is not merely a consequence of dispersion interactions. Bearing in mind the performance in describing adsorption energetics and dissociation barriers, we recommend M06 and PBE0 for modeling reactions with metal oxide clusters.

It is not possible to make a quantitative generalization of the transferability of the performance of the minimal cluster models to other metal oxides, as our test set is limited to ZrO_2, TiO_2 and Y_2O_3. Nevertheless, the very good agreement between computational and experimental data shows that these models constitute a simple and effective approach for modeling reactivity of defective particles of these oxides.

Acknowledgements

References

1 M. Soleymani, A. Moheb and D. Babakhani, *Chem. Eng. Technol.*, 2011, **34**, 49–55.

2 N. Rasti, E. Toyserkani and F. Ismail, *Mater. Lett.*, 2011, **65**, 951–954.

3 R. Pehrman, M. Amme, O. Roth, E. Ekeroth and M. Jonsson, *J. Nucl. Mater.*, 2010, **397**, 128–131.

4 J. N. Park, J. K. Shon, M. Jin, S. H. Hwang, G. O. Park, J. H. Boo, T. H. Han and J. M. Kim, *Chem. Lett.*, 2010, **39**, 493–495.

5 J. Mooi and P. W. Selwood, *J. Am. Chem. Soc.*, 1952, **74**, 1750–1754.

6 K. Yamaguchi, C. Yoshida, S. Uchida and N. Mizuno, *J. Am. Chem. Soc.*, 2004, **127**, 530–531.

7 N. Kitajima, S. Fukuzumi and Y. Ono, *J. Phys. Chem.*, 1978, **82**, 1505–1509.

8 W.-F. Huang, P. Raghunath and M. C. Lin, *J. Comput. Chem.*, 2011, **32**, 1065–1081.

9 A. Thetford, G. J. Hutchings, S. H. Taylor and D. J. Willock, *Proc. R. Soc. London, Ser. A*, 2011, **467**, 1885–1899.

10 M. Suh, P. S. Bagus, S. Pak, M. P. Rosynek and J. H. Lunsford, *J. Phys. Chem. B*, 2000, **104**, 2736–2742.

11 M. Anpo, M. Che, B. Fubini, E. Garrone, E. Giamello and M. Paganini, *Top. Catal.*, 1999, **8**, 189–198.

12 C. M. Lousada, A. J. Johansson, T. Brinck and M. Jonsson, *J. Phys. Chem. C*, 2012, **116**, 9533–9543.

13 C. M. Lousada and M. Jonsson, *J. Phys. Chem. C*, 2010, **114**, 11202–11208.

14 A. Amorelli, J. C. Evans and C. C. Rowlands, *J. Chem. Soc., Faraday Trans. 1*, 1988, **84**, 1723–1728.

15 E. Giamello, L. Calosso, B. Fubini and F. Geobaldo, *J. Phys. Chem.*, 1993, **97**, 5735–5740.

16 C. J. Rhodes, *Prog. React. Kinet. Mech.*, 2005, **30**, 145–213.

17 L. Khachatryan and B. Dellinger, *Environ. Sci. Technol.*, 2011, **45**, 9232–9239.

18 S. C. Ammal and A. Heyden, *J. Chem. Phys.*, 2010, **133**, 164703.

19 The code CRYSTAL permits the use of HF exchange and, therefore, of hybrid orbitals, and it includes the Grimme D3 dispersion correction. R. Dovesi, R. Orlando, B. Civalleri, C. Roetti, V. R. Saunders and C. M. Zicovich-Wilson, *Z. Kristallogr.*, 2005, **220**, 571–573; R. Dovesi, V. R. Saunders, C. Roetti, R. Orlando, C. M. Zicovich-Wilson, F. Pascale, B. Civalleri, K. Doll, N. M. Harrison, I. J. Bush, P. D'ArcoM. Llunell, *CRYSTAL09, CRYSTAL09 User's Manual*, University of Torino, Torino, 2009.

20 J. Paier, R. Hirschl, M. Marsman and G. Kresse, *J. Chem. Phys.*, 2005, **122**, 234102.

21 A. M. Pessoa, J. L. C. Fajín, J. R. B. Gomes and M. N. D. S. Cordeiro, *THEOCHEM*, 2010, **946**, 43–50.

22 M. P. Andersson and S. L. S. Stipp, *J. Phys. Chem. C*, 2011, **115**, 10044–10055.

23 W. Kohn, A. D. Becke and R. G. Parr, *J. Phys. Chem.*, 1996, **100**, 12974–12980.

24 A. D. Boese, J. M. L. Martin and N. C. Handy, *J. Chem. Phys.*, 2003, **119**, 3005–3014.

25 G. Pacchioni, *J. Chem. Phys.*, 2008, **128**, 182505.

26 J. L. F. Da Silva, M. V. Ganduglia-Pirovano, J. Sauer, V. Bayer and G. Kresse, *Phys. Rev. B: Condens. Matter Mater. Phys.*, 2007, **75**, 045121.

27 C. Di Valentin, G. Pacchioni and A. Selloni, *Phys. Rev. Lett.*, 2006, **97**, 166803.

28 A. M. Burow, M. Sierka, J. Dobler and J. Sauer, *J. Chem. Phys.*, 2009, **130**, 174710–174711.

29 J. P. Perdew and M. Levy, *Phys. Rev. B: Condens. Matter Mater. Phys.*, 1997, **56**, 16021–16028.

30 Y. Zhang and W. Yang, *J. Chem. Phys.*, 1998, **109**, 2604–2608.

31 M. Lundberg and P. E. M. Siegbahn, *J. Chem. Phys.*, 2005, **122**, 224103.

32 J. P. Perdew and A. Zunger, *Phys. Rev. B: Condens. Matter Mater. Phys.*, 1981, **23**, 5048–5079.

33 Y.-F. Zhang, W. Lin, Y. Li, K.-N. Ding and J.-Q. Li, *J. Phys. Chem. B*, 2005, **109**, 19270–19277.

34 S. Tosoni and J. Sauer, *Phys. Chem. Chem. Phys.*, 2010, **12**, 14330–14340.

35 C. L. Bailey, S. Mukhopadhyay, A. Wander, B. G. Searle, J. M. Carr and N. M. Harrison, *Phys. Chem. Chem. Phys.*, 2010, **12**, 6124–6134.

36 R. Evarestov, T. Bredow and K. Jug, *Phys. Solid State*, 2001, **43**, 1774–1782.

37 N. U. Zhanpeisov, *Kinet. Catal.*, 2010, **51**, 849–853.

38 N. Matthew, in *Studies in Surface Science and Catalysis*, ed. G. F. Froment and K. C. Waugh, Elsevier, 1997, vol. 109, pp. 3–34.

39 G. E. Brown Jr, T. P. Trainor and A. M. Chaka, in *Chemical Bonding at Surfaces and Interfaces*, Elsevier, Amsterdam, 2008, pp. 457–509.

40 R. A. van Santen and M. Neurock, *Principles of Molecular Heterogeneous Catalysis*, Wiley-VCH Verlag GmbH & Co. KGaA, 2007.

41 M. A. Henderson, *Surf. Sci. Rep.*, 2002, **46**, 1–308.

42 K. Takeuchi, S. S. Perry, M. Salmeron and G. A. Somorjai, *Surf. Sci.*, 1995, **323**, 30–38.

43 S. Raz, K. Sasaki, J. Maier and I. Riess, *Solid State Ionics*, 2001, **143**, 181–204.

44 Y. Kuroda, H. Hamano, T. Mori, Y. Yoshikawa and M. Nagao, *Langmuir*, 2000, **16**, 6937–6947.

45 J. Ahdjoudj and C. Minot, *Surf. Sci.*, 1998, **402–404**, 104–109.

46 X.-Q. Gong, A. Selloni, M. Batzill and U. Diebold, *Nat. Mater.*, 2006, **5**, 665–670.

47 I. M. Brookes, C. A. Muryn and G. Thornton, *Phys. Rev. Lett.*, 2001, **87**, 266103.

48 P. Deák, *Phys. Status Solidi B*, 2000, **217**, 9–21.

49 *Jaguar 7.7*, Schrodinger, LLC New York, 2010.

50 V. N. Staroverov, G. E. Scuseria, J. Tao and J. P. Perdew, *J. Chem. Phys.*, 2003, **119**, 12129–12137.

51 J. P. Perdew, K. Burke and M. Ernzerhof, *Phys. Rev. Lett.*, 1996, **77**, 3865.

52 K. Burke, M. Ernzerhof and J. P. Perdew, *Chem. Phys. Lett.*, 1997, **265**, 115–120.

53 C. Adamo and V. Barone, *J. Chem. Phys.*, 1999, **110**, 6158–6170.

54 J. P. Perdew, J. A. Chevary, S. H. Vosko, K. A. Jackson, M. R. Pederson, D. J. Singh and C. Fiolhais, *Phys. Rev. B: Condens. Matter Mater. Phys.*, 1992, **46**, 6671–6687.

55 Y. Zhao and D. G. Truhlar, *J. Chem. Phys.*, 2006, **125**, 194101.

56 M. Reiher, O. Salomon and B. A. Hess, *Theor. Chem. Acc.*, 2001, **107**, 48–55.

57 Y. Zhao and D. Truhlar, *Theor. Chem. Acc.*, 2008, **120**, 215–241.

58 Y. Zhao and D. G. Truhlar, *Acc. Chem. Res.*, 2008, **41**, 157–167.

59 S. Grimme, *J. Comput. Chem.*, 2006, **27**, 1787–1799.

60 X. Xu, H. Nakatsuji, M. Ehara, X. Lu, N. Q. Wang and Q. E. Zhang, *Chem. Phys. Lett.*, 1998, **292**, 282–288.

61 X. Lü, X. Xu, N. Wang, Q. Zhang, M. Ehara and H. Nakatsuji, *Chem. Phys. Lett.*, 1998, **291**, 445–452.

62 A. Christensen and E. A. Carter, *Phys. Rev. B: Condens. Matter Mater. Phys.*, 1998, **58**, 8050.

63 F. Rittner, B. Boddenberg, R. F. Fink and V. Staemmler, *Langmuir*, 1998, **15**, 1449–1455.

64 F. Rittner, R. Fink, B. Boddenberg and V. Staemmler, *Phys. Rev. B: Condens. Matter Mater. Phys.*, 1998, **57**, 4160–4171.

65 D. J. Brugh, R. D. Suenram and W. J. Stevens, *J. Chem. Phys.*, 1999, **111**, 3526–3535.

66 S. Li and D. A. Dixon, *J. Phys. Chem. A*, 2010, **114**, 2665–2683.

67 T. Merle-Méjean, P. Barberis, S. B. Othmane, F. Nardou and P. E. Quintard, *J. Eur. Ceram. Soc.*, 1998, **18**, 1579–1586.

68 S. T. Korhonen, M. Calatayud and A. O. I. Krause, *J. Phys. Chem. C*, 2008, **112**, 6469–6476.

69 A.-H. Lu, E. L. Salabas and F. Schüth, *Angew. Chem., Int. Ed.*, 2007, **46**, 1222–1244.

70 S. V. Ushakov and A. Navrotsky, *Appl. Phys. Lett.*, 2005, **87**, 164103.

71 M. A. Weibel, K. M. Backstrand and T. J. Curtiss, *Surf. Sci.*, 2000, **444**, 66–78.

72 A. Nilsson and L. G. M. Pettersson, in *Chemical Bonding at Surfaces and Interfaces*, Elsevier, Amsterdam, 2008, pp. 57–142.

73 D. J. McKay and J. S. Wright, *J. Am. Chem. Soc.*, 1998, **120**, 1003–1013.

74 Y. Zhao and D. G. Truhlar, *Theor. Chem. Acc.*, 2008, **120**, 215–241.

75 K. E. Riley and P. Hobza, *Wiley Interdiscip. Rev.: Comput. Mol. Sci.*, 2011, **1**, 3–17.

76 A. J. Johansson, E. Zuidema and C. Bolm, *Chem.–Eur. J.*, 2010, **16**, 13487–13499.

77 J. Jung, H.-J. Shin, Y. Kim and M. Kawai, *J. Am. Chem. Soc.*, 2011, **133**, 6142–6145.

78 X.-Q. Gong and A. Selloni, *J. Catal.*, 2007, **249**, 134–139.

79 Z.-P. Liu and P. Hu, *J. Am. Chem. Soc.*, 2003, **125**, 1958–1967.

80 M. A. A. Issa, N. M. Molokhia and Z. H. Dughaish, *J. Phys. D: Appl. Phys.*, 1983, **16**, 1109–1114.

81 G. Jayaram and V. G. Krishnan, *Phys. Rev. B: Condens. Matter Mater. Phys.*, 1995, **51**, 1294.

82 G. Balducci, G. Gigli and M. Guido, *J. Chem. Phys.*, 1985, **83**, 1909–1912.

83 E. Murad and D. L. Hildenbrand, *J. Chem. Phys.*, 1975, **63**, 1133–1139.

84 Y. Okamoto, *Appl. Surf. Sci.*, 2008, **255**, 3434–3441.

85 W. M. Haynes and D. R. Lide, *CRC Handbook of Chemistry and Physics: A Ready-Reference Book of Chemical and Physical Data*, CRC Press, Boca Raton, FL, 2011.

86 V. Brezova, A. Stasko, S. Biskupic, A. Blazkova and B. Havlinova, *J. Phys. Chem.*, 1994, **98**, 8977–8984.

87 M. Jonas, E. Stephan, T. Ralf and G. Stefan, *J. Phys.: Condens. Matter*, 2012, **24**, 424206.

88 A. V. Radha, O. Bomati-Miguel, S. V. Ushakov, A. Navrotsky and P. Tartaj, *J. Am. Ceram. Soc.*, 2009, **92**, 133–140.

89 I. M. Iskandarova, A. A. Knizhnik, E. A. Rykova, A. A. Bagatur'yants, B. V. Potapkin and A. A. Korkin, *Microelectron. Eng.*, 2003, **69**, 587–593.

90 F. Haase and J. Sauer, *J. Am. Chem. Soc.*, 1998, **120**, 13503–13512.

91 M. Egashira, S. Kawasumi, S. Kagawa and T. Seiyama, *Bull. Chem. Soc. Jpn.*, 1978, **51**, 3144–3149.

92 A. Vittadini, A. Selloni, F. P. Rotzinger and M. Grätzel, *Phys. Rev. Lett.*, 1998, **81**, 2954.

93 A. Hussain, J. Gracia, B. E. Nieuwenhuys and J. W. Niemantsverdriet, *ChemPhysChem*, 2010, **11**, 2375–2382.

94 B. Hammer, S. Wendt and F. Besenbacher, *Top. Catal.*, 2010, **53**, 423–430.

95 W. F. Huang, P. Raghunath and M. C. Lin, *J. Comput. Chem.*, 2011, **32**, 1065–1081.

96 P. Zhang, A. Navrotsky, B. Guo, I. Kennedy, A. N. Clark, C. Lesher and Q. Y. Liu, *J. Phys. Chem. C*, 2008, **112**, 932–938.

97 B. M. Gorelov, D. V. Morozovskaya, V. M. Pashkov and V. A. Sidorchuk, *Tech. Phys.*, 2000, **45**, 1147–1153.

"Enhanced hydrogen formation during the catalytic decomposition of H$_2$O$_2$ on metal oxide surfaces in the presence of HO radical scavengers"
Cláudio M. Lousada, Jay A. LaVerne, and Mats Jonsson, *Journal of Physical Chemisty C*, under review

VI

Enhanced hydrogen formation during the catalytic decomposition of H_2O_2 on metal oxide surfaces in the presence of HO radical scavengers

Cláudio M. Lousada,[†] * Jay A. LaVerne[‡] and Mats Jonsson[†]

† Applied Physical Chemistry, School of Chemical Science and Engineering, KTH Royal Institute of Technology, SE-100 44 Stockholm, Sweden
‡ Radiation Laboratory and Department of Physics, University of Notre Dame, Notre Dame, Indiana 46556, USA

* To whom correspondence should be addressed: Phone, (46) 8 790 87 89;
Fax, (46) 8 790 87 72; e-mail, cmlp@kth.se

Abstract

Presently and for the foreseeable future, hydrogen peroxide and transition metal oxides are important constituents of energy production processes. In this work, the effect of the presence of HO radical scavengers on the product yield from the decomposition of H_2O_2 on metal oxide surfaces in aqueous solution was examined experimentally. Scavenging the intermediate product $HO^\bullet$ by means of Tris or TAPS buffers leads to enhanced formation of H_2. In parallel, a decrease in the production of the main gaseous product O_2 is observed. Under these conditions, H_2 formation is a spontaneous process even at room temperature. The yields of both the H_2 and O_2 depend on the concentration of Tris or TAPS in the reaction media. We observed that TAPS has a higher affinity for the surface of ZrO_2 than does Tris. The difference in adsorption of both scavengers is reflected by the difference in their influence on the product yields. The observed sensitivity of the system H_2O_2-ZrO_2 towards the two different scavengers indicates that O_2 and H_2 are formed at different types of surface sites

Introduction

The reactivity of H_2O_2 towards transition metal oxide surfaces is a current topic of research due its importance in a variety of contexts such as energy production, catalysis, nuclear technology, geochemistry and medical sciences.[1-5] H_2O_2 can react with metal oxide surfaces both as an oxidant and as a reductant and can also react through catalytic decomposition.[6] This last type of reaction is known to occur on transition metal oxide surfaces where the metal cation cannot be further oxidized. The interfacial catalytic decomposition of H_2O_2 leads to the formation of reactive radical species that can affect the stability of materials and the chemistry of the interfaces between the solid surface of the catalyst and a contacting liquid phase.[7-9] These reactive species are formed at the interface where H_2O_2 undergoes decomposition. At the catalyst surface, the different types of surface sites display different reactivity depending on the metal cation coordination,[10,11] as the extent of coordination affects their interaction with both adsorbates and products of reactions of adsorbed species.[12] Analysis of the reactivity of H_2O_2 and its resultant products reveals that the defective surface sites such as edges and vertexes where metal cations are exposed, as the result of oxygen vacancies, are the most reactive surface sites for the decomposition of H_2O_2. Due to the surface site specificity of the reactions of H_2O_2 and its products, understanding the role of the intermediate species formed upon the catalytic decomposition of H_2O_2 on a real system is a difficult task.

Upon exposure to H_2O, transition metal oxide surfaces become hydroxylated with the exception of few special surface sites.[13] Experimental[6] and density functional theory (DFT)[14] studies have recently been able to show that HO radicals are formed at these hydroxylated surfaces as the primary product of the decomposition of H_2O_2. These radicals can adsorb onto the metal oxides at sites where the metal atoms are undercoordinated and they can react further to form H_2O and surface adsorbed $HO^\bullet$.[15,16] The formation of H_2O by reaction of $HO^\bullet$ with the hydroxylated surface of the metal oxides leads to the formation of a surface

1

O$^\bullet$ at the catalytically active site (S_{CA}). In terms of its bonding with the surface metal atoms, the adsorbed HO$^\bullet$ forms an open shell structure. This was confirmed by investigations of some of the local properties of its bonding with the surface, such as local spin density and Mulliken population. In many catalytic reactions, the build-up or removal of products from the surface of the catalyst leads to changes in the overall reaction mechanism. This variation occurs when the products are involved further in the reaction mechanism or if their presence at the surface will hinder another type of reaction or the adsorption of reactants. Changing the reaction scheme has consequences on the overall reaction mechanism, which translates as changes on the observed kinetic parameters and energy barriers.

Previous investigations on the reactivity of H_2O_2 with ZrO_2 and other metal oxides in aqueous solutions deduced the following mechanism for H_2O_2 decomposition[14]

$$H_2O_2 \text{ (ads)} + S_{CA} \rightarrow H_2O \text{ (ads)} + HO^\bullet \text{ (ads)} + S_{CA}^\bullet \quad (R1)$$
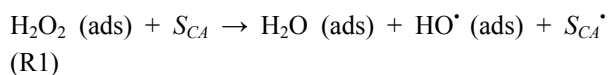
where ads represents a surface adsorbed state. At the surface sites where HO$^\bullet$ adsorption is weaker, the surface bound HO$^\bullet$ can react with H_2O_2 according to
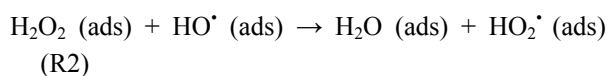
$$H_2O_2 \text{ (ads)} + HO^\bullet \text{ (ads)} \rightarrow H_2O \text{ (ads)} + HO_2^\bullet \text{ (ads)} \quad (R2)$$

the surface unpaired electron localized at $S_{CA}^\bullet$ is also a possible reaction site for further reactions of H_2O_2 such as[17]

$$H_2O_2 \text{ (ads)} + S_{CA}^\bullet \rightarrow HO_2^\bullet \text{ (ads)} + S_{CA}H \quad (R3)$$
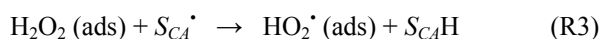
where $S_{CA}H$ represents and H$^\bullet$ bound onto the $S_{CA}^\bullet$ site. Another possible reaction pathway for H_2O_2 at the surface is
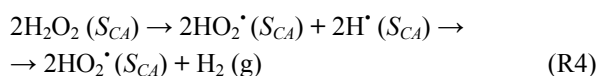
$$2H_2O_2 \text{ } (S_{CA}) \rightarrow 2HO_2^\bullet \text{ } (S_{CA}) + 2H^\bullet \text{ } (S_{CA}) \rightarrow$$
$$\rightarrow 2HO_2^\bullet \text{ } (S_{CA}) + H_2 \text{ (g)} \quad (R4)$$

where the state S_{CA} denotes that the corresponding species is adsorbed onto the surface catalytically active site. The S_{CA} site was described in a previous work.[14] H_2O_2 binds to the S_{CA} site by direct interaction of its O$^\bullet$ atoms with undercoordinated metal cations at the surface. This type of interaction leads to a considerable adsorption energy for H_2O_2; of up to 140 kJ·mol^{-1} for adsorption onto ZrO_2. Although adsorption of H_2O_2 through hydrogen bonding with surface bound HO$^\bullet$ is possible, this type of interaction is weaker than the direct binding of H_2O_2 with the surface by interaction with the exposed metal cations. As such, the adsorption of H_2O_2 would be facilitated by the removal of HO$^\bullet$ entities from the system because adsorbed HO$^\bullet$

2

competes with H_2O_2 for adsorption onto the same exposed surface metal cations. The present work is aimed at investigating the effects of HO$^\bullet$ scavengers (Tris and TAPS) on the products of the decomposition of H_2O_2 on the surface of ZrO_2.

2. Experimental Methods
2.1 Instrumentation

The surface area of ZrO_2 was determined with a Quantachrome Autosorb 1 surface area analyzer using the Brunauer-Emmet-Teller method of surface area calculation. The obtained surface area was 3.34 m^2·g^{-1}, which corresponds to spheres of about 320 nm if the particles were smooth.

Hydrogen and oxygen were determined in deaerated samples using an inline technique employing a gas chromatograph. Ultrahigh purity argon was used as the carrier gas with a flow rate of about 50 mL/min. The argon passed through a constant flow regulator, an injection septum, a four-way valve and into a 5 m molecular sieve column of an SRI 8610C gas chromatograph with a thermal conductivity detector. The samples cells were connected to the gas analysis system, purged of air, isolated, crushed and then the gases injected into the carrier gas stream. H_2 and O_2 were determined in each of the samples. Calibration of the detector was performed by injecting pure H_2 and O_2 with a gastight microliter syringe. The error in gas measurement was estimated to be about 5%.

UV-Vis spectra were collected using a thermo scientific Genesys 20 spectrophotometer.

2.2 Reagents and Experiments

All the solutions used in this work were prepared using water from a Millipore Milli-Q system and were purged with ultra-high purity argon (99.9999%). Monoclinic zirconia, ZrO_2, (Alpha Aesar, puratronic grade, 99.978%) was baked at 500 °C for 12 hours before use to remove hydrocarbon contaminates. The reaction mixtures were placed in Pyrex tubes (ϕ= 1 cm, L = 10 cm), purged, and flame sealed.

Scavenging of the HO$^\bullet$ radicals formed by H_2O_2 decomposition was performed using the two following compounds: 2-Amino-2-hydroxymethyl-propane-1,3-diol; (Tris) [CAS-77-86-1] and N-[Tris(hydroxymethyl)methyl]-3-aminopropanesulfonic acid sodium salt; (TAPS$^-$Na$^+$) [CAS-91000-53-2]. These two scavengers were used at pH 7.5 as adjusted with HCl. A proper assessment of the effects of each scavenger on the products of decomposition of H_2O_2 requires knowledge of the adsorption properties of each of the scavengers used. In the adsorption experiments, the determination of the amount of Tris and TAPS in

solution was done following a basic competition kinetic scheme. According to reference [18], the bleaching of methylene blue solutions (1-16 μM) under γ-radiolysis increases linearly up to doses on the order of 500 Gy. Here, a linear correlation for the bleaching of a methylene blue solution (18 μM) was observed as a function of γ dose up to 90 Gy, which was the dose used for measurement of the competition kinetic experiments (Figure 1).
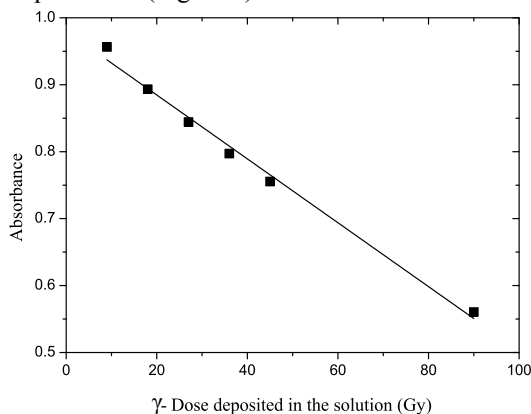

Figure 1. Calibration curve for the irradiation of a methylene blue (18 μM) solution showing a linear correlation between deposited dose of γ radiation and absorbance at 664 nm.

The methylene blue concentration was measured with UV-Vis spectrophotometry at 664 nm. γ-irradiation of a methylene blue solution undergoes less bleaching in the presence of another HO$^•$ radical scavenger than does a pure methylene blue solution. This protection is due to competition for the HO$^•$ radical between the methylene blue and the added HO$^•$ radical scavenger.[19] The competition kinetics between Tris or TAPS and the methylene blue for the HO$^•$ radical was used to determine the amount of Tris or TAPS removed from solution by adsorption. The reduction in bleaching of a methylene blue (18 μM) solution and the increase in concentration of Tris or TAPS is linear in the concentration range of 50-250 μM of Tris or TAPS. The measurement of the adsorption parameters for Tris and TAPS was done at 298 K using solutions of varying concentration of adsorbate. After adsorption equilibrium was reached, a sample aliquot was taken and filtered and the competition kinetic analysis with methylene blue was performed. The reaction media for the adsorption study consisted of 5 mL of Tris or TAPS solution with concentrations in the range 100-500 μM and ZrO$_2$ (2.5 g, Surface Area = 8.4 m^2) at pH 7.5 adjusted with HCl. The lower value of concentration of Tris and TAPS for

which we could determine measure adsorption using competition with methylene blue was 50 μM.

The effects of the HO$^•$ scavengers on the products of H$_2$O$_2$ decomposition were investigated using 2 mL of H$_2$O$_2$ (10 mM) solution and ZrO$_2$ (0.4 g, Surface Area = 1.34 m^2) at pH 7.5. The pH was adjusted with HCl.

3. Results and Discussion

An examination of the scavenging effect of Tris and TAPS on the mechanism of the decomposition of H$_2$O$_2$ on ZrO$_2$ requires their adsorption equilibrium constants in order to know the actual amount of these compounds on the surface. Upon exposure of a 5 mL solution of varying concentration of Tris or TAPS (100-500 μM, V = 5 mL) to ZrO$_2$ (2.5 g, S_A = 12.5 m^2) at pH 7.5, the amount of Tris and TAPS adsorbed onto the surface at equilibrium was determined from the γ-radiation induced bleaching of the methylene blue. This method measures the competition kinetics for the scavenging of the radiation induced production of HO$^•$ radicals. Methylene blue reacts with HO$^•$ radicals with a rate constant of 6.9×10^{10} M^{-1}·s^{-1}.[20] The rate constant for reaction of Tris with HO$^•$ radicals is 1.1×10^9 M^{-1}·s^{-1}.[21] The rate constant for the reaction of TAPS with HO$^•$ radicals has not been precisely determined. Based on structural factors and on the rate constants obtained for many of the other Good's buffers, it is expected to be on the order of 10^9 M^{-1}·s^{-1}.[21] Thus, it is not surprising that the optimal conditions for the competition kinetics are for a concentration of Tris or TAPS around 10 times higher than the concentration of methylene blue. The resulting data for the percentage of adsorbed Tris and TAPS at equilibrium as a function of their initial concentrations are represented in Figure 2. From Figure 2 it is obvious that TAPS has a higher affinity for the ZrO$_2$ surface than Tris. According to the Langmuir theory of adsorption, the adsorption at equilibrium conditions can be expressed by

$$q_e = \frac{X_m \cdot K \cdot C_e}{1 + K C_e} \qquad (1)$$

where q_e is the amount of adsorbate adsorbed per unit weight of adsorbent, X_m is the amount of adsorbate required for a monolayer coverage on the surface of the adsorbent, K is the Langmuir adsorption equilibrium constant and C_e is the equilibrium concentration of adsorbate in solution. The Langmuir adsorption equilibrium constant, K, is defined as k_a/k_d where k_a and k_d are the rate constants of adsorption and desorption. The linearization of equation 1 has the form

$$\frac{1}{q_e} = \frac{1}{X_m} + \left(\frac{1}{C_e}\right)\left(\frac{1}{K \cdot X_m}\right) \qquad (2)$$

The quantity K as defined above can give a comparative picture of the differences in terms of

surface coverage and adsorption energies for both molecules and can be obtained by plotting $1/q_e$ as a function of $1/C_e$. The value of K for Tris is 2.5×10^{-3} and for TAPS is 4.6×10^{-4}. Hence adsorption of TAPS is more exothermic than adsorption of Tris. Translated into the adsorption mechanism, these adsorption data suggests that the surface area covered surface is 4.5 times higher for adsorption of TAPS than for adsorption of Tris onto the ZrO_2 surface for the same initial concentration of adsorbate.
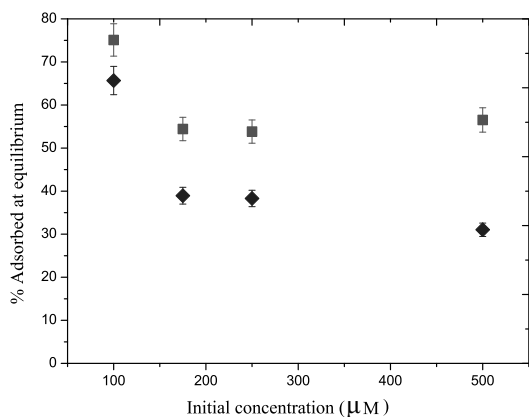

Figure 2. Percentage of Tris (♦) and TAPS (■) adsorbed at equilibrium as a function of their initial concentration in solution at pH = 7.5 for adsorption onto ZrO_2 (2.5 g) at 298 K in a volume of 5 mL.

The effect of the presence of either Tris or TAPS on the mechanism of H_2O_2 decomposition on the surface of ZrO_2 was investigated. In this procedure, we examined the gaseous products H_2 and O_2 formed upon decomposition of H_2O_2 in the presence of varying amounts of the $HO^\bullet$ scavengers Tris or TAPS. Test experiments were previously performed to ensure complete conversion of H_2O_2 when O_2 and H_2 were measured. Prior to the analysis of the amount of H_2 formed as a function of scavenger concentration, several background experiments were performed. The background experiments consisted of one of the $HO^\bullet$ scavengers, either Tris or Taps (200 mM) in a ZrO_2 particle suspension without H_2O_2 present. For all the cases where H_2O_2 was not present, there was no detectable production of H_2. The amount of H_2 produced was also studied for reaction media with different concentrations of H_2O_2 at a fixed concentration (200 mM) of $HO^\bullet$ scavenger. The resulting data is shown in Table **1.** It can be seen (Table 1) that the formation of H_2 is dependent on the amount of H_2O_2 present in the system. For the lower

concentration of H_2O_2 (0.2 mM) used, there was no detectable formation of H_2.

Table 1. H_2 detected (mM) in a ZrO_2 particle suspension with different amounts of H_2O_2 and a fixed concentration (200 mM) of Taps or Tris buffers .

$[H_2O_2]$ (mM)	$[H_2]$ detected (mM) (in Taps (200 mM))	$[H_2]$ detected (mM) (in Tris (200 mM))
0.2	0	0
1.0	1.6×10^{-5}	0
10	2.0×10^{-2}	1.7×10^{-3}

The study of the formation of H_2 as a function of $HO^\bullet$ scavenger concentration was done for a system of ZrO_2 particles with H_2O_2 (10 mM) and varying concentrations of Tris and Taps. The choice of this concentration of H_2O_2 was based on the results of test experiments shown in Table 1. The data obtained are represented in Figure 3 and 4 for Tris and TAPS, respectively.
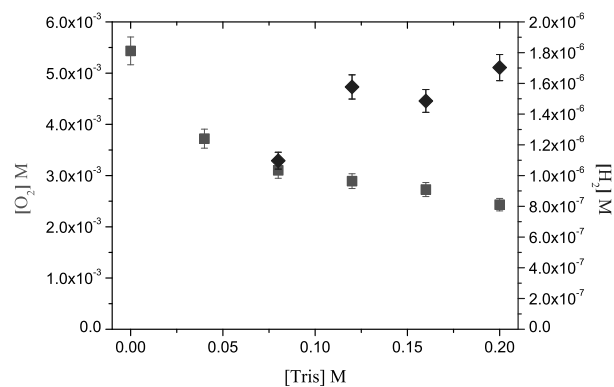

Figure 3. Production of O_2 (■) and H_2 (♦) in the decomposition of H_2O_2 on the surface of ZrO_2 in the presence of different concentrations of the $HO^\bullet$ scavenger Tris (0-0.2 M).
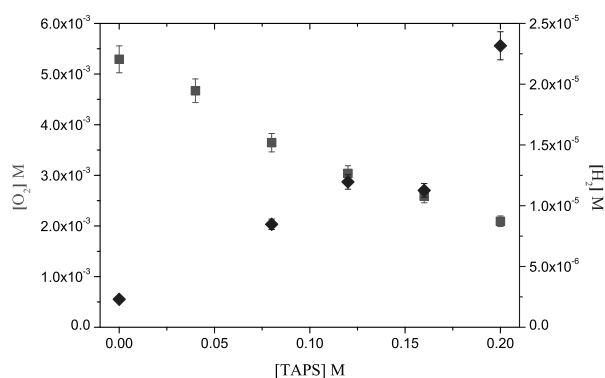
Figure 4. Production of O_2 (■) and H_2 (♦) in the decomposition of H_2O_2 on the surface of ZrO_2 in the presence of different concentrations of the $HO^{\bullet}$ scavenger TAPS (0-0.2 M).

Experiments without $HO^{\bullet}$ radical scavengers give amounts of O_2 that are in agreement with the proposed stoichiometry for the decomposition of H_2O_2, which is half of the initial concentration of H_2O_2.[22] The results in Figure 3 and 4 show that the presence of an $HO^{\bullet}$ radical scavenger, either Tris or TAPS, decreases the production of O_2 and increases that of H_2. Both the decrease in O_2 and the increase in H_2 are proportional to the amount of $HO^{\bullet}$ scavenger in the system. For the system with Tris (Figure 2) this is visible for concentrations of scavenger higher than 75 mM. Variation in how the two scavengers affect the O_2 yield is noticeable at scavenger concentrations above 0.08 M. For Tris, the decrease in O_2 yield becomes less pronounced for scavenger concentrations higher than 0.08 M, while the O_2 yield decreases linearly up to 0.2

M of TAPS. The changes in H_2 yield with increasing concentration of scavenger are also obvious. At the same initial solute concentrations, the production of H_2 is higher when TAPS is present than in the case of Tris. As discussed above, the surface coverage is 4.5 times higher for TAPS than for Tris for the same initial solute concentration. This also means that TAPS is able to scavenge more $HO^{\bullet}$ than Tris due to its higher concentration at the surface. This result suggests that the formation of H_2 is a surface process that depends on the presence and on the surface coverage of an $HO^{\bullet}$ scavenger. This reasoning is further supported by our test experiments with TiO_2 and CuO where the presence of Tris or TAPS has similar effects on the H_2 and O_2 yields (Table 2). As for the case of ZrO_2 when no scavenger was present, the amount of O_2 detected corresponded to the stoichiometric value predicted by the suggested mechanism for H_2O_2 decomposition for a system where no $HO^{\bullet}$ scavenger is present. For the reaction media where Tris or TAPS are present the yields of both O_2 and H_2 are shown in Table 2. Even though the yields of H_2 and O_2 for CuO and TiO_2 (Table 2) are different than for the case of ZrO_2, the same trends are found.

The presence of a $HO^{\bullet}$ scavenger enhances the formation of H_2 and decreases the yield of O_2. For all ZrO_2 as for the other two oxides, for both TAPS and Tris, the changes in the production of O_2 and H_2 do not seem to obey a specific mass balance. The presence of a $HO^{\bullet}$ scavenger influences the overall H_2O_2 reactivity by favoring the side reaction leading to H_2 formation and affecting the main reaction path that leads to the formation of O_2. This observation further illustrates the

Table 2. Yields of H_2 and O_2 (M) for the reaction of decomposition of H_2O_2 (10 mM) catalyzed by CuO or TiO_2 in the presence of the $HO^{\bullet}$ scavengers Tris or Taps (0.2 M).

$HO^{\bullet}$ scavenger	$CuO - O_2$	$CuO - H_2$	$TiO_2 - O_2$	$TiO_2 - H_2$
No scavenger	5.0×10^{-3}	0	5.0×10^{-3}	0
Tris (0.2 M)	2.7×10^{-3}	8.4×10^{-6}	1.0×10^{-4}	9.3×10^{-6}
TAPS (0.2 M)	1.2×10^{-3}	1.6×10^{-5}	8.9×10^{-4}	3.0×10^{-5}

importance of the HO$^•$ radical as an intermediate reactive species on the decomposition of H$_2$O$_2$. As previously reported, the HO$^•$ is the primary H$_2$O$_2$ decomposition product and it competes with H$_2$O$_2$ for the same adsorption sites at the surface of the metal oxides.[14] Removal of the HO$^•$ from the reaction system has an effect on the relative yields of the products formed. Without the HO$^•$ scavenger, H$_2$O$_2$ decomposes at the surface of the oxides according to the following stoichiometric relationship

$$H_2O_2 \rightarrow 1/2 O_2 + H_2O \qquad (R5)$$

The presence of the HO$^•$ scavenger changes the overall mechanism to R6.

$$H_2O_2 \rightarrow x O_2 + y H_2O + z H_2 \qquad (R6)$$
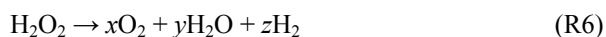
Reaction R6 could be explained in terms of a mechanism such as the one represented in Reaction R4. A determination of the coefficients x, y and z is not trivial since their values depend on the presence of the HO$^•$ scavenger. Overall, the removal of HO$^•$ from the S_{CA} site is expected to contribute in two distinctive ways to the formation of H$_2$. The first is that the increased removal of HO$^•$ from the surface facilitates the adsorption of H$_2$O$_2$ through direct interaction of its O atoms with the metal cations. This exchange will lead to a higher H$_2$O$_2$ coverage at the S_{CA} sites. The other contribution is that the alternative reactive pathway of H$_2$O$_2$ decomposition by breaking one of the H-O bonds is also enhanced because there is room at the S_{CA} site to accommodate the resulting products, the HO$_2^•$ and H$^•$ radicals. Surface adsorption of H$^•$ is known to occur for ZnO and the migration of adsorbed H$^•$ can have an activation energy as low as 38 kJ·mol^{-1}.[23-25] For metallic surfaces of Cu, H$^•$ adsorbed on neighboring surface metal atoms can easily recombine to form H$_2$.[26] A similar type of surface adsorbed H radical recombination is expected to occur at the surfaces of the oxides here examined. This recombination has been shown to be possible at surface sites where the adsorbed H atoms are bound to neighboring atoms as previously reported for TiO$_2$ surfaces.[16,27]

Conclusions

The presence of an HO$^•$ scavenger in an aqueous transition metal oxide particle suspension leads to an alteration of the relative amounts of product for the decomposition of H$_2$O$_2$ in this system. Upon addition of a HO$^•$ scavenger to the reaction media, the formation of H$_2$ was observed. This is accompanied by a decrease in O$_2$ yield. Both the amount of H$_2$ formed and the decrease in the amount of O$_2$ correlate with the amount of HO$^•$ scavenger present in solution and consequently at the surface. A possible explanation for this observation is that due to the presence of a HO$^•$ scavenger, the predominant mechanism for decomposition of H$_2$O$_2$ that has HO$^•$ as the reactive intermediate, decreases in predominance and instead the formation of H$^•$ and HO$_2^•$ starts to have increased impact on the reaction mechanism. This directs the decomposition of H$_2$O$_2$ towards the reaction path that involves formation of H$_2$. Further experimental and theoretical investigations are necessary to establish a clear mechanistic description of the effect of the presence of HO$^•$ scavengers in the mechanism of H$_2$O$_2$ decomposition. It is plausible that the formation of H$_2$ from neighboring adsorbed H$^•$ follows a mechanism similar to that was observed previously for pure metallic surfaces and for the recombination of neighboring H atoms adsorbed onto TiO$_2$.

References

(1)   Cox, B. *Journal of Nuclear Materials* **2005**, *336*, 331.

(2)   Sakai, K.; Kato, J.; Kurata, H.; Nakazawa, T.; Akashi, G.; Kameyama, A.; Hirai, Y. *Laser Phys.* **2007**, *17*, 1062.

(3)   Wang, B. Journal of Power Sources **2005**, 152, 1.

(4)   Disselkamp, R. S. *Energy & Fuels* **2008**, *22*, 2771.

(5)   Mousavi Shaegh, S. A.; Nguyen, N.-T.; Mousavi Ehteshami, S. M.; Chan, S. H. *Energy & Environmental Science* **2012**, *5*, 8225.

(6)   Lousada, C. M.; Jonsson, M. *The Journal of Physical Chemistry C* **2010**, *114*, 11202.

(7)   Li, L.; Goel, R. K. *Journal of Hazardous Materials* **2010**, *181*, 521.

(8)   Voinov, M. A.; Pagán, J. O. S.; Morrison, E.; Smirnova, T. I.; Smirnov, A. I. *Journal of the American Chemical Society* **2010**, *133*, 35.

(9)   Carrasco-Flores, E. A.; LaVerne, J. A. *J. Chem. Phys.* **2007**, *127*.

(10)   Epling, W. S.; Peden, C. H. F.; Henderson, M. A.; Diebold, U. *Surface Science* **1998**, *412–413*, 333.

(11)   Liu, P.; Kendelewicz, T.; Brown Jr, G. E.; Parks, G. A. *Surface Science* **1998**, *412–413*, 287.

(12)   Liu, P.; Kendelewicz, T.; Brown Jr, G. E. *Surface Science* **1998**, *412–413*, 315.

(13)   Brown, G. E.; Henrich, V. E.; Casey, W. H.; Clark, D. L.; Eggleston, C.; Felmy, A.; Goodman, D. W.; Grätzel, M.; Maciel, G.; McCarthy, M. I.; Nealson, K. H.; Sverjensky, D. A.; Toney, M. F.; Zachara, J. M. *Chemical Reviews* **1998**, *99*, 77.

(14)   Lousada, C. M.; Johansson, A. J.; Brinck, T.; Jonsson, M. *The Journal of Physical Chemistry C* **2012**, *116*, 9533.

(15)   Lousada, C. M.; Johansson, A. J.; Brinck, T.; Jonsson, M. *J. Phys. Chem. C* **2012**, *116*, 9533.

(16)   Hussain, A.; Gracia, J.; Nieuwenhuys, B. E.; Niemantsverdriet, J. W. *ChemPhysChem* **2010**, *11*, 2375.

(17)   Huang, W. F.; Raghunath, P.; Lin, M. C. *J. Comput. Chem.* **2011**, *32*, 1065.

(18)   LaVerne, J. A.; Tandon, L.; Knippel, B. C.; Montoya, V. M. *Radiation Physics and Chemistry* **2005**, *72*, 143.

(19)   Satoh, A. Y.; Trosko, J. E.; Masten, S. J. *Environmental Science & Technology* **2007**, *41*, 2881.

(20)   Alpert, S. M.; Knappe, D. R. U.; Ducoste, J. J. *Water Research* **2010**, *44*, 1797.

(21)   Hicks, M.; Gebicki, J. M. *FEBS Letters* **1986**, *199*, 92.

(22)   Hiroki, A.; LaVerne, J. A. *The Journal of Physical Chemistry B* **2005**, *109*, 3364.

(23)   Becker, T.; Hövel, S.; Kunat, M.; Boas, C.; Burghaus, U.; Wöll, C. *Surface Science* **2001**, *486*, L502.

(24)   Doh, W. H.; Roy, P. C.; Kim, C. M. *Langmuir* **2010**, *26*, 16278.

(25)   Bang, J.; Chang, K. J. *Applied Physics Letters* **2008**, *92*, 132109.

(26)   Johansson, A. J.; Lilja, C.; Brinck, T. *The Journal of Chemical Physics* **2011**, *135*, 084709.

(27)   Menetrey, M.; Markovits, A.; Minot, C. *Surface Science* **2003**, *524*, 49.

"Catalytic decomposition of hydrogen peroxide on transition metal and lanthanide oxides"
Cláudio M. Lousada, Miao Yang, Kristina Nilsson, and Mats Jonsson, *Applied Catalysis - Section A*, under review

VII

Catalytic decomposition of hydrogen peroxide on transition metal and lanthanide oxides

Cláudio M. Lousada,[*] Miao Yang, Kristina Nilsson, and Mats Jonsson

Applied Physical Chemistry, School of Chemical Science and Engineering, KTH Royal Institute of Technology, SE-100 44 Stockholm, Sweden

* To whom correspondence should be addressed: phone, (46) 8 790 87 89;

Fax, (46) 8 790 87 72; e-mail, cmlp@kth.se

Abstract

We have investigated the reactions of Fe_2O_3, CuO, HfO_2, CeO_2 and Gd_2O_3 with H_2O_2 in aqueous solution. The room temperature rate constants for the reactions were determined. From the temperature dependence of the rate constants we extracted the Arrhenius parameters and the standard enthalpies of activation for the reactions. In addition, we studied the dynamics of formation of the intermediate species formed during decomposition of H_2O_2, the HO radical. The kinetic data and the yields of hydroxyl radical formation differ considerably between many of the materials studied. We compared the energetic and mechanistic data obtained in this work with literature data, for a set of 9 oxides in total. The Arrhenius pre-exponential factors normalized to surface area for the decomposition of H_2O_2 vary by 9 orders of magnitude within the range of oxides discussed here. This indicates that the surfaces of the oxides have very different catalytic capacity towards cleavage of H_2O_2. The standard enthalpies of activation for H_2O_2 decomposition vary between 30 and 73 $kJ \cdot mol^{-1}$, revealing also differences in the catalytic efficiency. The mechanistic data analyzed consists of the amount of HO radical scavenged by tris(hydroxymethyl)aminomethane (Tris) during the course of the decomposition of H_2O_2 for the whole set of oxides. The yields and dynamics of scavenging of $HO^{\bullet}$ differ considerably between the oxides analyzed. Surprisingly, the time-independent plot of the amount of HO scavenged as a function of the conversion of H_2O_2 reveals that the quantity of HO scavenged has an inflection point for some oxides – there is a sudden increase in the yield of scavenged hydroxyl radicals.

1. Introduction

Interfacial radiation chemistry (radiation induced chemical reactions at solid-liquid interfaces) is crucial for the performance and safety of most nuclear technological applications [1-3]. Nevertheless, this is still a fairly unexplored field. In most systems of practical importance today, the liquid phase is water. Radiolysis of water produces H_2O_2, H_2, $HO^{\bullet}$, H and e^-_{aq} [4]. In homogeneous systems, the radiation chemical yields (G-values) are well known. However, in heterogeneous systems where the solid surface area to solution volume ratio is high, the radiation chemical yields are still unclear. For example, it has been shown that the yield for H_2 is different for heterogeneous systems containing water and solid oxides when compared to the homogeneous liquid water system [5]. When compared to the homogeneous system, some

oxides have no effect on the H_2 yield, some increase it and some decrease it [6]. These effects strongly depend on the solid oxide surface area to solution volume ratio. For the other molecular product, H_2O_2 in deaerated solutions, the presence of an oxide has been shown to have an effect although smaller than in the case of H_2 [7].

The reactivity of the aqueous radiolysis products towards metal and metal oxide surfaces is still not well understood. H_2O_2 has been shown to react with numerous oxide surfaces of relevance in nuclear technology. In addition, reactions between H_2O_2 and oxide surfaces are important also in various processes of catalysis, nuclear technological systems, hydrogen production and storage systems, geochemical processes and medical sciences [8-11].

H$_2$O$_2$ can react with oxide surfaces both via redox reactions and catalytic decomposition [12, 13]. Understanding the catalytic reaction pathway is crucial for understanding the chemistry of H$_2$O$_2$ containing systems and also provides a better comprehension of the redox reactivity of these systems. Catalytic decomposition of H$_2$O$_2$ leads to the formation of intermediate radical species which can bind to the surfaces where H$_2$O$_2$ undergoes decomposition [14]. In this process, the radicals are stabilized by forming bonded states between their unpaired electron and the oxide surface. As a consequence, the half-lives of the adsorbed states can become much longer – several hours up to days – than in solution [15, 16]. The interfacially generated radicals can also react further at the solid-liquid interface, thus affecting the chemistry of the whole system. The materials found in catalytic or nuclear technological applications where H$_2$O$_2$ undergoes decomposition, are characterized by extensive randomness in terms of surface structure and energy [17, 18]. The surfaces of these materials are defective and significantly different from surfaces grown in a controlled environment [19]. This means that studies of the reactivity of materials which were performed under ultra-high vacuum (UHV) chamber conditions will hardly be applicable to systems where H$_2$O$_2$ reacts in solution with a very defective metal oxide surface [18]. In spite of not providing a detailed description of the chemistry at the atomic scale, a good approach to study these systems of practical relevance is to use particle suspensions of the oxides and to determine kinetic parameters for the reactivity of H$_2$O$_2$ in solution. With these parameters in hand it is possible to apply the Arrhenius or the transition state theory (TS) and obtain activation energies or enthalpies, frequency factors and other parameters that can help understand the complex chemistry involved [20] .

An in depth molecular understanding of the reactivity of such systems has to make use of theoretical tools such as density functional theory (DFT) [20]. Using DFT we have demonstrated that even by using fairly simple models of the oxide surfaces it is possible to reproduce the energy barriers for the decomposition of H$_2$O$_2$ on transition metal oxides with accuracies of ± 5 kJ·mol^{-1} [20]. The models used provide a detailed picture of the microscale processes that determine the reactivity of H$_2$O$_2$. Phenomena such as hydrogen bonding of H$_2$O$_2$ with the hydroxylated surfaces of the transition metals; the degree of interaction between the O atoms of H$_2$O$_2$ and the surface exposed metal cations; the adsorption energies of the products formed – all these parameters will determine the pathway that the catalytic process for the H$_2$O$_2$ decomposition will follow. In fairly simple terms, H$_2$O$_2$ will first adsorb onto the surface of the oxide according to reaction R1 and then undergo decomposition (reaction R2) according to

$$H_2O_2 \text{ (aq)} + M_xO_y \rightarrow \quad H_2O_2\text{-}M_xO_y \qquad \text{(R1)}$$
$$H_2O_2\text{-}M_xO_y \rightarrow 1/2O_2 + H_2O + \quad M_xO_y \qquad \text{(R2)}$$
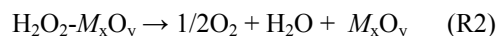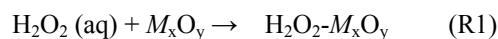
where M_xO_y is a surface site of an oxide of the metal M. When obtaining experimental kinetic data it is thus important to ensure that the measured parameters correspond to the process of interest. We have also shown previously that in some cases it is possible to tune the reaction conditions – for example by adjusting oxide surface areas (S_A) – in order to have the observed kinetics controlled either by the adsorption step or by the catalytic decomposition [20]. This is possible for systems where these two processes occur on different time scales. In such systems, where a good separability of the kinetics is possible, the errors introduced by such approach will be minimized and a fair comparison with DFT data can be made. For systems where a good separability of the two processes is not possible one has to be careful in drawing conclusions from the data obtained and in the comparisons with DFT data.

The main goal of this experimental work is to systematically study the reactivity of H$_2$O$_2$ towards a diversity of oxides. For this we determined kinetic parameters and activation energies as well as the second order rate constants from the mass dependence of the first order kinetics. Also, the dynamics of HO radical formation upon surface catalyzed decomposition of H$_2$O$_2$ were quantified and compared

2

for a series of oxides – Fe_2O_3, CeO_2, Gd_2O, HfO_2 and CuO. In order to broaden the discussion on the reactivity of H_2O_2 towards a diversity of oxides, previously published data for the reactions of H_2O_2 with ZrO_2, TiO_2, Y_2O_3 and UO_2 are used [20-22].

2. Experimental Details

2.1 Instrumentation

Specific surface areas of the powders were determined using the B.E.T. method of isothermal adsorption and desorption of a gaseous mixture consisting of 30% N_2, 70% He on a Micrometrics Flowsorb II 2300 instrument. The samples were weighted to $\pm 10^{-5}$ g, in a Mettler Toledo AT261 Delta Range microbalance. The reactions were performed under inert atmosphere with a constant flux of N_2 gas (AGA Gas AB) with a flow rate of 0.21 L·min^{-1} that was also used for stirring the solutions. The temperature was kept constant throughout the experiments by using a Huber CC1 or a Lauda E100 thermostat, calibrated against a Therma 1 Thermometer coupled to a submersible K-type (NiCrNi) temperature probe, with a precision of $\pm$ 0.1 K. UV/Vis spectra were collected using a WPA Lightwave S2000 or a WPA Biowave II UV/Vis Spectrophotometer.

2.2 Reagents and experiments

All the solutions used in this study were prepared using water from a Millipore Milli-Q system.

Iron (III) Oxide, Fe_2O_3, (CAS[1309-37-1], Aldrich 99%), Cerium Oxide, CeO_2, (CAS[1306-38-3], Alfa Aesar 99.99%), Hafnium Oxide, HfO_2, (CAS[12055-23-1], Alfa Aesar 99.95%), Gadolinium (III) Oxide, Gd_2O_3, (CAS[12064-62-9], Aldrich 99.9%) and Copper (II) Oxide, CuO, [CAS[1317-38-0], Aldrich 99.99%) were used without further purification. The B.E.T. surface areas of the oxides are: Fe_2O_3 (9.0 $\pm$ 1.0 m^2·g^{-1}); CeO_2 (14.3 $\pm$ 1.0 m^2·g^{-1}); HfO_2 (10.0 $\pm$ 0.1 m^2·g^{-1}); Gd_2O_3 (1.7 $\pm$ 0.1 m^2·g^{-1}); CuO (15.3 $\pm$ 0.1 m^2·g^{-1}). The particle size values were supplied by the manufactures. The H_2O_2 solutions were prepared from a 30% standard solution (Merck).

Kinetic studies:

The reaction media used for the kinetic studies of the reaction of H_2O_2 with the different oxides consisted of H_2O_2 (0.5 mM) in aqueous particle suspensions of the different oxides in a volume of 50 ml. The masses of oxides were: Fe_2O_3 [0.2–1.5] g; CeO_2 [0.06–0.52] g; HfO_2 [0.75–0.1] g; Gd_2O_3 [0.25–1.0] g; CuO [0.0025–0.1] g. After extraction of the sample from the reaction vessel, the sample was filtered through a Gema Medical 0.45μm/25mm Cellulose Acetate syringe filter. Subsequently, a sample volume of 0.2 ml was used for the measurement of H_2O_2 concentration. The concentration of H_2O_2 as a function of reaction time was then determined by the Ghormley triiodide method. In this method I^- is oxidized to I_3^- by the H_2O_2 [23, 24]. The absorbance of the product I_3^- was measured spectrophotometrically at the wavelength of 360 nm. A calibration curve where the absorbance of I_3^- was plotted as a function of the concentration of hydrogen peroxide was obtained in the range of concentrations 0.02-0.8 mM in H_2O_2 resulting in a linear correlation between absorbance and concentration.

Mechanistic study

For the quantification of the hydroxyl radicals formed as intermediate product in the reaction of H_2O_2 with the oxides we used a method previously described [21]. This consists of the reaction between tris(hydroxymethyl)aminomethane (Tris) (CAS[77-86-1], BDH Chemicals 99%) and the $HO^{\bullet}$ to produce formaldehyde, CH_2O [25]. In this study, the reactions between the oxides and H_2O_2 were performed at $T = 298$ K at the midpoint of the buffering range of the Tris. The reaction media consisted of Fe_2O_3 (1.5 g) or CeO_2 (1.6 g) or HfO_2 (2.25 g) or Gd_2O_3 (3.0 g) or CuO (0.06 g) with H_2O_2 (5 mM) and Tris (20mM) in 50 mL at a pH of 7.5, the pH was adjusted with HCl. The CH_2O produced was then quantified spectrophotometrically at 368 nm, by using a modified version of the Hantzsch reaction [26]. In this method the formaldehyde reacts with acetoacetanilide AAA (CAS[102-01-2], Alfa Aesar > 98%) in the presence of ammonium acetate (CAS[631-61-8], Lancaster 98%) to

form a dihydropyridine derivative which has the maximum absorption wavelength at 368 nm. A calibration curve of the absorbance of the dihydropyridine derivative as a function of formaldehyde concentration was obtained at 368 nm giving a linear correlation between absorbance and concentration, in the concentration range 0.15 µM to 1 mM in formaldehyde (Aldrich 37% wt in H_2O). The error associated with the determination of the concentration of formaldehyde in the initial solution was less than 2%.

3. Results and Discussion

A comparison of the reactivity of H_2O_2 towards different transition metal and lanthanide oxides can give us a broader picture of the interfacial processes that determine the reactivity of H_2O_2 in these systems. We studied the reactions of H_2O_2 with CeO_2, Fe_2O_3, HfO_2, Gd_2O_3 and CuO in aqueous powder suspensions. To enable comparison with our previously published data for other oxides, we used the same surface area of metal oxide material whenever this was possible. Fe_2O_3, CuO and Gd_2O_3 display higher overall reactivity towards H_2O_2 and the half-lifes of the reactions were too short to allow collection of a fair quantity of reliable kinetic data. For this reason we had to use a smaller total surface area than for the other oxides studied. The kinetic studies consisted in following the concentration of H_2O_2 with reaction time. The variation in concentration of H_2O_2 with reaction time, for the reactions of H_2O_2 with CeO_2, HfO_2, CuO, Gd_2O_3 and Fe_2O_3 at T = 298 K are shown in Figure 1. It can be seen (Figure 1) that the different oxides show only slightly different reactivity towards H_2O_2 under the present conditions. The only significant exception is Gd_2O_3. Interestingly, Gd_2O_3 displayed a high overall reactivity towards H_2O_2 when we used the same surface area as for the other oxides. When using a surface area of 1.7 m^2, the reactivity of Gd_2O_3 towards H_2O_2 is considerably lower than for the other oxides. This implies that the initial adsorption of H_2O_2 on

Gd_2O_3 is a very rapid process while the decomposition of adsorbed H_2O_2 is a slow process.
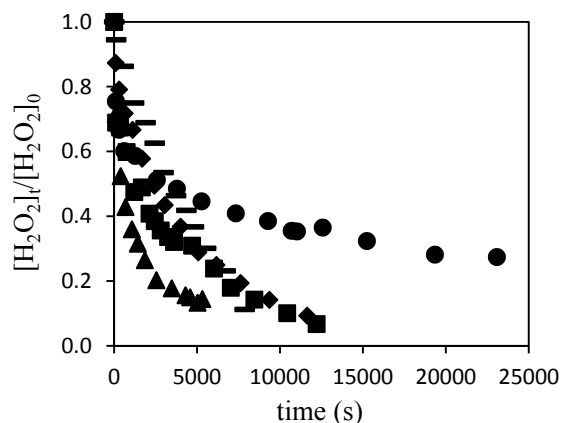
Figure 1. Normalized concentration of H_2O_2 (initially 0.5mM in 50 mL) as a function of reaction time for the reaction with CeO_2 (■), CuO (♦), HfO_2 (▲), Gd_2O_3 (●) and Fe_2O_3 (—) at T = 298.15 k. S_A: Fe_2O_3 (4.5 m^2), CeO_2 (7.5 m^2); CuO (0.3 m^2); HfO_2 (7.5 m^2); Gd_2O_3 (1.7 m^2).

When reducing the surface area, the capacity to adsorb H_2O_2 is reduced and the catalytic decomposition becomes the predominant process responsible for consumption of H_2O_2. In order to have comparable energetic data, the process determining the kinetics, from which the data is extracted, has to be the same for all oxides. It can be seen that for all oxides there is an initial faster disappearance of H_2O_2 from solution which is followed by a process that obeys first-order kinetics. The time frame for the adsorption process is different for the various oxides but considering the total reaction time, its contribution to the overall reaction is relatively small. The treatment of kinetic data was then straightforward and our kinetic data is obtained from the first-order process that follows the initial adsorption. The first-order rate constants k_1 obtained from the data of Figure 1 are given in

4

Table 1. In Figure 1 it can be seen that while for CuO and HfO_2, the plot shapes resemble first-order behavior during the whole reaction time, for CeO_2 and Gd_2O_3 the reaction fits a first-order kinetic treatment only within a limited H_2O_2 concentration range. Our previously published mechanism for the reaction of H_2O_2 with ZrO_2, TiO_2 and Y_2O_2 shows that the intermediate product, HO radicals, formed during decomposition of H_2O_2, adsorb to the catalytically active surface sites where H_2O_2 undergoes decomposition [27]. $HO^{\bullet}$ has shown a high affinity for forming bonded states with the exposed metal cations *i.e.* this reaction is exergonic with energies in the order of -500 $kJ \cdot mol^{-1}$. The binding energy of the $HO^{\bullet}$ with the surfaces is not isotropic with respect to all the types of surface sites present and at some surface sites, the binding energy is expected to be less exothermic than -500 $kJ \cdot mol^{-1}$ obtained for bonding onto a defective surface site. In cases where the interaction of $HO^{\bullet}$ with the surface is weak enough, reaction of H_2O_2 with interfacial HO radicals is possible. The reaction between surface bound $HO^{\bullet}$ and H_2O_2 will have an impact on the types of products existing at the interface between the solid surface and the bulk solution [28]. We will later in this paper discuss the significance of this process on the overall kinetics. The possibility that a first-order kinetic behavior corresponds to a process which is largely governed by the reaction of H_2O_2 with surface adsorbed $HO^{\bullet}$ must be considered.

The second-order rate constant was determined by studying the first-order rate constant as a function of

Table 1.

Table 1 that the values of k_2 are very far from the diffusion controlled reaction rate constants which we expect to be in the order of 10^{-5} $m \cdot s^{-1}$ for particles of this range of sizes [29]. The value of b_2 for Fe_2O_3 is considerably higher than for the other oxides. This indicates that for Fe_2O_3 a homogeneous reaction with H_2O_2 is also taking place and has increased significance on the overall reaction kinetics when compared with the other materials. Most likely the

solid surface-area-to-solution-volume-ratio S_A/V. For reactions of the particles used here, in aqueous suspension, the second-order rate expression can be obtained by [21]

$$-\frac{d[H_2O_2]}{dt} = k_2 \left(\frac{S_{A(MxOy)}}{V}\right)[H_2O_2] \qquad (1)$$

where $S_{A(MxOy)}$ denotes the surface area of the metal oxide powder, V is the volume of the reactant solution and k_2 is the second-order rate constant. The second-order rate constants were determined from experiments in which the first-order rate constants were obtained for different $S_{A(MxOy)}$ at $T = 298$ K. The resulting plots are represented in Figure 2.
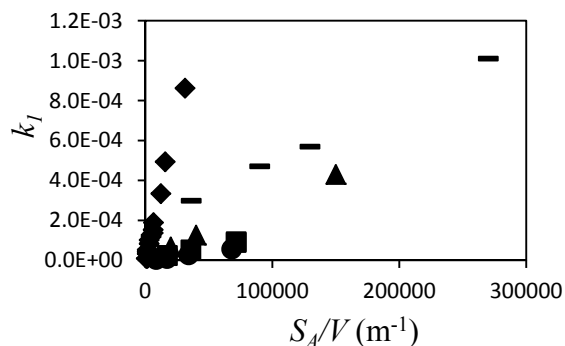
Figure 2. Variation in first-order rate constant with the surface-area-to-solution-volume-ratio (S_A/V) of oxide for decomposition of H_2O_2 (0.5 mM; 50 mL) at $T = 298.15$ K. CeO_2 (■), CuO (♦), HfO_2 (▲), Gd_2O_3 (●) and Fe_2O_3 (▬).

The second order rate constants and the intercepts at the zero coordinate (b_2) of the least squares fits for the plots of k_1 as a function of S_A/V are given in

It can be seen from the data presented in homogenous process is the Fenton reaction which takes place in the bulk solution due to the presence of dissolved Fe^{2+} released from the surface of Fe_2O_3 [12]. Fe^{2+} can be formed by reduction of Fe^{3+} initiated by a product of H_2O_2 decomposition, the HO_2 radical [30] and which involves directly O_2^- to form O_2 [31].

The Arrhenius activation energies were obtained from plots of the logarithm of the first-order rate constants as a function of the inverse absolute

5

temperature. The temperature dependence of the reaction rate constants for the different oxides was studied in the temperature interval $T = [298–334]$ K for Fe_2O_3, CuO, HfO_2 and $T = [298–353]$ K for CeO_2 and Gd_2O_3. The upper temperature limit was the value below which it was possible to collect enough data

Table 1. Obtained k_1, k_2 and b_2 for decomposition of H_2O_2 (0.5mM; 50 mL) catalyzed by different oxides at $T = 298$ K. k_1 was obtained with the following S_A of oxides: Fe_2O_3 (4.5 m^2), CeO_2 (7.5 m^2); CuO (0.3 m^2); HfO_2 (7.5 m^2); Gd_2O_3 (1.7 m^2).

Material	k_1 (s^{-1})	k_2 (m·s^{-1})	b_2 (s^{-1})
Fe_2O_3	$(2.1 \pm 0.4) \times 10^{-4}$	$(3.0 \pm 0.06) \times 10^{-9}$	2×10^{-4}
CeO_2	$(1.7 \pm 0.5) \times 10^{-4}$	$(2.80 \pm 0.07) \times 10^{-8}$	5×10^{-6}
CuO	$(1.90 \pm 0.05) \times 10^{-4}$	$(1.23 \pm 0.06) \times 10^{-9}$	6×10^{-6}
HfO_2	$(4.3 \pm 0.9) \times 10^{-4}$	$(2.78 \pm 0.02) \times 10^{-9}$	1×10^{-5}
Gd_2O_3	$(3.6 \pm 0.3) \times 10^{-5}$	$(9.4 \pm 1) \times 10^{-10}$	6×10^{-6}

points for the H_2O_2 concentration as a function of time, with minimal errors associated. This because the reaction becomes too fast to allow proper data Table 2. The respective standard reaction enthalpies of activation ($\Delta^{\ddagger}H^o$) were obtained using a linearization of the Eyring equation

$$\ln\left(\frac{k}{T}\right) = -\frac{\Delta^{\ddagger}H^o}{RT} + \frac{\Delta^{\ddagger}S^o}{R} + \ln\left(\frac{k_B}{h}\right) \qquad (2)$$

where k is the reaction rate constant, T is the absolute temperature, $\Delta^{\ddagger}H^o$ is the standard enthalpy of Table 2. The obtained E_a values vary significantly for the different oxides studied. There is no obvious correlation between E_a and the stoichiometry of the oxides.

This indicates that the activation energies are most likely dictated by microstructural properties of the

collection above a certain temperature, The Arrhenius plots are represented in Figure 3 and the resulting data are shown in activation, R is the gas constant, k_B is the Boltzmann constant, h is the Planck constant and $\Delta^{\ddagger}S^o$ is the standard entropy of activation. The data obtained from transition state theory are shown in

particles such as the type of atoms present at the catalytically active surface sites and the extent of hydroxylation at these sites.
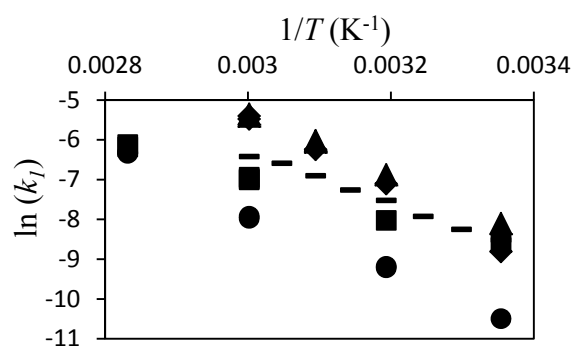

Figure 3. Arrhenius plots for the first-order rate constant as a function of reaction temperature for the decomposition of H_2O_2 (0.5mM; 50 mL) catalyzed by different oxides. CeO_2 (■), CuO (♦), HfO_2 (▲), Gd_2O_3 (●) and Fe_2O_3 (—). S_A: Fe_2O_3 (4.5 m^2), CeO_2 (7.5 m^2); CuO (0.3 m^2); HfO_2 (7.5 m^2); Gd_2O_3 (1.7 m^2).

Table 2. Arrhenius activation energies (E_a), standard enthalpies of activation ($\Delta^{\ddagger}H^{\circ}$), and frequency factors (A) for the decomposition of H_2O_2 catalyzed by different oxide materials.

Material	E_a (kJ·mol^{-1})	A (s^{-1})	$\Delta^{\ddagger}H^{\circ}$ (kJ·mol^{-1})	Particle size
Fe_2O_3	47 ± 1	2.2×10^3	44 ± 1	< 5 μm
CeO_2	40 ± 1	1.4×10^3	37 ± 1	14 μm
CuO	76 ± 1	3.5×10^9	73 ± 1	< 50 nm
HfO_2	60 ± 1	1.1×10^7	57 ± 1	44 μm
Gd_2O_3	63 ± 1	3.4×10^6	60 ± 1	12 nm

In aqueous solution, most of the metal oxide surfaces are hydroxylated, a phenomenon which is the result of dissociative adsorption of H_2O [32]. The structure and extent of this hydroxylation layer will in turn determine the rigidity of the interfacial water layers which lay slightly further from the surface but still interact with the surface HO-groups. The more rigid the interfacial layers of adsorbed water, the higher the barrier for diffusion of H_2O_2 through the layer before it reaches the catalytically active surface sites. Hence, the affinity of the surfaces towards water is expected to contribute to the observed activation energy barriers for H_2O_2 decomposition. Also the intermediate products formed during decomposition of H_2O_2 are oxygen species that in spite of being radicals, to some extent, have "water-like" properties such as the ability to form hydrogen bonds [32]. As mentioned above, the HO radical interacts with the surface by forming bonded states with the exposed metal cations through its unpaired electron localized at the O atom. Even though H_2O is a molecular species, it possesses non-bonding electrons more localized at its O atom and it is due to the interaction of these electrons with the available orbitals of exposed surface metal atoms that the more exothermic type of interaction of a H_2O molecule with the surface occurs.

We studied the dynamics of formation of the HO radical during decomposition of H_2O_2 on the above mentioned oxides. We used a method previously published for the detection of HO radicals [21]. This method consists of the reaction of HO$^{\bullet}$ with Tris buffer which leads to the formation of formaldehyde, CH_2O. As such, there is a correlation between the number of HO radicals produced in the system and the amount of CH_2O formed. The formaldehyde yield is also expected to depend on the relative reactivity of the adsorbed hydroxyl radicals. The data obtained for CH_2O-formation during decomposition of H_2O_2 in the presence of Tris is shown in Figure 4. It can be seen in Figure 4 that the dynamics of formation of CH_2O vary considerably for the different oxides. Whilst for Gd_2O_3 the amount of CH_2O formed is very low throughout the whole experiment, reaching a maximum of 0.014 mM, for CuO the amount of CH_2O formed reaches a plateau at slightly above 0.5 mM. The shape of the curves is also considerably different for the different oxides. Both the yields and shapes of the curves for the formation of CH_2O will be discussed further in the next section.


7
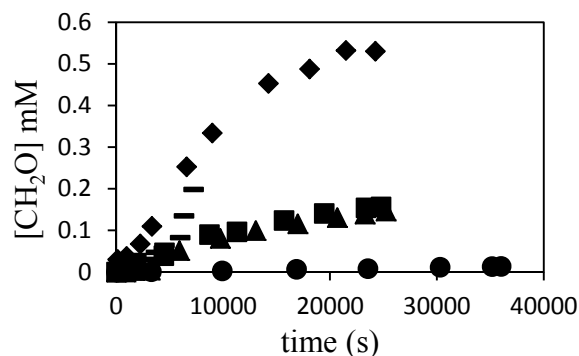
Figure 4. Formaldehyde formed by reaction of HO radicals with Tris during decomposition of H_2O_2 (5 mM; 50 mL) catalyzed by different oxides. CeO_2 (■), CuO (♦), HfO_2 (▲), Gd_2O_3 (●) and Fe_2O_3 (—).

A discussion on the kinetic and mechanistic parameters of the reaction of H_2O_2 with:
ZrO_2, TiO_2, Y_2O_3, Fe_2O_3, CuO, CeO_2, Gd_2O_3, HfO_2
and UO_2

In this section we compare kinetic, energetic and mechanistic data for the reaction of H_2O_2 with the Table **3**.

oxides: ZrO_2, TiO_2, Y_2O_3, Fe_2O_3, CuO, CeO_2, Gd_2O_3, HfO_2 and UO_2. For this we use the experimental data reported above in this work in combination with previously published data from our group for the remaining oxides. A fair comparison between all the data is possible because we have used the same experimental conditions, procedures and methods when obtaining the data for all oxides. E_a, A, and $\Delta^{\ddagger}H^{\circ}$ obtained in this work and retrieved from the literature for the reaction of H_2O_2 with the different oxides are shown in Table **3**.

Table 3. Arrhenius activation energies (E_a), surface area normalized pre-exponential factors (A), and standard enthalpies of activation ($\Delta^{\ddagger}H^{\circ}$) for the reaction of H_2O_2 with different oxides with specific surface area (S_a). Reaction parameters obtained from first-order kinetics except where stated otherwise[†].

Material	E_a (kJ·mol⁻¹)	$\Delta^{\ddagger}H^{\circ}$ (kJ·mol⁻¹)	A (s⁻¹)	Particle size	Crystal Structure	S_a (m²·g⁻¹)
ZrO_2[a]	33 ± 1	30 ± 1	30	< 5 μm	Monoclinic	5.0
TiO_2[b, †]	37 ± 1	34 ± 1	18 M·s⁻¹	32 nm	Anatase	14.3
Y_2O_3[b, †]	44 ± 5	44 ± 5	6.2×10^3 M·s⁻¹	< 10 μm	Cubic	4.5
Fe_2O_3	51 ± 1	44 ± 1	1.8×10^5	< 5 μm	Rhombohedral	9.0
CeO_2	40 ± 1	37 ± 1	1.4×10^3	14 μm	Cubic	14.3
CuO	76 ± 1	73 ± 1	8.6×10^{10}	< 50 nm	Monoclinic	15.3
HfO_2	60 ± 1	57 ± 1	1.1×10^7	44 μm	Monoclinic	10.0
Gd_2O_3	63 ± 1	60 ± 1	1.5×10^7	15 nm	Cubic	1.7

a) Data retrieved from reference [21] b) reference [27] †) Energetic data obtained from zeroth-order kinetics. The values of A were normalized to a surface area of 7.5 m² for the first-order reactions

It can be seen (Table **3**) that the values of E_a vary considerably, ranging from 33 to 76 kJ·mol⁻¹ for the reaction with ZrO_2 and CuO respectively. Even though the pre-exponential factors have been normalized to a surface area of 7.5 m² to allow direct comparison between them, they vary significantly with a maximum of 9 orders of magnitude. For every oxide the standard enthalpy of activation is 3 kJ·mol⁻¹ lower than the corresponding Arrhenius activation energy. This trend agrees with the value associated with the inter-exchangeability of the Arrhenius approach into the

Eyring transition-state theory. The differences in the values of A indicate that the catalytic capabilities of the oxides towards decomposition of H_2O_2 are very different. These differences can have several underlying reasons. The most obvious is that the number of actively reacting surface sites is different for the different oxides. In a previous work, we have determined the number of adsorption sites for H_2O_2 onto TiO_2 and Y_2O_3. Even though molecular adsorption is usually less surface site specific than an adsorbate bond breaking process [33, 34], the difference in the

number of adsorption sites for both oxides was 25 %. For the materials shown in Table 2, we also expect differences in the number of surface sites able to accommodate H_2O_2. Given the dissimilarities between many of the cations present in the oxides – *i.e.* from first row transition metals down to lanthanides – we expect these differences to be more pronounced in the present work. Other possible contributing factors to the differences in A are the number of catalytically active sites at the surfaces and the strength of bonding between the products of decomposition of H_2O_2 and these active sites. Due to the multitude of parameters that can have influence on the kinetic data obtained – *i.e.* on the values of k_1 and A – it is not possible to draw mechanistic conclusions from the kinetic study alone.

In Figure 5 the concentration of CH_2O detected in solution as a function of relative conversion of H_2O_2 is shown. The initial reaction conditions are identical in all experiments ($[H_2O_2]_0$= 5 mM and $[Tris]_0$= 20 mM). As described above, the amount of CH_2O produced in the system depends on the amount and also on the relative reactivity of hydroxyl radicals formed in the decomposition of H_2O_2. Additionally, as the CH_2O is formed at the oxide interface, the dynamics of its release into solution might be oxide specific. This could ultimately lead to differences in its bulk concentration even for the same interfacial concentration.
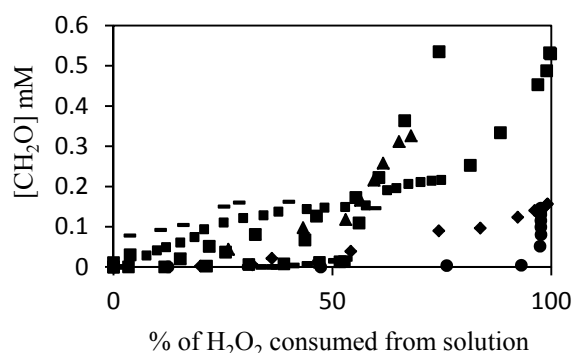

Figure 5. Amount of CH_2O present in the reaction system as a function of the percentage of H_2O_2 consumed from solution during reaction with different oxide materials. CeO_2 (♦); Gd_2O_3 (■); Y_2O_3 (▲); ZrO_2 (×); Fe_2O_3 (*); HfO_2 (●); CuO (+); TiO_2 (-); UO_2 (–).

A systematic study on CH_2O adsorption onto oxide surfaces – many of them analogues of the oxides investigated in this work – revealed that CH_2O shows a similar adsorption mechanism for different transition and non-transition metal oxides [35]. Based on this, we expect that the CH_2O desorption mechanisms and energy barriers are similar for the different oxides studied here. Besides, in the way that it is expressed, the data of Figure 5 is time-independent in what concerns the formation of CH_2O. It is then possible to compare the values directly. It can be seen in Figure 5 that the release of CH_2O as a function of H_2O_2 conversion differs widely for the different materials studied. At a given conversion of H_2O_2, the concentration of CH_2O differs by one order of magnitude between the different oxides. The differences observed in Figure 5 can be explained on the basis of the overall mechanism for formaldehyde formation. Initially, hydrogen peroxide in solution is consumed by adsorption to the oxide surface. If the catalytic decomposition is slow compared to the adsorption, only minute amounts of hydroxyl radicals are expected to be formed during the initial phase. As the surface coverage by H_2O_2 approaches the maximum, the rate of hydroxyl radical formation will approach its maximum. Hydroxyl radicals react with both hydrogen peroxide and Tris. In aqueous solution the rate constants for the two reactions differ by two orders of magnitude, $2.7 \times 10^7 \, M^{-1} \cdot s^{-1}$ and $1.1 \times 10^9 \, M^{-1} \cdot s^{-1}$ for H_2O_2 and Tris, respectively [36, 37]. Hence, the presence of H_2O_2 will influence the rate of formaldehyde formation. In the present case, the reactions occur at the oxide surface and the competition between hydrogen peroxide and Tris will depend on the rate constants for the two competing surface reactions as well as the relative surface coverage. It is worth to note that due to their different geometries and sizes, H_2O_2 and Tris will adsorb to the surfaces in different ways. Besides of hydrogen bonding, H_2O_2 can

also adsorb to the surfaces of the oxides by interaction of its O atoms with the surface metal cations leading to a strong type of interaction [20]. Tris, due to its size and geometry will not be able to interact with the surfaces at such a localized level as H_2O_2. Consequently, its adsorption energy is expected to be less exothermic than that of H_2O_2. This has been demonstrated in previous studies which show that hydrogen peroxide has a significantly higher affinity for oxide surfaces than Tris has [38]. For several of the oxides it is obvious that the formaldehyde production is very low up to a certain conversion of hydrogen peroxide. The inflection point at which the formaldehyde production rate starts to increase can be assumed to correspond to the hydrogen peroxide concentration where Tris becomes the dominating reactant at the surface. Interestingly, a recent study on the effects of Tris on the production of molecular oxygen upon catalytic decomposition of H_2O_2 on ZrO_2 shows that the oxygen yield decreases with increasing Tris concentration [39]. This is a direct consequence of the competition between H_2O_2 and Tris for hydroxyl radicals. A similar phenomenon was observed in a study of TiO_2 photocatalysis using Tris as a probe and various concentrations of H_2O_2 [38]. The latter was added to capture electrons formed in the initial photolysis of TiO_2 and thereby enhance the photocatalytic activity. It is interesting to note that for oxides where H_2O_2 adsorption appears to be faster than the decomposition reaction (e.g. TiO_2 and Gd_2O_3) a clear inflection point is never reached under the present conditions and very small amounts of formaldehyde are formed. ZrO_2 is a different case where the formaldehyde production starts almost instantly. This could indicate that the adsorption of H_2O_2 is relatively weak and that catalytic decomposition is a very fast process in comparison. For other more extreme cases such as HfO_2 there is an inflection point when the H_2O_2 is almost completely consumed form the solution. Tough, for all the materials, it is not possible to attribute the position of the inflection points as the result of a single effect.

For UO_2, the yield of CH_2O reaches a plateau corresponding to 20% of H_2O_2 consumed and in spite of the continuous disappearance of H_2O_2 from solution, the CH_2O yield does not increase. For this material, besides the decomposition, H_2O_2 is also able to oxidize U(IV) to U(VI) [40]. The oxidation product of this reaction is water soluble. As shown previously, the HO radicals produced in the redox reactions are not possible to scavenge with Tris [41]. The plateau in CH_2O production can be interpreted as the point in the course of the reaction where due to the constant regeneration of the surface due to oxidation of U(IV) to U(VI) – leading to the dissolution of the newly fresh surface – the catalytic reaction pathway will be hindered. The redox path is not hindered by accumulation of products on the surface since the product is readily soluble. Hence, the surface available for oxidation is continuously regenerated.

Conclusions

The systematic examination of the reactivity of H_2O_2 with the oxides studied in this work has revealed that in spite of the similarities between many of the materials studied, the energetic and kinetic parameters for the reactions differ significantly. This indicates that albeit the decomposition of H_2O_2 involves formation of intermediate HO radicals, the kinetic parameters for its decomposition are highly catalyst dependent. This is because the local properties of the catalytically active surface sites will largely affect the apparent reaction energy barriers and pre-exponential factors. For some oxides, there are differences of 9 orders of magnitude in the Arrhenius pre-exponential factors. The yields and dynamics of formation of scavenged HO• differ considerably for many of the oxides analyzed. The amount of scavengeable HO• by Tris changes in the course of the decomposition of H_2O_2, leading to inflection points where, for some oxides, an increase in the amount of scavenged HO• is visible. These inflection points correspond to different amounts of consumed H_2O_2 for the different materials. These results indicate that the adsorption energy of H_2O_2, Tris

and/or mechanism of binding of the HO radical with the surfaces of the oxides have an impact on the ability to scavenge the HO radicals formed.

This indicates that the properties of the catalysts surfaces which are directly related with the decomposition of H_2O_2 are very different. These differences should be mostly related with the number and reactivity of the surface catalytically active sites which in turn depend on the coordination and type of metal atom present. Also the extent of hydroxylation and configuration of adsorbed H_2O on the active sites should have an impact on the obtained kinetic and mechanistic parameters.

References

[1]   J. Medek, Z. Weishauptová, Journal of Nuclear Materials. 393 (2009) 306-310.
[2]   B. Cox, Journal of Nuclear Materials. 336 (2005) 331-368.
[3]   A.T. Motta, A. Yilmazbayhan, M.J.G. da Silva, R.J. Comstock, G.S. Was, J.T. Busby, E. Gartner, Q. Peng, Y.H. Jeong, J.Y. Park, Journal of Nuclear Materials. 371 (2007) 61-75.
[4]   G. Buxton, Charged Particle and Photon Interactions with Matter, CRC Press, 2003.
[5]   S. Le Caër, Water. 3 (2011) 235-253.
[6]   N.G. Petrik, A.B. Alexandrov, A.I. Vall, The Journal of Physical Chemistry B. 105 (2001) 5935-5944.
[7]   O. Roth, A. Hiroki, J.A. LaVerne, The Journal of Physical Chemistry C. 115 (2011) 8144-8149.
[8]   M. Ozawa, J. Alloy. Compd. 275 (1998) 886-890.
[9]   H.H. Li, S.Q. Liu, Z.H. Dai, J.C. Bao, X.D. Yang, Sensors. 9 (2009) 8547-8561.
[10]   C. Thomas, M. Mackey, A. Diaz, D. Cox, Redox Report. 14 (2009) 102-108.
[11]   A.A. Burke, L.G. Carreiro, R.C. Urian, Journal of Fuel Cell Science and Technology. 7 (2010) 034502.
[12]   F. Haber, J. Weiss, Naturwissenschaften. 20 (1932) 948-950.
[13]   A. Hiroki, J.A. LaVerne, The Journal of Physical Chemistry B. 109 (2005) 3364.
[14]   D. Zigah, J. Rodriguez-Lopez, A.J. Bard, Physical Chemistry Chemical Physics. 14 (2012) 12764-12772.
[15]   E. Giamello, L. Calosso, B. Fubini, F. Geobaldo, The Journal of Physical Chemistry. 97 (1993) 5735-5740.
[16]   C.J. Rhodes, Progress in Reaction Kinetics and Mechanism. 30 (2005) 145-213.
[17]   T. Bligaard, J.K. Nørskov, Chemical Bonding at Surfaces and Interfaces, Elsevier, Amsterdam, 2008, pp. 255-321.
[18]   G.E. Brown Jr, T.P. Trainor, A.M. Chaka, Chemical Bonding at Surfaces and Interfaces, Elsevier, Amsterdam, 2008, pp. 457-509.
[19]   P. Liu, T. Kendelewicz, G.E. Brown Jr, Surface Science. 412–413 (1998) 315-332.
[20]   C.M. Lousada, A.J. Johansson, T. Brinck, M. Jonsson, J. Phys. Chem. C. 116 (2012) 9533-9543.
[21]   C.M. Lousada, M. Jonsson, J. Phys. Chem. C. 114 (2010) 11202-11208.
[22]   C.M. Lousada, M. Trummer, M. Jonsson, Journal of Nuclear Materials. 434 (2013) 434-439.
[23]   C.J. Hochanadel, The Journal of Physical Chemistry. 56 (1952) 587-594.
[24]   J.A. Ghormley, A.C. Stewart, Journal of the American Chemical Society. 78 (1956) 2934-2939.
[25]   H. Shiraishi, M. Kataoka, Y. Morita, J. Umemoto, Free Radical Research. 19 (1993) 315-321.
[26]   Q. Li, P. Sritharathikhun, S. Motomizu, Analytical Sciences. 23 (2007) 413-417.
[27]   C.M. Lousada, A.J. Johansson, T. Brinck, M. Jonsson, The Journal of Physical Chemistry C. 116 (2012) 9533-9543.
[28]   L.C. Anderson, M. Xu, C.E. Mooney, M.P. Rosynek, J.H. Lunsford, Journal of the American Chemical Society. 115 (1993) 6322-6326.
[29]   M. Jonsson, in: J.F. Wishart, Rao, B. S. M. (Ed.), Recent Trends in Radiation Chemistry World Scientific Singapore 2010, pp. 301-323.
[30]   H.B. Dunford, Coordination Chemistry Reviews. 233–234 (2002) 311-318.
[31]   T.G.D. E. T. Denisov, T. S. Pokidova, Handbook of Free Radical Initiators, John Wiley & Sons, Inc, Hoboken, NJ., April 2003.
[32]   D.M. Chipman, The Journal of Physical Chemistry A. 115 (2011) 1161-1171.
[33]   S. Shimizu, H. Noritake, T. Koitaya, K. Mukai, S. Yoshimoto, J. Yoshinobu, Surface Science. 608 (2013) 220-225.
[34]   M. Teliska, V.S. Murthi, S. Mukerjee, D.E. Ramaker, The Journal of Physical Chemistry C. 111 (2007) 9267-9274.
[35]   G. Busca, J. Lamotte, J.C. Lavalley, V. Lorenzelli, Journal of the American Chemical Society. 109 (1987) 5197-5202.
[36]   G.V. Buxton, C.L. Greenstock, W.P. Helman, A.B. Ross, Journal of Physical and Chemical Reference Data. 17 (1988) 513-886.

[37]   M. Hicks, J.M. Gebicki, FEBS Letters. 199 (1986) 92-94.

[38]   V. Diesen, M. Jonsson, Journal of Advanced Oxidation Technologies. 16 (2013) 16-22.

[39]   J.A.L. Cláudio M. Lousada, Mats Jonsson, Work to be published (2013).

[40]   R. Pehrman, M. Trummer, C.M. Lousada, M. Jonsson, Journal of Nuclear Materials. 430 (2012) 6-11.

[41]   C.M. Lousada, M. Trummer, M. Jonsson, Journal of Nuclear Materials.

"Application of reactivity descriptors to the catalytic decomposition of hydrogen peroxide at oxide surfaces"
Cláudio M. Lousada, Tore Brinck, and Mats Jonsson, *Chemistry a European Journal*, under review

VIII

Application of reactivity descriptors to the catalytic decomposition of hydrogen peroxide at oxide surfaces

Cláudio M. Lousada,* Tore Brinck, and Mats Jonsson

Applied Physical Chemistry, School of Chemical Science and Engineering, KTH Royal Institute of Technology, SE-100 44 Stockholm, Sweden

* To whom correspondence should be addressed: phone, (46) 8 790 87 89;
Fax, (46) 8 790 87 72; e-mail, cmlp@kth.se

Abstract

We have employed density functional theory (DFT) calculations using the PBE0 functional to study the reaction of decomposition of H_2O_2 on clusters of: ZrO_2, TiO_2, Y_2O_3, Fe_2O4, CeO_2, CuO, HfO_2, Al_2O_3, NiO_2, PdO_2 and Gd_2O_3. The formation of the products of decomposition of H_2O_2 and their binding onto these oxides are discussed. The obtained energy barriers for H_2O_2 decomposition deviate from experimental data in absolute average by 4 kJ·mol^{-1}. The only exceptions are CeO_2 and Fe_2O_3 for which the deviations are very large. The adsorption of HO radicals onto the clusters was also studied. Reactivity descriptors obtained with DFT calculations are correlated with experimental data from literature. We found that a direct correlation between the adsorption energy of HO radicals and the change in Mulliken charge of the cation present in the oxide, upon adsorption of these radicals. Other DFT and experimental reactivity descriptors based on properties of the cations present in the oxides, such as the ionization potential, Pauling electronegativity and Mulliken electronegativity are plotted against experimental Arrhenius activation energies. Following the Brønstead-Evans Polianiy principle, there is a correlation between the adsorption energy of the product HO radical and the energy barrier for decomposition of H_2O_2. The good correlations obtained using DFT data produced with minimalistic cluster models indicate that on the real systems the processes that determine the reactivity of H_2O_2 are the result of localized properties of the surface *i.e.* at the atomic scale.

Introduction

In general terms, the reactivity of surfaces is determined by the type of chemical elements that constitute the surface and by their chemical connectivity and environment. The reactivity of a surface adsorbed species is determined by the type of bonding with the surface.[1] This means that after adsorption, the fate of the adsorbate is dictated by how it interacts with the surface. If the interactions with the surface are strong enough, the adsorbate bonds suffer changes such as elongations and bond breaking in the adsorbate can occur. When interactions between the adsorbate and surface occur, new molecular orbitals are formed and the resulting interaction energy is determined by the distribution of electrons over the bonding and anti-bonding orbitals that form the bonds with the surface.[2] The shape and energy of these newly formed molecular orbitals and their occupancy will determine the reactivity of the surface-adsorbate system. In this way, the type of adsorption is an important factor for determining the reactivity of the adsorbed molecule.

Several models have been developed with the goal of correlating the reactivity of a surface towards an adsorbate, in terms of the surface *d*-band or other properties.[3] One successful model for the prediction of surface reactivity, is the bond order conservation-Morse potential model and its more recent developments by Shustorovich.[4] Utilizing both reported and estimated

heats of atomic chemisorption on transition metal surfaces, these models, which incorporate both theoretical and empirical aspects, allow the calculation of not only heats of adsorption of polyatomic species, but also activation barriers for their decomposition and recombination on surfaces. Consequently, for many reactions on metal surfaces, various reaction pathways can be proposed and the energetics associated with each pathway can be estimated. However, there are obstacles to the usage of such models for calculating surface reaction energy profiles. The major problem is the lack of experimental atomic chemisorption data on which these methods depend.[4b] Another limitation of these methods is the fact that the chemisorption data is dependent on surface defects, coverage and type of dominating surface (if any) in terms of crystallographic orientation. Surface coverage and coadsortpion effects change the enthalpies of chemisorption and energy barriers in a non-linear way and the empirical models have to be adapted to deal properly with these non-linear changes.[5] Even for the same material with the same crystal structure, these factors make the transferability of the empirical correlations for different surfaces very difficult.

The adsorption structures – *i.e.* if the molecule adsorbs atop, bridging or in higher coordination – relates to the effects that determine the structures and energies of transition-states of reacting surface species.[3c, 3e] As such, being able to foresee the interactions that are determined by the adsorption complexes is a long term goal of surface chemists because this would provide a better picture of the transition-state structures and of the reactivity of the adsorbed complex. For a homologous series of reactions, Brønsted, Evans and Polanyi (BEP) demonstrated that there is a linear correlation between the transition state energies and the adsorption energies.[6] This is because the activation energies and the adsorption energies are governed by the same physical principles. That correlation is simply explained by

$$\Delta E_{TS} = \alpha_{BEP} \Delta E_{React} \qquad (1)$$

where ΔE_{TS} is the activation energy, ΔE_{React} is the adsorption energy of the reactant, and α_{BEP} is the proportionality constant. When $\alpha_{BEP} < \frac{1}{2}$ the transition state is said to occur early. When $\alpha_{BEP} > \frac{1}{2}$ the transition-state structure occurs late. The structure of an early transition state is more resembling of the reactant while that of the late transition state is more resembling of the product.[7] Another useful concept is that of the tight or loose transition-state structure.[8] The tight transition-state structure occurs when in the reaction complex the interactions between adsorbate and surface are localized. These reactions are sensitive to the surface topology and constitute the surface sensitive class of reactions. Loose transition-states have higher mobility and as such the interactions of the reaction complex with the surface are weaker than in the tight case. This type of reactions is then rather insensitive to surface topology and to differences in the coordinative unsaturation of the surface atoms. Translated to a real particle system, this means that a reaction occurring through a tight transition-state will preferably occur at surface defects which are the sites with the highest coordinative unsaturation.[9] At these sites the adsorption is generally more exothermic.[10]

In general, the interaction between adsorbates and surfaces are a localized event. In many cases the resultant structures from adsorbed molecules onto metal atoms that constitute surfaces, resemble the structures of the corresponding organometallic complexes.[11] In the case of a defective surface, the degree of localization of these interactions is even higher.[12] As such, approaches such as the *d*-band type model developed for ideal surfaces, breaks when applied to defects, as the density of states of the bulk or of a perfect surface are broken at the defect sites.[13] The more undercoordinated is an atom at a defect, the more free-atom-like character the density of states of that atom will have.[10] In the bulk, the density of states is influenced by the bonding on the extended crystal structure and the extent of delocalization of the bulk atoms electrons is significant. In the defects, the lack of extended structure adds a more localized character to the orbitals. This makes the orbitals of the defect atom more available for interactions with adsorbates than the orbitals of less undercoordinated surface atoms.

There are many examples of success of frontier molecular orbital based approaches to describe the reactivity of organic compounds.[14] Simple descriptors such as electronegativity, electron affinities, ionization potentials, hardness and softness have been used for predicting trends in the reactivity of many molecules. These approaches are classified as global reactivity descriptors (GRD). They became wide-spread in recent times because electronic structure calculations are easier to perform due to the increase in computational power.

The above mentioned GRD arise naturally from conceptual density functional theory (DFT), as they can be described in terms of the electron density as follows

$$\mu = \left(\frac{\partial E}{\partial N}\right)_Z = -\chi \tag{2}$$

$$\mu = \begin{cases} -\text{IP} \ (Z - 1 < N < Z) \\ -\text{EA} \ (Z < N < Z + 1) \end{cases} \tag{3}$$

equation 2 means that the chemical potential (μ) is dependent on the derivative of the energy (E) with respect to the number of electrons (N). The second equality in this equation corresponds to the electronegativity (χ) and is valid for $N = Z$. Z is the nuclear charge of the atom, IP is the ionization potential of the system and EA is the electron affinity. The chemical potential μ of DFT measures the escaping tendency of the electrons from the system. The slope, $(dE/dN)_Z$, of equation 2 is equal to the chemical potential μ of DFT.[15] Equation 3 was used by Perdew and coworkers to derive[16]

$$\varepsilon_{max} = \begin{cases} -\text{IP} \ (Z - 1 < N < Z) \\ -\text{EA} \ (Z < N < Z + 1) \end{cases} \tag{4}$$

where ε_{max} is the maximum Kohn-Sham (KS) occupied orbital energy. The interpretation of equation 3 is that the highest occupied KS orbital energy of an N-electron system is the negative of the ionization potential within exact KS-DFT.[17] Because of the discontinuity in μ in equation 2, it can be inferred from equation 3 that $\mu = -\text{IP}$ for all the $Z-1 < N < Z$ and $\mu = -\text{EA}$ for all $Z < N < Z+1$. When $N = Z$, μ becomes the average value $\mu = -(\text{IP}+\text{EA})/2$ which is related to the Mulliken definition of electronegativity χ.[18] According to Mullikens definition, $\chi = (\text{IP}+\text{EA})/2$. In an analogous way, from equation 4, when $Z-1 < N < Z$, ε_{max} represents the energy of one KS orbital corresponding to the highest occupied molecular orbital (HOMO), whereas when $Z < N < Z+1$, ε_{max} represents the KS energy of the orbital corresponding to the lowest unoccupied molecular orbital (LUMO) of the Z electron system or the HOMO of the $Z+1$ electron system.

The concept of chemical hardness (η) was developed from the formulation of Parr and Pearson.[19] This is the second derivative of E with respect to N according to

$$\eta = \left(\frac{\partial^2 E}{\partial N^2}\right)_Z = \left(\frac{\partial \mu}{\partial N}\right)_Z \tag{3}$$

this definition can be expressed in terms of the KS orbitals as the gap between the HOMO-LUMO energies. Within Hartree-Fock (HF) theory, the interpretation of the orbitals energies is done according to

$$I_i = E_{HF}(n - 1, i) - E_{HF}(N) \tag{4}$$

where I_i is the ionization potential of an electron in an orbital ϕ_i, $E_{HF}(N)$ is the energy of the N-electron system before ionization and $E_{HF}(N-1,i)$ is the energy of the system after removal of the electron from ϕ_i. From Koopmans theorem arises the assumption that the removal of an electron from ϕ_i, will generate a stable conformation with respect to further variation in ϕ_i. This approach neglects the fact that the removal of an electron produces a rearrangement in the spatial charge distribution in the remaining orbitals which leads to the stabilization of the ion. In a similar way as with the HF approach, with DFT, the application of the frontier molecular orbital approach is valid within the region of validity of the Koopmans theorem.[20] Politzer *et al.*,[20] have shown that the hybrid DFT functionals in spite of producing a systematic deviation from the experimental ionization potentials, produce the same deviation for all of the valence orbitals of the same molecular system. Larger deviations were obtained for different molecular systems, but these deviations are still smaller than 58 kJ·mol^{-1}.

In the present work we investigate the existence of structure-reactivity relationships for the reactions of different transition metals, lanthanide and a group 13 oxide towards H_2O_2 and its decomposition product the HO radical. For this we use cluster models of the oxides together with DFT calculations. Applying concepts derived from frontier-molecular-orbital theory, the following properties of the reacting surface atoms or clusters: IP, EA, and χ; obtained from DFT are discussed as possible descriptors of the reactivity of the oxides with HO$^{\bullet}$ and H_2O_2. The BEP relation between adsorption energy of the product HO$^{\bullet}$ and the activation energy for H_2O_2 decomposition is also investigated. Quantities obtained from experimental data retrieved from literature are correlated with our DFT data. Good correlations were obtained between reactivity descriptors for the metal oxides and experimental data for H_2O_2 reactivity.

Results and discussion

The reaction of H_2O_2 with clusters of some transition metal oxides was as previously described by our group.[21] The same methodology applied then is applied here. Our clusters consist of the smallest possible stoichiometric units of the metal oxides, of the type

$(M_xO_y)_n$, where M is the metal oxide cation and n is the number of stoichiometric units of the metal oxide. The values of n are 1 or 2 depending on if the oxide is of the type M_2O_3 or MO_2 respectively. The terminations of the stoichiometric clusters were truncated with H atoms following a procedure that has been used successfully for studying TiO_2 surfaces with very small cluster models.[22] Also previous works done by our group show that this can be applied to a series of other oxides producing good data when compared with experimental values.[21a, 23] These clusters were then further hydroxylated with the products of H_2O dissociative adsorption – (HO^-) and (H^+) binding to the cation and to the O atoms respectively. This procedure decreases the coordinative unsaturation of the models which leads to a more realistic modeling of the surfaces of the oxides in solution.[24] When exposed to water – with the exception of few surface sites – the surfaces of the oxides studied here will be hydroxylated with the products of dissociative adsorption of water.[25] This process leads to a decrease in the coordinative unsaturation of the exposed surface atoms. In order to maintain a charge neutral system, the clusters of the oxides of the type M_2O_3 reacted with the products of dissociation of one water molecule and the clusters of the type MO_2 have reacted with those of two water molecules. The resultant clusters of these reactions with water are the initial reactants for the study of the reactivity of H_2O_2 and are shown in Figure 1. The most stable spin states were found to be the singlet, with the exceptions of CuO-quintet and Fe_2O_3-eleventh. The CuO cluster quintet state shown in Figure 1 is only 150 kJ·mol^{-1} more stable than the singlet state. During the course of the reactions investigated here, no spin crossover was found. It can be seen that the oxides of the elements belonging to the same group have a tendency to form similar structures upon dissociative adsorption of H_2O. For example, the model clusters of the oxides of Ti(IV), Zr(IV) and Hf(IV) (elements of the group IV) show structural similarities among them in what concerns the way the HO^- groups bind to the structures. Ni(IV) and Pd(IV) (elements of the group X) also form similar structures upon the dissociative adsorption of H_2O. Overall, in terms of structural similarities we can divide the clusters into two groups according to the stoichiometry of the oxides – $i.e.$ the oxides of the type MO_2 and M_2O_3.
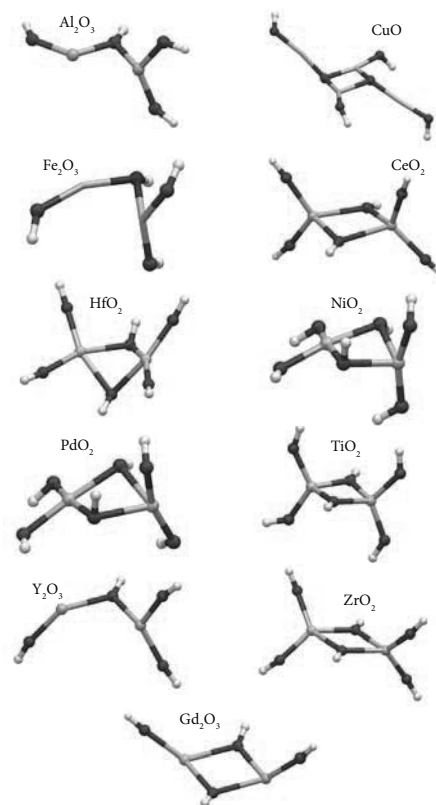

Figure 1. Structures of the hydroxylated clusters used to study the adsorption and further decomposition of H_2O_2. The clusters consist of stoichiometric units of the mentioned oxides, where H_2O has been dissociatively adsorbed. Metal (⬤), O (⬤), H(◯).

The first step studied for the reaction of H_2O_2 with the clusters was the molecular adsorption. This procedure was done previously to model the decomposition of H_2O_2 in aqueous solution and has produced data in very good agreement with experiments.[21a, 26] Analogously, in the present case, upon addition of H_2O_2 to the clusters, for all oxides, a structure corresponding to the molecular adsorption of H_2O_2 was found. We only investigated the reactions of H_2O_2 with the oxides for which there are coherent literature data to compare with. The resulting geometries are shown in Figure 2.
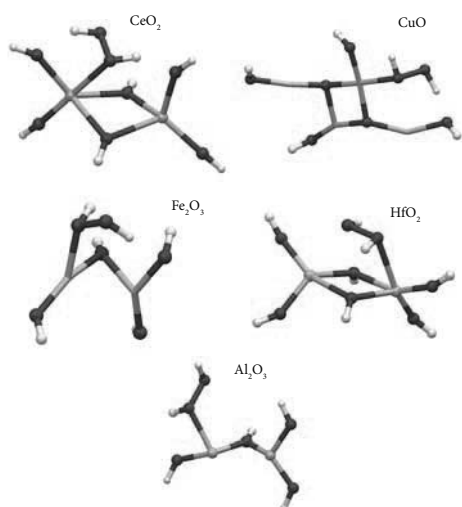
Figure 2. Adsorption of H_2O_2 onto hydroxylated clusters of CeO_2, CuO, Fe_2O_3, HfO_2 and Al_2O_3. Metal cation (⚪), O (⚫), H(◯).

In order to form the molecular adsorption structure, H_2O_2 binds to the clusters by direct interaction of its O atoms with the oxide metal cation. Another type of interaction present is hydrogen bonding, and in this case H_2O_2 acts both as a donor and acceptor. From these energy minima, H_2O_2 undergoes decomposition to form stable products. The obtained structures of the transition-states for the decomposition of H_2O_2 are shown in Figure 3. And the reaction energy barriers are given in Table 1.

The transition-states shown in Figure 3 are similar to those previously obtained for clusters of the transition metal oxides ZrO_2, TiO_2 and Y_2O_3.[21a] For all the oxides studied then and now, the decomposition of H_2O_2 consists of a first molecular adsorption step followed by the cleavage of its O-O bond. The only exception is Fe_2O_3. In this case, the decomposition of H_2O_2 follows the path involving the cleavage of the H-OOH bond to form a -O-H_2O- structure and a surface O radical. This reaction has been discussed as a possible pathway for the decomposition of H_2O_2.[27] Though, for all oxides studied so far with our cluster models, with the exception of Fe_2O_3, this is a side reaction and not the main reaction path because of its higher energy barrier and lower exothermicity than the cleavage of the O-O bond.
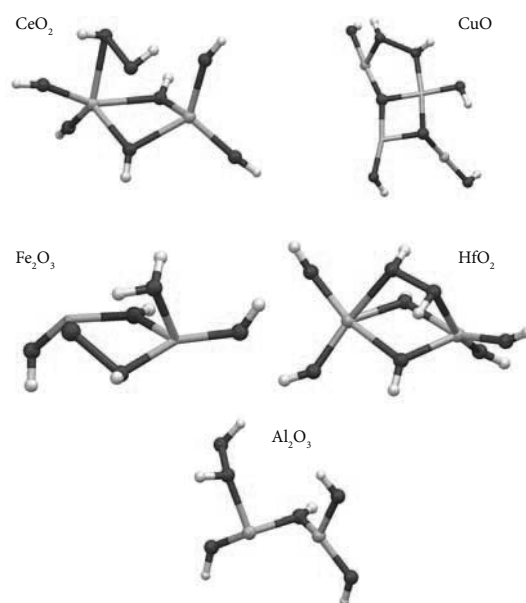

Figure 3. Transition-states for the decomposition of H_2O_2 catalyzed by hydroxylated clusters of CeO_2, CuO, Fe_2O_3, HfO_2, Al_2O_3. Metal cation (⚪), O (⚫), H(◯).

Table 1. Obtained reaction energy barriers with zero point energy correction (E_a^{ZPE}), molecular adsorption energy of H_2O_2 ($\Delta E_{ads}(H_2O_2)$); reaction energy (ΔE_r) for the decomposition of H_2O_2 on the surfaces of the clusters shown in Figure 2 and the BEP coefficient obtained from equation 1 (α_{BEP}). The transition-state structures are shown in Figure 3. Energy values are in kJ·mol⁻¹.

Oxide	$\Delta E_{ads}(H_2O_2)$	E_a^{ZPE}	ΔE_r	α_{BEP}
CeO_2	-88	60	-435	0.68
CuO	-62	71	-358	1.15
Fe_2O_3	-150	11	-320	0.07
HfO_2	-54	56	-573	1.22
Al_2O_3	-66	36	-153	0.55
ZrO_2 [a]	-150	42	-634	0.28
TiO_2 [a]	-68	41	-490	0.60
Y_2O_3 [a]	-92	45	-684	0.49

a) Data retrieved from ref [21b]

From the BEP coefficients shown in Table 1 (equation 1), it can be seen that the type of transition-states for the cleavage of H_2O_2 vary considerably in terms of the BEP classification methodology. The decomposition of H_2O_2 cannot be easily categorized within the two major classes of surface reactions for all the oxides. For some of the oxides the decomposition of H_2O_2 is more structure sensitive than for others. Fe_2O_3 produces the more structure sensitive reaction path and HfO_2 the less structure sensitive. Relaxing the transition-states obtained (Figure 3) leads to the formation of the products shown in Figure 4. The corresponding reaction energies are shown in Table 1.
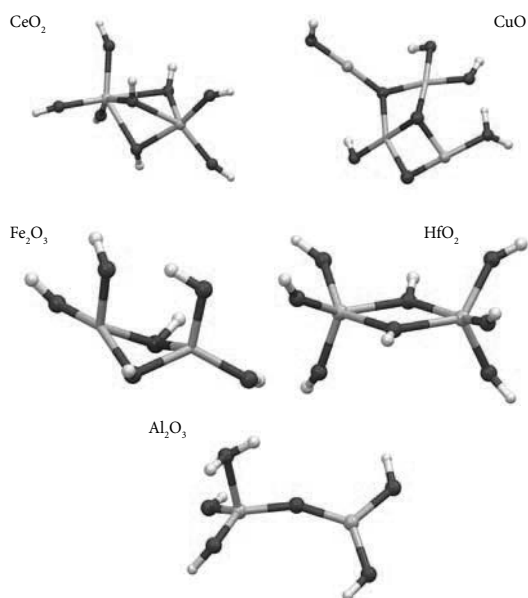

Figure 4. Products of the decomposition of H_2O_2 catalyzed by hydroxylated clusters of CeO_2, CuO, Fe_2O_3, HfO_2 and Al_2O_3. Metal cation (⬤), O (⬤), H(◯).

The primary stable products consist of both adsorbed HO radical and H_2O. These interact with the clusters by forming bonded states with the metal cations, via the unpaired electron of $HO^\bullet$ and the available non-bonding electrons more localized on the O atom in H_2O. These products had been reported previously as the primary products of the decomposition of H_2O_2 for ZrO_2, TiO_2 and Y_2O_3.[21a, 27a] Here a similar mechanism for the formation of surface adsorbed H_2O is also seen. It consists of the abstraction of a structural H atom by the $HO^\bullet$ resultant of the cleavage of the O-O bond in H_2O_2 –

the H atom is initially bound to an O atom of the cluster. This process leads to formation of adsorbed H_2O and to a surface O radical. The only cases where the primary product formed consists of 2 adsorbed HO radicals are Fe_2O_3 and HfO_2. This is interesting since the obtained transition state for H_2O_2 decomposition on Fe_2O_3 is an H atom transfer from H_2O_2 to a surface HO group which would indicate that water could be the primary product. Relaxing this geometry leads to a rearrangement of the structure which spontaneously forms 2 adsorbed HO radicals. This suggests that the H atom transfer mechanism might play an important role in the decomposition of H_2O_2 even in the cases where the main mechanism does not involve this process. We have recently published an experimental study that presents evidence for the importance of this reaction pathway – with surface adsorbed H atoms as a product of the decomposition of H_2O_2.[28] Under certain conditions, this process can ultimately lead to the formation of H_2. In an extensive comparison for H_2O_2 reactivity done for a series of transition metal oxides, it has been demonstrated that Fe_2O_3 behaves differently from the other oxides in terms of kinetic parameters and $HO^\bullet$ formation dynamics. The contribution of the Fenton reaction for the measured experimental energy barrier has been suggested. This would mean that the experimental data for Fe_2O_3 would have a contribution from a redox process which could also explain the discrepancy with our DFT data. [29]

χ,IP, EA, and ΔE_{ads} (2HO$^\bullet$) as reactivity descriptors for the decomposition of H_2O_2 catalyzed by transition metal, lanthanide and aluminum oxides

In this section we discuss the applicability of reactivity descriptors to the reaction of decomposition of H_2O_2 catalyzed by the oxides: ZrO_2, TiO_2, PdO_2, NiO_2, HfO_2, Fe_2O_3, Y_2O_3, Al_2O_3, Gd_2O_3, CeO_2 and CuO. Whenever possible, we use reactivity descriptors whose parameters are values extracted from the literature and from our DFT calculations and apply correlations with our DFT calculations or the literature data respectively.

One correlation that we previously discussed is how the ionization potential of the metal cation present on the oxide influences the adsorption energy of HO radicals. This can be explained with the fact that upon adsorption of the HO radical, some of the electron density initially localized on the orbitals of the surface exposed metal
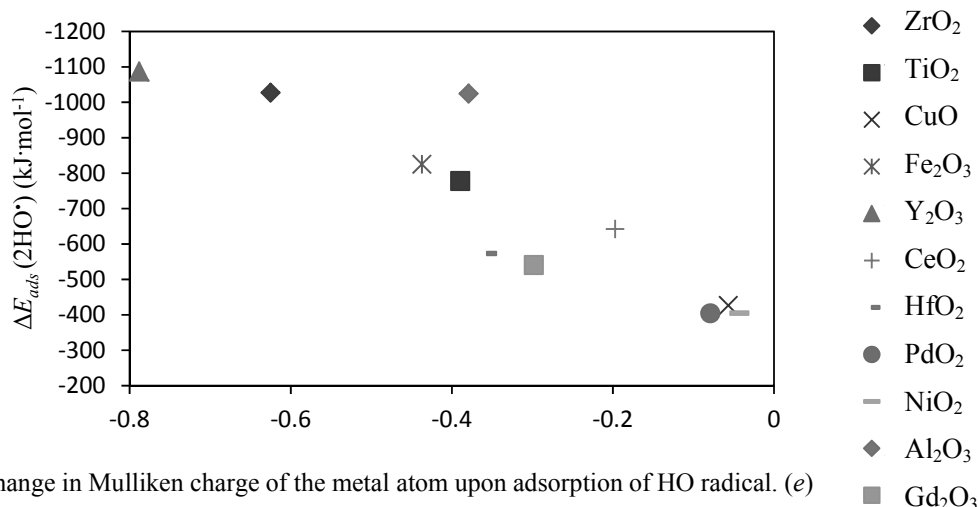
Figure 5. Adsorption energy (ΔE_{ads} (2HO$^\bullet$)) of 2HO radicals as a function of the change in Mulliken charge of the metal cations accommodating the HO radicals (e). The value of e is an average of the individual e of the cations involved in the bonding with the 2HO$^\bullet$. Data obtained with DFT calculations using the minimal cluster models of the oxides (Figure 1).

atom, has to be delocalized in order to form bonding states with the unpaired electron of the HO radical. This causes the partial oxidation of the metal atoms that bind to the HO$^\bullet$. Following this, we discuss here how the changes in Mulliken charge of the metal atom correlate with the adsorption energy of the HO radicals for the various materials considered. We studied the adsorption energies of 2 HO radicals onto each of the hydroxylated clusters shown in Figure 1. The resulting plot showing the adsorption energy of the HO radicals as a function of the change in Mulliken charge (e) of the cations of the clusters is shown in Figure 5. The values for the change in Mulliken charges (e) were obtained as $e = Mp\text{-}Mr$. Where Mp is the Mulliken charge of the cations in the product, and Mr is the Mulliken charge of the cations in the reactant. The cations considered here are those to which the 2 HO radicals bind upon adsorption. It can be seen in Figure 5 that there is a correlation between the adsorption energies of HO and the values e. The easier it is to delocalize electron density from the surface metal cation orbitals in order to form bonding states with the HO$^\bullet$, the stronger these bonds will be. Ultimately the strength of these bonds will have implications on the mechanism of decomposition of H$_2$O$_2$ because it is

expected that for the cases where the adsorption of HO$^\bullet$ is stronger, surface poisoning by HO$^\bullet$ should affect the overall reaction mechanism. On the other hand for the cases where HO$^\bullet$ adsorption onto the surface is weaker, the HO$^\bullet$ will probably be able to react with H$_2$O$_2$ to form H$_2$O and HO$_2^\bullet$. The main outlier in the trend of Figure 5 is Al$_2$O$_3$. This can be reasoned with the fact that Al does not have d-orbitals or f-orbitals forming its valence shell. The more "adsorbate readily available" shape of the $2p$ orbitals accommodating the valence electrons of Al^{3+} might explain why a smaller change in e for this cation, leads to a stronger ΔE_{ads} for HO$^\bullet$.[30]

A measure of the tendency of an atom to attract electrons towards itself, is the Pauling electronegativity χ_P.[31] A plot of the ΔE_{ads} of 2 HO$^\bullet$ as a function of χ_P is shown in

Figure **6**.
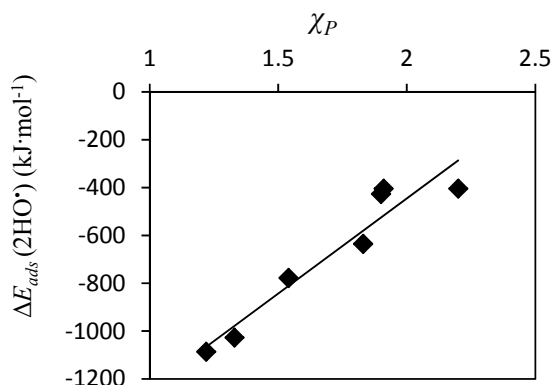
Figure 6. Adsorption energy of 2 HO radicals ($\Delta E_{ads}(2HO^{\bullet})$) obtained with DFT calculations using minimal cluster models of the oxides (Figure 1), as a function of the Pauling electronegativity of the transition metal atom present in the oxide (χ_P). χ_P are experimental data retrieved from literature.[32]

There is a good correlation (*i.e.* correlation coefficient of 0.92) between the Pauling electronegativity of the metal atom (in oxidation state 0) and the adsorption energy of the HO$^{\bullet}$. This correlation holds for the transition metal oxides. This can be explained with the following basis. The Pauling electronegativity is determined for the element in oxidation state 0. The removal of electrons to form the cationic species found in the oxides will cause relaxation of the electrons of the cation to minimize the energy of the new electron configuration. This relaxation will be different depending on the type of orbitals occupied in the different cations. Thus is expected that the more different the occupied orbitals are, the more different is the relaxation contribution that influences the shape and energy of the final relaxed orbitals after formation of the cationic species. From

Figure **6** we can state that for the transition metal oxide clusters here studied: ΔE_{ads} (2HO$^{\bullet}$) $\approx$ (796 $\times$ χ_P - 2036).

Experimental literature data for the Arrhenius activation energies for decomposition of H_2O_2 on the surfaces of several oxides as well as the DFT data from this work and literature data are shown on

Table **2**.

Table 2. Experimental Arrhenius activation energies (E_a); DFT electronic activation energies with zero-point-energy-corrections (E_a^{ZPE}) for decomposition of H_2O_2 on the surface of different oxides; and adsorption energies of 2 HO radicals onto the hydroxylated clusters of the oxides ΔE_{ads} (HO). All values in kJ·mol^{-1}.

Material	Experimental	DFT	
	E_a	E_a^{ZPE}	ΔE_{ads} (HO$^{\bullet}$)
ZrO$_2$	33 ± 1[a]	42[b]	-1028
TiO$_2$	37 ± 1[b]	41[b]	-778
Y$_2$O$_3$	44 ± 5[b]	45[b]	-1087
Fe$_2$O$_3$	51 ± 1[c]	11	-824
CeO$_2$	40 ± 1[c]	60	-642
CuO	76 ± 1[c]	71	-427
HfO$_2$	60 ± 1[c]	56	-572
Al$_2$O$_3$	38[d]	36	-1025
NiO$_2$	–	–	-404
PdO$_2$	–	–	-404
Gd$_2$O$_3$	63 ± 1[c]	–	-540

a) Ref.[26] b) Ref.[21b] c) Ref.[29] d) Ref. [33]

The DFT obtained energy barriers for H_2O_2 decomposition are in reasonable good agreement with the available experimental data (

Table **2**). The larger deviation found for CeO$_2$ and the fact that it was not possible to locate a transition-state for H_2O_2 decomposition on the Gd$_2$O$_3$ cluster show the limitations of the DFT methodology in describing the chemistry of lanthanides, especially that of Gd.[34] The transition-states for decomposition of H_2O_2 are a challenging system from a computational chemistry perspective. They consist of semi-radical states which are usually difficult to reproduce with DFT.[35] The transition-state for CeO$_2$ was found and the reaction energy barrier lays 20 kJ·mol^{-1} above the experimentally determined value. Though the levels of theory used were able to describe with good accuracy the adsorption of HO radicals and the electronic properties of the clusters and of the cations present in the clusters. This will be discussed in the next section of this paper.

Following the concept by BEP, we plotted the adsorption energy of the HO radicals as a function of the experimental Arrhenius activation energy barriers. The adsorption of the HO radical (due to its higher

8

exothermicity) contributes the most for the overall reaction energy when compared with the contribution from H_2O molecular adsorption. This last lays in the range -50 to -100 kJ·mol^{-1} for similar clusters of ZrO_2, TiO_2 and Y_2O_3.[23]
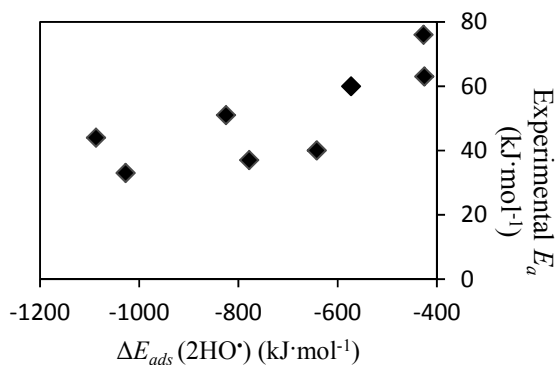

Figure 7. Experimental Arrhenius activation energies for H_2O_2 decomposition (E_a) as a function of the adsorption energies of 2HO radicals (ΔE_{ads} (2HO$^{\bullet}$)) obtained with DFT calculations using minimal cluster models of the oxides (Figure 1). Data from Table 2.

It is visible (Figure 6) that, following the BEP principle, the more exothermic is the adsorption of the HO radicals onto the oxide the lower is the activation energy barrier for H_2O_2 decomposition. It is worth of notice that the clusters used to study the adsorption energies of HO$^{\bullet}$ consisted of 1 or 2 stoichiometric units of the metal oxides. The good trend obtained by plotting these adsorption energies against the experimental energy barriers, indicates that in the real particle systems where H_2O_2 undergoes decomposition, the adsorption of product is a localized phenomenon. Worth remarking is also the fact that the reactions where the experimental energies were measured consisted of particle suspensions in solution. Our reactant cluster models consist of minimal sized clusters of stoichiometric units of the metal oxides whose terminations were truncated with H atoms and further hydroxylated. As our DFT data is for gas phase and given the good agreement with experiments, it seems plausible that the solvation effects have a small contribution for the energy of the reactions of adsorbed species during H_2O_2 decomposition in the real systems. Nevertheless the extent and stability of the surface hydroxylation have an impact on the activation

energy barriers for H_2O_2 decomposition as it will be shown. In order to verify how the local properties of the surface atoms correlate with the experimental activation energies for H_2O_2 decomposition, we plotted the experimental data as a function of the DFT values for I.P. and Mulliken electronegativities (χ) of the cations present in the oxides (Figures 8 and 9).
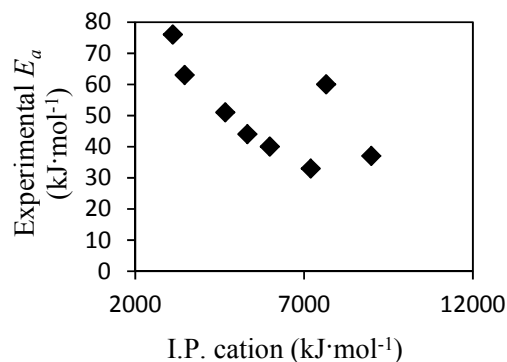

Figure 8. Experimental Arrhenius activation energies (E_a) as a function of the ionization potential of the cation present in the metal oxide.
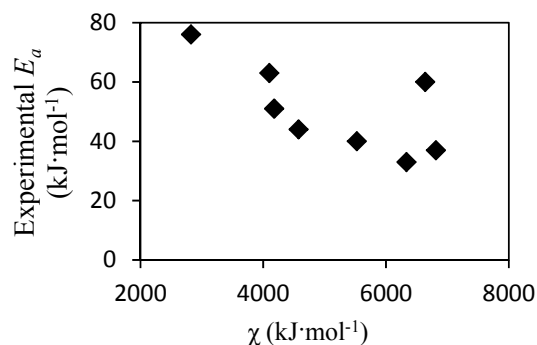

Figure 9. Experimental Arrhenius activation energies (E_a) as a function of the DFT Mulliken electronegativities (χ) of the cations present in the metal oxide.

The I.P. values (Figure 8) are the SCF converged HOMO energies of the cations in the oxidation states present in the oxides, calculated at the PBE0/LACV3P++** using fully analytical accuracy and the maximum grid density, in gas phase. In a similar way, for the determination of χ (Figure 9), the E.A. values used are the corresponding LUMO energies of the cations, in the oxidation states found in the oxides, in gas phase. The trend in Figure 8

does not follow a direct BEP relation in the sense that a lower I.P. of the cation means that the adsorption of HO radical product is more exothermic and as such the energy barrier for the reaction would be lower with decreasing I.P. This simple correlation – depending only on the parameter: product adsorption energy – would be true for a reaction occurring on a dry surface (*e.g.* in UHV conditions). It has been previously discussed that the I.P. is proportional to the Lewis acidity of the cation present in the oxide.[21b, 36] In aqueous media this means that the more Lewis acidic is the cation, the stronger it will bond with the HO^- groups resulting from dissociative adsorption of H_2O. This will lead to more extensive surface reconstruction and make the reactive surface site less available for accommodating H_2O_2 and its decomposition products ultimately leading to an increase in the energy barrier for H_2O_2 decomposition at those cations which are more Lewis acidic. This trend is visible in the plot of Figure 8. Also, these different hydroxylation effects will, for the different materials, lead to different contributions (*i.e.* from geometric and electronic effects) to the BEP relation which causes its deviation from linearity.[36]

The good correlation between both properties (i.e. IE and χ) and the experimental data, indicates that the reaction of H_2O_2 in the real particle systems is determined by localized phenomena which is dependent on properties of the cations such as the I.P. or χ. This had been previously suggested by our group for ZrO_2, TiO_2 and Y_2O_3 cases. The present work demonstrates that this relation is valid for a series of 8 oxides, 2 of which are lanthanides. The outlier is HfO_2. This can be explained with the fact that even though hybrid DFT shows good performance for determining the HOMO/LUMO energies even for lanthanides,[37] Hf is a special case in the sense that relativistic effects have to be considered, but the quasirelativistic ECP scheme applied here to Hf, implemented by Cundari and Stevens was parameterized for lanthanides with oxidation states 2+ and 3+.[38] This fact contributes to the deviation in HOMO/LUMO energies prediction for Hf^{4+}.[39]

Besides the theoretical limitations of DFT in accounting for energy barriers for lanthanide reactions, another reason for the higher discrepancies of our DFT energy barriers for Fe_2O_3 and CeO_2 when compared with the experimental data can be explained with the adsorption process of H_2O_2. This is a fairly loose process with more degrees of freedom than the decomposition (which is rigid in comparison). Our cluster models studied here, given their small size, are not a complete representation of the surface in accounting for all the possible adsorption geometries that contribute to the overall adsorption energy of H_2O_2. Nevertheless with the exception of CeO_2 and Fe_2O_3, the average absolute deviation from the experimental energy barriers shown in Table 1 is 4 kJ.mol^{-1}. The origin of the discrepancy for CeO_2 can be attributed to the DFT limitations in modeling lanthanide reactivity. It is plausible that for Fe_2O_3, the transition-state predicted here with DFT does not correspond to the process determining the energy barrier in the real system.

Conclusions

Our minimal sized clusters were able to reproduce, with a slight deviation of 4 kJ·mol^{-1}, the experimental data for decomposition of H_2O_2 on the surface of 8 oxides. The exceptions to this good agreement are CeO_2 and Fe_2O_3. By plotting the experimental data against DFT calculated reactivity descriptors we found good correlations which agree with well-established Brønsted-Evans-Polanyi principle. Overall we found that:

- The adsorption of HO radicals causes delocalization of electron density of the metal cation accommodating those radicals. The more delocalization occurs, the more exothermic is the adsorption of HO$^•$ onto those surface atoms.
- For the oxides of the transition metal oxides, the adsorption energy of HO radicals is inversely proportional to the Pauling electronegativity of the metal atom present in the oxide.
- There is a correlation between the adsorption energies of the HO radicals and the energy barrier for H_2O_2 decomposition. The stronger is the adsorption of product HO, the lower is the energy barrier, following the BEP principle.
- Both the DFT ionization potential and the Mulliken electronegativity of the bare metal cation (in the same oxidation state as it is present in the oxide) are inversely proportional to the energy barrier for H_2O_2 decomposition. This because the ionization potential is related with Lewis acidity of the cation which in turn determines the extent of its hydroxylation. The Mulliken electronegativity is related with the ease

of delocalizing electron density from the metal cation.

All the reactivity descriptors obtained with DFT were calculated using minimal sized clusters consisting of one or two stoichiometric units of the oxides. Given the very good correlations between computational and experimental data we can state that for real oxide materials, the processes that account for the pathway and energetics of the decomposition of H_2O_2 are *very* localized (*i.e.* at the atomic scale) and are highly dependent on the local properties of the cations present in the oxides.

Computational Details

DFT calculations were performed using the Molecular Cluster Model (MCM)[40] approach and the software package Jaguar 7.7.(Ref.[41]). Cluster geometries of the transition metals were optimized using the hybrid functional B3LYP (Refs. [42]) with the LACVP+* basis set. The basis set LACVP+* is a combination of the split valence basis set 6-31+G(d) and the Los Alamos effective core potential (ECP) for the transition metals studied here. The functional PBE0 (Refs. [43]) has shown improved performance over other hybrid functionals in describing lanthanide and heavy metal chemistry.[44] For the clusters of HfO_2, CeO_2 and Gd_2O_3 the geometries were optimized using the PBE0 functional and the CSDZ+* basis set for the metal atoms and 6-31G+* for H and O. CSDZ is the implementation in Jaguar of the Cundari and Stevens ECP basis set for lanthanides.[38] Single-point evaluations of the energies were performed using PBE0 with LACV3P++** basis set for the clusters of transition metals. For HfO_2, CeO_2 and Gd_2O_3 we used the CSDZ++** basis set for the metal atoms and the 6-311G++** for the O and H atoms. The basis set LACV3P++** is triple-ζ in the valence space and is supplemented with polarization and diffuse functions on all atoms. For the non-lanthanides, the Mulliken electronegativities of the cations present in the metal oxides were determined from the I.P and E.A. both calculated at the PBE0/LACV3P++** using fully analytical accuracy and the maximum grid density.

Tight SCF convergence criteria were used for all calculations. Transition states were located using the quadratic synchronous transit (QST) method implemented in Jaguar 7.7. To characterize the stationary points and make vibrational zero point energy corrections, a frequency analysis was done for all stationary points. All transition states were found to have one imaginary frequency.

The adsorption energies reported herein were calculated as

$$\Delta E_{ads} = E_{adsorbate/cluster} - (E_{adsorbate} + E_{cluster}) \qquad (5)$$

were $E_{adsorbate/cluster}$, $E_{adsorbate}$, $E_{cluster}$, represent the electronic energies for the adsorbate binding to the cluster, free adsorbate and bare cluster respectively. This means that the more negative the adsorption energy, the stronger is the adsorption.

Corrections to obtain the thermodynamic potential enthalpy (H) were calculated from a Hessian matrix of harmonic force constants using the partition functions of an ideal -/non-interacting gas at $T = 298.15$ K and $P = 1$ atm. The vibrational frequencies obtained from the Hessian matrix were also used to verify the first-order saddle point nature of the transition states.

References

[1] R. A. van Santen and M. Neurock, *Principles of Molecular Heterogeneous Catalysis*, Wiley-VCH Verlag GmbH & Co. KGaA, **2007**, p. 19-81.
[2] A. Nilsson and L. G. M. Pettersson in *Chapter 2 - Adsorbate Electronic Structure and Bonding on Metal Surfaces*, *Vol.* Elsevier, Amsterdam, **2008**, pp. 57-142.
[3] a) B. Hammer and J. K. Nørskov in *Theoretical surface science and catalysis—calculations and concepts*, *Vol. Volume 45* (Ed. H. K. Bruce C. Gates), Academic Press, **2000**, pp. 71-129; b) M. Mavrikakis, B. Hammer and J. K. Nørskov, *Physical Review Letters* **1998**, *81*, 2819-2822; c) D. M. Newns, *Physical Review* **1969**, *178*, 1123-1135; d) T. Olsen and J. Schiotz, *The Journal of Chemical Physics* **2010**, *133*, 034115-034111; e) P. W. Anderson, *Physical Review* **1961**, *124*, 41-53.
[4] a) E. Shustorovich, *Surface Science Reports* **1986**, *6*, 1-63; b) E. Shustorovich in *The Bond-Order Conservation Approach to Chemisorption and Heterogeneous Catalysis: Applications and Implications*, *Vol. Volume 37* Eds.: H. P. D.D. Eley and B. W. Paul), Academic Press, **1990**, pp. 101-163.

[5] a) A. P. Angelopoulos, *Journal of Colloid and Interface Science* **2001**, *243*, 292-299; b) M. F. Luo and G. R. Hu, *Surface Science* **2009**, *603*, 1081-1086.

[6] a) J. N. Bronsted, *Chemical Reviews* **1928**, *5*, 231-338; b) M. G. Evans and M. Polanyi, *Transactions of the Faraday Society* **1938**, *34*, 11-24.

[7] B. Hammer, *Topics in Catalysis* **2006**, *37*, 3-16.

[8] R. A. Vansanten and M. Neurock, *Catalysis Reviews-Science and Engineering* **1995**, *37*, 557-698.

[9] J. Jung, H.-J. Shin, Y. Kim and M. Kawai, *Journal of the American Chemical Society* **2011**, *133*, 6142-6145.

[10] C. A. Scamehorn, N. M. Harrison and M. I. McCarthy, *The Journal of Chemical Physics* **1994**, *101*, 1547-1554.

[11] R. A. Santen and M. Neurock, *Russian Journal of Physical Chemistry B* **2007**, *1*, 261-291.

[12] a) K. D. Rendulic, *Applied Physics A* **1988**, *47*, 55-62; b) A. Haras, H. A. Duarte, D. R. Salahub and M. Witko, *Surface Science* **2002**, *513*, 367-380.

[13] A. Haras, M. Witko, D. R. Salahub and H. A. Duarte, *Surface Science* **2003**, *538*, 160-170.

[14] a) A. Vektariene, G. Vektaris and J. Svoboda, *Arkivoc* **2009**, 311-329; b) J. Martínez, *Chemical Physics Letters* **2009**, *478*, 310-322; c) M. Karelson, V. S. Lobanov and A. R. Katritzky, *Chemical Reviews* **1996**, *96*, 1027-1044.

[15] R. G. Parr, R. A. Donnelly, M. Levy and W. E. Palke, *The Journal of Chemical Physics* **1978**, *68*, 3801-3807.

[16] J. P. Perdew, R. G. Parr, M. Levy and J. L. Balduz, Jr., *Physical Review Letters* **1982**, *49*, 1691-1694.

[17] a) J. P. Perdew and M. Levy, *Physical Review B* **1997**, *56*, 16021-16028; b) J. Katriel and E. R. Davidson, *Proceedings of the National Academy of Sciences* **1980**, *77*, 4403-4406.

[18] R. S. Mulliken, *The Journal of Chemical Physics* **1934**, *2*, 782-793.

[19] R. G. Parr and R. G. Pearson, *Journal of the American Chemical Society* **1983**, *105*, 7512-7516.

[20] P. Politzer and F. Abu-Awwad, *Theoretical Chemistry Accounts* **1998**, *99*, 83-87.

[21] a) C. M. Lousada, A. J. Johansson, T. Brinck and M. Jonsson, *The Journal of Physical Chemistry C* **2012**, *116*, 9533-9543; b) *Phys. Chem. Chem. Phys.*, DOI:10.1039/C3CP44559C., p.

[22] a) F. Rittner, R. Fink, B. Boddenberg and V. Staemmler, *Physical Review B* **1998**, *57*, 4160-4171; b) F. Rittner, B. Boddenberg, R. F. Fink and V. Staemmler, *Langmuir* **1998**, *15*, 1449-1455.

[23] *Phys. Chem. Chem. Phys.*, DOI:10.1039/C3CP44559C.

[24] J. R. T. Johnson and I. Panas, *Inorganic Chemistry* **2000**, *39*, 3181-3191.

[25] J. Ahdjoudj and C. Minot, *Surface Science* **1998**, *402-404*, 104-109.

[26] C. M. Lousada and M. Jonsson, *The Journal of Physical Chemistry C* **2010**, *114*, 11202-11208.

[27] a) A. Thetford, G. J. Hutchings, S. H. Taylor and D. J. Willock, *Proceedings of the Royal Society A: Mathematical, Physical and Engineering Science* **2011**, *467*, 1885-1899; b) W. F. Huang, P. Raghunath and M. C. Lin, *Journal of Computational Chemistry* **2011**, *32*, 1065-1081.

[28] J. A. L. Cláudio M. Lousada, and Mats Jonsson, *Journal of Physical Chemisty C* **2013**.

[29] M. Y. Cláudio M. Lousada, Kristina Nilsson, and Mats Jonsson, *Applied Catalysis - Section A* **2013**.

[30] A. Nilsson and L. G. M. Pettersson in *Adsorbate Electronic Structure and Bonding on Metal Surfaces*, Vol. Elsevier, Amsterdam, **2008**, pp. 57-142.

[31] W. B. Jensen, *Journal of Chemical Education* **1996**, *73*, 11.

[32] *CRC, Handbook of Chemistry and Physics*, CRC Press, Cleveland, OH, **1997**, p.

[33] A. Hiroki and J. A. LaVerne, *The Journal of Physical Chemistry B* **2005**, *109*, 3364-3370.

[34] a) O. Eisenstein and L. Maron, *Journal of Organometallic Chemistry* **2002**, *647*, 190-197; b) Y. Luo, P. Selvam, M. Koyama, M. Kubo and A. Miyamoto, *Chemistry Letters* **2004**, *33*, 780-785.

[35] A. Bassan, M. R. A. Blomberg, P. E. M. Siegbahn and L. Que, *Journal of the American Chemical Society* **2002**, *124*, 11056-11063.

[36] J. K. Norskov, T. Bligaard, B. Hvolbaek, F. Abild-Pedersen, I. Chorkendorff and C. H. Christensen, *Chemical Society Reviews* **2008**, *37*, 2163-2171.

[37] C. Xiaoyan and D. Michael, *Molecular Physics* **2003**, *101*, 2427-2435.

[38] T. R. Cundari and W. J. Stevens, *The Journal of Chemical Physics* **1993**, *98*, 5555-5565.

[39] D. A. Pantazis and F. Neese, *Journal of Chemical Theory and Computation* **2009**, *5*, 2229-2238.

[40] P. Deák, *physica status solidi (b)* **2000**, *217*, 9-21.

[41] in *Jaguar 7.7*, Vol. Schrodinger, LLC New York **2010**.

[42] a) A. D. Becke, *Physical Review A* **1988**, *38*, 3098; b) C. Lee, W. Yang and R. G. Parr, *Physical Review B* **1988**, *37*, 785; c) A. D. Becke, *The Journal of Chemical Physics* **1993**, *98*, 5648-5652; d) P. J. Stephens, F. J. Devlin, C. F. Chabalowski and M. J. Frisch, *The Journal of Physical Chemistry* **1994**, *98*, 11623-11627.

[43] a) K. Burke, M. Ernzerhof and J. P. Perdew, *Chemical Physics Letters* **1997**, *265*, 115-120; b) C. Adamo and V. Barone, *The Journal of Chemical Physics* **1999**, *110*, 6158-6170.

[44] V. Vetere, C. Adamo and P. Maldivi, *Chemical Physics Letters* **2000**, *325*, 99-105.

[45] a) X. Xu, H. Nakatsuji, M. Ehara, X. Lu, N. Q. Wang and Q. E. Zhang, *Chemical Physics Letters* **1998**, *292*, 282-288; b) X. Lü, X. Xu, N. Wang, Q. Zhang, M.

Ehara and H. Nakatsuji, *Chemical Physics Letters* **1998**, *291*, 445-452.